# STUDIES OF MICROSTRUCTURES, OPTICAL, NANOMECHANICAL AND THERMAL EXPANSION PROPERTIES OF $Y_2O_3$, $ZrO_2$, $CeO_2$ AND $Gd_2O_3$ THIN FILMS AND $Y_2O_3/ZrO_2$ AND $CeO_2/Gd_2O_3$ MULTILAYERS PREPARED BY PULSED LASER DEPOSITION

*By*

**MANEESHA MISHRA**

**Enrolment No: CHEM02200804001**

*Indira Gandhi Centre for Atomic Research*
*Kalpakkam, Tamil Nadu, India, 603 102*

*A thesis submitted to the*
*Board of Studies in Chemical Sciences*
*in partial fulfillment of requirements*
*for the Degree of*

**DOCTOR OF PHILOSOPHY**

***of***

**HOMI BHABHA NATIONAL INSTITUTE**

**January, 2013**

# Homi Bhabha National Institute

## Recommendations of the Viva Voce Board

As members of the Viva Voce Board, we certify that we have read the dissertation prepared by **Maneesha Mishra** entitled "**Studies of Microstructures, Optical, Nanomechanical and Thermal expansion properties of $Y_2O_3$, $ZrO_2$, $CeO_2$ and $Gd_2O_3$ thin films and $Y_2O_3/ZrO_2$ and $CeO_2/Gd_2O_3$ Multilayers Prepared by Pulsed Laser Deposition.**" and recommend that it may be accepted as fulfilling the dissertation requirement for the Degree of Doctor of Philosophy.

**Date:** 29/7/2013

Chairman- Dr. K. V. G. Kutty

PKuppusami **Date:** 29/7/2013

Convener- Dr. P. Kuppusami

**Date:** 29/07/2013

Examiner- Prof. M. K. Jayaraj

**Date:** 29/07/2013

Member 1 - Dr. S. Saroja

**Date:** 29/07/13

Member 2 - Dr. P. Ch. Sahu P. Ch. Sahu

**Date:** 29/07/2013

Technology Advisor – Shri. E. Mohandas

Final approval and acceptance of this dissertation is contingent upon the candidate's submission of the final copies of the dissertation to HBNI.

I hereby certify that I have read this dissertation prepared under my direction and recommend that it may be accepted as fulfilling the dissertation requirement.

PKuppusami

**Date:** 29/7/13

**Place:** Kalpakkam

(Dr. P. Kuppusami)

# STATEMENT BY AUTHOR

This dissertation has been submitted in partial fulfillment of requirements for an advanced degree at Homi Bhabha National Institute (HBNI) and is deposited in the Library to be made available to borrowers under rules of the HBNI.

Brief quotations from this dissertation are allowable without special permission, provided that accurate acknowledgement of source is made. Requests for permission for extended quotation from or reproduction of this manuscript in whole or in part may be granted by the Competent Authority of HBNI when in his or her judgment the proposed use of the material is in the interests of scholarship. In all other instances, however, permission must be obtained from the author.

Maneesha Mishra

**Maneesha Mishra**

# DECLARATION

I, hereby declare that the investigation presented in the thesis has been carried out by me. The work is original and has not been submitted earlier as a whole or in part for a degree/diploma at this or any other Institution/University.

Maneesha Mishra

**Maneesha Mishra**

*Dedicated*

*to*

*My Parents*

# ACKNOWLEDGEMENTS

At the outset, I would like to express my deepest gratitude to my supervisor **Dr. P. Kuppusami, Professor, Homi Bhaba National Institute and Head, X-ray Diffraction and Surface Engineering Section (Retired) of MSSCD, IGCAR** for his guidance, help and encouragement throughout my research work. His dedication, valuable suggestions, motivation, support and creative thinking have inspired me at each moment and helped me to carry out my research successfully.

I am grateful to my doctoral committee chairman, **Dr. K. V. G. Kutty** and members **Dr**. **S. Saroja**, **Dr. P. Ch. Sahu** and **Shri E. Mohandas** for their support and evaluation of the progress of my research work and valuable suggestions.

My sincere thanks to **Dr. M. Vijayalakshmi,** Associate Director, Physical Metallurgy Group for her constant support and encouragement. I would like to thank **Dr. T. Jayakumar**, Director, MMG, IGCAR, **Shri S. C. Chetal**, Director, IGCAR and **Dr. Baldev Raj**, former Director, IGCAR for their support and for providing research facilities of the Centre for carrying out this research work.

I must thank **Dr. R. Divakar**, Scientific Officer/ H, Physical Metallurgy Group and **Shri Chanchal Ghosh,** Scientific Officer / D, Physical Metallurgy Group for TEM analysis. I would like to extend my warm wishes to **Dr. S. Murugesan**, Scientific Officer/E, MSSCD, IGCAR and **Shri R. Thirumurugesan** and **Mrs. M. Jyothi** for their help and support in carrying out the conventional and HTXRD experiments. I am extremely thankful to **Mr. Akash Singh** for his constant support throughout my research during the last 4 years.

I would like to thank **Dr. T. N. Sairam** and **Dr. V. Sivasubramanian**, Scientific Officer, IGCAR for their contribution in optical measurements. I also thank **Dr. R. Ramashesan,** Scientific Officer, for nanoindentation measurements. I would also like to thank **Dr. S. Ramaya** for her help in Raman experiments.

I must thank **Dr. V. R. Reddy and Dr. V. Ganesan** of UGC-DAE-CSR, Indore for carrying out the XRR and AFM measurements.

I would like to thank **Dr. V. Ganesan,** Dean (Chemical Sciences) for the excellent co-ordination with HBNI and Dr**. M. Saibaba,** Associate Director, Resource Management Group for providing me a comfortable stay at Research Scholar enclave.

I am grateful to IGCAR for the financial support provided under the Department of Atomic Energy research fellowship scheme for the entire duration of the work.

My affectionate thanks to my friends **Prasana, Pravati, Pradeep, Debasmita, Sudhansu, Smiti, Soumee and Madhusmita** for their love, affection and encouragements during my Ph.D and to make my stay at Kalpakkam enjoyable.

I must thank God for giving me a loving and caring family without whose support, encouragements and dedication, I would not be able to complete my PhD. I must thank my Father **Shri. Hemant Kumar Mishra**, mother **Smt. Sangeeta Mishra**, sisters **Ms. Ipsita Mishra** and **Arunima Mishra** and my husband **Mr. Subhrajit Rout** for their love, affection, care and support that have made me confident to overcome all the difficulties in life.

# ***ABSTRACT***

Metal oxide thin films have found applications in many fields such as superconducting films, insulating films, luminescent films, thin film capacitors, anti reflection coatings, protective coatings and thermal barrier coatings etc. Properties of materials are mainly dependent on the microstructures which can be tailored by deposition conditions as well as by deposition techniques. Although the thin film structures of many materials are useful in many applications, there are still some requirements that cannot be fullfilled by a single material. Such requirements have directed the research towards preparation of multilayer structure by combining the required properties of two different materials.

The present work consists of the preparation of single layers of $Y_2O_3$, $ZrO_2$, $CeO_2$ and $Gd_2O_3$ by pulsed laser deposition technique under various deposition conditions. Taking in to account the deposition conditions to obtain the best quality films of the above four materials, multilayers of $ZrO_2/Y_2O_3$ and $CeO_2/Gd_2O_3$ multilayers were prepared by PLD technique. Both the films and the multilayers of these oxides were deposited on Si (100), quartz and Inconel-783 substrates in order to study the optimization of process parameters, optical properties and nanomechanical properties, respectively. Characterization of the films and the multilayers were carried out by conventional and high temperature x-ray diffraction (XRD), X-ray reflectivity (XRR), Raman spectroscopy, atomic force microscopy (AFM), high resolution transmission electron microscopy (HRTEM), UV-visible spectroscopy, XRR and nanoindentation techniques to study the effect of the process parameters on the microstructural, optical and nanomechanical properties.

Thin films of $Y_2O_3$ and $ZrO_2$ films were deposited on Si (100) and quartz substrates as a function of substrate temperature and oxygen partial pressure. The $Y_2O_3$ films were found to be

x-ray amorphous at room temperature and crystalline film was formed at 673 K. In the case of $ZrO_2$ films, the phase formation of the $ZrO_2$ is influenced by both substrate temperature and oxygen partial pressure. For instance tetragonal $ZrO_2$ (t-$ZrO_2$) was formed at high substrate temperature and oxygen partial pressure. Unlike $Y_2O_3$ films, a mixture of monoclinic and t-$ZrO_2$ phases were formed even at room temperature. But a phase pure t-$ZrO_2$ or m-$ZrO_2$ could not be achieved from a target containing a mixture of phases. The crystallite size of these films was found to increase with the increase in substrate temperature. As a consequence, the roughness of the film was found to increase with increase in crystallite size. The $Y_2O_3$ films showed higher transmittance and band gap values for the film deposited at 873 K, while $ZrO_2$ films showed higher transmittance for the films deposited at lower substrate temperature, where monoclinic phase is more formed. The $ZrO_2$/$Y_2$O3 multilayers show better crystallinity at higher substrate temperature. It was found that the multilayers show good transmittance in the wavelength range of 200-900 nm. However, the hardness values did not show any significant changes with $ZrO_2$ layer thickness, possibly due to the similar values of elastic constants of $ZrO_2$ and $Y_2O_3$. The coefficient of thermal expansion (CTE) was calculated for the single as well as multilayers of $ZrO_2$ and $Y_2O_3$from the HTXRD analysis. The CTE of the multilayers were higher than that of the single layers due to the partial dissolution of $Y_2O_3$ into $ZrO_2$ layers with increasing temperature.

$CeO_2$ and $Gd_2O_3$ single layer films were prepared at different process parameters and $CeO_2$ films showed a change in preferred orientation from (111) to (200) with increase in the substrate temperature and oxygen partial pressure. The $CeO_2$ films were crystallized in cubic structure and showed good transmittance in the range 200-900 nm. The $Gd_2O_3$ films deposited at different substrate temperatures and oxygen partial pressures showed mostly monoclinic peaks, along with small fraction of cubic $Gd_2O_3$ at lower temperature. The $Gd_2O_3$ films showed higher band gap of 5.80 eV for the films deposited at 873 K and oxygen partial pressure of 0.2 Pa. The $CeO_2/Gd_2O_3$ multilayers were deposited at 300 K and 873K at oxygen partial pressure of 2 Pa and showed better crystalline films at higher substrate temperature. Films showed good transmittance within the wavelength range 200- 900 nm. The band gap values of the $CeO_2/Gd_2O_3$ multilayers were found to increase with increase in bilayer thickness and substrate temperature. Hardness values obtained for $CeO_2/Gd_2O_3$ multilayers showed higher values than that of the hardness of single layers of $CeO_2$ and $Gd_2O_3$. The increase in hardness for $CeO_2/Gd_2O_3$ multilayers has been explained on the basis of difference in elastic modulus of these oxide materials. The CTE values were calculated for the single as well as multilayer structures from the HTXRD data. It was observed that the CTE values of $CeO_2$ were higher in multilayer structures than that of the single layers owing to interdiffusion effects with increasing temperature.

In summary, the present study focused on the preparation of single and multilayer films of various oxides such as $Y_2O_3$, $ZrO_2$, $CeO_2$ and $Gd_2O_3$ by PLD technique and on the study of the correlation of growth parameters and bilayer thickness on the microstructural, optical and nanomechanical properties of these single and multilayer films. The investigation also generated a vast amount of data on optical, nanomechanical and especially the thermal expansion coefficients which may be of great use for the design of new oxide coatings for technological applications.

# TABLE OF CONTENTS

**Title** **Page No.**

**Chapter 1 Introduction**

**Chapter 2 Experimental Methods and Characterization**

Chapter 3 $Y_2O_3$ and $ZrO_2$ thin films and $ZrO_2/Y_2O_3$ multilayer thin films: Preparation and properties

## Chapter 4 $CeO_2$ and $Gd_2O_3$ thin films and $CeO_2$/$Gd_2O_3$ multilayer thin films: Synthesis and properties

## Chapter 5 Thermal Expansion Behavior of Single and multilayer Films

## Chapter 6 Summary and Conclusions

# List of Figures

# List of tables

# *Chapter 1*

# *Introduction*

## 1.1 Introduction

Metal oxides are an important part of both day to day life and industrial applications due to their low cost, easy availability, tunable properties and environmental friendly nature. Properties of metal oxides can be tailored by various techniques which are useful to fullfill almost all type of technological application requirements. Metal oxides have potential applications almost in every field, especially in sensors [1], solid oxide fuel cells (SOFC) [2], semiconductor industry [3], electronic industry [4], laboratory reaction (catalyst) [5], flat screen displays and electro-chromic devices [6 ,7], spintronics [8] and solar cells [9]. Physical [10-14], mechanical [15,16] as well as chemical [17-19] properties of materials can be tuned by changing the crystallite size of materials, which is possible either by synthesizing the material in the form of nanocrystalline powder or by making thin films structure, depending on the mode of application.

The common oxides such as $SnO_2$, ZnO, $In_2O_3$, $WO_3$, $SrTiO_3$, $Ga_2O_3$, $AlVO_3$ and $BaTiO_3$-CuO [1,20-25] are used in sensor application. The oxides used in SOFC applications are yttria stabilized zirconia (YSZ), samaria doped ceria (SDC), gadolinia doped ceria (GDC), $BaCeO_3$, $LaMnO_3$, [26-29]. YSZ, $ZrSiO_4$, $Nd_2Ce_2O_7$, $BaZrO_3$, $SrZrO_3$ and $CaZrO_3$ [30-33] are the candidate materials used in thermal barrier coating (TBC) application. $ZrO_2$, $Y_2O_3$, $SiO_2$, $Al_2O_3$ and $Y_4Al_2O_9$ [34-37] have found applications as optical coatings. $Al_2O_3$ [38], $ZrO_2$ [39], MgO [40] and erbium oxide [41], are used as corrosion resistant coatings.

## 1.2 Advantages of Thin Films

Thin films are layers prepared by a thin film deposition technique with a layer thickness of few micrometers. Most of the thin films applications involve a thickness below 1 micron. Most common applications of thin films coatings are as protective coatings, transparent optical coatings, contacts and intercontacts, semiconducting films, photoconducting films, superconducting films, insulating films, luminescent films, antireflection coatings, gas sensors and thin film capacitors [42]. The main advantages of thin film technology are miniaturization of devices and cost reduction. The fundamental properties of materials are mainly dependent on the microstructure and it is possible to tune the properties of any material from that of the bulk properties by synthesizing it in nanocrystalline form (either in nanocrystalline powder or in the form of thin fims). Along with the process parameters of a deposition technique, microstructure of materials is also dependent on the film thickness. Chen et al. [43] have reported an increase in NiO crystallite size with increase in film thickness. Similar results have been reported by Jiaguo et al. [44] for $TiO_2$ thin films.

Optical coatings are used to modify the optical properties of the surfaces, i. e. the interface between optical media. The interfaces are normally smooth and when light is incident on to, a part of it is reflected and part of it is refracted. In case of mirrors, the reflection should be higher and for lenses the refraction phenomena has more importance. The optical properties of the thin films are dependent on the microstructure. Ruby et al. [45] have compared the optical properties of CdS bulk and thin films and found an increase in band gap energy in comparison to that of the bulk as a result of the decrease in crystal size. Quantum confinement effects are only significant for systems in which the Bohr radius of the exciton is of the order of, or larger than, the size of the confined system. The most immediate consequence of the confinement effect is an increase in the band gap energy [46]. In case of thin films, the crystallite size is lower than that of the bulk values, therefore the band gap values have been reported to have higher values. Gottmann et al. [47] have reported a decrease in refreactive index value by altering the deposition conditions, which in turn will decrease the thermal conductivity of the material, as reported by Nicholls et al.[48].

Thin films are materials in which the thickness direction is much smaller than that of the other two. So the properties are mostly affected by the size constraint rather than the microstructure [49]. Decrease in size results in an increase in mechanical properties, as a result of the restriction in the dislocation movement [50]. As the thin films always contain materials in nanocrystalline structure, the mechanical properties of thin films are quite different than that of the bulk values due to difference in microstructure, large surface to volume ratio and smaller crystallite size [51].

Sensors and SOFC require high reaction kinetics and enhanced conductivity of materials of interest. Ionic conductivity of a material can be increased by doping with another material. But beyond some critical doping concentration, the ionic conductivity decreases. An alternative solution is to increase the ionic mobility which in turn is dependent on the microstructure and grain boundary. Kosacki et al. [52] have reported an increase in ionic conductivity of about 3 orders than that of the bulk yttria stabilized zirconia (YSZ) by decreasing the layer thickness; similarly the electrical properties of $BiFeO_3$ are also found to be enhanced than that of the bulk values when deposited in the form of thin films [53]. Thin films of rare earth oxides such as $HfO_2$, $ZrO_2$, $Y_2O_3$, $La_2O_3$, $Lu_2O_3$ have great application as a dielectric layers in microelectronics [54]. Thin films also have great advantages in fabrication of thin film sensor devices. Sberveglieri et al. [55] have reviewed the common thin films based sensors on $SnO_2$, $Li/SnO_2$, ZnO, $Cu_2O$ and $Nb_2O_5$ etc.

Thin films also have advantages in stabilizing the high temperature phases at room temperature by varying the deposition conditions. Formation of pure rutile and anatase phase of

$TiO_2$ has been reported by Murugesan et al. [56] by suitable selection of deposition temperature and oxygen partial pressure. Similarly Molle et al. [57] have reported the phase transformation of $Gd_2O_3$ as a result of layer thickness. Tetragonal phase of $ZrO_2$ is also found to have dependence on crystallite size which is dependent on the film thickness.

### 1.3 Application of Multilayers

Although single layer thin films are able to fulfill many technological necessities, there are still some needs in which a single material is unable to satisfy all requirements. In those situations multilayer films can be used as an alternative. Multilayer films popularly called "superlattices" in which two or more materials are deposited as alternate layers in nanometer scale.

Hardness values of multilayer films are found to be enhanced over the single layer films of constituent materials. The hardness values shows an increasing trend with a decrease in modulation wavelength (sum of the two individual thickness), then remains steady and finaly decreases with further decrease in bilayer thickness [49]. Higher modulation wave lengths results in an dislocation pile up and increase in hardness, whereas in smaller modulation wavelengths, the dislocation movement is no longer aided by pile up but due to large amount of stress the hardness values decreases. Yashar et al. [58] also have reviewed different mechanisms behind the enhancement in case of multilayer structure which includes dislocation blocking, Hall-Petch strengthening and interface strain. The examples of the multilayer systems that showed enhancement in hardness values are TiN/VN [59], Ag/Fe [60], TiN/NbN [61] and AlN/TiN [62].

Ionic conductivity is enhanced by several orders of magnitude than that of the individual constituents. The enhancement in conductivity is attributed to the increase in charge carrier densities and mobility at the interfaces as well as due to the sublattice disorders developed due to the interfaces [63]. Yang et al. [64] have reported an enhancement in ionic conductivity of GDC/YSZ multilayer than that of the single layers of YSZ and GDC single layer films. The increase in ionic conductivity is due to the formation of local space charge region around the interfaces due to the discontinuity of structures [65]. Similar results were also seen by Cavallaro et al. [66] for YSZ/STO multilayers and $CaF_2/BaF_2$ superlattices [67].

Multilayer optical coatings mainly involve anti reflection coatings, in which the reflection was lowered by forming a multilayer structure of a high and low refractive index materials. Formation of alternating layers of high and low refractive index materials creates constructive and destructive regions, which can be adjusted in order to get either higher transmittance or reflectance. Singh et al. [68] have prepared a multilayer optical coating that can be used as UV mirrors. The other examples of multilayer filters are $HfO_2/SiO_2$ [69], $B_4C$/Mo/Si [70] and Mo/Si [71]. Huang et al. [72] have studied the effect of film thickness on the dielectric property of $SrTiO_3/BaTiO_3$ multilayer structure and reported such multilayers for DRAM capacitors.

Shinguu et al. [73] have reported an enhancement in photocatalytic activity of $TiO_2/WO_3$ multilayers than that of the single layer of $TiO_2$. Khatko et al. [74] have reported enhanced catalytic properties in $Pd/SiO_2$ and $Pt/SiO_2$ multilayers than that of Pd and Pt films, which are useful in sensor application.

Nicholls et al. [48] have reviewed different methods to reduce the thermal conductivity of thin films by addition of dopant and by layering. They have reported that the decrease in thermal conductivity is due to the heat loss as a result of small crystallite size and phonon scattering at the interfaces in multilayers.

Another important application of the multilayer film is the stabilization of metastable phases of a material at room temperature by forming multilayer. It has been reported in literature that the high temperature phases of $ZrO_2$ can be stabilized at room temperature by decreasing the crystallite size below some critical value. In multilayer structures the crystallite size is constrained by the layer thicknesses, resulting in stabilization of tetragonal and cubic phases at much lower temperatures. Balakrishnan et al. [75,76] have reported the formation of tetragonal $ZrO_2$ at room temperature by forming a multilayer of $ZrO_2$ with $Al_2O_3$ and $CeO_2$. Barshilla et al. [77] also have reported the stabilization of tetragonal and cubic $ZrO_2$ phases by forming multilayers with $Al_2O_3$ and $Y_2O_3$, respectively.

## 1.4 Properties of Materials

The following materials used in the present investigation are discussed in detail with respect to crystal structure, applications and deposition methods based on the literature information.

### 1.4.1 Yttrium oxide ($Y_2O_3$)

$Y_2O_3$ is a transition metal oxide of molecular weight 225.8 g/mol. It exists in body centered cubic (BCC, $a$=10.602 Å, space group $Ia3$) (Fig. 1.1) structure up to a temperature ~2600 K and at ambient pressure [78,79]. At higher temperature it transfers to an hexagonal structure (space group $P\bar{3}m$, $a$=3.81 Å, $c$=6.08 Å) [78,80] or fluorite type structure [81,82] ($a$= 5.2 Å). At high pressure it exists as a monoclinic phase ($a$=13.899 Å, $b$=3.493 Å, $c$= 8.611 Å) [83-85].

The fundamental properties of $Y_2O_3$ are listed in Table 1.1. Due to these properties $Y_2O_3$ thin films have found important applications such as dielectric layers in electroluminescent devices [86], complementary metal-oxide-semiconductor devices [87], high-density dynamic random access memory [88] and electrochemical sensors [89]. It is an important material in optical applications due to its wide band gap and its ability to be a host material for rare earth ions [90,91].

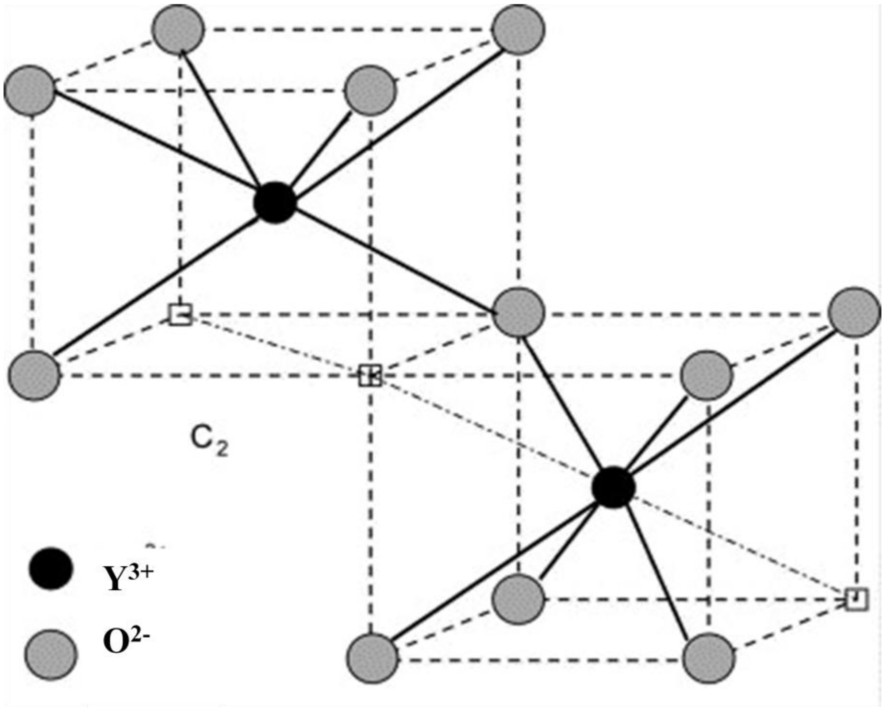

**Fig. 1.1 Crystal structure of cubic $Y_2O_3$ [92].**

**Table 1.1 Properties of $Y_2O_3$.**

| | |
|---|---|
| Molecular weight | 225.8 g |
| Density | 5.3 g/cm$^3$ |
| Melting point | 2673 K |
| Band gap | 5.4 eV |
| Refractive index | ~2 |
| Elastic modulus | 170 GPa |
| Hardness | 8 GPa |
| Thermal expansion coefficient | 9 x 10$^{-6}$ K$^{-1}$ |

$Y_2O_3$ thin films have been prepared by different methods like pulsed liquid injection plasma enhanced metal organic chemical vapor deposition (MOCVD) [93,94], plasma–enhanced chemical vapor deposition [95], ion beam sputtering [96], thermal decomposition [97], radio frequency sputtering [98-100], electron beam evaporation [101], UV–assisted pulsed laser deposition [102] and pulsed laser deposition (PLD) [90,103,104] to study microstructural [103,104], optical [97,104], mechanical [105], electrical [106] and thermal [99] properties.

### 1.4.2 Zirconium oxide ($ZrO_2$)

Three different phases of $ZrO_2$ are reported in literature [107]: monoclinic $ZrO_2$ (m-$ZrO_2$, space group $P2_1/c$, $a$=5.169Å, $b$=5.232 Å, $c$=5.341 Å) [108,109] in the temperature <1443 K, tetragonal (t-$ZrO_2$) in the range 1443–2643 K (Space group $P4_2/nmc$, $a$=3.591Å, $b$=5.169Å) [110] and cubic phase (c-$ZrO_2$) in the range 2643–2903 K (Space group Fm3m, $a$=5.12 Å) [111] (Fig. 1.2).

$ZrO_2$ offers several interesting technological applications due to its properties like high melting point, good thermal, chemical and mechanical stabilities and wide band gap (Table 1.2). All three phases find applications in different fields; monoclinic phase has application in biological fields [112,113], t-$ZrO_2$ is normally used in coating applications due to its superior mechanical properties, and c-$ZrO_2$ has applications in sensors and fuel cells. $ZrO_2$ also find applications in many fields such as optical coatings, protective coatings and insulating layers [114,115], catalyst for alcohol synthesis [116], in fuel cells [117] as well as in thermal barrier coatings [118].

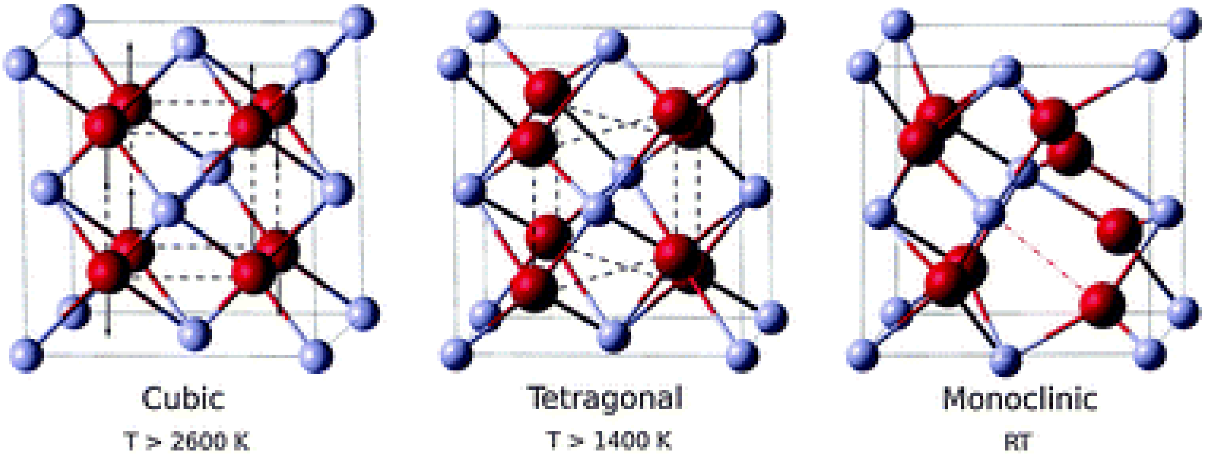

**Fig. 1.2 Crystal structures of the $ZrO_2$ [119].**

**Table 1.2 Properties of $ZrO_2$.**

| | |
|---|---|
| Molecular weight | 123.2 g |
| Density | 5.68 g/cm$^3$ |
| Melting point | 2953 K |
| Band gap | 5.0 eV |
| Refractive index | ~2.15 |
| Elastic modulus | 205 GPa |
| Hardness | 11.8 GPa |
| Thermal expansion coefficient | 15.3 x 10 $^{-6}$ K$^{-1}$ |

Among the three phases, tetragonal and cubic phases are formed at very high temperatures. The high temperature phases can be retained at room temperature by doping with some suitable oxides such as $Al_2O_3$ [120], $Y_2O_3$ [121], MgO [122], and CaO [123-125] etc. However, it is interesting to note that un-doped zirconium oxide can also be retained in tetragonal phase at room temperature in thin film forms [125,126], as a result of small crystallite size [125-128] and compressive stress [129].

Various methods such as MOCVD [125,130], chemical vapor deposition (CVD) [131], atomic layer deposition (ALD) [132,133], ultrasonic nebulisation and pyrolysis technique [134], pulsed laser deposition (PLD) [,135,136], sol–gel method [137], sputtering technique [138], thermal evaporation [139], cathodic vacuum arc deposition [140], and electron beam deposition [141] have been used to prepare $ZrO_2$ films to study the microstructural [134,136], optical [136,138], electrical [134], phase transformation [130], wear [142], luminescence [143], nanomechanical [144] and bioactivity and cytocompatability [145] properties.

### 1.4.3 Cerium oxide ($CeO_2$)

Most stable state of stoichiometric cerium oxide ($CeO_2$) is face centered cubic structure (FCC, space group *Fm3m*, *a*=5.411 Å) [146] (Fig. 1.3), from room temperature to melting point (~2873 K) at ambient conditions [147], whereas nonstoichiometric cerium oxide exists in $Ce_2O_3$ structure (hexagonal structure) (space group $P\bar{3}m1$) at higher temperature [146].

$CeO_2$ has wide applications in the field of dielectric layers [148], optical coatings [149], catalysts [150,151], corrosion resistant coatings [152], and UV blocking filters [149], and sensors [153-155] due to its excellent properties (Table 1.3). When doped with di or trivalent ions, $CeO_2$ shows high ionic conductivity suitable for use as solid electrolyte in SOFCs [156,157]. $CeO_2$ thin films were deposited onto graphite electrodes for application in lithium ion batteries [158].

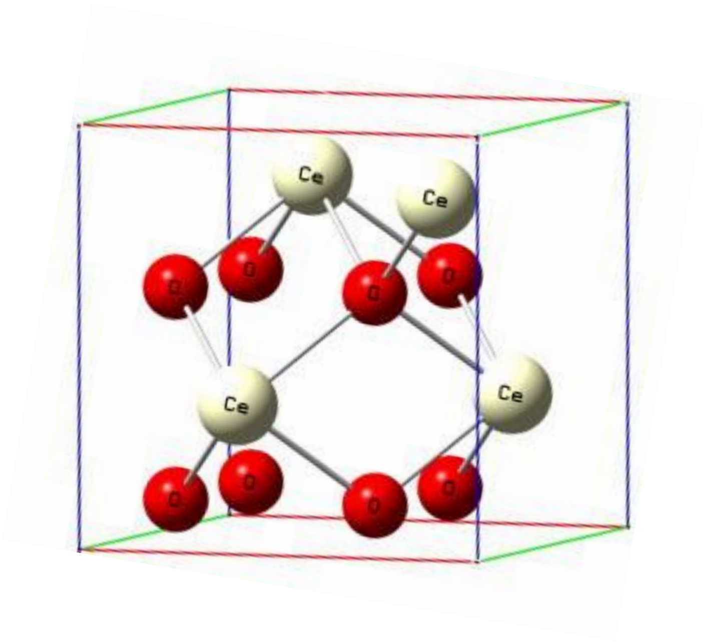

**Fig. 1.3 Crystal structure of cubic $CeO_2$ [159].**

**Table 1.3 Properties of $CeO_2$.**

| | |
|---|---|
| Molecular weight | 172.1 g |
| Density | 7.65 g/cm$^3$ |
| Melting point | 2750 K |
| Band gap | 3.0 eV |
| Refractive index | ~2.1 |
| Elastic modulus | 181 GPa |
| Hardness | 6 GPa |
| Thermal expansion coefficient | 13 x 10 $^{-6}$ K$^{-1}$ |

$CeO_2$ films were also deposited on $Al_2O_3$ substrates for oxygen sensor application [160]. Similarly ceria thin films were deposited on indium tin oxide (ITO) coated glass substrates in application related to cholesterol biosensor [150]. $CeO_2$ is also a candidate material for corrosion preventive coatings [153,161].

$CeO_2$ thin film have been prepared by various methods such as sol-gel [150,153,161], electron beam evaporation [148,162], metal organic deposition [162], vapor phase deposition [164], DC magnetron sputtering [165], thermal evaporation [166] and PLD technique [167,168 ] to study the properties like electrical [169], optical [167,170], microstructural [167,171], electrochemical [172], thermal [173] and mechanical [174] properties.

### 1.4.4 Gadolinium oxide ($Gd_2O_3$)

$Gd_2O_3$ exists in cubic structure (BCC, space group Ia3, *a*= 10.813 Å) from room temperature to ~1473 K, and transforms to monoclinic structure (C2/m) above 1473 K , monoclinic → hexagonal phase transition temperature is at ~2443 K [79] (Fig. 1.4).

Application of $Gd_2O_3$ is based on the properties listed in Table 1.4. Due to the above properties, $Gd_2O_3$ has found wide applications as optical coating, dielectric layers in devices and host material for rare earth ions.

$Gd_2O_3$ thin films have been deposited by different technique like metal organic chemical vapor deposition (MOCVD) [175-177], magnetron sputtering [178], e-beam evaporation [179,180], oxidation [181,182], molecular beam deposition [183,184], electrolytic deposition [185], atomic layer deposition [186] , PLD [187], to study the properties like microstructural [175], optical [179] and electrical [188] properties.

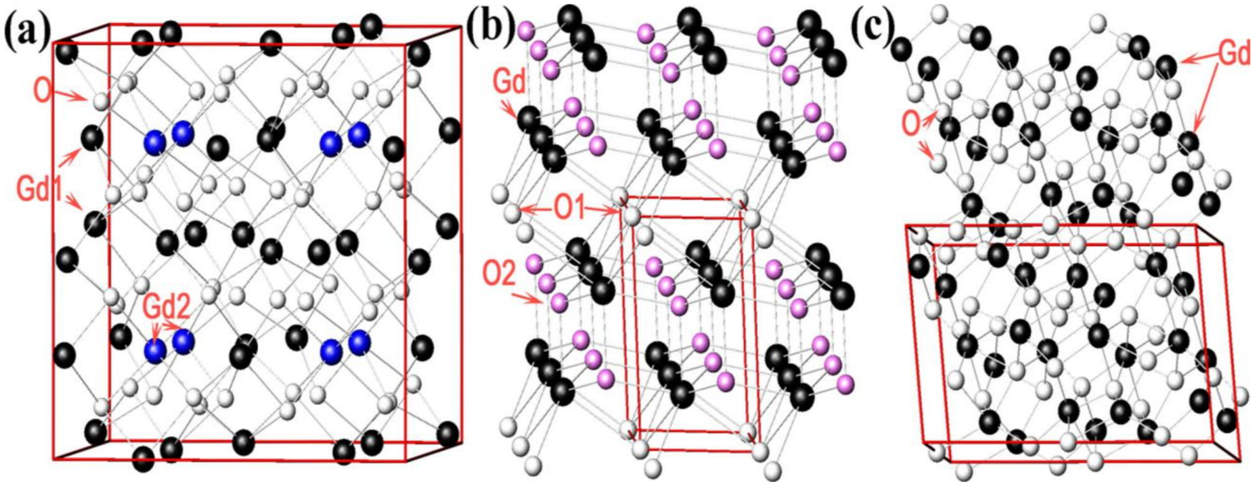

**Fig. 1.4 Crystal structures of $Gd_2O_3$ (a) cubic (b) hexagonal and (c) monoclinic [189].**

**Table 1.4 Properties of $Gd_2O_3$.**

| | |
|---|---|
| Molecular weight | 362.5 g |
| Density | 7.41 g/cm$^3$ |
| Melting point | 2443 K |
| Band gap | 5.2 eV |
| Refractive index | ~1.8 |
| Elastic modulus | 124 GPa |
| Hardness | 4.7 GPa |
| Thermal expansion coefficient | $7.5 \times 10^{-6}$ K$^{-1}$ |

## 1.5 Deposition Techniques for Thin Films

Many deposition methods have been used to prepare single as well as multilayer thin films. This can be broadly divided into two main categories (i) physical vapor deposition (PVD) and (ii) chemical vapor deposition (CVD).

Physical vapor deposition deals with the following steps involving (i) vaporization of material in atomic or molecular form (ii) transfer of the vapor through low pressure environment and (iii) condensation at the substrate surface [190]. Different types of PVD techniques are listed in Fig. 1.5.

In contrast to PVD process, CVD deals with the chemical reactions, to produce stable reaction product, which are deposited as thin films at the substrate surface. CVD involves a reactive carrier gas, which contains precursors of desired product. Gas phase reaction occurs in the reaction chamber at the substrate surface to produce films. The reaction by products is transported away using a carrier gas [191].

## 1.6 Advantages of Pulsed Laser Deposition

Out of all the deposition methods, PLD has the ability to retain stoichiometry of the film same as that of the target. PLD is mainly useful for deposition of multi-component targets. Another important advantage of PLD is that the laser source is outside the vacuum chamber, which is useful for easy operation and less complexity for thin film synthesis process. Almost all materials can be abalated by using suitable laser energy. As the deposition takes place by nonequillibrium mechanisms, it is also useful to prepare metastable materials which cannot be prepared under normal thermodynamical conditions [192]. In addition to these advantages, PLD has also many drawbacks such as particulate formation and inability to deposit over larger area due to narrow angular distribution of the plume [193].

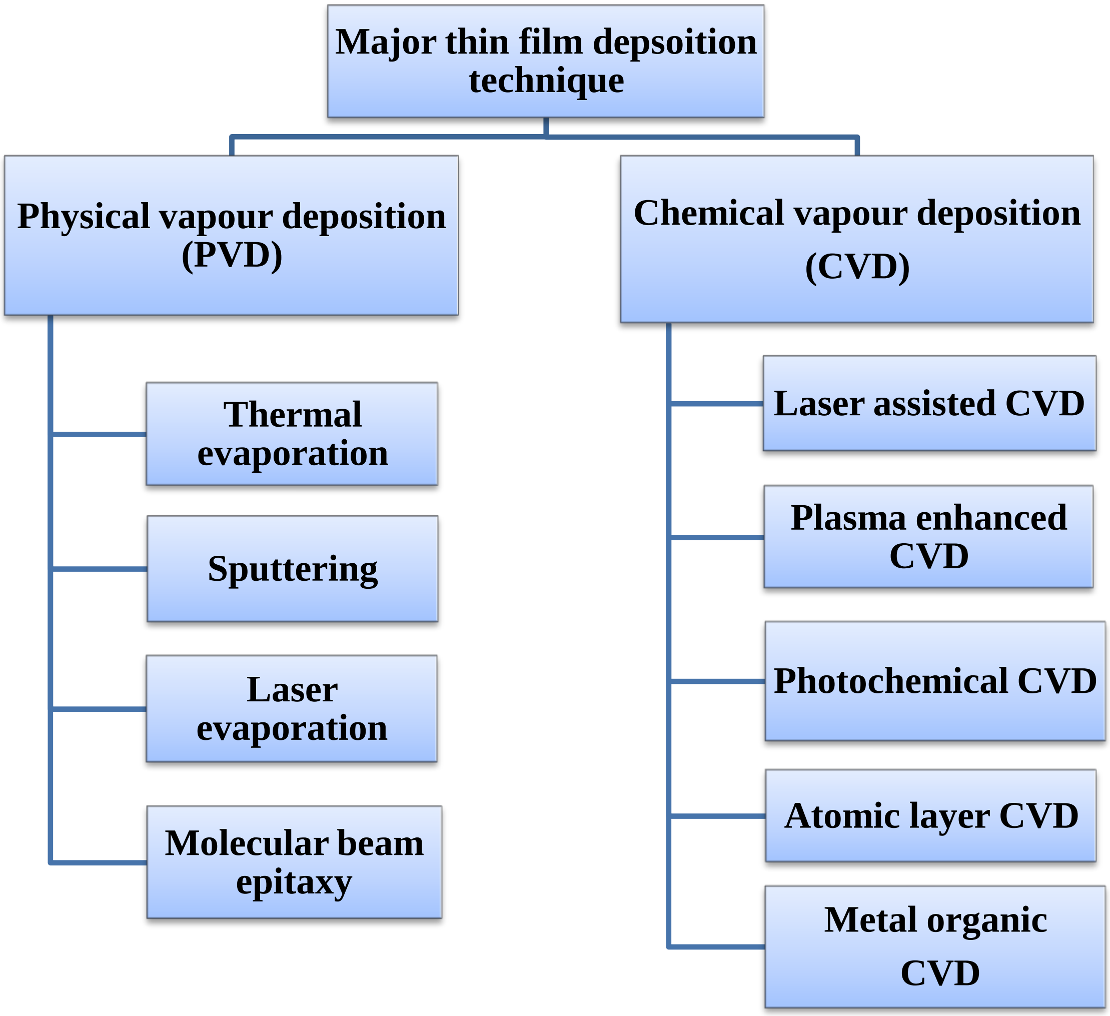

**Fig. 1.5 Different types of thin film deposition techniques.**

## 1.7 Lasers

A PLD system mainly consists of two parts, a laser system, to evaporate materials and a deposition chamber where the actual deposition takes place. The most common lasers being used to evaporate the material by PLD are excimer lasers and Nd-Yad lasers (possible output λ=1064, 532, 355 and 266 nm). The wavelength range of laser light useful for deposition process lies between 200-400 nm, because of the strong absorption by most materials within this wavelength range. Absorption coefficient value decreases with decrease in laser wavelength, as a result of which the penetration depth of the light decreases.

The fundamental laser emission of Nd:YAG occurs at wavelength (λ) 1064 nm, which can be made to 532 nm by using a nonlinear crystal. But in order to produce a laser light in UV range, the 532 nm is mixed with 1064 nm and results in light at 355 and 266 nm with very low efficiencies of 20% and 15 %, respectively. Whereas excimer lasers have an advantage of producing laser light directly in the UV range and have long life. Unlike that of the solid state lasers the repetition rate of excimer lasers can be varied from one to several hundreds.

Several excimers laser have been developed that have wavelength in the desired range. For example ArF (λ=193 nm), KrF (λ=248 nm), KrCl (λ=222nm), XeCl (λ=308 nm) and XeF (λ=351 nm). Although KrCl and ArF lasers are having lower λ than that of the KrF lasers, but KrF lasers are the most commonly used lasers for deposition process, due to its highest gain [194]. The spot size, beam homogeneity, laser energy and repetition rate are the important parameters that affect the film quality and microstructure.

## 1.8 Basic Principles of PLD

PLD is a type of physical vapor deposition technique, in which high energy laser light is used to evaporate the materials. In this technique an intense laser light is allowed to fall onto the material, the material gets evaporated due to its interaction with light energy. Due to very high energy the material gets evaporated and removed from the surface in the form of plume (Fig. 1.6). The threshold energy needed for evaporation depends on the property of material. The evaporated material in the plume is again allowed to condense onto a substrate for thin film preparation [195]. The movement of the evaporated materials towards the substrate is governed by the gas dynamics and show forward peaking phenomena. The shape of the plume is governed by $Cos^n\Theta$, where the value of n varies from 2 to 15 [196].

The other part of a PLD system is the deposition chamber which is attached with the vacuum systems, target carousal, substrate holder and heater. Film growth and chemistry can be enhanced or modified by carrying out depositions in an ambient background gas. Gases are often used either to thermalize the plasma species through multiple collisions or to compensate for the loss of an elemental component of the target through incongruent evaporation. On the other hand in reactive PLD process, different type of gases, such as hydrogen ($H_2$), methane ($CH_4$), nitrogen ($N_2$) and oxygen ($O_2$) are used to induce associative reactions of metallic elements to produce hydrides, carbides, nitrides or oxides, respectively [195].

PLD technique has been widely used to prepare thin films of polymers, superconductors, ceramics, oxides nitrides, metals, biomaterials and ferroelectric materials etc. in addition to the preparation of the single layers, PLD is also a useful technique to prepare multilayer films, due to easy control over the deposition rates which can be optimized [197].

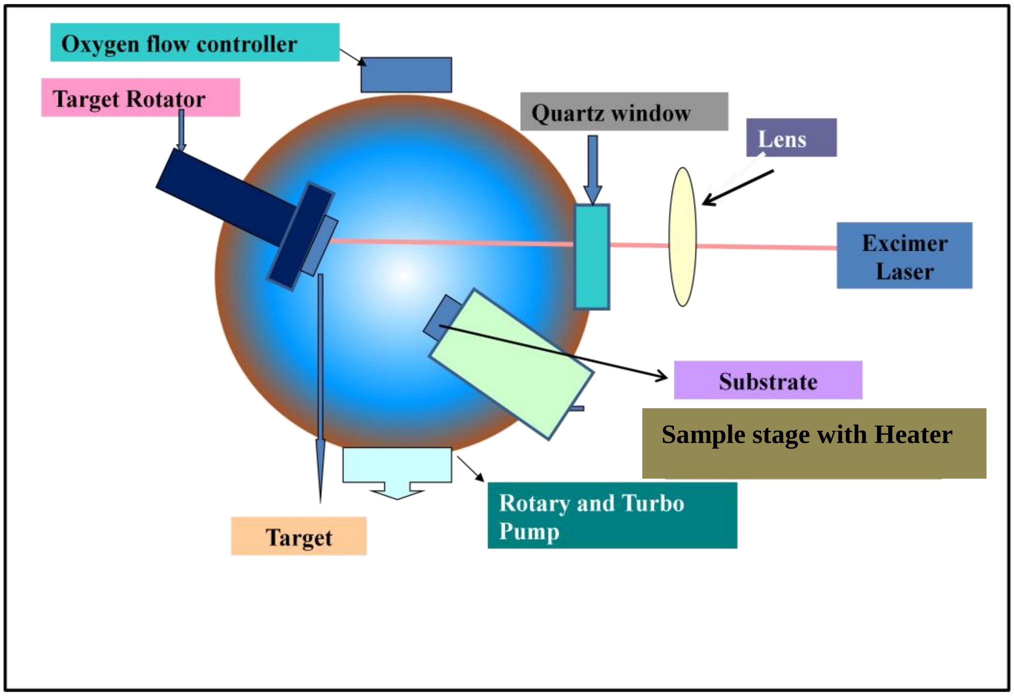

Fig. 1.6 Schematic diagram of PLD.

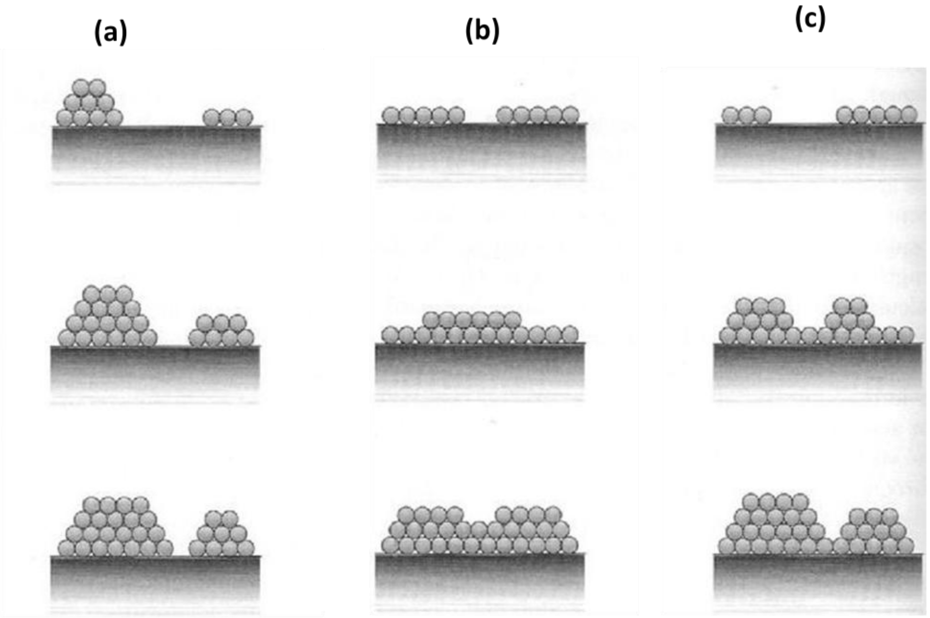

Figure 1.7 Different growth modes during thin film growth
(a) Volmer-Weber (b) Frank-van der Merwe and (c) Stranski-Krastanov [198].

## 1.9 Nucleation and Growth of Thin Films

Thin film deposition process takes place mainly in two steps, the nucleation followed by growth. Thin films are most commonly deposited by condensation of atoms from vapor phase to solid phase. The atomistic condensation is known as nucleation which then grows to form a film by diffusion controlled process. The structural behavior of the thin film is ascribed by the growth process. The condensation of the vapor atom occurs due to interaction of atoms with surface and loss of velocity. The vapor atoms then adsorbed on the substrate surface by releasing heat. The amount of the adatom gets impinged to the surface is known as sticking coefficient [198]. After arriving at the substrate surfaces the vapor atoms can either diffuse across the surface, encounter other clusters, or reevaporated from the surface. The balance between growth and dissolution process is controlled by the total free energy change (equation 1.1) [194].

$$\Delta G = a_1 r^2 \Gamma_{c-v} + a_2 r^2 \Gamma_{s-c} - a_2 r^2 \Gamma_{s-v} + a_3 r^3 \Delta G_v \ldots\ldots\ldots\ldots\ldots\ldots\ldots\ldots\ldots (1.1)$$

Where r is the radius of cluster, Γ is the interface energy, $\Delta G_v$ is the change in total volume free energy, and the a's are the constants. The subscripts *c*, *s* and *v* refer to the cluster, substrate and vapor. When for a given cluster size the derivative of the free energy change is positive then the cluster is not stable, but if it is negative then the cluster formation occurs.

The volume free energy per unit volume of the cluster is given by (equation 1.2)

$$\Delta G_v = -\frac{kT}{\Omega} ln\left(\frac{P}{P_e}\right) = -\frac{kT}{\Omega} ln(\zeta) \ldots\ldots\ldots\ldots\ldots\ldots\ldots\ldots\ldots (1.2)$$

P is the pressure of the arriving atoms, $P_e$ is the equilibrium vapor pressure of the film atoms, *k* is the boltzmann's constant, *T* is the absolute temperature, *Ω* is the atomic volume of the film atoms and $\zeta$ is the super saturation. Taking equation 1.1 into account, the growth of thin films can be described using the following three mechanisms [194].

(i) Volmer- Weber growth: The surface free energy terms will be positive for

$$a_1\boldsymbol{\Gamma}_{\boldsymbol{c-v}} + a_2\boldsymbol{\Gamma}_{\boldsymbol{s-c}} > a_2\boldsymbol{\Gamma}_{\boldsymbol{s-v}} \text{ ..............................(1.3)}$$

Which favors three dimensional (3-D) island growths, in which small clusters are nucleated directly onto the substrate. The clusters then grow in to island, which in turn coalesce to form continuous films. This type of growth is observed for the materials having strong boding within each other. Examples are metals or insulators (Fig. 1.7 (a)).

(ii) Frank-Vander Merwe growth: If the equation 1.3 is not satisfied, then monolayer formation is more favored, with the condition

$$\frac{\boldsymbol{\Gamma}_{\boldsymbol{s-v}}}{\boldsymbol{\Gamma}_{\boldsymbol{c-v}}} - \frac{\boldsymbol{\Gamma}_{\boldsymbol{s-c}}}{\boldsymbol{\Gamma}_{\boldsymbol{c-v}}} \geq \mathbf{1} \text{ ..............................................(1.4)}$$

This is the layer by layer growth mechanism. This type of mechanism is followed when the binding energy of the film atoms are equal or less than that of the binding energy of the film and substrate (Fig. 1.7 (b)).

(iii) Stranski-Krastinov growth: The third growth process is a combination of the above two mechanisms, in which film growth occurs by forming one or two monolayers followed by island growth (Fig. 1.7 (c)). This type of growth occurs as a result of the increase in layer thickness, which results in a change in surface energies and development of stress.

## 1.10 Stability of Multilayers

Unlike that of the single layer films the situation becomes more complicated for the multilayers structures, where alternate layers contain different materials. In this situation the interfacial energy as well as the grain boundary energy also comes into picture. In the stability of multilayers the elastic strain energy and interfacial energy play a major role for stabilization of the layer structure.

When the materials that constitute the layer structure have positive heat of mixing then the layer structure is stable and becomes unstable for negative heat of mixing. The stability of the multilayer structure is decided from the ratio between free energy of grain boundary and interfacial energy ( known to be groove angle $\theta$)(equation 1.5).

$$2\ Cos\theta = \frac{\gamma_{GB}}{\gamma_{Int}} \text{ ..........................................(1.5)}$$

When the ratio is large the layer structure becomes unstable and it is stable for small values of the ratio [199].

## 1.11 Objective of The Thesis

- Preparation of $Y_2O_3$, $ZrO_2$, $CeO_2$ and $Gd_2O_3$ thin films on different substrates under various substrate temperature and oxygen partial pressure to study the effect of these parameters on the microstructural, optical and nanomechanical properties.
- Deposition of multilayer films of $Y_2O_3/ZrO_2$ and $CeO_2/Gd_2O_3$ to study the effect of layer thickness on microstructural, optical and nanomechanical properties.
- Study of the thermal stability and determination of coefficient of thermal expansion of the single and multilayers of the above oxide films and their multilayers.

## 1.12 References

1. G. Korotcenkov, Mater. Sci. Eng. B 139 (2007) 1.
2. W.Z. Zhu, S. C. Deevi, Mater. Sci. Eng. A 362 (2003) 228.
3. H. Hosono, Thin Solid Films 515 (2007) 6000.
4. L. Manchanda, M.D. Morris, M.L. Green, R.B. Van Dover, F. Klemens, T.W. Sorsch,P.J. Silverman, G. Wilk, B. Busch, S. Aravamudhan, Microelectron. Eng. 59 (2001) 351.
5. L. Hu, Q. Peng, Y. Li, J. Am. Chem. Soc. 130 (48) (2008) 16137.
6. C. G. Granqvist, Sol. Energ. Mater Sol. Cells 60 (2000) 201.
7. C. G. Granqvist, Sol. Energ. Mater Sol. Cells 99 (2012) 1.
8. A. Vomiero, I. Concina, E. Comini, C. Soldano, M. Ferroni, G. Faglia, G. Sberveglieri, Nano Energy (2012), doi:10.1016/j.nanoen.2012.02.012.
9. K. Keis, C. Bauer, G. Boschloo, A. Hagfeldt, K. Westermark, H. Rensmo, H. Siegbahn, J. Photoch. Photobio. A: Chemistry 148 (2002) 57.
10. X. Batlle and A. Labarta, J. Phys. D: Appl. Phys. 35 (2002) R15.
11. H. T. Martirenat, J. C. Burfoot, J. Phys. C, 7 (1974) 3182.
12. V. Markovich, I. Fita, A. Wisniewski, D. Mogilyansky, R. Puzniak, L. Titelman, C. Martin and G. Gorodetsky, Phy. Rev. B, 81 (2010) 094428.
13. N. Trivedi, N. W. Ashcroft, Phy. Rev. B, 38 (17) (1988) 12298.
14. Wen Chu Huang, Juh Tzeng Lue, Phy. Rev. B, 49 (24) (1994) 17279.
15. E. Arzt, Acta Mater. , 46 (16) (1998) 5611.
16. J. R. Greer , W. C. Oliver , W. D. Nix, Acta. Mater. 53 (2005) 1821.
17. M. A. K. Lodhi, Justin B. Briggs, Int. J. Electrochem. Sci., 2 (2007) 469.

18. K. J. J. Mayrhofer, B. B Blizanac, M. Arenz, V. R. Stamenkovic, P. N. Ross, and N. M. Markovic, J. Phys. Chem. B, 109 ( 2005) 14433.
19. Michael P. Rosynek, Catalysis Reviews, 16 (1) (1977) 111.
20. B.W. Licznerski, K. Nitsch, H. Teterycz, T. Sobanski, K. Wisniewski, Sensor. Actuator. B 103 (2004) 69.
21. H. Meixner, U. Lampe, Sensor. Actuator. B 33 (1996) 198.
22. H. Meixner, J. Gerblinger, U. Lampe, M. Fleischer, Sensor. Actuator. B 23 (1995) 119.
23. K. Wetchakuna, T. Samerjaia, N. Tamaekonga, C. Liewhirana, C. Siriwonga, V. Kruefua, A. Wisitsoraatb, A. Tuantranontb, S. Phanichphant, Sensor. Actuator. B 160 (2011) 580.
24. J. W. Fergus, Sensor. Actuator. B 121 (2007) 652.
25. N. Barsan, D. Koziej, U. Weimar, Sensor. Actuator. B 121 (2007) 18.
26. A. B. Stambouli, E. Traversa, Renew. Sust. Energy Rev. 6 (2002) 433.
27. S. P. S. Badwal, K. Foger, Ceram. Int. 22 (1996) 257.
28. N. Q. Minh, Solid State Ionics 174 (2004) 271.
29. M. Yano, A. Tomita, M. Sano, T. Hibino, Solid State Ionics 177 (2007) 3351.
30. T. E. Strangman, Thin Solid Films, 127 (1985) 93.
31. H. Dai, X. Zhong, J. Li, J. Meng, X. Cao, Surf. Coat. Technol. 201 (2006) 2527.
32. R. Vaben , M. O. Jarligo, T.Steinke, D. E. Mack, D. Stover, Surf. Coat. Technol. 205 (2010) 938.
33. D. R. Clarke, S. R. Phillpot, Mater. Today, (2005) ISSN: 1369 7021.
34. W. T. Pawlewicz, D. D. Hays, P. M. Martin, Thin Solid Films 73 (1980) 169.
35. X.Q. Cao, R. Vassen, D. Stoever, J. Eur. Ceram. Soc. 24 (2004) 1.
36. Z. Hongming, YI Danqing, J. Rare Earth 26 (6) (2008) 770.

37. D. R. Clark, S. R. Phillpot, Mater. Today, 8 (6) (2005) 22.
38. H. Kakati, A.R. Pal, H. Bailung, J. Chutia, Appl. Surf. Sci. 255 (2009) 7403.
39. H. Hasuyama, Y. Shima, K. Baba, G. K. Wolf, H. Martin, F. Stippich, Nucl. Instrum. Methods 127/I28 (1997) 827.
40. F. Stippich, E. Vera, G.K. Wolf, G. Berg, Chr. Friedrich, Surf. Coat. Technol. 103–104 (1998) 29.
41. K. M. Hubbard, B. F. Espinoza, Thin Solid Films 366 (2000) 175.
42. L. Niinisto, J. Therm. Anal. Calorim. 56 (1999) 7.
43. H. Chen, Y. Lu, W. Hwang, Mater. Trans., 46(4) (2005) 872.
44. J. Yu, X. Zhao, Q. Zhao, J. Mater. Sci. Lett. 19 (2000) 1015.
45. R. Das, S. Pandey, Inter. J. Mater. Sci. 1 (1) (2011) 35.
46. P. F. Trwoga, A. J. Kenyon, C. W. Pitt, J. Appl. Phys. 83 (7) (1998) 3789.
47. J. Gottman, E. W. Kreutz, Surf. Coat. Technol. 116-119 (1999) 1189.
48. J. R. Nicholls, K. J. Lawson, A. Johnstone, D. S. Rickerby, Surf. Coat. Technol. 151-152 (2002) 383.
49. E. Arzt, Acta. Mater. 46 (16) (1998)5611.
50. N. Wang, Z. Wang , K. T. Aust, U. Erb, Acta. Metal. Mater. 43(2)(1995)519.
51. P. S. Alexopoulos, T. C. O'Sullivan, Annu. Rev. Mater. Sci. 20(1990)391.
52. I. Kosacki, C. M. Rouleau, P. F. Becher, J. Bentley, D. H. Lowndes, Solid State Ionics 176 (2005) 1319.
53. K. Y. Yun, D. Ricinschi, T. Kanashima, M.Okuyama, Appl. Phys. Lett. 89(2006)192902.
54. M. Leskel, K. Kukli, M. Ritala, J. Alloy. Compd. 418(2006) 27.
55. G. Sberveglieri , Sensor. Actuator. B 23 (1995) 103.

56. S. Murugesan, P. Kuppusami , N. Parvathavarthini, E. Mohandas, Surf. Coat. Technol. 201 (18) (2007) 7713.
57. A. Molle, C. Wiemer, Md. N. K. Bhuiyan, G. Tallarida, M Fanciulli, Appl. Phys. Lett. 90 (2007) 193511.
58. P. C. Yashar, W. D. Sproul, Vacuum 55 (1999) 179.
59. U. Helmersson, S. Todorova, S. A. Barnett, J.-E. Sundgren, L. C. Markert, J. E. Greene, J. Appl. Phys. 62 (1987) 481.
60. Z. Xiao-ying, L. Xue-jing, Z. Fei, PAN Feng, Nonferrous Met. Soc. China 20(2010) 110.
61. S. H. Kim, Y. J Baik, Dongil Kwon, Surf. Coat. Technol. 187 (1) (2004) 47.
62. G. Li, J. Lao, J. Tian, Z. Han, M. Gu, J. Appl. Phys. 95 (1) (2004) 92.
63. T. J. Pennycook, M. J. beck, K. Varga, M. Varela, S. J. Pennycook, S. T. Pantelides, Phys. Rev. Lett. 104 (2010) 115901.
64. Y. Wang, E. Linan An, L. V. Saraf, C. M. Wang, V. Shutthanandan, D. E. McCready, E. S. Thevuthasan, J. Mater. Sci. 44 (2009)2021.
65. E. Fabbri, D. Pergolesi, E. Traversa, Sci. Technol . Adv. Mater. 11(2010) 054503.
66. A. Cavallaro, M. Burriel , J. Roqueta, A. Apostolidis, A. Bernardi, A. Tarancon, R. Srinivasan, S. N. Cook, H. L. Fraser, J. A. Kilner, D. W. McComb, J. Santiso, Solid State Ionics 181 (2010) 592.
67. J. Maier, Solid State Ionics 131(2000) 13.
68. M. Singh, J. J. M. Braat, Appl. Opt. 39 (13) (2000) 2189.
69. M. M. Abdel-Aziz, O. A. Azim, L. A. Abdel-Wahab, M. M. Seddik, Appl. Surf. Sci. 252 (2006) 8716.

70. J. Gautier, F. Delmotte, M. Roulliay, F. Bridou, M. Ravet, A Jerome, Appl. Opt. 44(3) (2005) 384.
71. J. F. Seely, M. P. Kowalski, W. R. Hunter, J. C. Rife, T. W. Barbee, Jr., G. E. Holland, C. N. Boyer, C. M. Brown, Appl. Opt. 32( 25) (1993) 4890.
72. H. Huang, M. Wang. Ceram. Int. 37 (2011) 3167.
73. H. Shinguu, M. M. M. Bhuiyan, T. Ikegami, K. Ebihara, Thin Solid Films 506-507 (2006)111.
74. V. V. Khatko, R. E. Soltis, J. R. McBride, K. E. Nietering, Sensor. Actuator. B 77 (2001) 548.
75. G. Balakrishnan, P. Kuppusami, S. Murugesan, C. Ghosh, R. Divakar, E. Mohandas, D. Sastikumar, Mater. Chem. Phy. 133 (2012) 299.
76. G. Balakrishnan, P. Kuppusami, S. Murugesan, C. Ghosh, R. Divakar, E. Mohandas, D. Sastikumar, Trans IIM, 64 (3) (2011) 297.
77. H. C. Barshilia, B. Deepthi, K. S. Rajam, J. Appl. Phys. 104 (2008) 113532.
78. V. Swamy, H. J. Seifert, F. Aldinger, J. Alloy. Compd. 269 (1998) 201.
79. M. Zinkevich, Prog. Mater. Sci. 52 (2007) 597.
80. P. Zhang, A. Navrotsky, B. Guo. I. Kennedy, A. N. Clark, C. Lesher, Q. Liu, J. Phys. Chem. C, 112 (2008) 932.
81. S. Katagiri, N. Ishizawa, F. Marumo, Powder Diffraction 8 (1993) 60.
82. V. Swamy, N. A. Dubrovinskaya, L. S. Dubrovinsky, J. Mater. Res., 14 (2) (1999) 456.
83. E. Husson, C. Proust, P. Gillet, J. P. Ipie, Mater. Res. Bull. 34 (12-13) (1999) 2085.
84. V. Gourlaouen, G. Schnedecker, A. M. Lejus, M. Boncoeur, R. Collongues, Mat. Res. Bull. 28 (1993) 415.

85. T. Atou, K. Kusaba, K. Fukuoka, M. Kikuchi, Y. Syono, J. Solid State Chem. 89 (1990) 378.

86. R. Mach, G.O. Muller, Phys. Status Solidi A 69 (1982) 11.

87. G.D. Wilk, R.M.Wallace, J.M. Anthony, J. Appl. Phys. 69 (2001) 5243.

88. R.N. Sharma, A.C. Rastogi, J. Appl. Phys. 74 (1993) 6691.

89. R. Ivanic, V.R. Ehacek, I. Novotny, V. Breternitz, L. Spiess, Ch. Knedlik, V. Tvarozek, Vacuum 61 (2001) 229.

90. P. B. W. Burmester, T. Ishii, G. Huber, M. Kurfiss, M. Schilling, Mater. Sci. Eng. B 105 (2003) 25.

91. S. Bar, G. Huber, J. Gonzalo, A. Perea, A. Climent, F. Paszti , Mater. Sci. Eng. B 105 (2003) 30.

92. **E.** Antic-Fidancev, J. Holsa, M. Lastussari Journal of Alloys and Compounds 341 (2002) 82.

93. M. Agarwal, M. R. DeGuire, A. H. Heuer Appl. Phy. Lett., 71 (7) (1997) 891.

94. C. Durand, C. Dubourdieu, C. Vallee, V. Loup, M. Bonvalot, O. Joubert, H. Roussel, O. Renault, J. Appl. Phys. 96 (2004) 1719.

95. D. Niu, R.W. Ashcraft, G.N. Parsons, Appl. Phys. Lett. 80 (19) (2002) 3575.

96. M. Jublot, F. Paurnier, F. Pailloux, B. Lacroix, E. Leau, P. Guerin, M. Marteau, M. Jaouen, R.J. Gaboriaud, D. Imhoff, Thin Solid Films 515 (2007) 6385.

97. A. Ohta, M. Yamaoka, S. miyazaki, Microelectrron. Eng. 72 (2004) 154.

98. M. Spankova, I. Vavra, S. Chromik, S. Harasek, R. Luptak, J. Soltys, K. Husekova , Mater. Sci. Eng. B 116 (2005) 30.

99. Ho-Soon Yang, J. W. Kim, G. H. Park, C. S. Kim, K. Kyhm, S. R. Kim, K. C. Kim, K. S. Hong, Thermocimica. Acta. 455 (2007) 50.

100. W. M. Cranton, D. M. Spink, R. Stevens, C. B. Thomas, Thin Solid Films 226 (1993) 156.

101. R. N. Sharma S. T. Lakshmikumar, R. C. Rastogi , Thin solid films 199 (1991) 1.

102. V. Cracium , J. Howard, E. S. Lambers, R. K. Singh, D. Cracium, J. Perriere, Appl. Phys A 69 (1999) S535.

103. S. Zhang, R. Xiao, J. Appl. Phys. 83 (7) (1998) 3842.

104. X. Cheng, Z. Qi, G. Zhang, H. Zhou, W. Zhang, M. Yin, Physica B 404 (2009) 146.

105. S.A. Barve, Jagannath, M.N. Deo, R. Kishore, A. Biswas, L.M. Gantayet, D.S. Patil, Appl. Surf. Sci. 257 (2010) 215.

106. A. Dimoulas, G, Vellianitis, A. Travlos, V. Loannou-Sougleridis, A. G. Nassiopoulou, J. Appl. Phys. 92 (1) (2002) 126.

107. R. J. Brook, Concise Encyclopedia of Advanced Ceramic Materials, Pergaman Press, 1990, Page 494.

108. J. D. McCullough, K. N. Trueblood, Acta. Cryst. 12 (1959) 507.

109. D. K. Smith, H. W. Newkirk, Acta. Cryst. 18 (1965) 983.

110. N. Igawa, Y. Ishii, T. Nagasaki, Y. Morii, S. Funahashi, H. Ohno, J. Am. Ceram. Soc. 76 (10)(1993) 2673.

111. R. Srinivasan, R. J. De Angelis, G. Ice, B. H. Davis. J. Mater. Res.6 (6) (1991) 1287.

112. P. F. Manicone, P. R. Iommetti, L. Raffaelli, J. Dentistry 35 (2007 ) 819.

113. I. Denry, J. Robert Kelly, Dent. Mater. 24 (2008) 299.

114. V. Craciun, D. Craciun, I. W. Boyd, Electron. Lett. 34 (15) (1998) 1527.

115. K. V. S. R. Apparao, N. K. Sahoo, T. C. Bagchi, Thin solid films 129 (1985) L71.

116. A. Methievier, M. Pijolat, J. Catal. 139 (1993) 329.

117. R. J. Gorte, J. M. Vohs, J. Catal. 216 (2003) 132.

118. Y. H. Sohn, K. Vaidyanathan, M. Ronski, E. H. Jordan, M. Gell, Surf. Coat. Technol. 146 (2001) 132.

119. F. Gallino , C. Di Valentin, G. Pacchioni Phys. Chem. Chem. Phys.13 (2011) 17667.

120. S. Tekeli, U. Demir, Ceram. Int. 31 (2005) 973.

121. A. K. Shukla, Vandana Sharma, N. Arul Dhas, K. C. Patil, Mater. Sci. Eng. B 40 (1996) 153.

122. A. N. Shengli, T. Zhou, W. U. Weijiang , Q. LIU, Solid State Ionics, 40/41 (1990) 750.

123. S. K. Durrani, J. Akhtar, M. Ahmad, M. A. Hussain, Mater. Chem. Phys. 100 (2006) 324.

124. O. Bernard, A. M. Huntz, M. Andrieux, W. Seiler, V. Ji S. Possonnet, Appl. Surf. Sci. 253 (2007) 4626.

125. G. Pengtao, L. J. Meng, M. P. Dos Santos, V. Teixeira, M. Andritschky, Vacuum 64 (2002) 267.

126. D. R Clark, F. Adar, J. Am. Ceram. Soc. 75 (3) (1982) 284.

127. T. Chraska, A. H. King, C. C. Berndt, Mater. Sci. Engg. A 286 (2000) 169.

128. R. C. Garvie, J. Phys. Chem. 82 (1978) 218.

129. P. Bouvier, J. Godlewski , G. Lucazeau , J. Nucl. Mater. 300(2002) p 118.

130. B. Benali, A. M. Huntz, M. Andrieux, M. Ignat, S. Poissonnet, Appl. Surf. Sci. 254 (2008) 5807.

131. J. P. Holgado, J. P. Espinos, F. Yubero, A. Justo, M. Ocana, J. Benitez and A. R. Gonzalez-elipe, Thin Solid Films 389 (2001)34.

132. S. Duenas, H. Castan, J. Barbolla, K. Kukli, M. Ritala, M. Leskela, Solid- State Electron. 47 (2003) 1623.

133. J. P. Chang, Y. S. lin, Appl. Phys. Lett. 79 (22)(2001) 3666.

134. Y-M Gao, P. Wu, R. Kershaw, K. Dwight, A. Wold, Mat. Res. Bull. 25 (1990) 871.

135. C. Flamini, A. Giardini Guidoni, R. teghil, V. Marotta, Appl. Surf. Sci. 138-139 (1999) 344.

136. G. Balakrishnan, T. N. sairam, P. Kuppusami, R. Thirumurugesan, E. Mohandas, V. Ganesan, D. Sasti Kumar, Appl. Surf. Sci. 257 (2011) 8506.

137. A. Mehener, H. Klumper-Westkamp, F. Hoffmann, P. Mayr, Thin Solid Films 208-309 (1997) 363.

138. S. Venkataraj, L. Kappertz, H. Weis, R. Drese, R. Jayavel, M. Wuttig , J. Appl. Phy. 92 (7) (2002) 3599.

139. S. Miyazaki, M. Narasaki, M. Ogasawara, M. Hirose, Solid State Electron. 46 (2002)1679.

140. Z. W. Zhao, B. K. Tay, G Q Yu, S P Lau, J. Phys. 15 (2003) 7707.

141. M. G. Krishna, K. N. Rao, S. Mohan, Thin Solid Films 193/194 (1990) 690.

142. I. K. Then , M. Mujahid, B. Zhang, Surf, Coat. Technol. 198 (2005) 104.

143. H. K. yueh, B. Cox, J. Nuclear Materials 323 (2003)57.

144. Y. Sun, Yibin Li, min Teng, Y. Wang, Xiaodong he, Nanoscience & Nanotechnology Letters, 1 (2009)140.

145. J. Gottmann, A. Husmann, T. Klotzbucher, E.W. Kreutz, Surf. Coat. Technol. 100–101 (1998) 415.

146. N. V. Skorodumova, R. Ahuja, S. I. Simak, I. A. Abrikosov, B. Johansson, B. I. Lundqvist, Phys. Rev. B, 64() 115108.

147. M. Mogensena, N. M. Sammes, G. A. Tompsett, Solid State Ionics 129 (2000) 63.

148. M. Hartmanova, K. Gmucova, I. Thurzo, Solid State Ionics 130 (2000) 105.

149. M. A. Sainz, A. Duran, J. M. Fernandez Navarro, J. Non-Crystalline Solids 121 (1990) 315.

150. A. Trovarelli, Catal. Rev. Sci. Eng. 38(4) (1996) 439.

151. G. C. Pontelli, R. P. Reolon, A. K. Alves, F. A. Berutti,C. P. Bergmann, Appl. Catal. A: General 405 (2011) 79.

152. X. Zhong, Q. Li, J. Hu, Y. Lu, Corrosion Sci. 50 (2008) 2304.

153. A. A. Ansari, A. Kaushik, P.R. Solanki, B.D. Malhotra, Electro. Comm. 10 (2008) 1246.

154. P. Jasinski, T. Suzuki, H. U. Anderson , Sensor. Actuator. B 95 (2003) 73.

155. S. Saha, S. K. Arya, S. P. Singh, K. Srinivas, B. D. Malhotra, V. Gupta, Biosensors Bioelectron. 24 (2009) 2040.

156. K. Eguchi, T. Setoguchi, T. Inoue, H. Arai, Solid State Ionics 52 (1992) 165.

157. E. Gourba , P. Briois , A. Ringuede , M. Cassir, A. Billard, J Solid State Electrochem 8 (2004): 633.

158. J. S. Wiatowskaa, V. Lair, C. Pereira-Nabaisa, G. Coteb, P. Marcusa, A. Chagnes, Appl. Surf. Sci. 257 (2011) 9110.

159. A. Bumajdad, J. Eastoe, A. Mathew, Advances in Colloid and Interface Science 147–148 (2009) 56.

160. Z. L. Liu, H. M. Yue, Y. Wang, K. L. Yao, Q. Liu, Solid State Comm. 124 (2002) 171.

161. A. Nazeri, P.P. Trzaskoma-Paulette, D. Bauer, J. Sol-Gel Sci. Technol 10, (1997) 317.

162. F. Sutara, M. Cabala, L. SedlAcek, T. Skala, M. Skoda, V. Matolín, K.C. Prince, V. Chabc, Thin Solid Films 516 (2008) 6120.

163. A. Guibadj, P.Odier, B.Benbarta, L.Ortega, J. Cry. Growth 328 (2011) 102.

164. J. Zhou, D.R. Mullins, Surf. Sci. 600 (2006) 1540.

165. N. Savvides, A. Thorley, S. Gnanarajan, A. Katsaros, Thin Solid Films 388 (2001) 177.

166. P. Roura , J. Farjas, S. Ricart, M. Aklalouch, R. Guzman, J. Arbiol, T. Puig , A. Calleja , O. Peña-Rodríguez, M. Garriga, X. Obradors, Thin Solid Films 520 (2012) 1949.

167. G. Balakrishnan, S. Tripura Sundari, P. Kuppusami , P. Chandra Mohan, M. P. Srinivasan, E. Mohandas, V. Ganesan, D. Sastikumar, Thin Solid Films 519 (2011) 2520.

168. J. H. Joo, G. Man Choi, J. Eur. Ceram. Soc. 27 (2007) 4273.

169. K. Eguchi, T. Setoguchi, T. Inoue and H. Arai, Solid State lonics 52 (1992) 165.

170. N. Ozer, Solar Energy Mater. C. 68 (2001) 391.

171. I. Kosacki, T. Suzuki, V. Petrovsky, H. U. Anderson, Solid State Ionics 136–137 (2000) 1225.

172. U. Lavren, Stangar, B. Orel, I. Grabec, B. Ogorev, K. Kalcher, Solar Energy Mater. C 31 (1993) 171.

173. J. J. Roa, E. Gilioli, F. Bissoli, F. Pattini, S. Rampino, X.G. Capdevila, M. Segarra, Thin Solid Films 518 (2009) 227.

174. D. Jia, L. Lu, W.M. Yen, Opt. Comm. 212 (2002) 97.

175. J. McAlees, J. C. Plakatouras, B. C.H. Steele, Thin Solid Films 286 (1996) 64.

176. M. P. Singh, S. A. Shivashankar, J. Cryst. Growth 276 (2005) 148.

177. J. X. Wang, A. Laha, A. Fissel, D. Schwendt, R. Dargis, T. Watahiki, R. Shayduk, W. Braun, T. M. Liu, H. J. Osten, Semicond. Sci. Technol. 24 (2009) 045021.

178. Y. Lia, N. Chena, J. Zhou, S. Songa, L. liu, Z. Yina, C. Caia, J. Cryst. Growth 265 (2004) 548.

179. S. Thakur, N. K. Sahoo, M. Senthilkumar, R. B. Tokas, Optical Mater., 27 (2005) 1402.

180. H. D. B. Gottlob, T. Echtermeyer, T. Mollenhauer, J.K. Efavi, M. Schmidt, T. Wahlbrink, M.C. Lemme, H. Kurz, M. Czernohorsky,E. Bugiel, H.-J. Osten, A. Fissel, Solid-State Electronics 50 (2006) 979.

181. J. C. Chen, G.H. Shen, L.J. Chen, Appl. Surf. Sci. 142 (1999) 120.

182. A. A. Dakhel, J. Alloy. Compd. 388 (2005) 177.

183. A. Molle, S. Spiga, M. N. K.Bhuiyan, G. Tallarida, M. Perego, C. Wiemer, M. Fanciulli, Mat. Sci. Semicon. Proc. 11 (2008) 236.

184. J. X. Wang, A Laha, A Fissel, D Schwendt, R Dargis, T. Watahiki, R Shayduk,WBraun, T M Liu, H J Osten, Semicond. Sci. Technol. 24 (2009) 045021.

185. I. Zhitomirsky, A. Petric, Mater. Lett. 42 (2000) 273.

186. A. Molle, S. Spiga, M.N.K.Bhuiyan, G.Tallarida, M.Perego, C.Wiemer, M.Fanciulli, Mater. Sci. Semicond. Process. 11 (2008) 236.

187. X. Cheng, D. Xu, Z. Song, D. He, Y. Yu, Q. Zhao, D. Shen, Appl. Surf. Sci. 256 (2009) 921.

188. R. Endres, Y. Stefanov, U. Schwalke, Microelectronics Reliability 47 (2007) 528.

189. F. X. Zhang, M. Lang, J. W. Wang, U. Becker, and R. C. Ewing, Phys. Rev. B 78 (2008) 064114.

190. Donald M. Mattox , “Handbook of Physical vapor deposition Processing”, NOYES PUBLICATIONS (1998) ISBN: 0-8155-1422-0.

191. A. E. Riad, Fred DD Barlow,"Thin Film Technology". (1998) ISBN No: 0-07-019025-9, McGraw –Hill Publication.

192. Ian W.Boyd, Ceram. Int. 22 (1996) 429.

193. Robert Eason , "Pulsed laser deposition of thin films, Applications-led growth of functional materials", , Wiley-Interscience, ISBN: 0-471-44709-9 (2007).

194. D. B. Chrisey, G. K. Hubler, "Pulsed Laser Deposition of thin films". Wiley Interscience Publication (1994) (ISBN No. 0-471-59218-8).

195. P. R. Willmott, J. R. Huber, Reviews of Modern Physics, Vol. 72, No. 1, 2000, 315.

196. Q. Bao, C. Chen, D. Wang, Q. Ji, T. Lei, Appl. Surf. Sci. 252 (2005) 1538.

197. D. H. Lowndes, D. B. Geohegan, A. A. Puretzky, D. P. Norton, C. M. Rouleau, Science 273 (1996) 898.

198. K. L. Chopra ,"Thin film Phenomena", McGraw-Hill Company (1969).

199. A. C. Lewis, D. Josell, T. P. Weihs, Scripta Mater. 48 (2003)1079.

# Chapter 2
# Experimental Methods and Characterization

## 2.1 Introduction

This chapter explains the principles and experimental procedures of thin film deposition and characterization followed during the course of investigation. First part of the chapter gives the details of target synthesis and thin film deposition by PLD. In the second part, details of the characterization techniques used in the present study are explained along with the basic principle of each characterization method.

## 2.2 Thin Film Synthesis

### 2.2.1 Target preparation

To prepare good quality films by PLD, high density and highly homogeneous targets are required to avoid melting of target as well as particulate formation [1,2]. In addition to this the other main requirement is flat surface. To obtain a highly dense target, the powders are sintered at high temperatures (~2/3rd of the melting point of the material) [3], after forming a pellet. The sintered density was measured from weight and volume change before and after sintering.

### 2.2.1.1 Preparation of $Y_2O_3$ target

$Y_2O_3$ target was prepared from commercially available $Y_2O_3$ powder of ~99.99% purity (Alfa Aeser, CAS No.1314-36-9). The powder was fine ground and compacted to a pellet of 20 mm diameter and 3 mm thick by applying a load of 10 MPa. The pellet was sintered at 1723K for 4 h. The pellet had a sintered density ~90%. The pellet was characterized by XRD. Figure 2.1 shows the XRD pattern of $Y_2O_3$ target used to prepare $Y_2O_3$ films [4]. XRD pattern showed a phase pure cubic-$Y_2O_3$ (BCC) [JCPDS file no # 41-1105]. XRD pattern indicated the absence of any impurities in $Y_2O_3$ target.

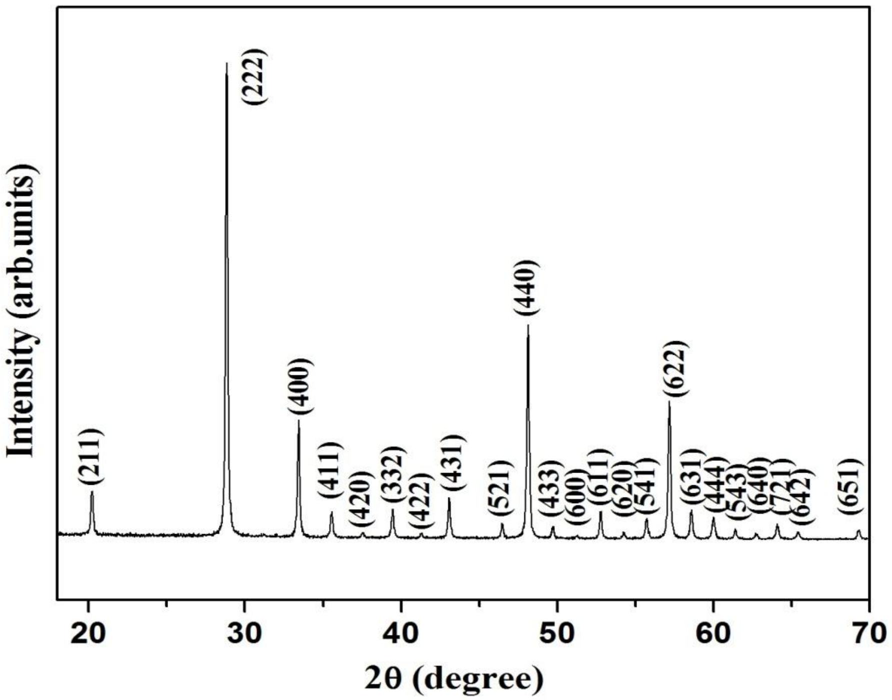

**Fig. 2.1 XRD pattern of sintered $Y_2O_3$ target.**

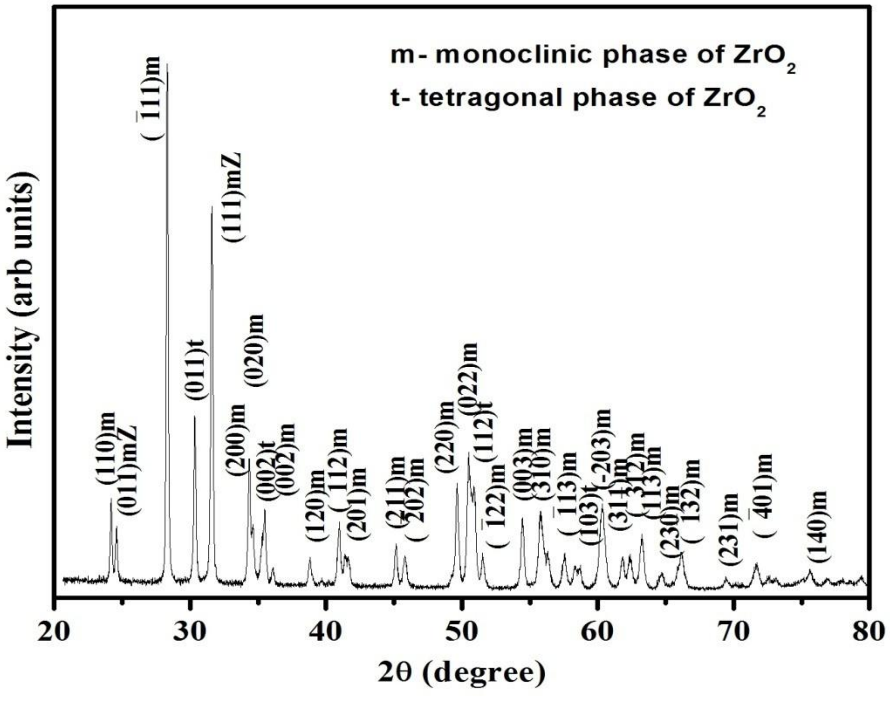

**Fig. 2.2 XRD pattern of a sintered $ZrO_2$ target.**

### 2.2.1.2 Preparation of $ZrO_2$ target

A $ZrO_2$ target of 25 mm diameter and 3 mm thickness was prepared from commercially available $ZrO_2$ powder of 99.99% purity (Sigma-Aldrich, CAS No.1314-23-4). Powder was fine ground and a pellet (20 mm diameter and 3 mm thickness) was prepared by applying a pressure of 10 MPa using a uniaxial press and was sintered at 1673 K for 6 h. The purity and microstructure of the target was analyzed by XRD. Fig. 2.2 shows the XRD pattern of a sintered $ZrO_2$ target, consisting of two phases of $ZrO_2$ i.e monoclinic (JCPDS file no. #37-1484) and tetragonal phase (JCPDS file no. # 50-1089). The phase content of the sintered pellet was qualitatively determined from the strongest line of the monoclinic phase and tetragonal phase obtained from the XRD analysis. The monoclinic phase content was found to be more than that of tetragonal phase from XRD analysis [5].

### 2.2.1.3 Preparation of $CeO_2$ target

Target of $CeO_2$ was prepared from ~99.99% pure $CeO_2$ powder supplied by Alfa Aesar (CAS No. 1306-38-3). The powder was pressed to a 20 mm diameter and 3 inch thick pellet, applying a pressure of 10 MPa. The pellet was heat treated at 1673 K for 4 hrs in a box furnace. After the heat treatment the pellet was analyzed by XRD for purity of target. XRD pattern of sintered $CeO_2$ target is shown in Fig. 2.3. The XRD pattern shows a phase pure cubic $CeO_2$ of Face centered cubic (FCC) structure (JCPDS File NO. 00-044-0593).

### 2.2.1.4 Preparation of $Gd_2O_3$ target

$Gd_2O_3$ target of 20 mm diameter and 3 mm thickness was prepared from commercial $Gd_2O_3$ powder (Hysec Internationals of ~99.99% purity). The pellet was prepared by pelletizer, followed by heat treatment at 1823 K for 6 hrs. The sintering temperature was selected with reference to melting point of $Gd_2O_3$ [6]. Characterization of the target was carried out by XRD.

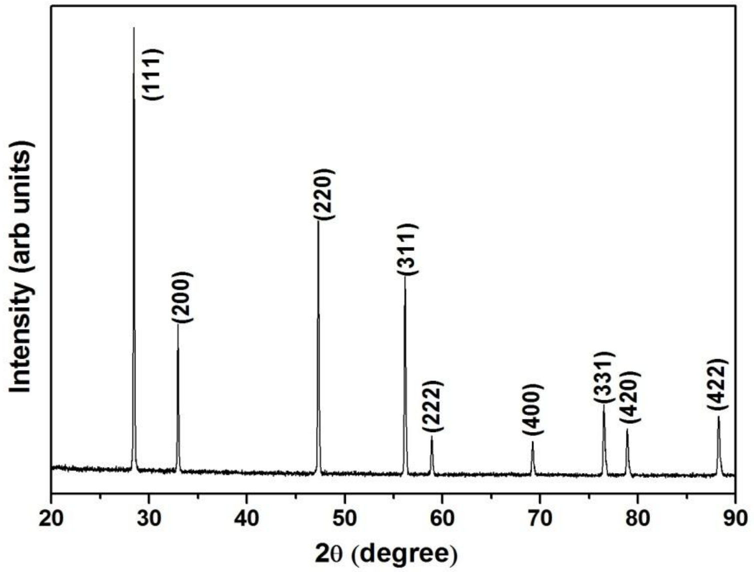

Fig. 2.3 XRD pattern of sintered $CeO_2$ target.

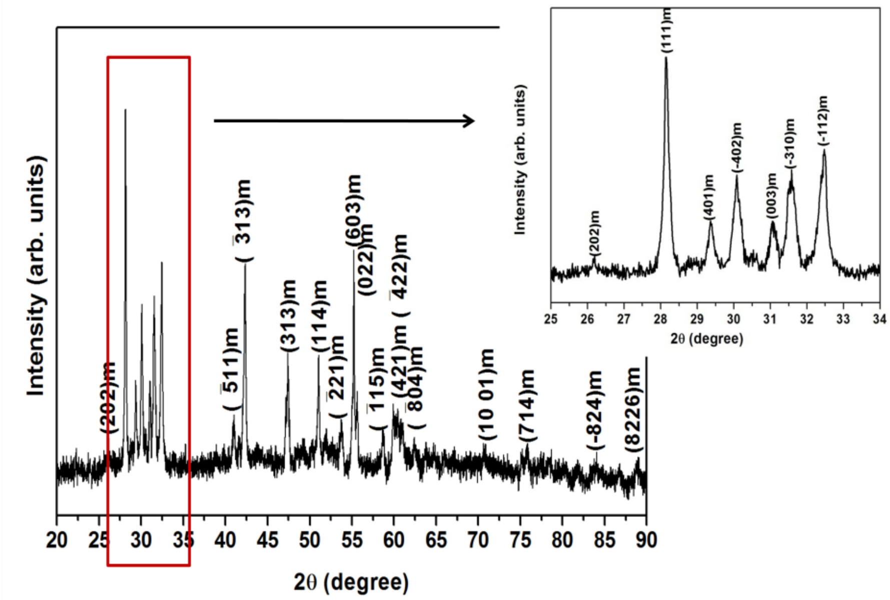

Fig. 2.4 XRD pattern of a sintered $Gd_2O_3$ target showing monoclinic phase.

Fig. 2.4 shows the XRD pattern of sintered $Gd_2O_3$ target after heat treatment. The inset shows the reflections in the 2ϴ range of 25- 34˚. XRD pattern shows the presence of monoclinic phase of $Gd_2O_3$ (JCPDS File NO. 01-077-8312).

### 2.2.2 Substrate preparation

For the thin film deposition substrates of size 10 mm × 10 mm × 0.5 mm were cut from Si (100), quartz and Inconel-783 wafers. The details of the Inconel-783 composition are given in Table 2.1. The substrates were washed with soap solution to remove the dust particles from the surface followed by ultrasonic cleaning with water and methanol ($CH_3$-OH), respectively. Inconel-783 substrates were polished using successive grade of SiC paper, followed mechanical polishing by oxide dispersed silica suspension (OPS solution). After cleaning, the substrates were dried and mounted onto the substrate holder using silver paste. Inconel-783 substrates were used only for measuring the nanomechanical properties, while silicon and quartz substrates were used for the study of microstructural and optical properties, respectively.

**Table 2.1 Chemical composition of major elements of Inconel-783 (wt. %)**

| Element | Ni | Co | Fe | Al | Nb | Cr |
|---|---|---|---|---|---|---|
| composition | 34 | 25 | 5.4 | 3 | 3.2 | 0.01 |

### 2.2.3 Thin film deposition by pulsed laser deposition

Deposition system consists of two parts: 1. Deposition chamber and 2. Laser source. Figure 2.5 shows the PLD system used for thin film preparation. The deposition chamber consists of a spherical chamber attached with rotary, turbo molecular pump and substrate and target carousel for six targets, oxygen mass flow controller, target rotator, heater and a lens.

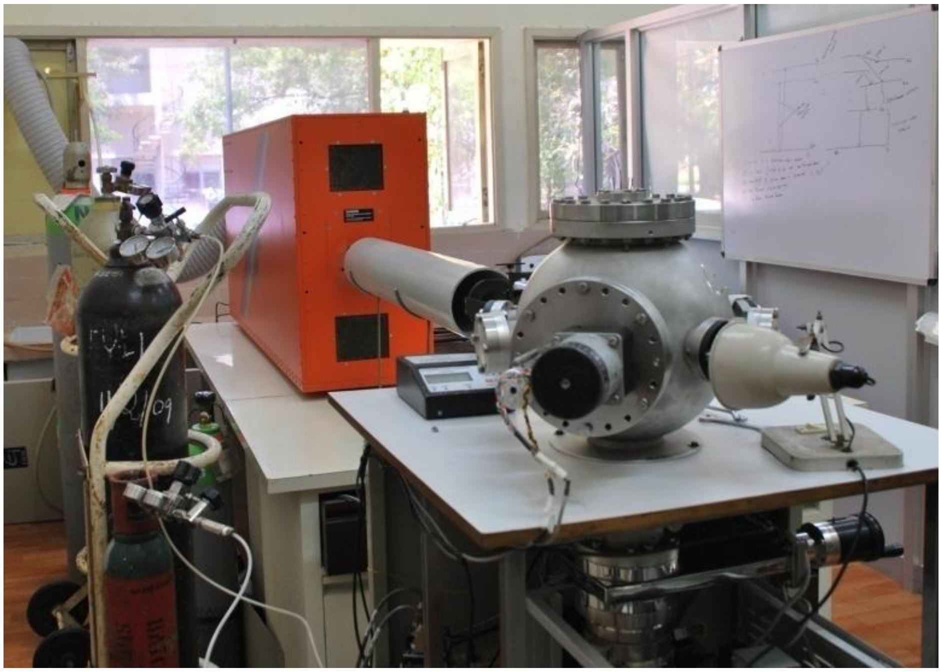

**Fig. 2.5 PLD system used for preparation of thin films.**

All the four targets ($Y_2O_3$, $ZrO_2$, $CeO_2$ and $Gd_2O_3$) were mounted on to the target carousel using silver paste. The cleaned substrates were mounted onto the substrate holder. Deposition chamber was evacuated to a base pressure of ~ 0.002 Pa, using a rotary and turbo pump combination. After the base vacuum was achieved, the substrates were heated using a resistive heater (which is under the substrate holder) to required temperature. Oxygen gas was released into the chamber using a mass flow controller and pressure inside the chamber was measured by a cold cathode ionization gauge.

To grow a thin film, the useful range of laser wave length is between 200-400 nm [1]. Shorter wavelength leads to small penetration depth, which in turn increases the efficiency of deposition. Most of the thin film deposition methods reported in the literature are based on excimer and Nd-YAG lasers [1]. In an excimer laser, the laser light is produced due to the lasing action between upper bound electronic state and lower ground electronic state. Out of different excimer lasers, KrF laser is most widely used due to its high gain [7].

In the present study, a KrF excimer laser (Lambda Physik Compex-205, 248 nm wavelength) was used as the energy source for the deposition of thin films and multilayer films of various oxides. The laser light was focused onto the target using a cylindrical lens of focal length 50 cm. The depositions were carried out at laser energy of 300 mJ/pulse and repetition rate of 10 Hz. The following two important precautions were regularly followed at the end of at least two depositions: (i) cleaning of quartz window of the chamber and (ii) polishing of the target to remove grooving due to the laser and target interaction. The cleaning of the quartz window was useful to avoid loss of energy of laser due to scattering from the deposited materials, while polishing of the target was beneficial to retain a uniform deposition rate from the target. Targets were rotated (10 rpm) to avoid grooving of the targets. The substrate temperature and oxygen partial pressure were adjusted according to the requirements of experimental conditions. All the single layer films were deposited for 1h at each experimental condition.

Deposition rate of each material was determined by depositing each material for 15 min at room temperature and 2 Pa of oxygen partial pressure. From the thickness data, the deposition rates were calculated, which were later used for preparing multilayer structures by adjusting the time of deposition. In the multilayer structures of $Y_2O_3/ZrO_2$ and $Gd_2O_3/CeO_2$, the layer thickness of $Y_2O_3$ and $Gd_2O_3$ were kept constant (~10 nm), while $ZrO_2$ and $CeO_2$ layer thickness were varied from 5- 30 nm. After deposition the samples were analyzed by different techniques. The experimental conditions used in the deposition of single and multilayer of oxides are given in the subsequent sections.

## 2.3 Characterization Techniques

### 2.3.1 Thickness measurement

There are many methods such as weight gain, profilometer, spectroscopic reflectrometer and ellipsometer etc, by which thickness of a film can be measured. In the present work, thickness of both single as well as multilayer films were measured by a profilometer (DEKTAK6M-stylus profiler), and the method is useful to measure a thickness in the range 20 nm-1 mm with 1 nm accuracy. To measure the thickness of the film, a step was created using a mask. The tip of the stylus was moved on the surface across the step. The step size was measured by taking the difference between the height of coated and uncoated regions of the sample.

### 2.3.2 X-ray diffraction

X-ray diffraction (XRD) is a nondestructive technique used to determine the microstructure, crystallinity, phase, texture and stress. An X-ray diffraction pattern is a plot of intensity versus diffraction angle. In the diffraction pattern 2θ position represents the angle of diffraction of a particular plane from which the d-spacing as well as lattice parameter can be derived. The crystallite size of the film is determined from the full width at half maximum (FWHM), while the analysis of the intensity provides a measure to estimate the phase content. It is also possible to obtain the nature of preferred orientation (texture) qualitatively by monitoring the intensity ratio of any two strong reflections of a phase.

Microstructural characterization of the single and multilayer films was carried out by using X-ray diffractometer (INEL XRG-3000, France) (Figure 2.6) attached with a curved position sensitive detector using $CuK\alpha_1$ (1.5406 Å) radiation. Sample was loaded onto a holder, which was spinned horizontally to collect data from whole sample. The patterns were collected with incident angle (ω) of 5˚ in the 2θ range of 10 - 100˚ with an angular resolution of 0.0125˚.

By Gaussian fitting of the peaks, the exact 2θ and full width at half maximum (FWHM) values were determined. From the 2θ values, d-spacings (d) were calculated using Bragg's equation (equation. 2.1) [8]

$$\boldsymbol{n\lambda = 2dSin}\Theta \quad \ldots\ldots\ldots\ldots\ldots\ldots\ldots\ldots\ldots\ldots \quad \textbf{(2.1)}$$

Where n is the order of reflection, λ is the wavelength, d is the spacing between the planes in the atomic lattice and Θ is the Bragg's angle. The peaks were indexed with reference to JCPDS files of star (*) quality of the respective material. Lattice parameters were calculated using "Unit Cell program" [9], from the 2Θ and (hkl) values. The basic equations for calculating lattice parameter from d-values (which can be derived from 2Θ values) for cubic, tetragonal and monoclinic phases are given in the equations 2.2, 2.3 and 2.4, respectively [10].

$$\frac{1}{d^2} = \frac{(h^2+k^2+l^2)}{a^2} \quad \ldots\ldots\ldots\ldots\ldots\ldots\ldots\ldots\ldots\ldots \quad \textbf{(2.2)}$$

$$\frac{1}{d^2} = \frac{h^2+k^2}{a^2} + \frac{l^2}{c^2} \quad \ldots\ldots\ldots\ldots\ldots\ldots\ldots\ldots\ldots\ldots \quad \textbf{(2.3)}$$

$$\frac{1}{d^2} = \frac{1}{Sin^2\beta}\left\{\frac{h^2}{a^2} + \frac{k^2 Sin^2\beta}{b^2} + \frac{l^2}{c^2} - \frac{2hlCos\beta}{ac}\right\} \quad \ldots\ldots\ldots \quad \textbf{(2.4)}$$

Where *a*, *b* and *c* are the lattice parameters. The 2Θ and FWHM values were used to index the peaks and calculate the crystallite size by using Scherrer formula (equation 2.5).

$$\boldsymbol{D} = \frac{0.9\,\lambda}{\beta Cos\Theta} \quad \ldots\ldots\ldots\ldots\ldots\ldots\ldots\ldots\ldots\ldots \quad \textbf{(2.5)}$$

β is the FWHM after subtracting instrumental broadening and $\beta=\sqrt{(B^2 - b^2)}$,where B is the FWHM of the peak and b is the instrumental broadening obtained from the standard Si powder.

Preferred orientation (texture coefficient) of a plane is calculated by equation 2.6

$$\boldsymbol{TC}_{(hkl)} = \frac{\frac{I_{(hkl)}}{I_{0(hkl)}}}{\sum\frac{I_{(hkl)}}{I_{0(hkl)}}} \quad \ldots\ldots\ldots\ldots\ldots\ldots\ldots\ldots \quad \textbf{(2.6)}$$

Where $I_{(hkl)}$ intensity of the particular peak, and $I_{0(hkl)}$ is the standard intensity of the plane from JCPDS data. In the case of presence of mixed phases, the volume fraction of a particular phase was calculated by taking into account the highest intensity of the two peaks corresponding to both the phases. For example, in the case of $ZrO_2$ containing monoclinic $ZrO_2$ and tetragonal $ZrO_2$, the volume fraction ($V_t$) of tetragonal phase is calculated using the following equation 2.7.

$$\boldsymbol{V_t = \frac{I_{t(002)}}{I_{m(200)}+I_{t(002)}}} \text{..............................} \textbf{(2.7)}$$

Where $I_t$ and $I_m$ represent the intensity of the tetragonal and monoclinic phases.

The strain values were estimated by the change in d-spacing with respect to the d-spacings in JCPDS file (equation 2.8).

$$\textbf{Strain=} \boldsymbol{\frac{\Delta d}{d}} \text{ ................................} \textbf{(2.8)}$$

Where $\Delta d = d - d_0$ , $d$=the d-spacing from the experiment and $d_0$ is the d-spacing from JCPDS file.

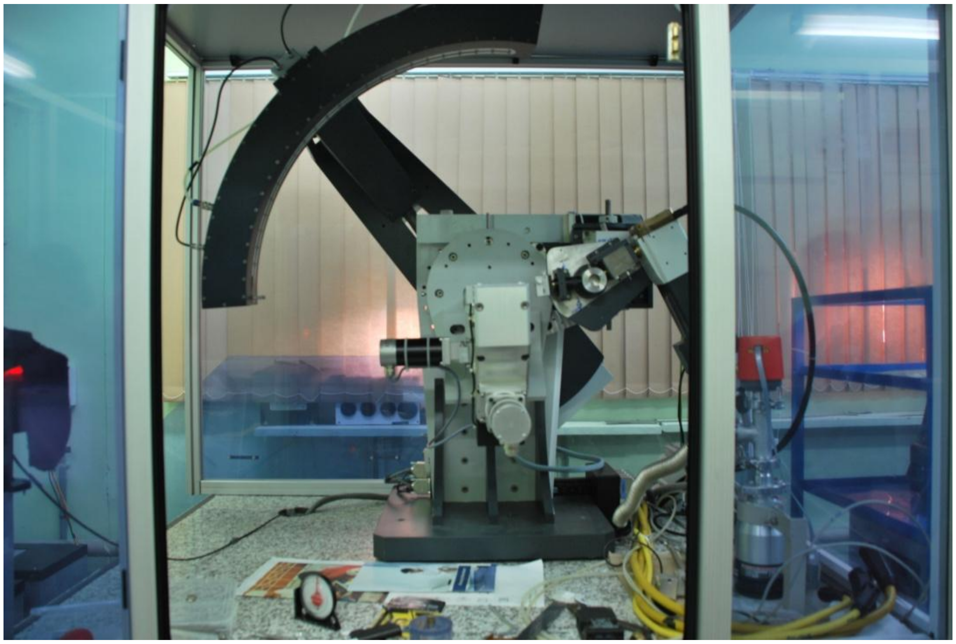

**Fig. 2.6 X-ray Diffractometer used for XRD analysis.**

### 2.3.3 High temperature X-ray diffraction

High temperature X-Ray Diffraction (HTXRD) is a technique in which samples are heated and XRD patterns are recorded at a particular temperature. In the present work HTXRD is used to study the phase stability and to determine the coefficient of thermal expansion (CTE) of the thin films and multilayers.

HTXRD experiments of single as well as multilayer samples were carried out using an INEL XRG-3000 X-ray diffractometer attached with a high temperature arrangement (Buhler HDK 2.4). Films deposited on Si (100) substrates were kept on a tantalum base and in-situ heated in a temperature range of 300 - 1373 K, with a heating rate of 10K/min. To maintain a uniform temperature, the substrate holder was radiatively heated by surrounding heater made up of tantalum. The temperature was measured using a W-Re thermocouple with ±2$^{o}$ K tolerance. Data were recorded with incident angle $\omega = 5^{\circ}$, for a 2Θ range of 10$^{o}$ – 100$^{o}$, for a time period of 15 min, after 3 minutes of stabilization time using a curved position sensitive detector. After heating, samples were cooled with a rate of 50 K/min to room temperature.

From the HTXRD pattern, lattice parameter changes and phase stability were monitored. From the lattice parameter data, average linear coefficient of thermal expansion as well as instantaneous coefficient of thermal expansion ($\alpha_{\text{inst}}$) values were calculated using equation 2.9 and 2.10, respectively [11,12].

$$\boldsymbol{\alpha_{\mathrm{a}} = \frac{1}{a_{Rt}}\left[\frac{a_T - a_{Rt}}{T - RT}\right]} \;\ldots\ldots\ldots\ldots\ldots\ldots\ldots\ldots\ldots\ldots\ldots\; \mathbf{(2.9)}$$

$$\boldsymbol{\alpha_{\mathrm{inst}} = \frac{1}{a_T}\left[\frac{\partial a}{\partial t}\right]} \;\ldots\ldots\ldots\ldots\ldots\ldots\ldots\ldots\ldots\ldots\ldots\ldots\mathbf{(2.10)}$$

Where $\alpha_a$ is the average thermal expansion coefficient along a axis, $a_T$ and $a_{RT}$ are the lattice parameter values at temperature, T and room temperature (RT), respectively.

### 2.3.4 Raman spectroscopy

Raman spectroscopy is a nondestructive technique, used to identify the structure, symmetry, crystallinity and phase of the material [13]. Raman spectroscopy deals with the inelastic scattering of light after its interaction with material, resulting in a difference in incident and scattered energy. In Raman spectroscopy, the scattered light is observed in perpendicular direction to the incident light. Scattered light consists of two types of light: (i) light due to Rayleigh scattering, where the frequency is same as that of the frequency of incident light ($\nu_0$) and (ii) Raman scattering where the light frequency is either greater or lesser than that of the incident light. In Raman spectroscopy, the shift in frequency from that of the incident frequency is measured. The shift in frequency ($\Delta\nu$) in Raman spectroscopy can be written as (equation 2.11)

$$\boldsymbol{\Delta\nu = \nu_0 \pm \nu_m} \quad \ldots\ldots\ldots\ldots\ldots\ldots\ldots\ldots\textbf{(2.11)}$$

Where $\nu_0$ - $\nu_m$ and $\nu_0$ + $\nu_m$ lines are called the Stokes and anti-Stokes lines, respectively [14].

Raman spectroscopy was performed using a spectrometer (HR 800, Jobin Yvon) equipped with 1800 grooves/mm holographic grating. The samples were placed under an Olympus BXFM-ILHS optical microscope mounted at the entrance of the Raman spectrograph. Argon ion ($Ar^+$) laser of wavelength 488 nm and 514 nm (depending on material) was used as an excitation source. The laser spot size of 3 mm diameter was focused tightly on the sample surface using a diffraction limited (numerical aperture = 0.25 at 10x) long distance objective. The laser power at the sample was kept at 15 mW. The slit width of the monochromator was 400 μm. The back scattered Raman spectra were recorded using a supercooled (~383 K) charge-coupled device (CCD) detector.

### 2.3.5 X-ray reflectivity measurement

X-ray reflectivity (XRR) measurement is an analytical technique that deals with the specular reflection of X-rays from sample surface. It is a nondestructive technique, used to analyze mainly multilayer structures of thickness range from one to a few hundred nanometers. XRR profile analysis provides information on individual layer thickness, electron density function, surface and interfacial roughness.

When X-ray beam is incident onto a material, it is diffracted from the lattice planes according to Bragg's law. But if the incident angle (ϴ) is decreased beyond certain critical values, then total external reflection of X-rays occurs. The critical angle ($\Theta_c$) is defined as [15-17] (equation 2.12).

$$\mathbf{Cos\Theta_c = \boldsymbol{n} = 1\text{-}\delta} \text{ ........................................ } \mathbf{(2.12)}$$

Where $n$ is the refractive index and δ is the light scattering factor of material. Applying Taylor approximation for n~1

$$\mathbf{(\Theta c)^2 = 2\delta = \frac{\lambda^2 r_e}{\pi}\rho} \text{ .......................................} \mathbf{(2.13)}$$

Where ρ is the electron density function, $r_e$ is the classical radius of electron, λ is the wavelength of incident radiation. Typical values of $\Theta_c$ lie in the range of 0.2-0.6 for CuKα radiation.

When X-ray beam is incident onto material, both reflection and transmission phenomena occur. The specular reflection (R(ϴ)) is defined as (equation 2.14)

$$\mathbf{R(\Theta) = \frac{I(\Theta)}{I_0}} \text{ ............................................... } \mathbf{(2.14)}$$

I(ϴ) is the reflected intensity at ϴ angle, and $I_0$ is the incident intensity.

XRR deals with the specular reflection i.e. angle of incidence is equal to angle of reflection. In such situation, the momentum transfer ($Q_z$) along the surface normal is given by equation 2.15.

$$Q_z = \frac{4\pi}{\lambda} Sin\,\alpha \quad \ldots\ldots\ldots\ldots\ldots\ldots\ldots\ldots\ldots\ldots \quad (2.15)$$

Where α is the incident angle. An XRR profile is obtained with scattered X-ray intensity versus incident angle and the angle of incidence is converted to momentum transfer vector ($Q_z$) using equation 2.12, and the intensity is normalized with respect to the intensity at critical angle.

Multilayer samples were analyzed using BRUKER D8 diffractometer, using CuK$\alpha_1$ (1.5406 Å) at 0.001° step size with angular range of 0.2°-8°. The intensity versus 2Θ plots were converted to reflectivity versus $Q_z$ plots using equation 2.10. The XRR profiles were fitted using Parrat 1.5 software [18]. From the profile fitting, individual layer thickness, surface and interfacial roughness were measured.

### 2.3.6 Atomic force microscopy

Atomic force microscopy (AFM) is a nondestructive surface characterization technique, used to analyze the surface morphology from a few angstroms to micron ranges. Unlike that of scanning tunneling microscope (STM), AFM technique can be used to analyze conducting as well as insulating materials. The main advantage of AFM is to analyze the surface at ambient condition, without any special preparation [19].

An AFM instrument consists of a cantilever tip used to scan the sample surface, while maintaining a constant force (can be attractive or repulsive) between sample surface and tip. The tip radius determines the resolution limit of AFM instruments. Laser light is allowed to fall onto the tip and the deflected laser light is detected by a photo diode. As the cantilever moves across the sample surface, the tip is deflected in z direction in order to maintain a constant force. The deflection in tip results in a deflection in laser light which in turn is converted to digital signals to form an AFM image.

An AFM instrument can be used in different modes: (i) contact mode, (ii) noncontact mode and (iii) tapping mode [20,21]. In contact mode, the distance between the cantilever tip and the sample is about few angstroms and the force is repulsive. In the noncontact mode the cantilever is held some tens of angstroms from the sample surface by Van-der Waals forces. Tapping mode images are produced from the force of the intermittent contacts of the tip with the sample surface.

In the present work all the images for single as well as multilayers were taken using a Nanoscope E Digital instrument (INC, USA) in contact mode. A diode laser was used as a light source and a photo diode as a detector and the cantilever tip was made up of $Si_3N_4$ of 20 nm tip radius.

### 2.3.7 High resolution transmission electron microscopy

When electron beams incidences onto a crystal, the beam is diffracted at certain angles satisfying Bragg's law. The diffracted beams are collected at the back focal plane and are observed as electron diffraction pattern. In electron microscope analysis, when transmitted beam is selected to generate images it is called bright field (BF) image, while the diffracted beam is selected it is called dark field (DF) image [22,23]. When more than two beams are used to form electron microscope images (using a large objective aperture), the mode is called High resolution electron microscopy (HRTEM). As the images are formed due to the phase difference between transmitted and diffracted beam, HRTEM is also called phase contrast microscopy [22]. As the sample is very thin, only phase of incident electron wave gets changed, whereas amplitude remains constant.

The instrumentation of the HRTEM consists of the following parts: electron gun, condenser lens, objective lens, magnification and projection systems and detector. Electron beam produced by the gun is focused onto the sample of ~ 100 nm thickness using a condenser lens. The electron beam passes through the sample and the image is formed and recorded on a photographic film or is captured in digital form. The image that is formed is not the atom position; rather it corresponds to the projection of atoms. The contrast in HRTEM is strongly dependent on the sample thickness.

For plane view analysis, films deposited on Si substrates were cut into a dimension of 2 mm× 2 mm x 0.5 mm. The samples were thin down from the opposite of film side to around 30 µm by grinding followed by dimpling. Then the samples were ion milled using and ion miller (Technoorg Linda IV 4 ion miller) up to electron transparency using argon gas at 6 kV and ion current of 2 mA.

For HRTEM cross sectional specimen preparation, the multilayer samples were cut into small cuboids and two such pieces were glued with G1 epoxy with the film-surfaces facing each other. The whole assembly was then fitted into titanium slot grids. This was thinned down mechanically to ~ 30 µm and subsequently ion-milled to electron transparency in Technoorg Linda IV 4 ion miller. Extreme care was taken to remove the surface damage of the samples induced by the high-energy ion milling by low energy ion milling at 6 kV and 2 mA in a Technoorg Linda IV 6 Gentle Mill.

HRTEM studies were carried out in a JEOL 2000 EX II (T) transmission electron microscope having a point resolution of 0.19 nm at an operating voltage of 200 kV. Phase identification was made from high resolution digital images by calculating power spectra from ~ 10 nm wide crystalline regions and analysing them for inter-planar spacings and angles. From HRTEM images of multilayers, the individual layer thickness, interface structure, interdiffusion between layers and defects were studied.

### 2.3.8 UV-Visible spectroscopy

UV-Visible spectrophotometer is an instrument useful for measurement of optical properties of materials using Beer-Lambert law. When light of intensity $I_0$ passes through a material, both transmission and absorption occur. The % of transmittance is given by equation 2.16.

$$\%T=\frac{I}{I_o}*100 \text{ ......................................................} (2.16)$$

The relation between absorbance and transmittance is given by equation 2.17.

$$A=\log (1/T) \text{ ................................................} (2.17)$$

Where A is the absorbance of the film and T is the transmittance of the film [25,26].

The absorbance data was used to calculate the absorption coefficient (α) using the equation 2.18:

$$\alpha= 2.303*A/t \quad \text{ ..........................................} \quad (2.18)$$

Where t is the film thickness. Band gap ($E_g$) of the films, deposited at different experimental conditions was determined from Tauc plot using the equation 2.19 [27,28].

$$\alpha h\nu= A(h\nu-E_g)^n \text{ ................................} (2.19)$$

Where n =2,3… represents indirect band gap, and n=1/2, 2/3… represents direct band gap, and h is the Planck's constant and ν is the frequency of light used.

To measure the optical properties, single and multilayer films were prepared on quartz substrates. Then the optical transmittance and absorbance were measured within the wavelength range of 200-900 nm in transmission mode using an ultraviolet visible spectrometer (UV-Visible spectrometer, Jasco V-670 spectrophotometer) capable of measuring a wavelength in the range of 190-2700 nm with ± 0.3 nm accuracy. The spectrophotometer contains two light sources to cover the whole range of wavelength: deuterium source (190-350 nm), and halogen source (330-

2700 nm). A photomultiplier tube was used as a detector to detect the light in the wavelength range of 190-900 nm. From the absorbance data Tauc plot was made and band gap was measured by extrapolation of the straight line portion of the curve.

From the transmittance curve, the refractive index (η) of the films was calculated using equation 2.20 [29].

$$\boldsymbol{\eta} = \left[\boldsymbol{N} + \left(\boldsymbol{N}^2 - \boldsymbol{n_0^2 n_1^2}\right)^{\frac{1}{2}}\right]^{\frac{1}{2}} \ldots\ldots\ldots\ldots\ldots\ldots\ldots\ldots\ldots\ldots \ (2.20)$$

Where $$\boldsymbol{N} = \frac{(\boldsymbol{n_0^2+n_1^2})}{2} + 2\boldsymbol{n_0 n_1}\left(\frac{(\boldsymbol{T_{max}-T_{min}})}{\boldsymbol{T_{max}T_{min}}}\right) \ldots\ldots\ldots\ldots\ldots\ldots(2.21)$$

$n_0$ is the refractive index of air (1.0), $n_1$ the refractive index of the quartz substrates (~1.458), $T_{max}$ and $T_{min}$ are the maximum and minimum transmittance, respectively.

### 2.3.9 Nanomechanical properties

Mechanical properties of thin films as well as bulk materials are dependent on the microstructure, interfaces, composition, phases, and porosity of film**.** Nanoindentation is used to measure the hardness and the Young's modulus of the films. Indentation load (P) and displacement (h) were continuously recorded during one complete cycle of loading and unloading. Hardness (H) of a material is given by equation 2.22.

$$\mathbf{H} = \frac{\boldsymbol{P(max)}}{\boldsymbol{A}} \ldots\ldots\ldots\ldots\ldots\ldots\ldots\ldots\ldots\ldots\ldots\ldots\ldots\ldots \ (2.22)$$

Where P(max) is the maximum load applied and A is the residual indentation area. The hardness is usually the mean contact pressure under the indenter [29]. The slope of the unloading curve gives stiffness of the contact (S), which is used to calculate the reduced modulus of elasticity ($E_r$) (equation 2.23).

$$\boldsymbol{E_r} = \frac{\sqrt{\boldsymbol{\pi}}\boldsymbol{S}}{\boldsymbol{\beta}^2\sqrt{\boldsymbol{A(h_c)}}} \ldots\ldots\ldots\ldots\ldots\ldots\ldots\ldots\ldots\ldots\ldots\ldots\ldots\ldots(2.23)$$

Where $A(h_c)$ is the area of the indentation at the contact depth, $h_c$ (the depth of the residual indentation prior to elastic recovery of its shapes), and β is a geometrical constant on the order of unity. Relation between reduced elastic modulus ($E_r$) and elastic modulus of specimen ($E_s$) is given in equation 2.24. Subscript i and s stands for indenter material, and sample materials and Poisson's ratio is denoted by ν [30,31].

$$\frac{1}{E_r} = \frac{1-\nu_i^2}{E_i} + \frac{1-\nu_s^2}{E_s} \quad \text{.............................................}(2.24)$$

From the hardness (H) and elastic modulus (E), values the toughness ($K_{IC}$) or resistance to plastic deformation of the film is emperically measured by equation 2.25 [32].

$$\textbf{Toughness } (K_{IC}) = \frac{H^3}{E^2} \quad \text{.............................................} \quad (2.25)$$

The nanohardness measurements were carried out by means of a nanoindenter (CSM, Switzerland) equipped with a Berkovich diamond indenter tip of radius 200 μm, at a load of 10 mN on the films in the range of 1.2–1.5 μm thickness deposited on Inconel-783 substrates. While measuring the nanomechanical properties, indentation depth was kept less than 1/10th of the film thickness in order to eliminate the substrate effect. The load and depth resolution of the instruments is 0.04 μN and 0.04 nm, respectively. From the hardness and elastic modulus values the toughness of the films was also calculated using equation 2.25.

## 2.4 References

1. D. B. Chrisey, G. K. Hubler, “Pulsed laser deposition of thin films”, Wiley Interscience Publication (1994) (ISBN No. 0-471-59218-8).
2. J. Kim, S. Lee, H. Im, Appl. Surf. Sci. 151 (1999) 6.
3. S. Mustofa, T. Araki, T. Furusawa, M. Nishida, T. Hino, Mater. Sci. Engg. B 103 (2003) 128.
4. M. Mishra, P. Kuppusami, T. N. Sairam, A. Singh, E. Mohandas, Appl. Surf. Sci. 257 (2011) 7665.
5. M. Mishra, P. Kuppusami, A. Singh, S. Ramaya, V. Sivasubramanian, E. Mohandas, Appl. Surf. Sci. 258 (2012) 5157.
6. F. Soderlind “Colloidal synthesis of metal oxide nanocrystals and thin films”, (2008). ISBN 978-91-7393-899-0.
7. W. T. Silfvast “Laser Fundamentals”, Cambridge Univ. Press, 2nd edition (2009) ISBN No. 978-0-521-13847-5.
8. A. L. Patterson, Phys. Rev. 56 (1939) 978.
9. T. J. B. Holland, S. A. T. Redfern, J. Appl. Crystallogr. 30 (1997) 84.
10. B. D. Cullity “Elements of X-ray diffraction”, 3rd edition (2001). ISBN No: 0-201-61091-4.
11. J. D. James, J. A. Spittle, S.G. R. Brown, R. W. Evans, Meas. Sci. Technol. 12 (2001) R1-R15.
12. M. A. White, Cryst. Engg. (1999) 273.
13. Gwenael Gouadec, Philippe Colomban, Prog. Cryst. Growth Charact. Mater, 53 (2007) 1.

14. J. R. Ferraro, Kazuo Nakamoto, Chris W. Brown "Introductory Raman spectroscopy", Elsevier Publication (2003), ISBN No: 978-0-12-254105-6.
15. G. Amarendra, B. Raj, M. H. Manghnani, "Advances in material characterization" Chapter 3., (2007). ISBN- 1420047299.
16. A. Gibaud, S. Hazra, Curr. Sci.India.78 (12) (2000) 1467.
17. E. Chason, T. M. Mayer, Crit. Rev. Solid State 22 (1) (1997) 1.
18. L. G. Parratt, Phy. Rev. 95 (2) (1954) 359.
19. E. Meyer, Prog. Surf. Sci. 41 (1992) 3.
20. N. Jalili, K. Lakxminarayana, Mechatronics 14 (2004) 907.
21. G. Binnig, C. F. Quate and C. H. Gerber, Phy. Rev. Lett. 56 (6) (1986) 930.
22. D. Shindo, K. Hiraga, "High-resolution electron microscopy for material science", Springer publication (ISBN 4-431-70234-2).
23. David J Smith, Rep. Prog. Phys. 60 (1997) 1513.
24. D. Shi, "Functional thin film and functional materials", Springer publication, (ISBN-3-540-00111-5).
25. M. Fox, "Optical Properties of Solids", Oxford University Press, ISBN No: 0-19-850612-0.
26. D. F. Swainehart , J. Chem. Educ. 39 (7) (1962) 333.
27. J. Tauc, R. Grigorovic and A**.** Vancu**,** Phys. Stat. Sol., 15 (1966) 627.
28. W. Zhou, S. Xie, S. Qian, T. Zhou, R. Zhao, G. Wang, L. Qian, W. Li, J. Appl. Phys. 80 (1)(1996) 459.
29. R. Swanepoel, J. Phys. E : Sci Instrum., 16 (1983) 1214.
30. J. Ahn, D. Kwon, Mater. Sci. Engg. A285 (2000) 172.

31. D. A. Hardwick, Thin Solid Films 154 (1987) 109.

32. A. Leyland, A. Matthews, Wear 246 (2000) 1.

# Chapter 3

# $Y_2O_3$ and $ZrO_2$ Thin Films and $ZrO_2/Y_2O_3$ Multilayer Thin Films: Preparation and Properties

## 3.1 Introduction

Yttrium oxide ($Y_2O_3$) thin films have received much attraction due to its important technological application and excellent mechanical, optical, thermal and electrical properties. $Y_2O_3$ thin films grown on Si substrates are considered to be the most promising candidate material in CMOS devices [1], electroluminescent devices [2], high-density dynamic random access memory [2] and electrochemical sensors [3]. $Y_2O_3$ films were deposited by different thin film deposition techniques such as sputtering [4], e-beam evaporation [5], plasma spray [6], atomic beam deposition [7], metal organic chemical vapor deposition (MOCVD) [8] and pulsed laser deposition [1,9] to study the microstructural [5,7,8], optical [9], electrical [4,7,8] and nanomechanical [10] properties.

$ZrO_2$ is another transition metal oxide which finds applications in many industrial areas due to its properties like high melting point, high refractive index, good thermal, chemical and mechanical stabilities, wide band gap, high dielectric constant and electrical resistivity. It exists in three different phases, namely monoclinic, tetragonal and cubic phase which find applications in the field of biological, hard coatings and sensors as well as solid oxide fuel cells, respectively. Tetragonal and cubic phases of $ZrO_2$ are the high temperature phases that can be retained at lower temperature either by doping with other oxides [11-13] or by forming multilayer structures [14,15]. Various methods such as MOCVD [16], chemical vapor deposition (CVD) [17], ion assisted deposition (IAD) [18], pulsed laser deposition (PLD) [19-21], sol–gel method [20], sputtering technique [21] and electron beam deposition [22] have been used to prepare $ZrO_2$ thin films to study the structural [21], optical [21], electrical [23], wear [24] and bioactivity and cytocompatibility [25] properties.

Multilayers are found to have wide applications in the fields of sensors, optical coatings, thermal barrier coatings, solar cells, solid oxide fuel cell and spintronics as a result of the enhanced optical, nanomechanical, ionic conductivity properties than those of the individual single layers [26-28]. Multilayers have been deposited by different techniques, such as sputtering [15,29], sol gel methods [30], chemical vapor deposition [31], and pulsed laser deposition [32-33]. Multilayers of $ZrO_2/Y_2O_3$ have been prepared by Barshilia et al. [15] and Yashar et al. [34] by sputtering technique to study the microstructure, thermal stability and nanomechanical properties of the multilayer films.

In this Chapter single layers of $Y_2O_3$ and $ZrO_2$ were prepared by PLD technique at different process parameters such as substrate temperature and oxygen partial pressure to study the effect of these parameters on microstructural, phase evolution and optical properties. Taking into account the optimized temperature and pressure conditions, multilayer films consisting of alternate layers of $ZrO_2$ and $Y_2O_3$ were prepared at two different substrate temperatures i.e. 300 K and 873 K, and at optimized oxygen partial pressure of 2 Pa. $ZrO_2$ layer thicknesses was varied from 5 to 30 nm, keeping $Y_2O_3$ layer thickness constant to study the effect of temperature and $ZrO_2$ layer thickness on microstructural, optical and nanomechanical properties on $ZrO_2/Y_2O_3$ multilayers.

## 3.2 Experimental Procedure

Targets of $Y_2O_3$ and $ZrO_2$ were prepared from commercially available $Y_2O_3$ and $ZrO_2$ powders (99.99% purity). The details of the target preparation methods, conditions and target characterization were already explained in Chapter 2.

The pellets were used to prepare thin films of $Y_2O_3$, $ZrO_2$ and $Y_2O_3/ZrO_2$ multilayer films by PLD technique on Si, quartz as well as Inconel-783 substrates to study the microstructural, optical and nanomechanical properties, respectively. The Si, quartz and Inconel-783 substrates are used because they are widely used in semiconductor, and aerospace industries.

$Y_2O_3$ and $ZrO_2$ single layers were prepared at different substrate temperatures and oxygen partial pressures to study the effect of these parameters on the microstructural and optical properties. Details of the experimental conditions for preparing $Y_2O_3$ and $ZrO_2$ thin films are given in Table 3.1. Few samples of 8 mol percent $Y_2O_3$ doped $ZrO_2$ (8YSZ) were also prepared on Si (100) and quartz substrates, at different process parameters to study the effect of these parameters on phase stabilization of $ZrO_2$.

Multilayer structures of $ZrO_2/Y_2O_3$ were prepared at the substrate temperatures of 300 K and 873 K and at the oxygen partial pressure of 2 Pa. $ZrO_2$ layer thickness was varied from 5 to 30 nm, whereas $Y_2O_3$ layer thickness was kept constant (10 nm), taking into account the predetermined deposition rates of both $ZrO_2$ and $Y_2O_3$ (Table 3.3). Total thicknesses of the multilayers were kept constant by varying the number of bilayers. The numbers of bilayers prepared for each multilayer were 3, 4, 6 and 8 for $ZrO_2$ layer thickness of 30, 20,10 and 5 nm (Table 3.3).

The films and the multilayers were characterized by XRD, Raman spectroscopy, AFM, XRR and TEM. The optical properties of the films deposited on quartz substrates were measured by using a UV-Visible spectrophotometer in the wavelength range of 200–900 nm. The nanomechanical properties of the single layer films deposited at 873 K and at oxygen partial pressure of 2 Pa was also measured using nanoindentation technique.

**Table 3.1 Details of experimental conditions for $Y_2O_3$ and $ZrO_2$ thin film preparation.**

| **Parameters** | **$Y_2O_3$** | **$ZrO_2$** |
|---|---|---|
| Target Size | 20 mm diameter and 3 mm thickness | 25 mm diameter and 3 mm thickness |
| Sintering Condition | 1723 K, 4 h. | 1673 K, 6 h. |
| Sintered Density | ~95 % | ~90 % |
| Laser Energy | 200 mJ/pulse | 200 mJ/pulse |
| Repetition rate | 10 Hz | 10 Hz |
| Substrate | Si (100), quartz, Inconel-783 | Si (100), quartz, Inconel-783 |
| Oxygen partial pressure | 2-0.002 Pa | 2- 0.002 Pa |
| Substrate temperature | 300-873 K | 300- 973 K |

**Table 3.2 Experimental details for $ZrO_2/Y_2O_3$ multilayer preparation.**

| **Parameters** | **Details** |
|---|---|
| Targets | $Y_2O_3$ and $ZrO_2$ |
| Laser Energy | 300 mJ/pulse |
| Repetition rate | 10 Hz |
| Substrate | Si (100), quartz, Inconel-783 |
| Oxygen partial pressure | 2 Pa |
| Substrate temperature | 300 K and 873 K |
| Deposition rate | $Y_2O_3$ (~8 nm/min) and $ZrO_2$ (~5 nm/min) |
| Layer thickness $(ZrO_2/Y_2O_3)_{\text{(number of bilayers)}}$ (nm) | $(5/10)_8$, $(10/10)_6$, $(20/10)_4$,$(30/10)_3$ |

## 3.3 Results

The following section includes the results of microstructural optical and nanomechanical propertries of $Y_2O_3$, $ZrO_2$ films and the multilayers of $ZrO_2/Y_2O_3$.

### 3.3.1 $Y_2O_3$ thin films

### 3.3.1.1 XRD analysis

Figure 3.1 shows the XRD pattern of $Y_2O_3$ thin films, deposited at different substrate temperatures on Si (100). $Y_2O_3$ films grown at substrate temperatures of 300 - 573 K were found to be X-ray amorphous. Crystallization of $Y_2O_3$ was noticed at the substrate temperature of 673 K as characterized by (222), (332), (422), (440), (611), (622) and (651) planes. With further increase in the substrate temperature, the intensity of the peak corresponding to (222) plane increased. Appearance of several peaks at 673K indicated the formation of a polycrystalline cubic $Y_2O_3$, with highest intensity for (222) plane. The lattice parameters were calculated using unit cell program and are found to vary from $10.69 \pm 0.002$ to $10.65 \pm 0.003$ Å with the increase in substrate temperature from 300 to 873 K. The observed lattice parameters of the films were found to be slightly higher than that of the bulk lattice parameter of $Y_2O_3$ (10.6 Å) reported in the JCPDS file no 41-1105 indicating presence of tensile stress in the films. The crystallite size for (222) reflection was calculated using Scherrer's formula (equation 2.5) and is listed in Table 3.3. The crystallite size of the $Y_2O_3$ films on Si substrate were found to increase from $6 \pm 2$ to $24 \pm 2$ nm with the increase in the substrate temperature from 673 to 873 K in agreement with the results reported elsewhere [35]. $Y_2O_3$ was found to exist in pure cubic phase in the above range of temperature and oxygen partial pressure.

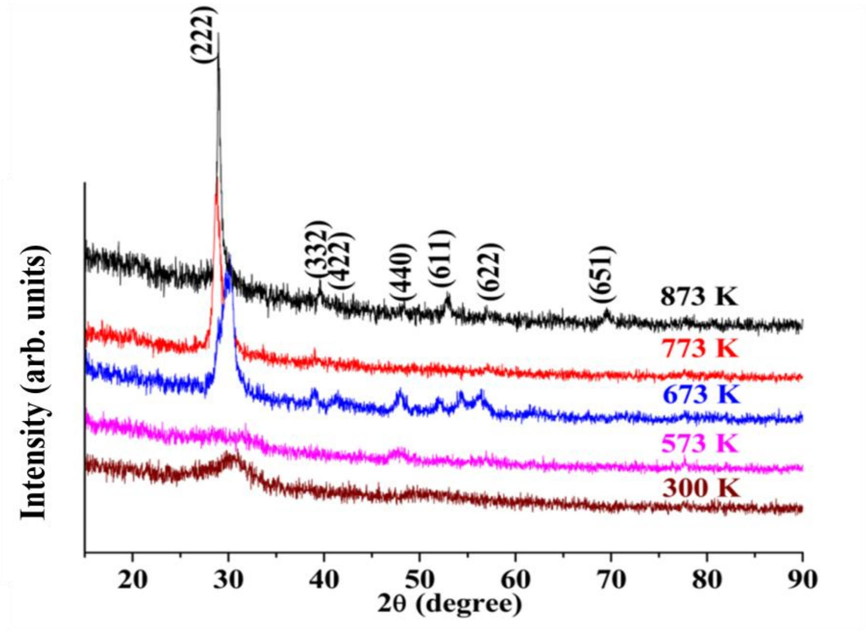

**Fig. 3.1 XRD pattern of $Y_2O_3$ films deposited on Si substrates at different substrate temperatures and oxygen partial pressure of 0.2 Pa.**

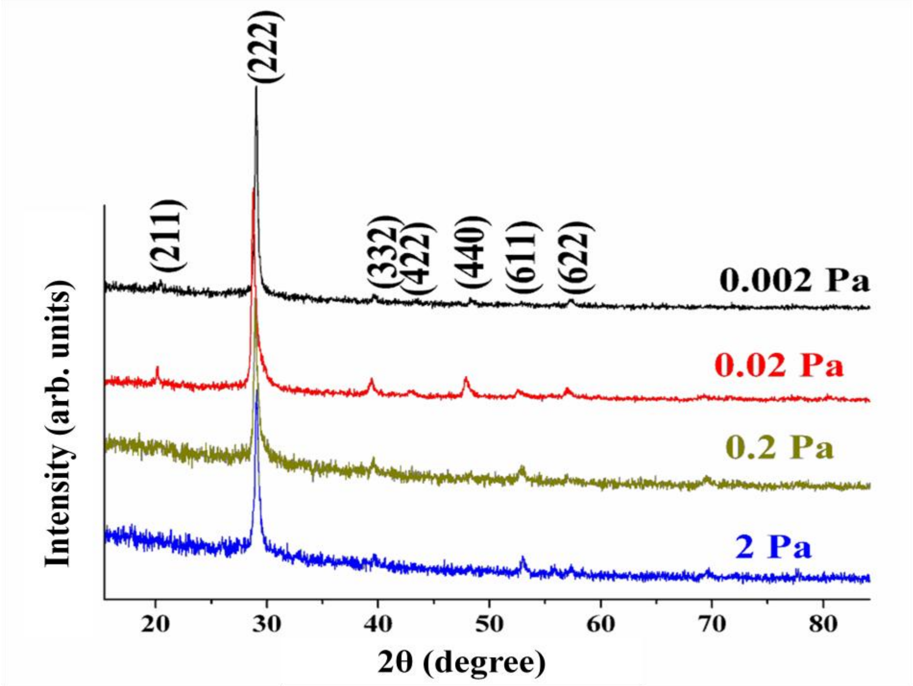

**Fig. 3.2 XRD pattern of $Y_2O_3$ films deposited on Si substrates at different oxygen partial pressures and substrate temperature of 873 K.**

XRD pattern of $Y_2O_3$ thin films deposited on Si substrates at substrate temperature of 873 K and at various oxygen partial pressures were recorded and were shown in Fig. 3.2. Films deposited in the above pressure range contains peaks corresponding to diffraction planes of (211), (222), (332), (422), (440), (611) and (622) reflections of cubic phase of $Y_2O_3$. Lattice parameters of the films deposited at different oxygen partial pressures were calculated using unitcell program and is listed in Table 3.4. Lattice parameters and crystallite size of $Y_2O_3$ films deposited at various oxygen partial pressures were found to vary from 10.64±0.003 to 10.65 Å ±0.002 and 29 ± 2 to 23 ±2 nm, respectively. No significant change in the crystallite size was observed with change in oxygen partial pressures. The lattice parameters of the $Y_2O_3$ films deposited at various oxygen partial pressures were found to be higher than that of the bulk value, indicating the presence of stress in the films.

### 3.3.1.2 Raman analysis

Figure 3.3 shows a typical Raman spectrum of $Y_2O_3$ film deposited at the substrate temperature of 873 K and oxygen partial pressure of 0.2 Pa. In the spectrum, the peak at 378 $cm^{-1}$ belongs to c-$Y_2O_3$, whereas all other peaks correspond to Si substrate. Similar results have also been reported by Repelin et al. [36] and Pearce et al. [37]. Repelin et al. [36] have reported the Raman spectroscopy study of bulk polycrystalline c-$Y_2O_3$. They have reported a shift and decrease in line width for the Raman peak at 376 $cm^{-1}$ with the increase in temperature. The Raman peak at 376 $cm^{-1}$ corresponds to the $F_g+A_g$ mode of $Y_2O_3$. The broadening in the Raman peak was due to the smaller crystallite size of $Y_2O_3$ [38].

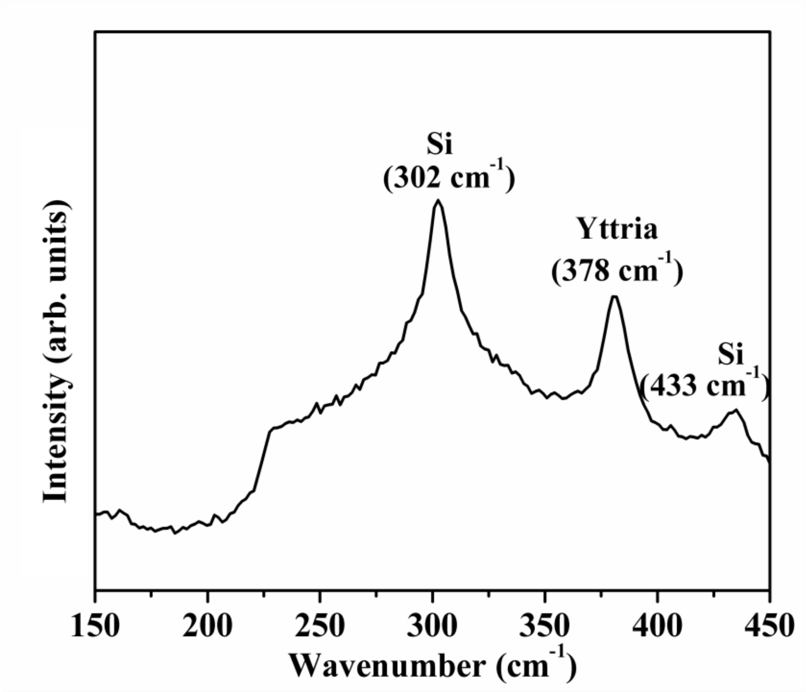

**Fig. 3.3 A typical Raman spectrum of $Y_2O_3$ film deposited on Si substrate at oxygen partial pressure of 0.2 Pa and substrate temperature of 873 K.**

### 3.3.1.3 AFM analysis

Fig. 3.4 and 3.5 show the AFM images of $Y_2O_3$ films, prepared under various substrate temperature and oxygen partial pressure, respectively. The AFM images (Fig. 3.4) show the growth of crystallites as a function of substrate temperature. AFM images of $Y_2O_3$ film deposited at 300 K show a smooth surface indicating amorphous nature. Crystallite size was found to increase from ~10 to 35 nm with the increase in substrate temperature from 673 to 873 K. AFM images show that the films were quite dense and free from any voids. The roughness values of the $Y_2O_3$ films were found to increase from 0.1 to 1.23 nm as the substrate temperature was increased from 300 to 873 K. The increase in the roughness values with the increase in substrate temperature was attributed to the increase in the crystallite size.

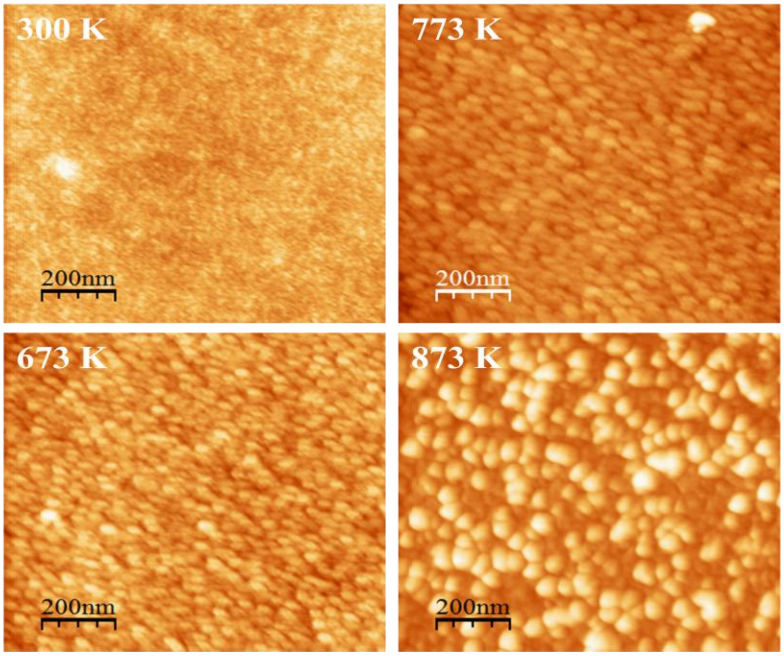

**Fig. 3.4 AFM images of $Y_2O_3$ films deposited on Si substrates at different substrates temperature and oxygen partial pressure of 0.2 Pa.**

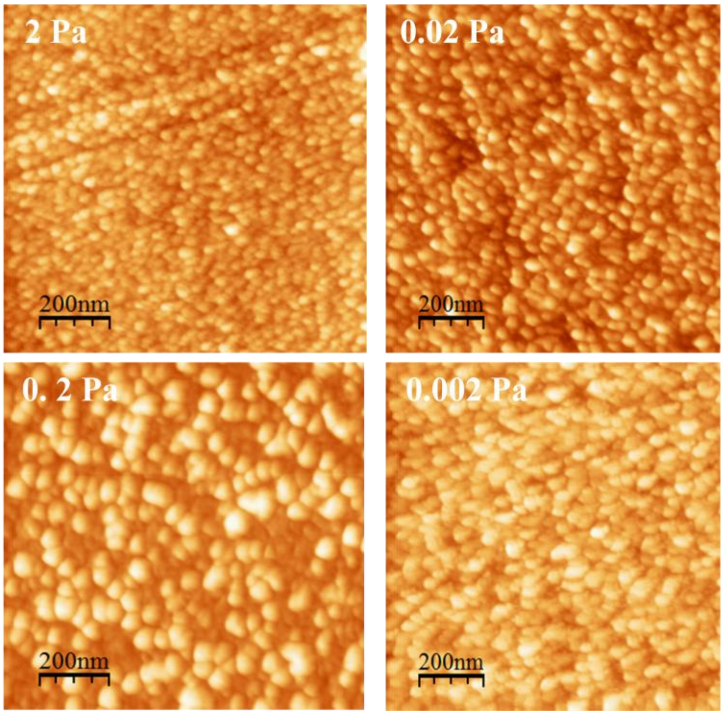

**Fig. 3.5 AFM images of $Y_2O_3$ films deposited on Si substrates at different oxygen partial pressure and substrate temperature of 873 K.**

Figure 3.5 shows the surface morphology of $Y_2O_3$ films deposited under different oxygen partial pressures and at the substrate temperature of 873 K. The AFM images show that the growth of crystallite was not significant with change in the oxygen partial pressure and was found to vary from ~30 to 50 nm. The crystallite size obtained from AFM analysis show higher values than that of the values determined from XRD analysis because of the overlapping of the crystallities.The roughness values of the $Y_2O_3$ films were determined and were found to vary from 0.7 to 1.2 nm under different oxygen partial pressure conditions.

#### 3.3.1.4 TEM analysis

The microstructure of $Y_2O_3$ film deposited at 873 K and oxygen partial pressure of 2 Pa on Si substrate was analyzed by TEM (Fig. 3.6). Fig. 3.6 (a) shows the low magnification bright field image of $Y_2O_3$ film, and it shows a nonuniform crystallite size distribution in the range of 5- 25 nm. The selected area diffraction (SAD) pattern, obtained from the $Y_2O_3$ film is shown in Fig. 3.6 (b). The SAD pattern shows the formation of a polycrystalline film with reflections from (222), (400), (332), (521), (622), (444) planes of cubic $Y_2O_3$. Presence of bright spoty ring pattern indicated the presence of preferred orientation along certain directions and larger crystallite size.

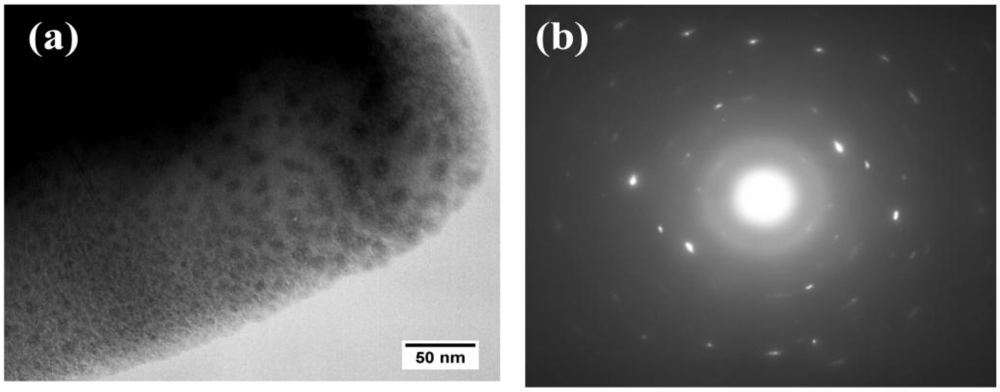

**Fig. 3.6 (a) TEM image of $Y_2O_3$ films deposited on Si substrate at the substrate temperature of 873 K and oxygen partial pressure of 0.2 Pa and (b) SAD pattern.**

### 3.3.1.5 Optical properties

The microstructural properties of $Y_2O_3$ films were found to be similar for the films deposited on the substrates of Si and quartz. Therefore optical properties of the films were reported on the films deposited on quartz substrates.

Optical properties of the $Y_2O_3$ films deposited on quartz substrates at various process parameters were measured in transmission mode using a UV-Visible spectrophotometer. Fig. 3.7 (a) and (b) show absorbance and transmittance values of the $Y_2O_3$ films deposited at the oxygen partial pressure of 0.2 Pa and at different substrate temperatures. The films deposited at different substrate temperatures showed strong absorbance at wavelength ~ 210-220 nm and a transmittance value ≥ 80%. Films deposited at the substrate temperature of 873 K showed the highest transmittance of 92%. This indicated the formation of best quality films at the substrate temperature of 873 K.

Figure 3.8 (a) and (b) shows the absorbance and transmittance of $Y_2O_3$ films deposited at different oxygen partial pressure in the UV-visible range. The films deposited at oxygen partial pressures 0.02 and 0.002 Pa showed transmittance of about 80%, whereas films deposited at oxygen partial pressure of 2 and 0.2 Pa showed the highest transmittance of about 92%. At low oxygen partial pressure, the films were less transparent. The lower value of transmittance is due to the increase in crystallite size, which results in the increased roughness values and lead to loss of light by scattering [2].

From the transmittance values, the refractive index ($\eta$) of the $Y_2O_3$ films deposited under different substrate temperatures and oxygen partial pressures were determined and are listed in Tables 3.3 and 3.4. The details of the formulae and method of calculation of $\eta$ were explained in Chapter 2. The refractive index values obtained at different process parameters vary between

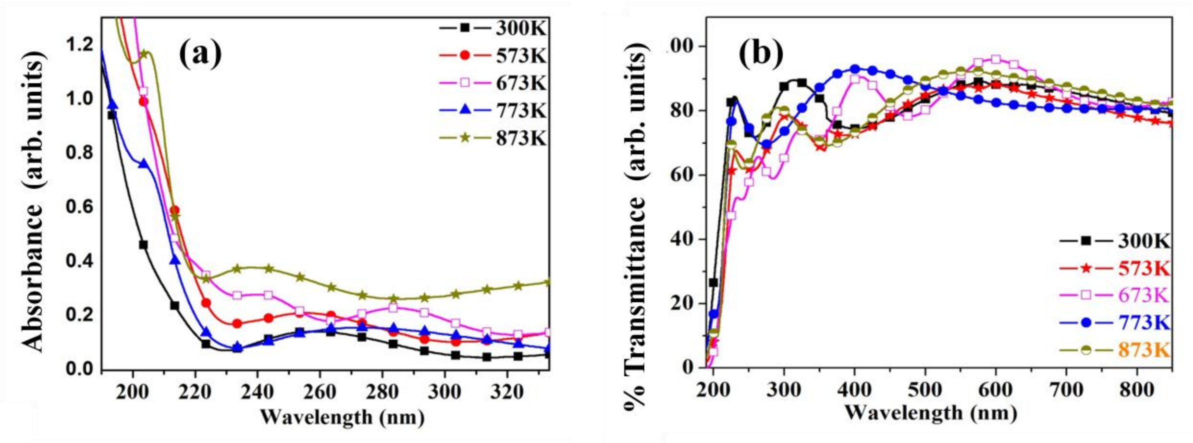

**Fig. 3.7 The (a) Absorbance and (b) Transmittance versus wavelength plot of $Y_2O_3$ films deposited on quartz substrates at different substrate temperature and oxygen partial pressure of 0.2 Pa.**

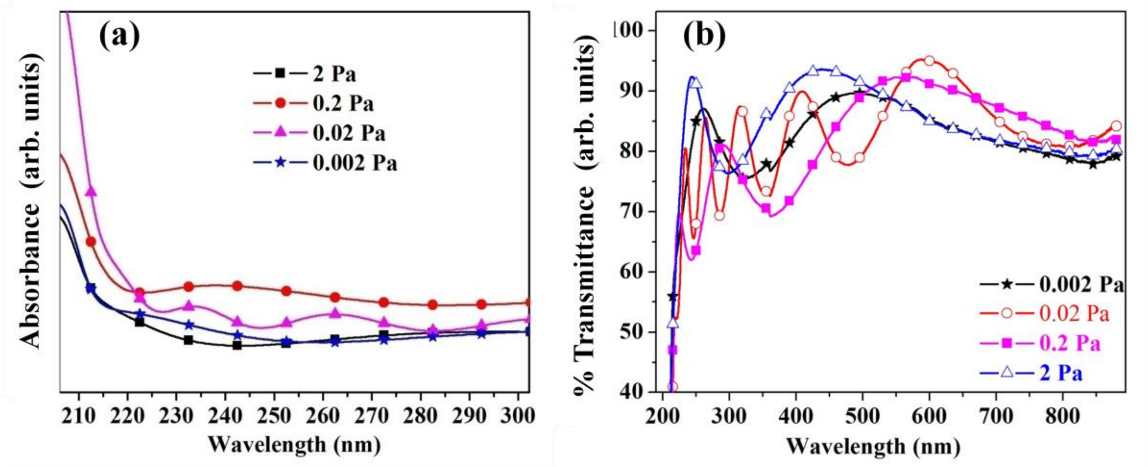

**Fig. 3.8 Variation of (a) Absorbance and (b) Transmittance values of $Y_2O_3$ films deposited on quartz substrates as a function of oxygen partial pressures and substrate temperature of 873 K.**

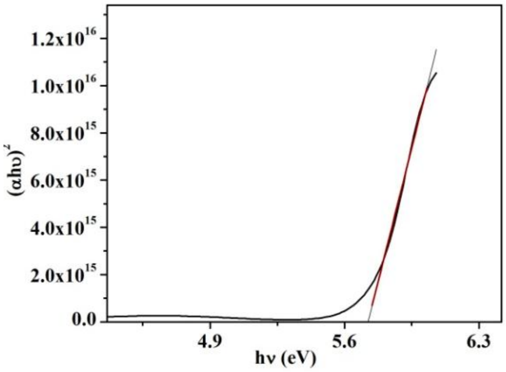

**Fig. 3.9 A typical Tauc plot of $Y_2O_3$ thin film deposited at substrate temperature of 873 K and oxygen partial pressure of 0.2 Pa.**

1.60-1.61 and no significant change in η was observed with respect to change in the oxygen partial pressure as well as substrate temperature. This may be due to the high packing density of the films and the similar transmittance values [39].

The optical band gap ($E_g$) was estimated using Tauc plot (Fig. 3.9). The details of the band gap measurement by Tauc plot were already explained in Chapter 2. The band gap values obtained from Tauc plot for the films deposited at different process parameters showed a higher value than that of the reported bulk value (4.8 eV) [40]. This increase in the band gap for the thin films than that of the bulk value was due to the formation of nanocrystals in the films due to quantum confinement effect [41].The band gap values obtained for the films deposited at different substrate temperature and oxygen partial pressure are listed in Table 3.3 and 3.4.

**Table 3.3 Microstructural and optical properties of $Y_2O_3$ films deposited at various substrate temperatures and oxygen partial pressure of 0.2 Pa.**

| Temperature (K) | Crystallite Size (±2 nm) | Roughness (nm) | Band gap (±0.01 eV) | Refractive index (±0.01) |
|---|---|---|---|---|
| 300 | - | 0.1 | 5.63 | 1.60 |
| 573 | - | - | 5.69 | 1.61 |
| 673 | 6 | 0.3 | 5.72 | 1.61 |
| 773 | 11 | 0.6 | 5.73 | 1.60 |
| 873 | 24 | 1.1 | 5.76 | 1.61 |

**Table 3.4 Variation in microstructural and optical properties of $Y_2O_3$ films deposited under different oxygen atmosphere and substrate temperature of 873 K.**

| Oxygen Partial pressure (Pa) | Crystallite Size (±2 nm) | Roughness (nm) | Band gap (±0.01 eV) | Refractive index (±0.01) |
|---|---|---|---|---|
| 2 | 23 | 0.5 | 5.63 | 1.60 |
| 0.2 | 24 | 1.1 | 5.76 | 1.61 |
| 0.02 | 26 | 0.7 | 5.72 | 1.61 |
| 0.002 | 29 | 0.8 | 5.73 | 1.60 |

respectively. The band gap values calculated for the $Y_2O_3$ films deposited at different substrate temperature conditions are found to increase from 5.63 – 5.76 eV with increase in the substrate temperature. Similarly the band gap values obtained for the $Y_2O_3$ films deposited at different oxygen partial pressures are found to vary from 5.63-5.76 eV. The highest band gap was obtained for the films deposited at 873 K and oxygen partial pressure of 0.2 Pa.

### 3.3.1.6 Nanomechanical properties

Hardness and elastic modulus values for a typical $Y_2O_3$ thin film deposited on Inconel-783 alloy at 873 K and 2 Pa was measured by nanoindentation technique (Fig. 3.10) and was found to be 5.4 GPa and 173 GPa, respectively. The hardness value of the film was lower than the bulk value of $Y_2O_3$ (8 GPa) reported by Gautier et al [42] whereas the values were higher than that of the hardness value (~2.4 GPa) reported by Barve et al.[43]. The latter have reported lower hardness for $Y_2O_3$ film deposited by PACVD technique as a result of the increase in the multiphase character of the film.

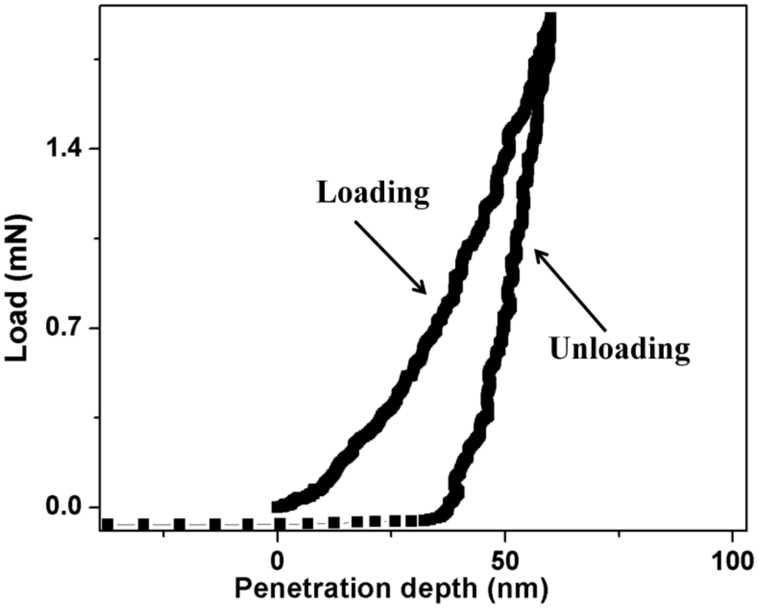

**Figure 3.10 Load versus penetration depth plot for $Y_2O_3$ thin film grown on Inconel-783 at 873 K and oxygen partial pressure of 2 Pa.**

### 3.3.2 $ZrO_2$ thin films

$ZrO_2$ films were prepared at different substrate temperature and oxygen partial pressures on Si(100) and quartz substrates to study the effect of these parameters on the microstructural and optical properties.

#### 3.3.2.1 XRD analysis

Figure 3.11 shows the XRD patterns of the $ZrO_2$ thin films that were deposited at different substrate temperatures (473 -973 K) and at the oxygen partial pressure of 2 Pa. XRD pattern showed the formation of polycrystalline films for the whole temperature range, containing both monoclinic and tetragonal phases of $ZrO_2$. XRD pattern of $ZrO_2$ thin films that were deposited at the substrate temperature of 473 K contains peaks corresponding to (200), (221) and $(\bar{3}21)$ planes of monoclinic phase of $ZrO_2$ with small amount of tetragonal phase (identified by the (110) reflection). The intensities of the (002) and (013) planes of t-$ZrO_2$ phase was found to increase with the increases in the substrate temperature. At the substrate temperature of 973 K, the peaks corresponding to tetragonal phase showed highest intensity. The study indicated an increase in the tetragonal phase content with the increase in the substrate temperature. Also, at the temperature of 973 K, the film showed preferred orientation of (002) for tetragonal phase. It was also observed that at 473 K, the film was less crystalline and the volume fractions of monoclinic and tetragonal phases were similar to that of the target.

XRD patterns of $ZrO_2$ thin films deposited at different oxygen partial pressures (2 to 0.002 Pa) and at the substrate temperature of 973 K is shown in Fig. 3.12. At all oxygen partial pressures, the film has preferred orientation along (002) plane of tetragonal phase. XRD patterns showed peaks from $(\bar{1}11)$, (200), (002), $(\bar{2}02)$, (122) and (311) reflections of m-$ZrO_2$ and (011), (002), (112) and (013) reflections of t-$ZrO_2$. XRD results clearly indicated the polycrystalline nature of $ZrO_2$ films at all oxygen partial pressures. Intensities of the peaks corresponding to monoclinic phase was found to decrease with increase in the oxygen partial pressure, which means tetragonal phase formation was more favored at higher oxygen partial pressure. At the oxygen partial pressure of 2 Pa, almost all the peaks except the (211) reflection corresponding to monoclinic phase disappeared and only peaks belonging to t-$ZrO_2$ appeared. This clearly indicated that higher oxygen partial pressure was favored for t-$ZrO_2$ formation [44].

Crystallite size was calculated for the (200) and (002) peaks of m- and t-$ZrO_2$, respectively, and listed in Table 3.5 and 3.6 for variation in substrate temperature and oxygen partial pressures, respectively. For monoclinic phase, the crystallite size was calculated for (200) peak and was found to vary from 6 to 24 nm and 19 to 30 nm for the films deposited at 2 and 0.002 Pa, respectively in the temperature range 473-873 K. The crystallite size of the monoclinic peak was found to decrease to ~17-19 nm at temperature > 873 K. Whereas the crystallite size calculated for the (002) plane of t-$ZrO_2$ increased from 12 to 35 nm and 9 to 27 nm, with increase in the substrate temperature from 473 to 973 K, and for oxygen partial pressure of 2 and 0.002 Pa, respectively. The above result was in accordance with the trend reported in the literature [45].

No significant change was observed for the crystallite size calculated for the films at different oxygen partial pressures in accordance with the results obtained for $Y_2O_3$ thin films [35]. The calculated crystallite size using (002) reflection was in the range of 23 to 25 nm. Due to in sufficient number of reflections to run “unit cell program”, the lattice parameter values for $ZrO_2$ monoclinic and tetragonal phase were not calculated.

The volume fraction of tetragonal phase was calculated using the reflection of (200) of monoclinic and (002) of the tetragonal phase using the equation 2.7 given in Chapter 2. The

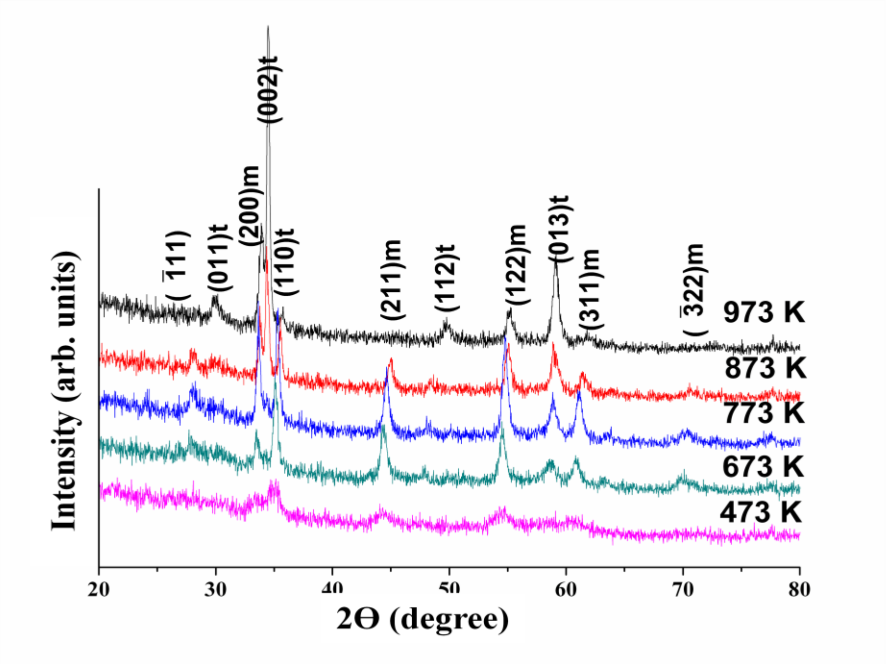

**Fig. 3.11 XRD pattern of $ZrO_2$ thin films deposited on Si (100) substrates at the oxygen partial pressure of 2 Pa as a function of substrate temperature.**

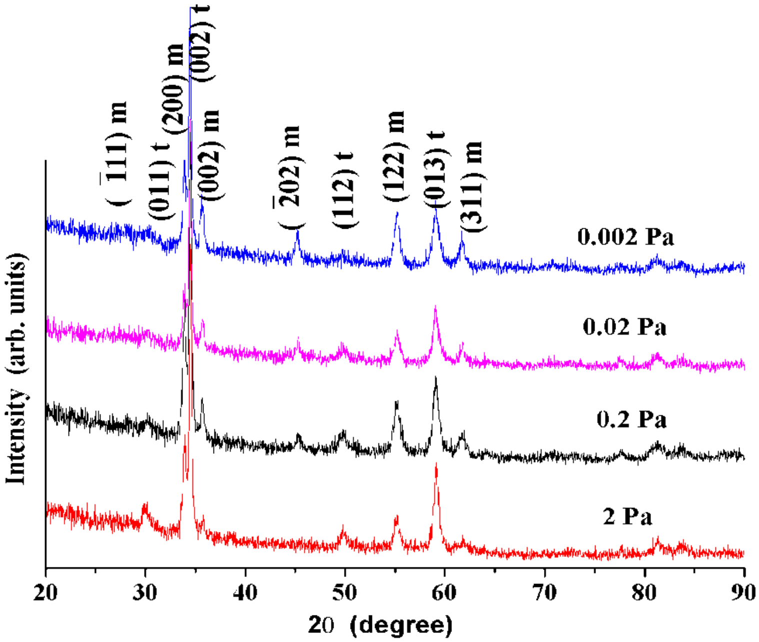

**Fig. 3.12 XRD pattern of $ZrO_2$ thin films prepared on Si (100) substrates at different oxygen partial pressures and substrate temperature of 973 K.**

value of the tetragonal volume fraction was found to be varied from 10-76% at different temperature and oxygen partial pressure. The monoclinic volume fraction was found to increase up to 773 K for all the oxygen partial pressures except for 0.001 Pa and then it decreased. In the case of oxygen partial pressure of 0.001 Pa, the volume fraction was increased only up to 673 K and then decreased indicating an increase in the tetragonal phase content with increase in the substrate temperature.

#### 3.3.2.2 Raman analysis

From the group theory analysis of $ZrO_2$, different numbers of bands for three different phases of $ZrO_2$ have been suggested. The most intense peaks for monoclinic and tetragonal $ZrO_2$ are at 178, 190 $cm^{-1}$ and 150, 260 $cm^{-1}$, respectively [46-48]. Raman analysis of $ZrO_2$ films were carried out on two sets of samples at different substrate temperature and oxygen partial pressure of 2 Pa (Fig. 3.13) and 0.002 Pa (Fig. 3.14). Figure 3.13 shows the Raman peaks at 147 and 180, 191 $cm^{-1}$ belonging to tetragonal and monoclinic phases, respectively [46-50]. Raman peak is affected by the parameters such as crystallite size, stress and stoichiometry [51]. The intensity and FWHM of Raman peaks at 147 (tetragonal), 178 and 191 $cm^{-1}$ (monoclinic) showed an increasing and decreasing trend with increase in the substrate temperature. Intensity of the Raman peak at 147 $cm^{-1}$, which belongs to tetragonal phase of $ZrO_2$ (Fig. 3.13) for the films deposited at 973 K and 2 Pa, which indicated that tetragonal phase formation was favored at higher substrate temperature and oxygen partial pressure. The shift in the position of Raman peak at 147 $cm^{-1}$ towards higher wave number side indicates strain relaxation. In contrary the Raman peaks at 178 and 191 $cm^{-1}$ shift to lower wave number side with the increase in the substrate temperature, indicating an increase in the strain in the monoclinic phase, which can also be observed from XRD patterns (Fig 3.13).

Figure 3.14 shows the Raman spectra of $ZrO_2$ films deposited at different substrate temperatures and oxygen partial pressure of 0.002 Pa. No Raman peak corresponding to tetragonal phase (147 $cm^{-1}$) was observed for the substrate temperature of 773 and 873 K. Raman peak at 147 $cm^{-1}$ (corresponding to tetragonal $ZrO_2$) was present only in the $ZrO_2$ film deposited at 973 K and the oxygen partial pressure of 0.002 Pa. This may be due to lower content of tetragonal phase at 773 and 873 K. Intensity of the peaks at 178 and 191 $cm^{-1}$ was the highest for the films at 973 K, indicating a good crystallinity at higher substrate temperature. The shift in the Raman peaks (178 and 191 $cm^{-1}$) was almost negligible for these three substrate temperatures (773-973 K).

Tetragonal volume fractions in the films were calculated quantitatively from the area under the peaks of 147 and 180 $cm^{-1}$ belonging to tetragonal and monoclinic phase, respectively using equation 3.1.

$$\boldsymbol{V_t = \frac{A_t}{(A_t + A_m)}} \quad \ldots\ldots\ldots\ldots\ldots\ldots\ldots\ldots\ldots\ldots \textbf{(3.1)}$$

Where $V_t$ is the volume fraction of tetragonal phase, $A_t$ is the area under the peak at 147 $cm^{-1}$ and $A_m$ is the area under peak at 180 $cm^{-1}$. The volume fraction calculated from the Raman data shows that the highest volume fraction of the tetragonal $ZrO_2$ (~67 %) was obtained for the films deposited at the substrate temperature of 973 K and oxygen partial pressure of 2 Pa. The trend in the volume fraction of the phases as a function of temperature and oxygen partial pressure obtained from Raman analysis was comparable with the XRD results [44] reported in the previous section.

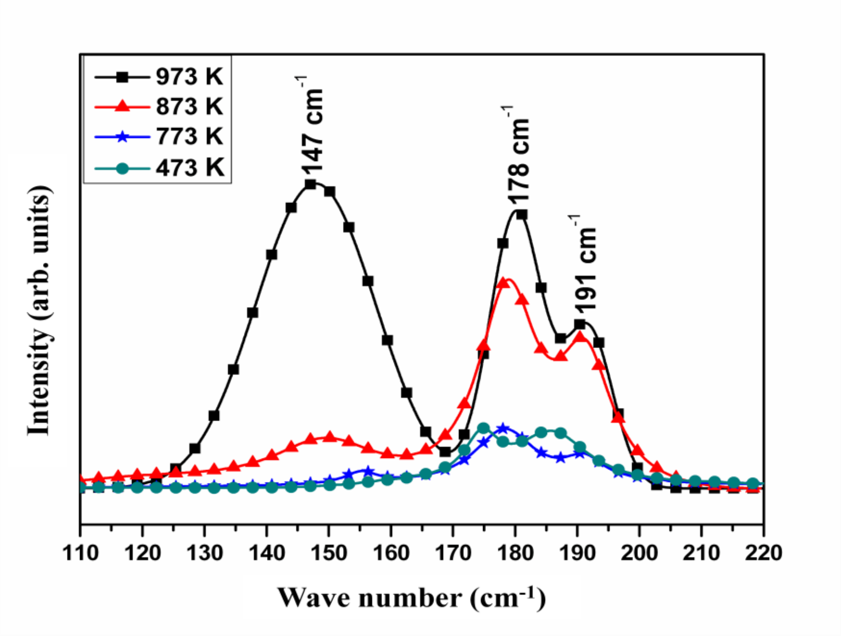

**Fig. 3.13 Raman spectra of $ZrO_2$ thin films grown on Si(100) substrates at different substrate temperatures and oxygen partial pressure of 2 Pa.**

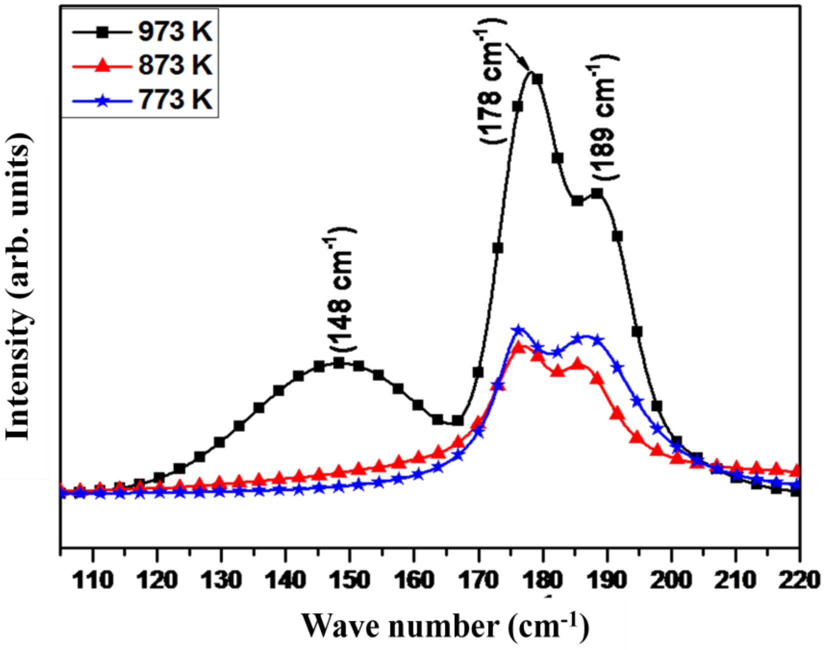

**Fig. 3.14 Raman analysis for the $ZrO_2$ films prepared under different substrate temperature conditions and at oxygen partial pressure of 0.002 Pa.**

### 3.3.2.3 AFM analysis

Figure 3.15 shows the AFM images of $ZrO_2$ thin films deposited at different substrate temperatures and oxygen partial pressure of 2 Pa. The AFM image of the $ZrO_2$ film deposited at 473 K showed less crystalline films, and an improvement in the crystallinity was observed with the increase in the substrate temperature. The RMS roughness values were measured for the films deposited at different substrate temperature conditions and were found to vary from 0.6 to 2.3 nm with increase in the substrate temperature from 473 to 873 K. The roughness values obtained for $ZrO_2$ films under different substrate temperatures were in accordance with the results reported by Balakrishnan et al. [52].

The surface morphology of the $ZrO_2$ films deposited under various oxygen partial pressures were shown in Fig. 3.16. The surface morphology of the films did not show any significant changes with change in oxygen partial pressure. The roughness values obtained from the films remained almost constant for all the films and are found to vary from 1.3-1.5 nm.

### 3.3.2.4 HRTEM analysis

The microstructure of $ZrO_2$ thin film deposited at 973 K and oxygen partial pressure of 2 Pa was analyzed by TEM (Fig. 3.17) and the SAD pattern is shown in Fig. 3.17 (a). The spotty ring pattern of SAD confirms the polycrystalline nature of the films. The d-spacings obtained from the SAD pattern corresponds to (001), (110), $(\bar{1}11)$, (111), (200) and (211) planes of monoclinic $ZrO_2$ and (002) of t-$ZrO_2$.

Figure 3.17 (b) shows the bright field micrograph where the crystallites of $ZrO_2$ can be observed. The sizes of the crystallites are found to be ~40 nm and are uniform in nature. The contrast variation is due to the variation in extinction length and deviation parameter of the crystallites.

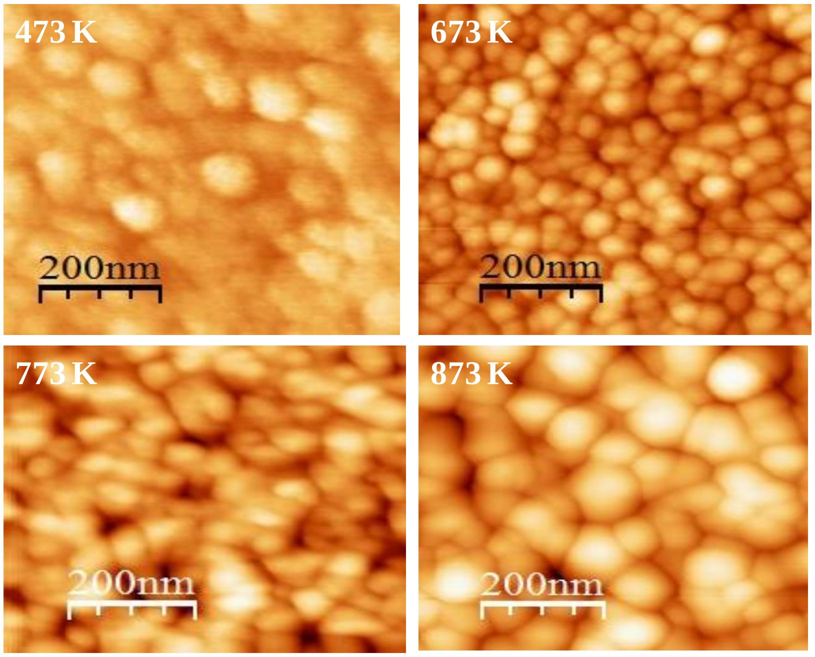

**Fig. 3.15 AFM images of $ZrO_2$ thin films grown at different substrate temperatures and at constant oxygen partial pressure of 2 Pa.**

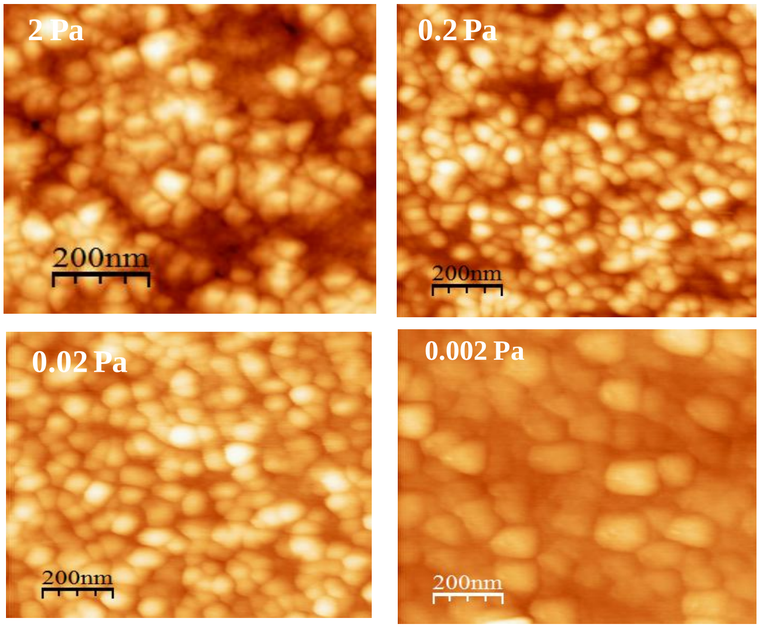

**Fig. 3.16 AFM images of $ZrO_2$ thin films grown under different oxygen partial pressures and at the substrate temperature of 973 K.**

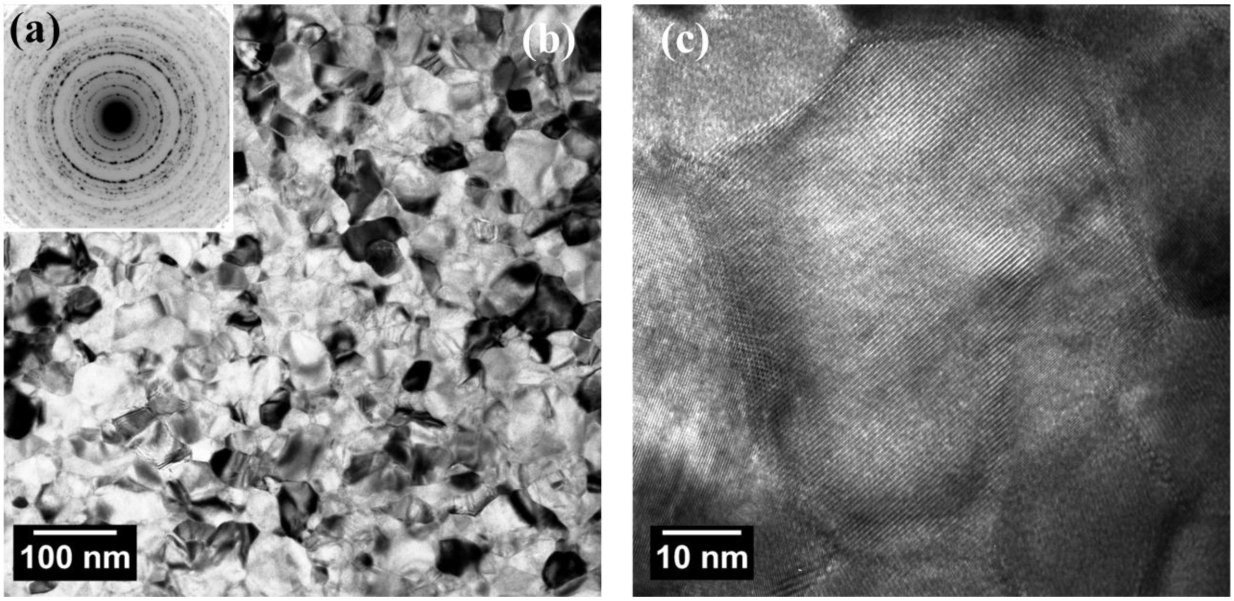

**Fig. 3.17 TEM micrograph of $ZrO_2$ film deposited at 973 K and oxygen partial pressure of 2 Pa on Si (100) substrates (a) SAD pattern, (b) relatively low magnification bright field image showing crystallite size distribution and (c) high magnification image showing lattice planes of m-$ZrO_2$ crystallite.**

Fig. 3.17 (c) shows the phase contrast image from a single grain of $ZrO_2$ . The lattice spacings has been calculated from the power spectrum, which corresponds to the (001) of monoclinic $ZrO_2$.

### 3.3.2.5 Optical property analysis

The absorbance of the films was measured in the wavelength range of 200-900 nm using a UV- visible spectrometer. Since we obtained similar structural and microstructural properties of $Y_2O_3$ films deposited on silicon and quartz for $Y_2O_3$ films [35], the optical properties obtained on quartz substrates alone is presented in the following section:

Fig. 3.18 (a) and 3.19 (a) show the absorbance versus wavelength plot of $ZrO_2$ thin films deposited at different substrate temperature and at the oxygen partial pressure of 2 Pa and 0.002 Pa, respectively. Similarly, Fig. 3.20 (a) shows the absorbance versus wavelength plot of $ZrO_2$ thin films deposited at different oxygen partial pressure (2-0.002 Pa) and at the substrate temperature of 773 K. All the films show two absorption edges at ~225 nm and ~250 nm, corresponding to two phases of $ZrO_2$. The results are in agreement with the observation by Balakrishnan et al [53]. Fig 3.18 (b) and 3.19 (b) show the variation of % transmittance versus wavelength plot for the films deposited at different substrate temperatures and constant oxygen partial pressure of 2 and 0.002 Pa, respectively. Fig. 3.20 (b) also represents the % transmittance of $ZrO_2$ films deposited at different oxygen partial pressures and substrate temperature of 773 K.

Except for the film deposited at 973 K and oxygen parial pressure of 2 Pa(~60%) most of the $ZrO_2$ films showed transmittance in the range 65-92 % measured at 550 nm. Fig. 3.19 (b) shows the transmittance of $ZrO_2$ films deposited at different substrate temperature and at oxygen partial pressure of 0.002 Pa. The transmittance values vary from 60-85% as a function of the substrate temperature except for the films deposited at 473 K, where the transmittance is very low. The lowest value of the transmittance of the films deposited at 473 K and 0.002 Pa can be related to the loss of crystallinity in the film which is in accordance with the XRD results reported elsewhere [44].

Fig. 3.20 (b) shows the % transmittance of $ZrO_2$ films deposited at different oxygen partial pressure and substrate temperature of 773 K. All the films showed good transmittance of 60-85%. Transmittance was the highest for the films deposited at higher oxygen partial pressure and decreased as a result of the low stoichiometry of oxygen in the films obtained at low oxygen partial pressures [53].

Band gap of the films was calculated by Tauc Plot [5]. All the $ZrO_2$ films deposited at different substrate and oxygen partial pressure showed two band gaps corresponding to tetragonal and monoclinic phases of $ZrO_2$. The band gap values calculated are listed in the Table 3.5 and 3.6. Band gap values vary from 4.52 to 5.15 eV and 5.01 to 5.58 eV corresponding to tetragonal and monoclinic phases, respectively for the films deposited at different substrate temperature and oxygen partial pressure of 2 Pa. Band gap values were increased with increase in the substrate temperature. Band gap values deposited at different oxygen partial pressure and substrate temperature of 973 K, were found to increase from 5.15 to 5.16 and from 5.58 to 5.39 corresponding to tetragonal and monoclinic phases, respectively.

The refractive index was calculated for the $ZrO_2$ films deposited at different substrate temperature and at the oxygen partial pressure of 2 and 0.002 Pa and listed in Table 3.5 and 3.6, respectively. The results clearly showed an increase in the refractive index with the increase in the substrate temperature and decrease in the oxygen partial pressure. The refractive index of the $ZrO_2$ films deposited at different substrate temperatures and oxygen partial pressure of 2 Pa, increases from 1.76 to 2.47. Similarly, the refractive index for the films deposited at different substrate temperature and oxygen partial pressure of 0.002 Pa were increased from 1.62 to 2.51. The change in the refractive index as a function of the processing conditions could related the change in the microstructure of the films, especially, which results in change in crystallite size, porosity and packing density [54-56.]. The lower value of refractive index of the films deposited at higher oxygen partial pressure may be attributed to low crystallite size and packing density of the films [48, 55,57].

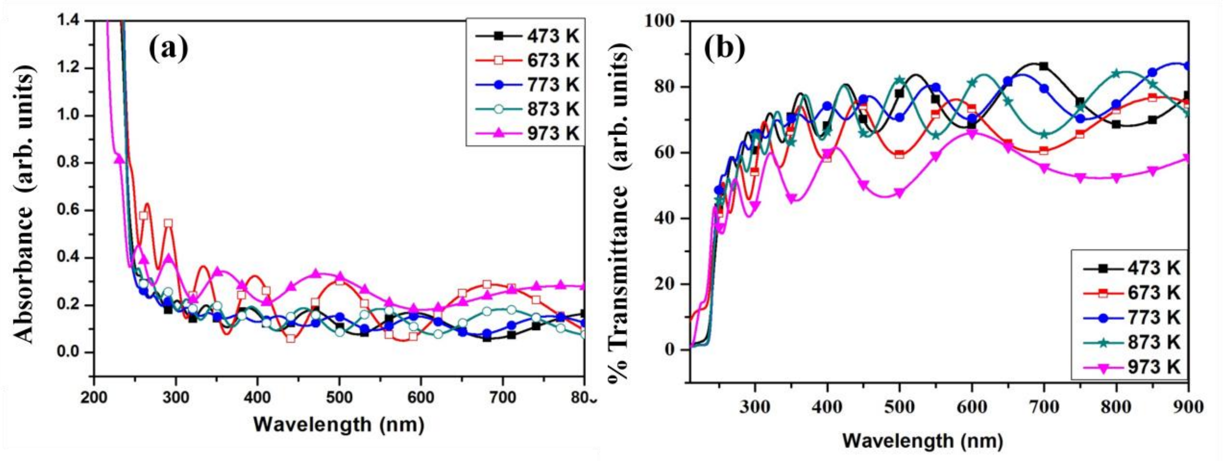

Fig. 3.18 The (a) Absorbance and (b) Transmittance spectra of $ZrO_2$ films deposited on quartz substrates at various substrate temperatures and oxygen partial pressure of 2 Pa.

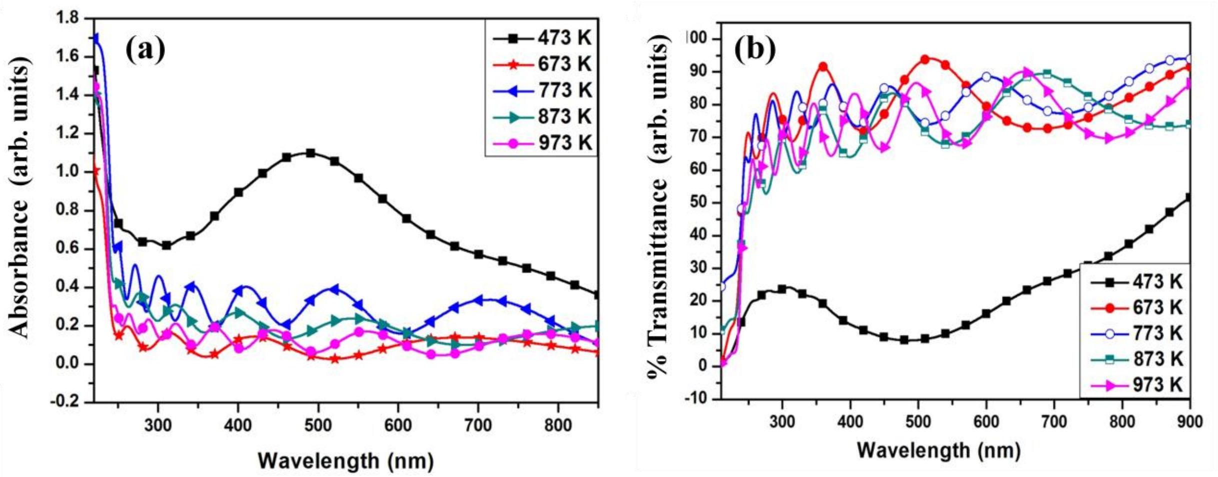

Fig. 3.19 The (a) Absorbance and (b) Transmittance of the $ZrO_2$ films grown on quartz substrates at different substrate temperatures and oxygen partial pressure of 0.002 Pa.

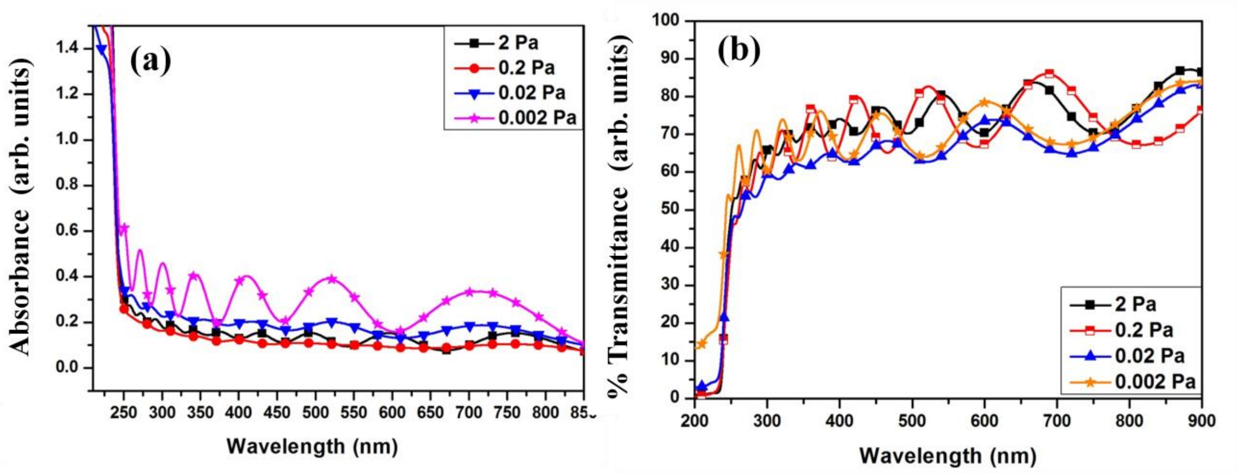

Fig. 3.20 The (a) Absorbance and (b) Transmittance values of $ZrO_2$ films in the wavelength range of 200- 900 nm, deposited at various oxygen partial pressures and substrate temperature of 773 K.

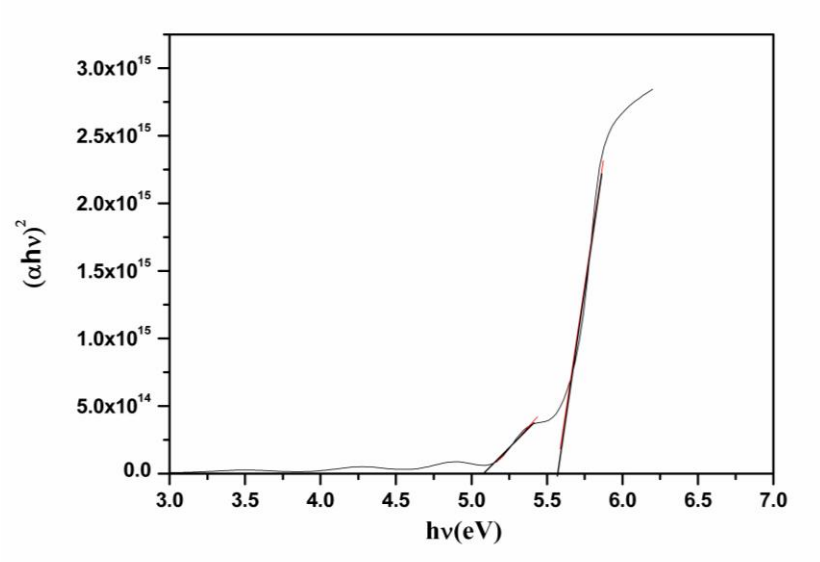

**Fig. 3.21 A typical Tauc plot for the $ZrO_2$ film deposited at the substrate temperature of 973 K and oxygen partial pressure of 2 Pa.**

**Table 3.5 Microstructural and optical properties of $ZrO_2$ films deposited at various substrate temperatures and oxygen partial pressure of 2 Pa.**

| **Substrate temperature (K)** | **Crystallite Size m-$ZrO_2$ (±3 nm)** | **Crystallite Size t-$ZrO_2$ (±3 nm)** | **Roughness (nm)** | **Band gap m-$ZrO_2$ (±0.01eV)** | **Band gap t-$ZrO_2$ (±0.01eV)** | **Refractive index (±0.01)** |
|---|---|---|---|---|---|---|
| 473 | 6 | 12 | 0.6 | 5.01 | 4.52 | 1.76 |
| 773 | 19 | 24 | 1.1 | 5.11 | 4.7 | 1.88 |
| 873 | 24 | 23 | 1.2 | 5.13 | 4.9 | 1.93 |
| 973 | 17 | 35 | 2.3 | 5.58 | 5.15 | 2.47 |

**Table 3.6 Variation in microstructural and optical properties of $ZrO_2$ thin films deposited under different oxygen partial pressures and substrate temperature of 973 K.**

| **Oxygen partial pressure (Pa)** | **Crystallite Size m-$ZrO_2$ (±3 nm)** | **Crystallite Size t-$ZrO_2$ (±3 nm)** | **Roughness (nm)** | **Band gap m-$ZrO_2$ (±0.01eV)** | **Band gap t-$ZrO_2$ (±0.01eV)** | **Refractive index (±0.01)** |
|---|---|---|---|---|---|---|
| 2 | 17 | 35 | 1.5 | 5.58 | 5.15 | 2.47 |
| 0.2 | 18 | 26 | 1.4 | | | |
| 0.02 | 17 | 28 | 1.3 | | | |
| 0.002 | 19 | 27 | 1.3 | 5.39 | 5.16 | 2.51 |

### 3.3.2.6 Nanomechanical property analysis

Hardness and elastic modulus of a typical $ZrO_2$ film deposited at 873 K and oxygen partial pressure of 2 Pa was measured using nanoindentation technique and was found to be 4.4 GPa and 172.2 GPa, respectively. Fig. 3.22 shows the typical load versus penetration depth plot for the $ZrO_2$ film grown on Inconel-783 at the substrate temperature of 873 K and the oxygen partial pressure of 2 Pa. The values obtained in this analysis were much lower than that of the values reported in the bulk $ZrO_2$ (Hardness- 11.8 GPa and Elastic modulus- 205 GPa) [58,59]. Zhang et al. [60] and Zlotnikov et al. [61] have reported where hardness and elastic modulus values of 1 GPa and 30 GPa and 0.6 GPa and 25 GPa, respectively. The decrease in hardness and elastic modulus values in the latter are attributed to the presence of porosity in the films [61].

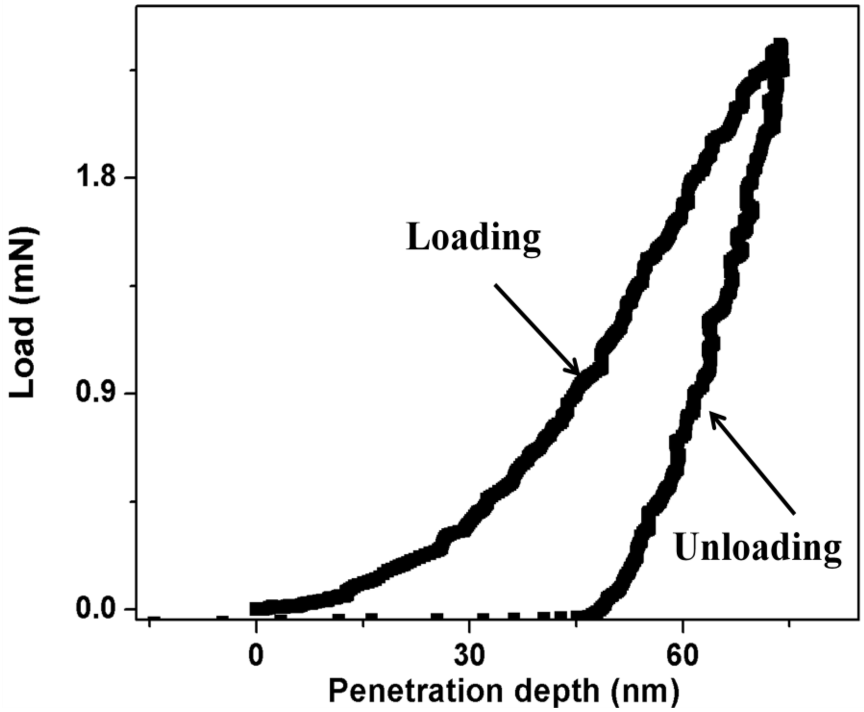

**Fig. 3.22 Load versus penetration depth plot of the $ZrO_2$ thin film deposited on Inconel-783 substrates at the substrate temperature of 873 K and the oxygen partial pressure of 2 Pa.**

### 3.3.3 Multilayers of $ZrO_2/Y_2O_3$

In this section, the results obtained on microstructural, optical and nanomechanical properties of the multilayers of $ZrO_2/Y_2O_3$ with varying thickness of $ZrO_2$ are presented. The $ZrO_2$ layer thickness is varied from 5 to 30 nm with a constant layer thickness of $Y_2O_3$ at 10 nm. The total number of bilayers are 3, 4, 6 and 8 for $ZrO_2$ layer thickness of 30, 20, 10 and 5 nm, respectively.

#### 3.3.3.1 XRD analysis

Fig. 3.23 and 3.24 show the XRD patterns of $ZrO_2/Y_2O_3$ multilayers grown on Si (100) substrates at substrates temperature of 300 K and 873 K and an oxygen partial pressure of 2 Pa. Except for a wide peak broadening at about 30˚ (2ϴ) , no peaks from either $ZrO_2$ or $Y_2O_3$ were observed for the multilayer deposited at 300 K indicating that the films were X-ray amorphous when deposited at 300 K, on the other hand films deposited at 873 K showed polycrystalline nature containing peaks of cubic-$Y_2O_3$, monoclinic-$ZrO_2$ and tetragonal-$ZrO_2$. However the multilayer of (5/10) nm thickness showed severe peak broadening due to lower thickness of the film. Crystallite sizes for the (222), ($\bar{1}$11) and (011) reflection corresponding to the c-$Y_2O_3$, m-$ZrO_2$ and t-$ZrO_2$ were calculated by Scherrer formula, and were found to be comparable with layer thickness [62].

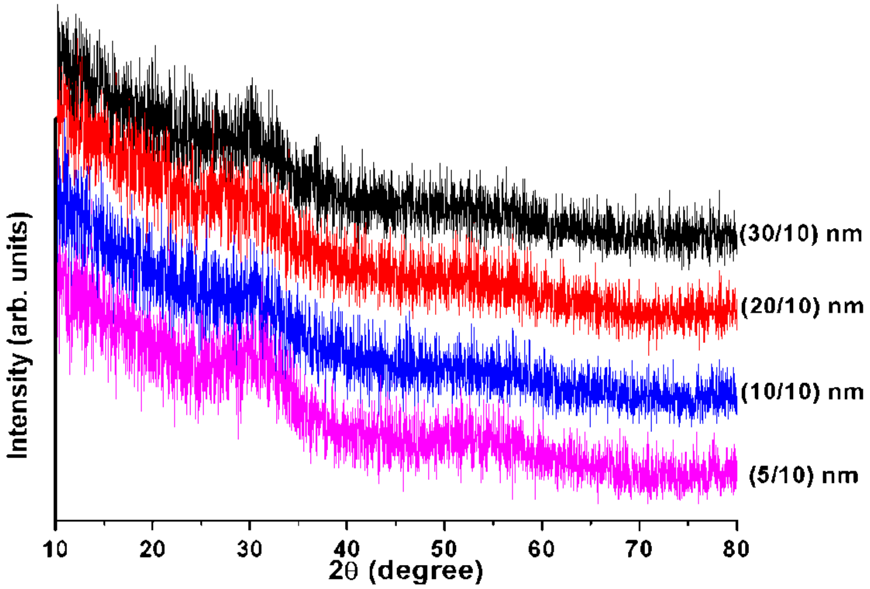

**Fig. 3.23 XRD pattern of $ZrO_2/Y_2O_3$ multilayers with different $ZrO_2$ layer thickness deposited on Si (100) substrates at substrate temperature of 300 K and oxygen partial pressure of 2 Pa.**

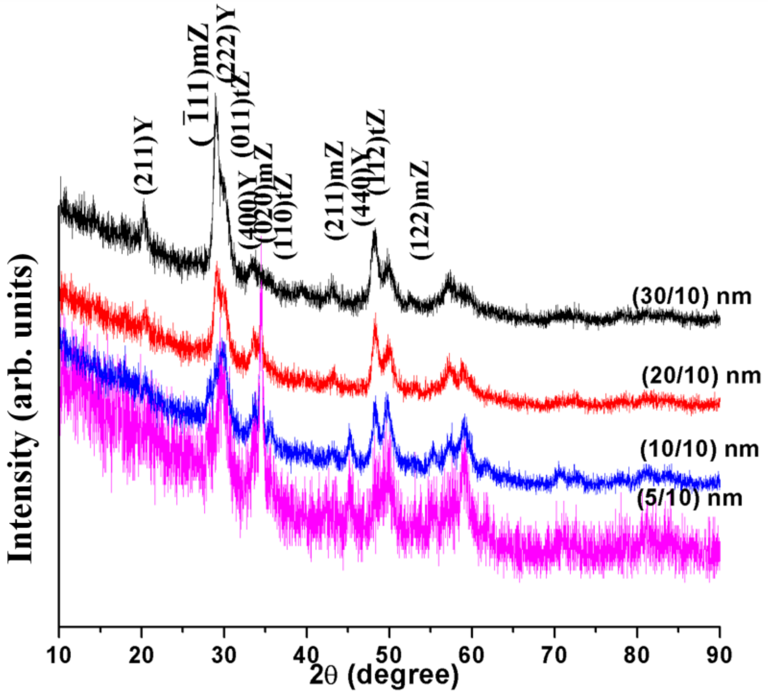

**Fig. 3.24 XRD patterns of $ZrO_2/Y_2O_3$ multilayer films deposited on Si (100) substrates with $ZrO_2$ layer thickness varied from 5 to 30 nm at substrate temperature of 873 K and oxygen partial pressure of 2 Pa.**

### 3.3.3.2 Raman analysis

Fig. 3.25 shows the Raman spectrum of $ZrO_2/Y_2O_3$ multilayers of (5/10) and (30/10) nm deposited on Si (100) at 873 K and oxygen partial pressure of 2 Pa. The figure shows peaks corresponding to m-$ZrO_2$ and c-$Y_2O_3$ at 179, 477 and 380 $cm^{-1}$, respectively [36,46-52]. Intensity of the peaks for c-$Y_2O_3$ was higher in the multilayer with $ZrO_2$ layer thickness of 5 nm. The Raman spectra of the multilayer structure with 30 nm of $ZrO_2$ layer thickness contained peaks from m-$ZrO_2$ and c-$Y_2O_3$, whereas there were no peaks from t-$ZrO_2$. Raman spectra of the multilayer structures deposited at 300 K did not show any characteristic peaks for $ZrO_2$ and $Y_2O_3$ due to the amorphous nature of the films.

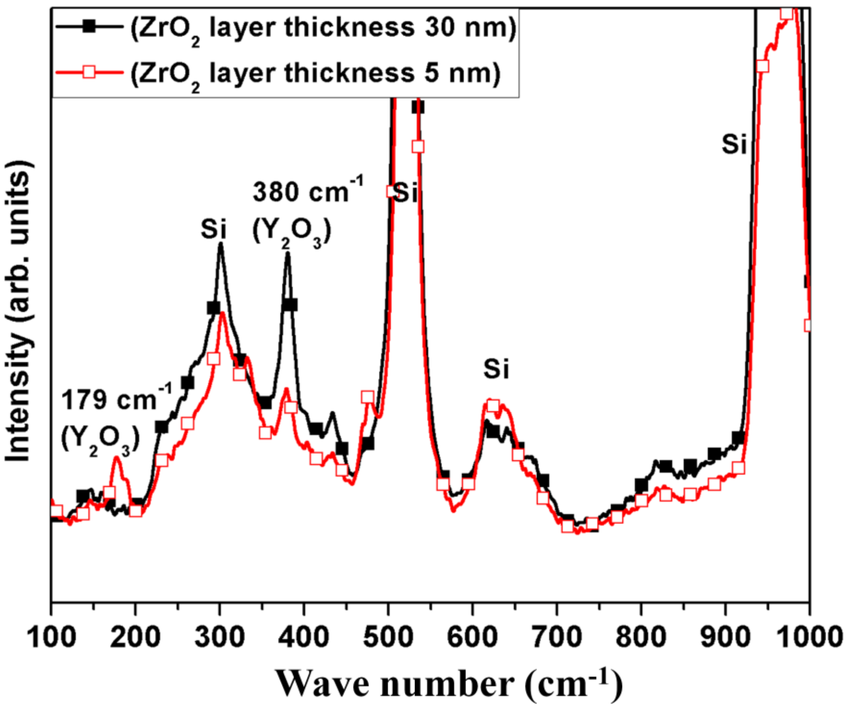

**Fig. 3.25 Raman spectroscopy analysis of $ZrO_2/Y_2O_3$ multilayers with $ZrO_2$ layer thickness of 5 and 30 nm deposited at 873 K and oxygen partial pressure of 2 Pa.**

### 3.3.3.3 X-ray reflectivity analysis

A typical example of XRR profile of the $ZrO_2/Y_2O_3$ multilayers of (30/10) nm along with the curve fitting for the samples deposited at 300 K is shown in Fig. 3.26. XRR measurements showed individual layer thicknesses of $ZrO_2/Y_2O_3$ multilayers (8.1/14.2), (9.5/12.7), (21.1/14.2) and (35.5/14.5) nm corresponding to the layer thickness of (5/10), (10/10), (20/10) and (30/10) nm determined the from deposition rates. The individual layer thickness was found to be within an error of ± 4 nm and is listed in Table 3.7. It is clear from the Table 3.7 that the individual layer thicknesses were measured to be close to that of obtained from the thickness determined from deposition rates. The surface roughness values were also calculated from the XRR profile fitting and were found to be lower for the films deposited at 300 K than that of the films deposited at 873 K. The change in the interfacial roughness value was more significant for the multilayers prepared at 873 K and was found to increase with increase in the $ZrO_2$ layer thickness. At 300 K, both $Y_2O_3$ and $ZrO_2$ films exists in amorphous structure [35,51], thus leading to low surface and interfacial roughness. At higher substrate temperature, both $ZrO_2$ and $Y_2O_3$ form crystalline structures, resulting in an increase in roughness values.

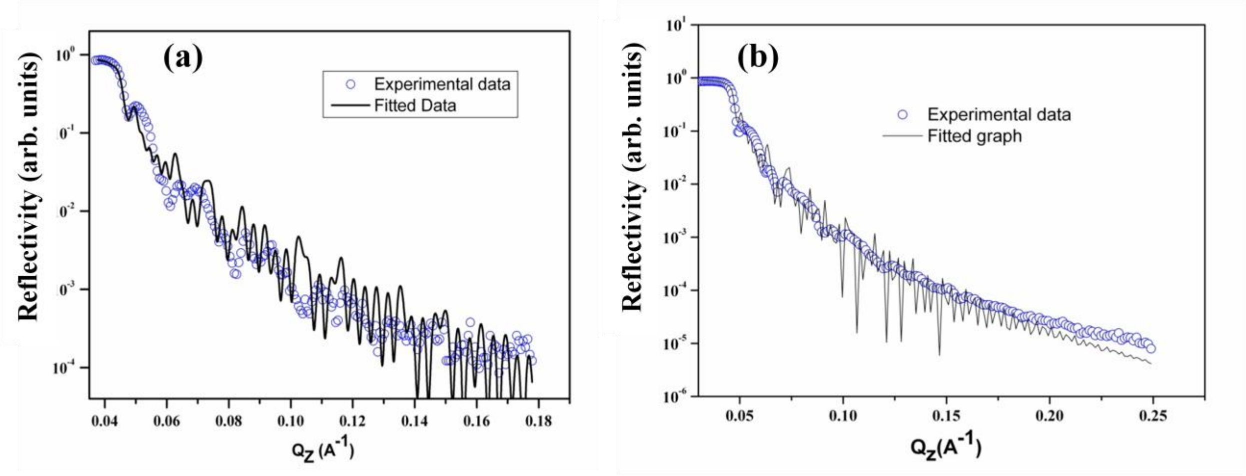

**Fig. 3.26 A typical X-ray reflectivity profile of $ZrO_2/Y_2O_3$ multilayer of (30/10) nm thickness deposited on Si substrate at (a) 300 K and (b) 873 K.**

**Table 3.7 XRR results of the $ZrO_2/Y_2O_3$ multilayers deposited at 300 K and 873 K.**

| **Bilayer structure ($ZrO_2/Y_2O_3$) (nm)** | **Films Deposited at 300 K** | | | **Films Deposited 873 K** | | |
|---|---|---|---|---|---|---|
| | **Thickness from XRR (nm)** | **Interfacial roughness (nm)** | **Surface roughness (nm)** | **Thickness from XRR (nm)** | **Interfacial roughness (nm)** | **Surface roughness (nm)** |
| 5/10 | 8.1/14.2 | 0.6 | 1.0 | 6.1/15.8 | 0.7 | 1.2 |
| 10/10 | 9.5/12.7 | 0.7 | 0.6 | 11.2/11.5 | 0.8 | 1.0 |
| 20/10 | 21.1/14.2 | 0.9 | 0.8 | 22.3/12.2 | 1.1 | 1.1 |
| 30/10 | 14.5/35.5 | 0.7 | 0.9 | 35.5/15.6 | 1.3 | 1.5 |

### 3.3.3.4 AFM analysis

Fig. 3.27 (a) and (b) show the AFM images of $ZrO_2/Y_2O_3$ multilayer of (30/10) nm deposited on Si substrates at 300 and 873 K, respectively. The films deposited at 300 K show amorphous structure wich can be observed from the smooth surface of the film deposited at 300 K. Whereas the surface morphology of the films deposited at a substrate temperature of 873 K show improved degree of crystallinity, which can be concluded from the small grains observed in the AFM images. The surface roughness values obtained from the AFM image analysis of the films deposited at 300 K and 873 K were 0.4 and 0.6 nm respectively. The roughness values obtained from AFM image analysis were slightly lower in comparision to the values obtained from X-ray reflectivity analysis.

### 3.3.3.5 HRTEM analysis

Figure 3.28 (a) shows a typical SAD pattern of $ZrO_2/Y_2O_3$ multilayer of (30/10) nm. The SAD pattern showed the formation of polycrystalline films consisting of c-$Y_2O_3$ and t-$ZrO_2$ and c-$ZrO_2$ even at room temperature. The SAD pattern was indexed and listed in Table 3.8.

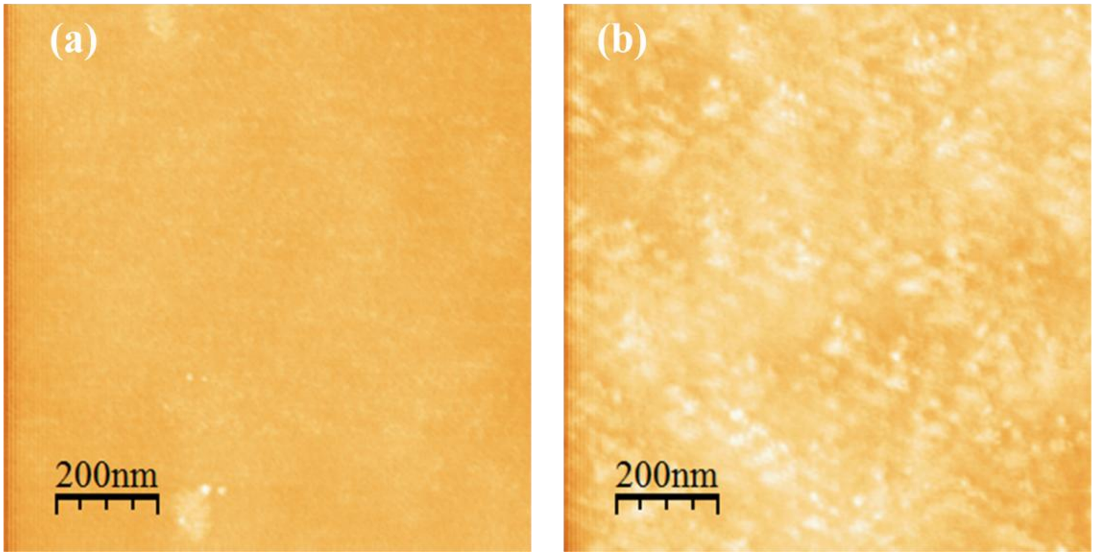

**Fig. 3.27 AFM images of $ZrO_2/Y_2O_3$ multilayer films of (30/10) nm thickness deposited on Si(100) at (a) 300 K and (b) 873 K.**

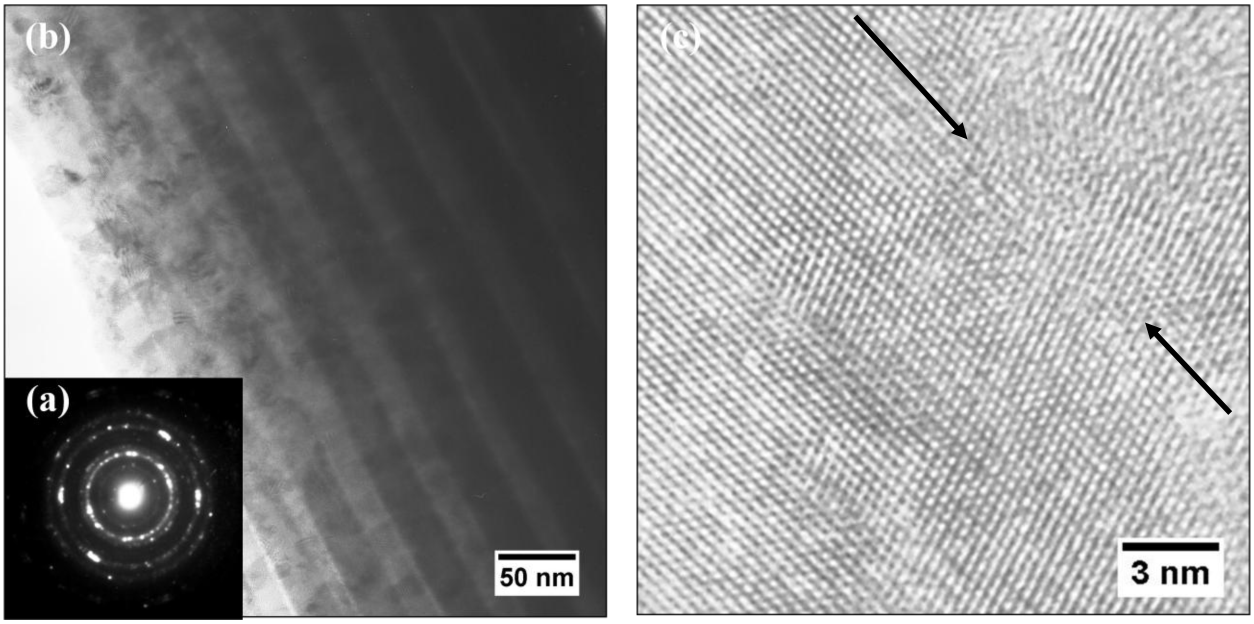

**Fig. 3.28 HRTEM images of $ZrO_2/Y_2O_3$ multilayer of (30/10) nm deposited on Si substrates at 300 K and oxygen partial pressure of 2 Pa (a) SAD pattern (b) Low magnification bright field image and (c) lattice image.**

**Table 3.8: Interplanar distances obtained from the SAD pattern of (30/10) nm thickness multilayer deposited at 300 K.**

| d(nm) (measured) | c-$Y_2O_3$ PDF # 81-0792 | | t- $ZrO_2$ PDF # 50-1089 | | c- $ZrO_2$ PDF # 89-9069 | |
|---|---|---|---|---|---|---|
| | d (nm) | h k l | d nm) | h k l | d (nm) | h k l |
| 0.296 | 0.3061 | 2 2 2 | 0.295 | 0 1 1 | 0.296 | 1 1 1 |
| 0.259 | 0.2651 | 4 0 0 | 0.257 | 0 0 2 | 0.256 | 2 0 0 |
| 0.247 | 0.249 | 4 1 1 | 0.254 | 1 1 0 | | |
| 0.222 | 0.226 | 3 3 2 | 0.209 | 0 1 2 | | |
| 0.203 | 0.207 | 4 3 1 | 0.209 | 0 1 2 | | |
| 0.184 | 0.187 | 4 4 0 | 0.180 | 1 1 2 | 0.181 | 2 2 0 |
| 0.176 | 0.176 | 6 0 0 | 0.179 | 0 2 0 | | |
| 0.157 | 0.156 | 6 3 1 | 0.154 | 0 1 3 | | |

Figure 3.28 (b) is the low-magnification bright-field TEM image showing the cross-sectional view of the multilayer of $ZrO_2/Y_2O_3$ of (30/10) nm deposited at 300 K and oxygen partial pressure of 2 Pa. Dark bands correspond to $ZrO_2$, while bright bands are $Y_2O_3$ layers. The thickness of the $ZrO_2$ nanolayers were found to vary in the range of 32-36 nm and that of the $Y_2O_3$ nanolayers were varied between 12-16 nm. The TEM images show that the interfaces are sharp and devoid of any interdiffusion for the multilayer deposited at 300 K [62].

Figure 3.28 (c) shows the micrograph taken from the interface region. The $Y_2O_3$ and $ZrO_2$ layers are marked in the image. The interface defects were quite prominent from the region. Presence of dislocations can also be observed from the micrograph. Power spectrum was generated from the HRTEM micrograph confirming the tetragonal $ZrO_2$ nanocrystallities were in the tetragonal structure. The present micrograph shows the (011) plane of t-$ZrO_2$.

### 3.3.3.6 Optical properties

Optical properties of the $ZrO_2/Y_2O_3$ multilayer film were measured for the films deposited on quartz substrates. Figure 3.29 (a) shows the absorbance versus wavelength plot for

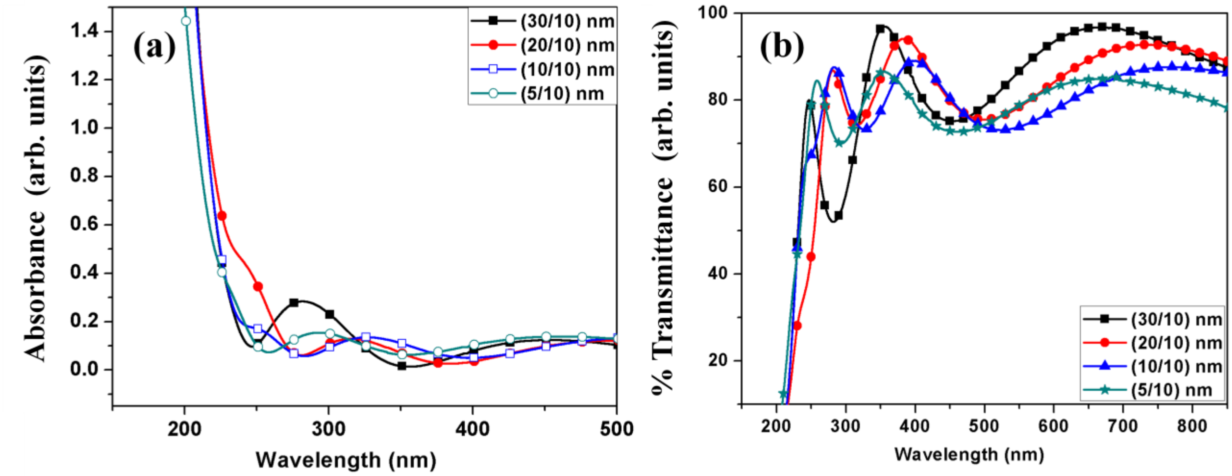

**Fig. 3.29 Effect of $ZrO_2$ layer thickness on the (a) absorbance (b) transmittance values of $ZrO_2/Y_2O_3$ multilayers deposited on quartz substrates at 300 K and oxygen partial pressure of 2 Pa.**

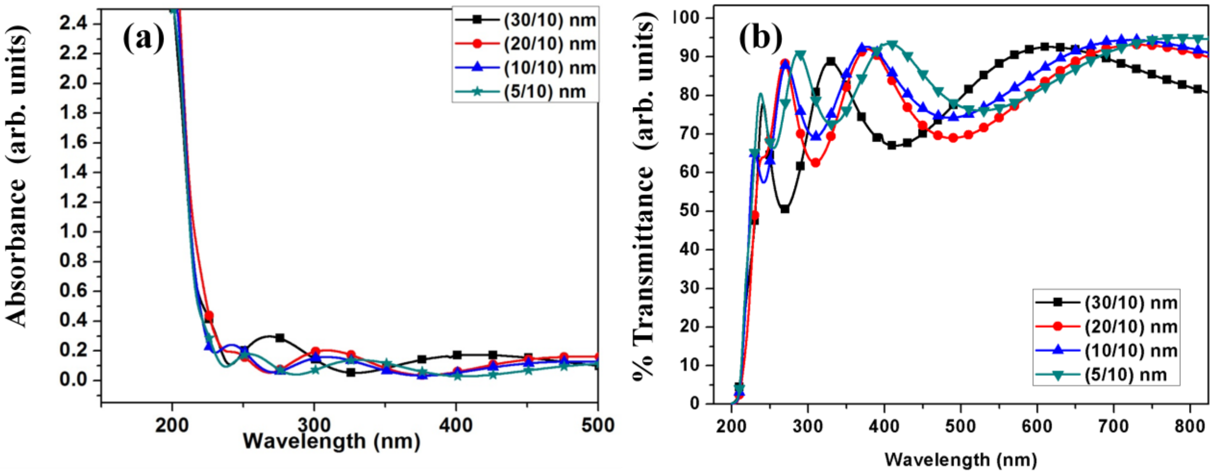

**Fig 3.30 Variation in (a) absorbance and (b) transmittance values of $ZrO_2/Y_2O_3$ multilayers deposited on quartz substrates at 873 K and oxygen partial pressure of 2 Pa as a function of $ZrO_2$ layer thickness.**

the multilayer films deposited at 300 K and oxygen partial pressure of 2 Pa as a function of $ZrO_2$ layer thickness in the range of 5 -30 nm. The films showed a strong absorbance near wavelength of 220 nm. The transmittance values of the multilayers were recorded as a function of wavelength for different $ZrO_2$ layer thickness and are found to decrease from 98 % to 88 % with the decrease in $ZrO_2$ layer thickness (Fig. 3.29 (b)).

The absorbance versus wavelength plot for $ZrO_2/Y_2O_3$ thin films deposited at 873 K is shown in Fig. 3.30 (a). The multilayers show a strong absorbance near 220 nm and the transmittance values for the multilayers were almost similar, showing a maximum of 90 % transmittance (Fig. 3.30 (b)).

Band gap values were calculated for the $ZrO_2/Y_2O_3$ multilayers by Tauc plot. The band gaps of the multilayers deposited at 300 K show an increase from 5.39 eV to 5.61 eV with increase in $ZrO_2$ layer thickness from 5 to 30 nm. Whereas the $ZrO_2/Y_2O_3$ multilyer films deposited at 873 K did not show any significant changes and were found to vary from 5.63- 5.68 eV.

### 3.3.3.7 Nanomechanical properties

The hardness and elastic modulus values of the $ZrO_2/Y_2O_3$ multilayers deposited on Inconel-783 substrates, at the sunstrate temperature of 873 K and the oxygen partial pressure of 2 Pa was measured by nanoindentation technique as a function of $ZrO_2$ layer thickness (Fig. 3.31).

No significant change in the hardness values were observed with change in $ZrO_2$ layer thickness. The values of hardness for different multilayer films were found to be ~5.4 GPa. The elastic modulus values measured from the indentation technique showed a dip for 10 nm thickness from the initial value of 229 GPa for the $ZrO_2$ layer thickness of 5 nm.

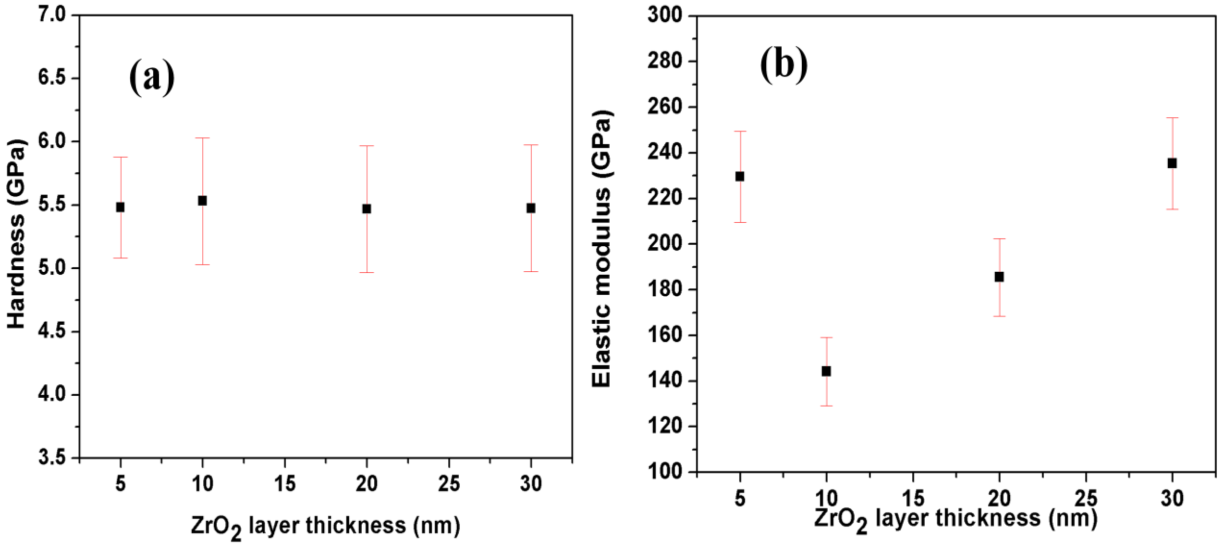

**Fig. 3.31 (a) Hardness and (b) Elastic modulus values of $ZrO_2/Y_2O_3$ multilayers as a function of $ZrO_2$ layer thickness deposited on Inconel-783 substrates at 873 K and oxygen partial pressure of 2 Pa.**

## 3.4 Discussion

The following section includes the discussion on the results obtained from different characterization techniques used for both $Y_2O_3$ and $ZrO_2$ thin films and $Y_2O_3$ /$ZrO_2$ multilayer films.

### 3.4.1 $Y_2O_3$ and $ZrO_2$ thin films

Microstructures of thin films deviate significantly from that bulk, which is dependent on the deposition parameters of a deposition technique. $Y_2O_3$ and $ZrO_2$ thin films were prepared on Si (111) and quartz substrates at various substrate temperatures and oxygen partial pressures. The crystallite size was calculated for the FWHM of the highest intensity peak, for both $Y_2O_3$ and $ZrO_2$ films and found to increase with increase in the substrate temperature, which is due to the increase in adatom mobility with increases in the substrate temperature. Similar results for $Y_2O_3$ films were reported by Cheng et al.[1]. As the substrate temperature is increased, the adatomic mobility at the substrates surface is also increased due to increase in thermal energy. As a result of which the adatoms get enough time to move across the substrate surface and form the lowest energy structure [63].

When the oxygen partial pressure is higher, the mobility of ablated species is restricted due to collision with oxygen molecules present in the chamber. This results in the decrease in probability of forming low energy structure. Whereas at low oxygen partial pressure, the collision between ablated species and oxygen atoms is less probable and the ablated species have higher mobility, which resulted in the formation preferred orientation with increase in crystallite size. Unlike the substrate temperature, the films deposited as a function of oxygen partial pressure showed a minor variation in the crystallite size at constant substrate temperature.

$Y_2O_3$ exists in cubic phase for the above substrate temperature and oxygen partial pressure range. Whereas $ZrO_2$ thin films contain a mixture of monoclinic and tetragonal phases. XRD analysis showed that higher substrate temperature and oxygen partial pressure favoured the tetragonal phase formation. The monoclinic phase was dominating up to the substrate temperature of 773 K and beyond 773 K, tetragonal phase was the dominating phase. Similarly for the films grown at 973 K and at different oxygen partial pressure, tetragonal phase was found to dominate. The results obtained from Raman analysis were also in favor of the XRD results. The increase in the stress in the films is generally attributed to the peening effect of the ablated atoms at the substrate surface and is influenced by the substrate temperature and oxygen partial pressure [64]. Strain values of the $ZrO_2$ films as a function of the substrate temperature and oxygen partial pressure were calculated using the equation 3.1 and are shown in Fig. 3.32.

$$\varepsilon = \beta / 4\tan\Theta \quad \ldots\ldots\ldots\ldots\ldots\ldots\ldots\ldots\ldots\ldots\ldots\ldots\ldots\ldots\ldots\ldots (3.1)$$

The strain value for the tetragonal phase was decreased with increase in the substrate temperature as a consequence of stress relaxation due to the increase in crystallite size. The change in the stress of the films as a function of the oxygen partial pressure could be related to reduction in the kinetic energy of the ablated species with the increase in the oxygen partial pressure. It was expected that the ablated species lose their energy with increase in the oxygen partial pressure due to the collisional process with surrounding oxygen molecules, leading to less strain at higher oxygen partial pressure.

From the above results it can be concluded that the synthesis of a phase pure $ZrO_2$ film from a target containing two phase structure by PLD process was constrained in the present range of substrate temperature and oxygen partial pressure. The variation in stress fields and the elastic properties of the crystallites could possibly prohibit the formation of a single phase film from a target containing a mixture of phases. The present study has demonstrated that synthesis of a film with single phase becomes more tedious when we deal with varying crystallite sizes as a function of the process parameters.

Phase pure cubic-$ZrO_2$ films were prepared with $ZrO_2$ with 8 mol% $Y_2O_3$ at oxygen partial pressure of 0.2 Pa and in the substrate temperature range 573–873 K. Table 3.9 lists the sintered condition, sintered density of the target and the deposition conditions used for the YSZ films. Fig. 3.33 shows the XRD pattern of the YSZ films deposited on Si (100) substrates at substrate temperature of 573–873 K and oxygen partial pressure of 0.2 Pa. XRD analysis shows peaks from (111), (200),

**Table 3.9 Experimental conditions for YSZ film preparation**

| **Parameters** | **YSZ** |
|---|---|
| Target size | 20 mm diameter and 3 mm thickness |
| Sintering conditions | 1823 K, 12 h |
| Sintered density | ~95% |
| Laser energy | 300 mJ |
| Repetition rate | 10 Hz |
| Target to substrate distance | 45 mm |
| Substrate | Si (100) |
| Substrate temperature | 300-873 K |
| Oxygen partial pressure | 2-0.002 Pa |

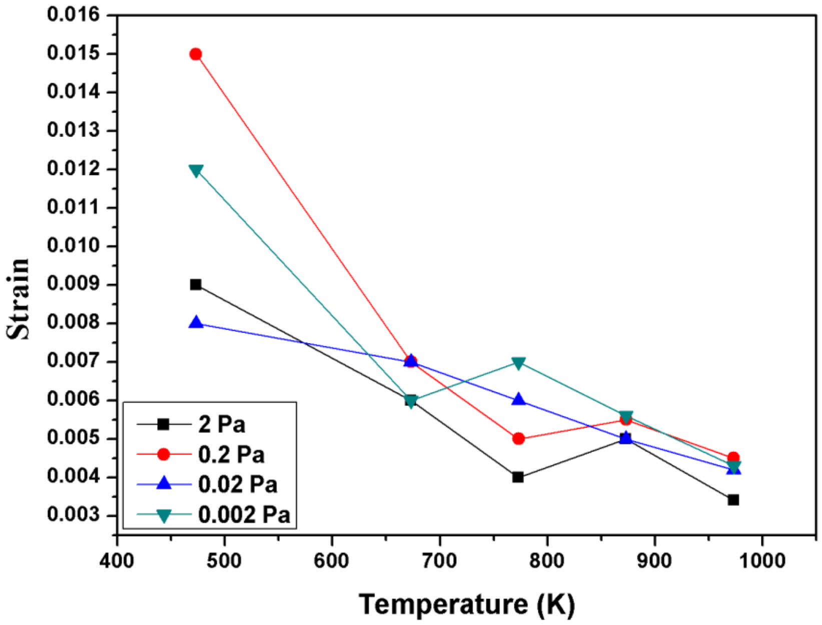

**Fig. 3.32 Variation in strain values in $ZrO_2$ thin films as a function of the substrate temperatures and oxygen partial pressures.**

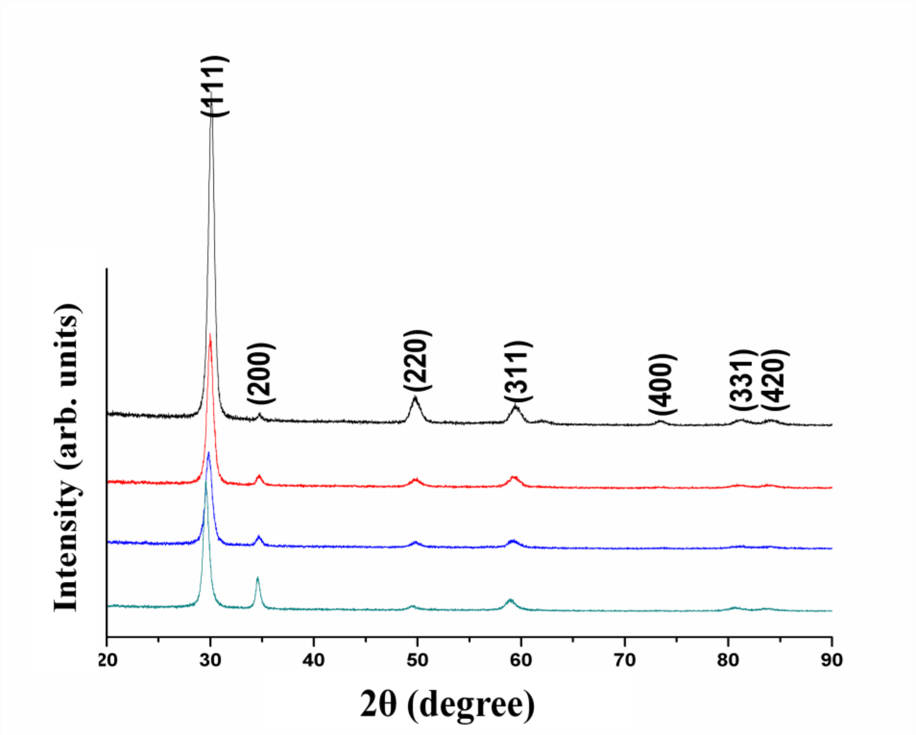

**Fig. 3.33 XRD patterns of the YSZ films deposited on Si (100) substrates at various substrate temperatures and oxygen partial pressure of 0.2 Pa.**

(220), (311), (400), (331) and (420) reflections of c-$ZrO_2$ (JCPDS file no: 49-1642). This study establishes that the synthesis of cubic phase of $ZrO_2$ is possible by PLD technique using the YSZ target.

Surface morphology of $Y_2O_3$ and $ZrO_2$ thin films were studied by AFM and showed an increase in the crystallite size with increase in the substrate temperature, which can be concluded from the larger size of grains observed in the AFM images. On the other hand, the crystallite size of the films deposited at different oxygen atmosphere did not show a very significant change. The roughness values obtained for the films increased with increase in the substrate temperature, as a result of the increase in the crystallite size. Whereas the films deposited under different oxygen partial pressures did not show a very significant change in the roughness values. The crystallite size obtained from AFM analysis showed higher values than that of the values obtained from XRD analysis. In AFM analysis, the crystallite size was measured from the surface images, which included the agglomeration of crystallites, whereas XRD gave the average crystallite size [65,66] and did not take strain into consideration.

The transmittance of a thin film depends on many factors such as thickness, microstructure, porosity, grain boundary, surface roughness and phases [54]. Transmittance values obtained from UV-Visible spectrophotometer shows a decrease in the values at higher substrate temperature as a consequence of the increase in the surface roughness due to the increase in the crystallite size, which was observed from XRD and AFM analysis. Higher surface roughness and irregular grain boundary structures could result in decrease in transmittance due to Scattering phenomena. Scattering phenomena also increase with the decrease in the crystallite size, due to the increase in total grain boundary area [67].

Band gap energy calculated for $Y_2O_3$ films deposited at different substrate temperatures showed a small increase from 5.63 to 5.76 eV with increase in the substrate temperature. This small increase in the band gap energy may be due to the increase in crystallite size with increase in the substrate temperature, which was against the quantum confinement. Similar results also have been reported by other authors [54,63,68]. According to quantum confinement theory, the band gap should decrease with the increase in the crystallite size [69-71]. But quantum confinement theory is applicable when the dimension of the particle is comparable to that of the exciton Bohr radii of a particular material. A particle behaves as if it were free when the confining dimension is large compared to the wavelength of the particle. During this state, the band gap remains at its original energy due to a continuous energy state. However, as the confining dimension decreases and reaches a certain limit, typically in nanoscale, the energy spectrum turns to discrete. As a result, the exciton behaves as an atom. This ultimately results in a blue shift in optical illumination [72]. However, in the present study, the band gap increases with increase in the crystallite size. This can be explained on the basis of band bending in nanocrystallities [54]. Surface to volume ratio is very high in case of nanocrystalline materials. This leads to band bending at the grain boundaries. In case of smaller crystallites, band bending will be more at the grain boundaries. For bigger crystallites, this band edge becomes sharp and the band gap energy is higher than that of smaller crystallites. Hence, the band gap value was increased with increasing substrate temperature and decreased with increasing oxygen partial pressure. Similarly the band gap energy calculated for the films deposited at various oxygen partial pressures did not show a significant change, which may be due to insignificant changes in the microstructure, and presence of mixed phases.

Refractive index values of the $Y_2O_3$ film did not show a change with change in the deposition conditions as this property was not significantly affected by the microstructural state of the films. Whereas refractive index of $ZrO_2$ films shows an increasing trend with increase in the substrate temperature and decrease with the oxygen partial pressure. The change in the refractive index as a function of the processing conditions could be related to the change in the microstructure of the films, especially, the crystallite size, porosity and packing density [54,51,52.]. The lower value of the refractive index of the films deposited at higher oxygen partial pressure may be attributed to lower crystallite size and packing density of the films [48,51,57].

Nanohardness and elastic modulus values of $Y_2O_3$ and $ZrO_2$ thin films were found to be lower values than that of the bulk, whereas according to Hall-Petch relationship the hardness should increase with decrease in the crystallite size. However many authors have reported the inverse of Hall-Petch relationship law when crystallite size was decreased to ~20 nm especially for oxides [73,74]. The softening was due to the high volume fraction of interfacial regions that lead to high deformation grain boundary sliding at lower crystallite sizes. Yue et al. [75] have described the effect of phase transformation and nature of stress on the hardness changes. The hardness values show a decrease with decrease in the compressive stress and increase in the tensile stress. The resistances to plastic deformation of $Y_2O_3$ and $ZrO_2$ films was determined from the H3/E2 ratio and were found to be 0.005 GPa and 0.002 GPa, respectively [76]. Chuang et al. [77] also have explained the effect of internal stress on the mechanical properties on thin films. They have observed degradation in mechanical properties with increase in internal stress, in the case of thin films.

### 3.4.2 $Y_2O_3$ /$ZrO_2$ multilayer films

In multilayer structures, the interfaces play a major role in altering the properties like optical [26], ionic conductivity [78], hardness [79] and thermal conductivity [80].

The multilayers of $ZrO_2/Y_2O_3$ were prepared at two different substrate temperatures of 300 K and 873 K and were characterized by XRD. Film deposited at 300 K was found to be X-ray amorphous because both $Y_2O_3$ and $ZrO_2$ formed amorphous structures at 300 K. The films deposited at 873 K were crystalline. The increase in the crystallinity with increase in the substrate temperature was due to the adatomic mobility with increase in substrate temperature [63]. The surface morphology studies by AFM were also in agreement with the XRD results.

The layer thickness was measured by HRTEM and was found to be almost close to those of the thickness obtained from XRR profile. XRR analysis shows higher values of surface roughness at higher substrate temperature as a result of the increase in the crystallinity of the films [81]. However, it must be mentioned that enough care was exercised while fitting the experimental data, since the reflectivity data does not show clear intensity oscillations owing to poor atomic number contrast of the elements of yttrium and zirconium. The XRR profile of the multilayer structure deposited at 873 K is not so clear which may be due to the higher value of surface and interfacial roughness at higher substrate temperature owing to interdiffusion of the layers into each other. The roughness values obtained from the AFM analysis are slightly lower in comparison with the XRR results.

The change in the surface and interfacial roughness show a significant effect on the optical properties. As a result of the higher surface and interfacial roughness, the transmittance for the films deposited at higher substrate temperature was found to decrease [54]. In case of multilayer films deposited at 300 K, the transmittance value of the films with 5 nm of $ZrO_2$ layer thicknesses was relatively lower than that of the multilayer structure with 30 nm $ZrO_2$ layer thickness. As the overall thickness of all the multilayer structures were same for all $ZrO_2$ layer thickness, the number of interface were higher in the case of multilayers with smaller $ZrO_2$ layer thickness more, resulting in the decrease of the transmittance value due to severe scattering at the interfaces. The increase in the band gap values with increase in the $ZrO_2$ layer thickness can be due to the presence of mixed phases. Similar results were also reported by Singh et al [82] for $Gd_2O_3$ thin films.

Enhancement in hardness values for multilayers is generally observed, when the modulation period is decreased to nanometer scale [83]. The important mechanisms for the hardness enhancement are Hall-Petch strengthening [84], modulus difference hardening [85], coherent stress hardening [86], structural barrier hardening [87] and solution strengthing [88]. In the present study, no significant change in hardness values were observed with change in $ZrO_2$ layer thickness, this can be due to the similar elastic modulus of $Y_2O_3$ and $ZrO_2$, as difference in elastic modulus values is an important mechanism to enhance the hardness values [85]. Another reason for insignificant change in the hardness can be interfacial diffusion. Similar results were observerd by Barshilia et al. for TiAlN/TiN multilayer structures where the hardness values were lowered due to the interfacial diffusion [89]. It is noted that the elastic modulus decreased significantly for the $ZrO_2$ layer thickness of 10 nm. The results indicate that the resistance to plastic deformation, which is represented by $H^3/E^2$ [76] is maximum (0.008 GPa) for the $ZrO_2$ layer with thickness 10 nm (Fig. 3.33). Since the quantity $H^3/E^2$ is the measure of toughness, multilayer with 10 nm of $ZrO_2$ layer thickness qualitatively indicates better toughness.

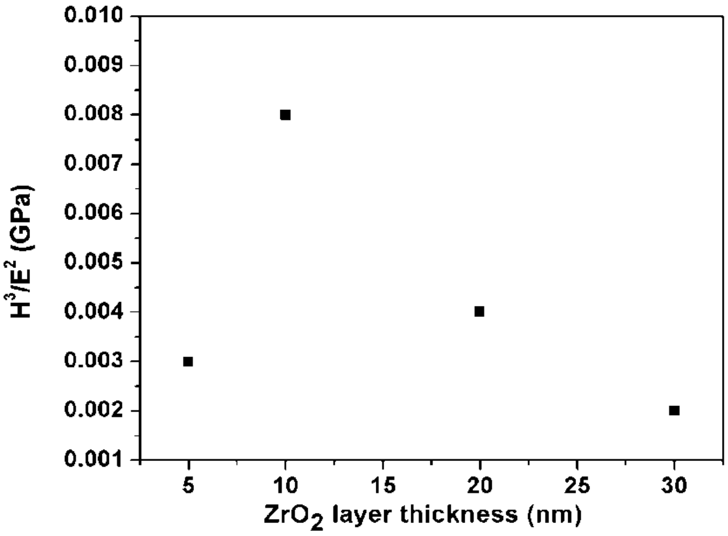

**Fig. 3.34 $H^3/E^2$ values of $ZrO_2/Y_2O_3$ multilayers deposited on Inconel-783 substrates at 873 K and oxygen partial pressure of 2 Pa as a function of $ZrO_2$ layer thickness.**

### 3.5 Conclusions

In the present Chapter, the effect of substrate temperature and oxygen partial pressures on the microstructural and optical properties of the films of $Y_2O_3$ and $ZrO_2$ prepared on Si and quartz substrates were studied. Taking into account the optimized conditions to prepare the best quality films, multilayers structures of $ZrO_2/Y_2O_3$ were prepared on Si, quartz and inconel-783 substrates to study the effect of $ZrO_2$ layer thickness on microstructural, optical and nanomechanical properties of the multilayer films.

### 3.5.1 $Y_2O_3$ thin films:

**(i)** $Y_2O_3$ formed amorphous structure in the temperature range of 300-573 K, crystallization of $Y_2O_3$ was noted at 673 K, and cubic form of $Y_2O_3$ was observed in the temperature range of 673 -873 K. The crystallite size of $Y_2O_3$ was found to increase with the increase in the temperature and decrease with the oxygen partial pressure.

**(ii)** AFM analysis showed an increase in roughness value with increase in the substrate temperature as a result of the increase in the crystallite size.

**(iii)** Highest transmittance value for $Y_2O_3$ films were recorded for the films deposited at 873 K and oxygen partial pressure of 2 Pa, indicating the formation of best quality films at these deposition conditions.

**(iv)** Nanomechanical properties were found to be lower than that of bulk due to low density of the films obtained in the deposition coniditons followed in the present work.

### 3.5.2 $ZrO_2$ thin films:

**(i)** Synthesis of $ZrO_2$ thin films on different substrates were carried out by PLD using a target containing a mixture of monoclinic and tetragonal phases .

**(ii)** Both X-ray and Raman analyses confirmed that tetragonal phase formation was favoured at high substrate temperature and oxygen partial pressure.

**(iii)** XRD analysis showed an increase in the crystallinity with the increase in the substrate temperature. The increase in the crystallinity was also supported by AFM results where an increase in the roughness value was observed with increase in the substrate temperature. The effect of oxygen partial pressure on the crystallite size could not be uniquely brought out as it influenced the stoichiometry and transformation of the phases simultaneously at any substrate temperature.

**(iv)** Except for the films deposited at 473 K and 0.002 Pa, all the films of $ZrO_2$ showed a good transmittance in UV–Vis region. The band gap calculated for $ZrO_2$ films showed an increasing trend with increase in the substrate temperature and decrease with the oxygen partial pressure. Refractive index was also found to increase with increase in the substrate temperature and decrease in the oxygen partial pressure as a consequence of variation in the microstructure of the films.

**(v)** Nanomechanical properties of the film were found to be lower than that of the bulk values due to the presence of mixed phases and films of low density.

### 3.5.3 $ZrO_2/Y_2O_3$ multilayers:

**(i)** Multilayers of $ZrO_2/Y_2O_3$ were prepared on Si, quartz and inconel-783 substrates at two different substrate temperatures of 300 and 873 K, and oxygen partial pressure of 2 Pa. The $ZrO_2$ layer thickness was varied from 5 to 30 nm to study the effect of $ZrO_2$ layer thickness on the optical microstructural and nanomechanical properties.

**(ii)** XRD analysis showed the formation of c-$Y_2O_3$ and m-$ZrO_2$ and t-$ZrO_2$ for the multilayers prepared at 873 K, whereas films deposited at 300 K was found to be X-ray amorphous. The layer thickness of $ZrO_2$ and $Y_2O_3$ measured from HRTEM in agreement with the expected thickness determined from the deposition rate and XRR measurement.

**(iii)** The roughness values obtained from XRR measurements were found to increase with the increase in the substrate temperature from 300 to 873 K, as a result of the increase in the crystallinity.

**(iv)** The transmittance of the multilayer films deposited at higher substrate temperature was found to be lower than that of the films deposited at 300 K. In the case of the films deposited at 300 K, the transmittance of the multilayer structure with 5 nm of $ZrO_2$ layer thickness was lower than that of the films with higher $ZrO_2$ layer thickness, as a consequence of the increased interface scattering.

**(v)** Nanomechanical properties of the multilayer films were measured on Inconel-783 substrates. No significant change in the hardness values were observed as the $ZrO_2$ layer thickness was varied. This may be attributed to the similar elastic modulus values of both $ZrO_2$ and $Y_2O_3$ thin films.

## 3.6 References

1. X. Cheng, Z. Qi, G. Zhang, H. Zhou, W. Zhang, Min Yin, Physica B 404 (2009) 146.
2. S. Zhang, R. Xiao, J. Appl. Phys. 83 (7) (1998) 3842.
3. R. Ivanic, V.R. Ehacek, I. Novotny, V. Breternitz, L. Spiess, Ch. Knedlik, V. Tvarozek, Vacuum 61 (2001) 229.
4. C. H. Ling, J. Bhaskaran, W. K. Choi, L. K. Ah, J. Appl. Phys. 77 (12) (1995) 6350.
5. A. Dimoulas, A. Travlos, G. Vellianitis, N. Boukos, K. Argyropoulos, J. Appl. Phys. 90 (8) (2001) 4224.
6. V. Gourlaouen, G. Schnedecker, A. M. Lejus, M. Boncoeur, R. Collongues, Mater. Res. Bull. 28 (5) (1993) 416.
7. S. Guha, E. Cartier, M. A. Gribelyuk, N. A. Bojarczuk, M. C. Copel, Appl. Phys. Lett. 77 (17) (2000) 2710.
8. C. Durand, C. Dubouedieu, C. Vallee, V. Loup, M. Bonvalot, O. Joubert, H. Roussel, O. Renault, J. Appl. Phys. 96 (3) (2004)1719.
9. S. Zhang, R. Xiao, J. Appl Phys., 83 (7) (1998) 3842.
10. S. A. Barve, Jagannath, M.N. Deo, R. Kishore, A. Biswas, L. M. Gantayet, D. S. Patil, Appl. Surf. Sci. 257 (2010) 215.

11. S. Tekeli, U. Demir, Ceram. Int. 31 (2005) 973.
12. A. K. Shukla, V. Sharma, N. A. Dhas, K.C. Patil, Mater. Sci. Engg. B 40 (1996) 153.
13. A. N. Shengli, T. Zhou, W. U. Weijiang, L. I. U. Qingguo, Solid State Ionics 40/41 (1990) 750.
14. G. Balakrishnan, P. Kuppusami, S. Murugesan, C. Ghosh, R. Divakar, E. Mohandas, D. Sastikumar, Trans IIM 64 (3) (2011) 297.
15. H. C. Barshilia, B. Deepthi, K. S. Rajam, J. Appl. Phys. 104 (2008) 113532.
16. O. Bernard, A.M. Huntz, M. Andrieux, W. Seiler, V. Ji, S. Possonnet, Appl. Surf. Sci. 253 (2007) 4626.
17. Y. Takahashi, T. Kawae, M. Nasu, J. Cryst. Growth 74 (2) (1986) 409.
18. O. R. Mckenzie, D. J. H. Cockyne, M. G. Sceats, P. J. Martin, W. G. Sainty, R. P. Netterfield, J. Mater. Sci. 22 (10) (1987) 3725.
19. H. Sankur, J. Denatale, W. Gunning, J. G. Nelson, J. Vac. Sci. Technol. A 5 (5) (1987) 2869.
20. J. C. Delgado, F. Sanchez, R. Aguiar, Y. Maniette, C. Ferrater, M. Varela, Appl. Phys. Lett. 68 (8) (1996) 1048.
21. F. Hanus, L.D. Laude, Appl. Surf. Sci. 127 (1998) 544.
22. A. Mehner, H. Klumper-Westkamp, F. Hoffmann, P. Mayr, Thin Solid Films 308–309 (1997) 363.
23. Y.M. Gao, P. Wu, R. Kershaw, K. Dwight, A. Wold, Mater. Res. Bull. 25 (1990) 871.
24. I. K. Then, M. Mujahid, B. Zhang, Surf. Coat. Technol. 198 (2005) 104.
25. J. Gottmann, A. Husmann, T. Klotzbucher, E.W. Kreutz, Surf. Coat. Technol. 100–101 (1998) 415.

26. T. Yasuda, S. Ikeda, S. Furukawa, Dyes and Pigments 86 (2010) 278.
27. A. Cavallaro, M. Burriel, J. Roqueta, A. Apostolidis, A. Bernardi, A. Tarancon, R. Srinivasan, S. N. Cook, H. L. Fraser, J. A. Kilner, D. W. McComb, J. Santiso, Solid State Ionics 181 (2010) 592.
28. U. Helmersson, S. Todorova, S. A. Barnett, J-E Sundgren, L. C. Markert, J. E. Greene, J. Appl. Phys. 62 (1987) 481.
29. C. A. Freyman, Yip-Wah Chung, Surf. Coat. Technol. 202(2008) 4702.
30. Z. Jiao, S. Wang, L. Bian, J. Liu, Mater. Res. Bull. 35 (2000) 741.
31. C. Bjormander, Surf. Coat. Technol. 201 (2006) 4032.
32. R. K. Gupta, K. Ghosh, P. K. Kahol, Mater. Lett. 64 (2010) 1487.
33. H. Shinguu, M. M. H. Bhuiyan, T. Ikegami, K. Ebihara, Thin Solid Films 506-507 (2006) 111.
34. P. C. Yashar, S. A. Barnett, L. Hultman, W. D. Sproul, J. Mater. Sci. 14 (1999) 3614.
35. M. Mishra, P. Kuppusami, T. N. Sairam, A. Singh, E. Mohandas, Appl. Surf. Sci. 257 (2011) 7665.
36. Y. Repelin, C. Proust, E. Husson, J. M. Beny, J. Solid State Chem. 118 (1995) 163.
37. S. J. Pearce, G. J. Parker, M. D. B. Charlton, J. S. Wilkinson, J. Vac. Sci. Technol. A 28, (2010) 1388.
38. S. Piscanec, M. Cantoro, A. C. Ferrari, J. A. Zapien, Y. Lifshitz, S. T. Lee, S. Hofmann, J. Robertson, Phys. Rev. B: Condensed Matter 68 (2003) 241312.
39. J. Aarik, A. Aidla, A. A. Kiisler, T. Uustare, V. Sammelselg, Thin Solid Films 340 (1999) 110.
40. Y. Xu, Z. Gu, W. Y. Ching, Phys. Rev. B 56 (23) (1997) 14993.

41. J. W. Haus, Phys. Rev. B (47) (3) (1993)1359.
42. M. Gautier, Jean-Paul Duraud, P. Maire, C. Le Gressus, J. Am. Ceram Soc. 72 (8) (1989) 1562.
43. S. A. Barve, Jagannath, M. N. Deo, R. Kishore, A. Biswas, L. M. Gantayet, D. S. Patil, Appl. Surf. Sci. 257 (2010) 215.
44. M. Mishra, P. Kuppusami, Akash Singh, S. Ramya, V. Sivasubramanian, E. Mohandas, Appl. Surf. Sci. 258 (2012) 5157.
45. J. R. Waterman, D. Farkas,K. Hemker, H. Kung, M. Mayo, R. Mitra, H. Van Swygenhoven, MRS Bull 24 (1992) 44.
46. Galicka-Fau, C. Legros, M. Andrieux, M. Brunet, J. Szade, G. Garry, Appl. Surf. Sci. 255 (2009) 8986.
47. X. M. Fan, J.S. Lian, Z.X. Guo, H.J. Lu, Appl. Surf. Sci. 239 (2005) 176.
48. Y. Shen, S. Shao, H. Yu, Z. Fan, H. He, J. Shao, Appl. Surf. Sci. 254 (2007) 552.
49. A. Sekulic, K. Furic, M. Stubicar, J. Mol. Struct. 410–411 (1997) 275.
50. A.A.M. Ali, K.I. Zaki, Thermichim. Acta 387 (2002) 29.
51. I. D. Wolf, Semicond. Sci. Technol. 11 (1996) 139.
52. G. Balakrishnan, K. Thanigaiarul, P. Sudhakara, Jung Il Song, Appl Phys A, DOI 10.1007/s00339-012-7232-8.
53. G. Balakrishnan, T.N. Sairam, P. Kuppusami, R. Thirumurugasen, E. Mohandas, V. Ganesan, D. Sastikumar, Appl. Surf. Sci. 257 (2011) 8506.
54. D. Beena, K.J. Lethy, R. Vinodkumar, V.P. Mahadevan Pillai, V. Ganesan, D.M. Phase, S.K. Sudheer, Appl. Surf. Sci. 255 (2009) 8334.

55. G. Balakrishnan, S. Tripura Sundari, P. Kuppusami, P. Chandramohan, M.P. Srinivasan, E. Mohandas, V. Ganesan, D. Sastikumar, Thin Solid Films 519 (2011) 2520.
56. P. Mohan Babu, G. Venkata Rao, P. Sreedhara Reddy, S. Uthanna, Mater. Lett. 60 (2006) 274.
57. S. H. Mohamed, H.A. Mohamed, H.A. Abd El Ghani, Physica B 406 (2011) 831.
58. J. F. Shackelford, W. Alexander, CRC Materials Science and Engineering Handbook, CRC Press, Boca Raton, FL, 2001, p. 724.
59. J. F. Shackelford, W. Alexander, "CRC Materials Science and Engineering Handbook", CRC Press, Boca Raton, FL( 2001) 766.
60. G. Zhang, Jane Y. Howe, D. W. Coffey, D. A. Blom, L. F. Allard, J. Cho, Mater. Sci. Engg. C 26 (2006) 1344.
61. I. Zlotnikov, I. Gotman, E.Y. Gutmanas, Appl. Surf. Sci. 255 (2008) 3447.
62. M. Mishra, P. Kuppusami, V. R. Reddy, A. Singh, G. Chinnamma, C. Ghosh, R. Divakar, E. Mohandas, J. Nanosci. Lett. 2013, 3: 4
63. Z. Zhang, Max. G. Lagally, Science 276 (1997) 377.
64. M. Pletea, R. Koch, H. Wendrock, R. Kaltofen, O. G. Schmidt, J. Phys. 21 (2009) 225008.
65. Y. Lee, S. Hu, W. Water, K. Tiong, Z. Feng, Y., J. Huang, J., C. Huang, J. Shen, M. Cheng, J. Luminescence 129 (2009) 148.
66. Z. B. Fang, Z. J. Yan, Y. S. Tan, X. Q. Liu, Y. Y. Wang, Appl. Surf. Sci. 241 (2005) 303.
67. W. Wu, B. Chiou, Appl. Surf. Sci. 68 (1993) 497.
68. V. Srikant, D.R. Clark, J. Appl. Phys. 81 (1997) 6357.

69. S. Dutta, S. Chattopadhyay, M. Sutradhar, A. Sarkar, M. Chakrabarti, D. Sanyal, D. Jana, J. Phys.: Condensed Matter. 19 (2007) 236218.
70. Y.G. Wang, S.P. Lau, H.W. Lee, S.F. YU, S.K. Tay, X.Z. Zang, H.H. Hing, J. Appl. Phys. 94 (2003) 354.
71. K. J. Lethy, D. Beena, R. Vinodkumar, V.P. Mahadevan Pillai, V. Ganesan, V. Sathe, Appl. Surf. Sci. 254 (2008) 2369.
72. K. J. Lethy, D. Beena, R. Vinodkumar, V.P. Mahadevan Pillai, V. Ganesan, V. Sathe, D.M. Phase, Appl. Phys. A 91 (2008) 637.
73. K. Vishwakarma, O.P. Vishwakarma, Int. J. Nanotechnol. Appl. 4 (1) (2010) 13
74. J. Musil, J. Vlcek, Czech J. Phys. B 48 (1998) 10.
75. Y. Sun, Y. Li, M. Teng, Y Wang, X. He, Nanoscience and Nanotechnology Lett. 1 (2009) 140.
76. B. D. Beake, V. M. Vishnyakov, R. Valizadeh, J. S. Colligon, J. Phys. D: Appl. Phys. 39 (2006) 1392.
77. C. T. Chuang, C. K. Rao, R. C. Chang, K. Y. Chu, J. Mater. Process. Technol. 201 (2008) 770.
78. E. Fabbri, D. Pergolesi, E. Traversa, Sci. Technol. Adv. Mater. 11 (2010)054503.
79. C. A. Freyman, Yip-Wah Chung, Surf. Coat. Technol. 202 (2008)4702.
80. J. R. Nicholls, K. j. Lawson, A. Johnstone, D. S. Rickerby, Surf. Coat. Technol.151-152 (2002) 383.
81. I. Kojima, B. Li, The Rigaku J. 16 (1999) 31.
82. M. P. Singh, S. A. Shivashankar, J. Cry. Growth 276 (2005) 148.
83. B. C. Kang, H. Y. Kim, Oh Y. Kwon, S. H. Hong, Scripta Materialia 57 (2007) 703.

84. R. C. Cammarata, T. E. Schlesinger, C. Kim, S. B. Qadri, A. S. Edelstein, Appl. Phys. Lett. **56** (1990) 1862.
85. X. Chu and S. A. Barnett, J. Appl. Phys. **77** (1995) 4403.
86. M. Shinn, L. Hultman, and S. A. Barnett, J. Mater. Res. **7** (1992) 901.
87. B. J. Daniels, W. D. Nix, and B. M. Clemens, Mater. Res. Soc. Symp. Proc. 343, (1994)549.
88. C. Kim, S. B. Qadri, M. R. Scanlon, and R. C. Cammarata, Thin Solid Films 240 (1994) 52.
89. H. C. Barshilia, K. S. Rajan, J. Appl. Phys. 98 (2005) 014311.

# Chapter 4

# $CeO_2$ and $Gd_2O_3$ Thin Films and $CeO_2/Gd_2O_3$ Multilayer Thin Films: Synthesis and Properties

## 4.1 Introduction

Cerium oxide ($CeO_2$) is a rare earth oxide having wide range of applications as an optical wave guide [1], oxygen sensor [2], buffer layer for YBCO thin film deposition on Ni alloy [3], electrochromic devices [4] and catalyst [5,6]. Thin films of $CeO_2$ have been prepared by different techniques such as sputtering [6,7], Spray pyrolysis [8], atomic layer deposition [9], MOCVD [10], flash evaporation [11] and pulsed laser deposition [12] to study the microstructural [12], optical [1] and electrical [2] properties.

Gadolinium oxide ($Gd_2O_3$) is another transition metal oxide used as protective coating [13], optical coating [14] and dielectric material in CMOS [15,16] as well as in device applications [17]. $Gd_2O_3$ thin films were deposited by various techniques such as electrolytic deposition [18], molecular beam epitaxy [16], sputtering [19], electron beam evaporation [20], sol gel [21], atomic layer deposition [22], and pulsed laser deposition method [23].

Although single layer films have wide range of application in different fields, but there are some applications where a single layer film's property is not sufficient and this leads to development of multilayer structures to combine the properties of materials for specific applications. Multilayers of $Al_2O_3/ZrO_2$ [24], $TiO_2/WO_3$ [25], and $ZrO_2/Y_2O_3$ [24] were already deposited by sputtering technique to study the microstructural and nanomechanical properties. Multilayer of $CeO_2/Gd_2O_3$ was prepared by sputtering technique by Burinskas et al. [26] to prepare a solid electrolyte by solid state sintering of the multilayers.

In the present Chapter, $CeO_2/Gd_2O_3$ multilayers were prepared on Si(100), quartz and inconel-783 substrates at 300 and 873 K substrate temperature and oxygen partial pressure of 2 Pa, with different $CeO_2$ layer thickness keeping $Gd_2O_3$ layer thickness constant to analyze the effect of the $CeO_2$ layer thickness on optical and nanomechanical properties of the multilayers.

## 4.2 Experimental Procedure

Two different targets of $CeO_2$ and $Gd_2O_3$ were prepared from commercial grade $CeO_2$ and $Gd_2O_3$ powders in order to use them for the synthesis of thin films and multilayers.

Using these two targets, films of $CeO_2$ and $Gd_2O_3$ were prepared on Si (100) and quartz substrates at different substrate temperatures and oxygen partial pressures to study the effect of process parameters on properties of both $CeO_2$ and $Gd_2O_3$ films. The details of the experimental parameters were listed in Table 4.1. The microstructural properties of the films were determined by techniques such as X-ray diffraction, Raman spectroscopy, AFM and UV-Visible spectrophotometer. Hardness and elastic modulus of the $Gd_2O_3$ and $CeO_2$ films deposited at 873 K and oxygen partial pressure of 2 Pa were measured using the nanoindentation technique. The details of the target sintering conditions and characterization were explained in Chapter 2.

Multilayers of $CeO_2/Gd_2O_3$ were prepared at oxygen partial pressure of 2 Pa and at substrate temperature of 300 K and 873 K. The choice of oxygen partial pressure of 2 Pa was based on the experiments carried out for $CeO_2$ and $Gd_2O_3$ as a function of Oxygen partial pressure. The $CeO_2$ layer thickness was varied from 5 to 30 nm and $Gd_2O_3$ layer thickness was kept constant (10 nm). The total thickness of the multilayers was kept constant by varying the number of bilayers for each multilayer. The numbers of bilayers deposited for each multilayer were 3, 4, 6 and 8 for $CeO_2$ layer thicknesses 30, 20, 10 and 5 nm. Taking into account the deposition rates of $CeO_2$ and $Gd_2O_3$ i.e. 6 nm/min and 14 nm /min, respectively, the desired layer thicknesses in the multilayers were made by adjusting the time of deposition for each layer. The multilayer structures were characterized by XRD, AFM, XRR and HRTEM. The optical properties of the films were measured by a UV–Visible spectrophotometer in the wavelength range of 200-900 nm. Nanohardness and elastic modulus values were measured using nanoindentation technique, to study the effect of layer thickness on the nanomechanical properties of multilayers.

**Table 4.1 Details of deposition conditions for $CeO_2$ and $Gd_2O_3$ thin film preparation**

| **Parameters** | **$CeO_2$** | **$Gd_2O_3$** |
|---|---|---|
| Target size | 20 mm diameter and 3mm thickness | 20 mm diameter and 3mm thickness |
| Sintering condition | 1673 K for 6 h | 1823 K for 4 h |
| Sintered density | ~ 95 % | ~95 % |
| Laser Energy | 300 mJ/pulse | 300 mJ/pulse |
| Repetition rate | 10 Hz | 10 Hz |
| Substrate | Si (100), quartz, Inconel-783 | Si (100), Quartz, Inconel-783 |
| Oxygen partial pressure | 2- 0.002 Pa | 2-0.002 Pa |
| Substrate Temperature | 300- 873 K | 300-873 K |
| Deposition time | 1 h | 1 h |

**Table 4.2 Details of experimental conditions for the deposition of multilayers of $CeO_2/Gd_2O_3$.**

| **Parameters** | **Details** |
|---|---|
| Targets | $Gd_2O_3$ and $CeO_2$ |
| Laser Energy | 300 mJ/pulse |
| Repetition rate | 10 Hz |
| Substrate | Si (100), Quartz, Inconel-783 |
| Oxygen partial pressure | 2 Pa |
| Substrate temperatures | 300 K, 873 K |
| Deposition rates | $CeO_2$ (~6 nm/min) and $Gd_2O_3$ (~14 nm/min) |
| $(CeO_2/Gd_2O_3)_{\text{(number of bilayers)}}$ layer thickness in nm | $(5/10)_8$, $(10/10)_6$, $(20/10)_4$, $(30/10)_3$ |

## 4.3 Results and Discussion

### 4.3.1 Results of $CeO_2$ thin films

The present section includes the deposition of $CeO_2$ films on Si (100), quartz and inconel-783 substrates in order to study the effect of process parameters on microstructural, optical and nanomechanical properties.

#### 4.3.1.1 XRD analysis

Figure 4.1 shows the X-ray diffractogram of $CeO_2$ films deposited at different substrate temperatures in the temperature range 300 K - 873 K at the oxygen partial pressure of 2 Pa. The XRD pattern shows the peaks from (111), (200), (220), (311), (331) and (420) reflections corresponding to the cubic $CeO_2$ even at room temperature. The crystallinity increases with the increase in substrate temperatures from 300 to 873 K. The films deposited at 300 K shows preferred orientation for (111) reflection. With the increase in substrate temperature the preferred orientation changes from (111) to (200). Similar observations were also observed by Narasima Rao et al. [27] and Balakrishnan et al. [28] for $CeO_2$ films deposited by electron beam evaporation. The crystallite size was calculated using Scherrer formula and is found to be 38 nm and 44 nm for (200) peak for the substrate temperatures of 773 and 873 K. The crystallite size for the films deposited at 300 K and 573 K were not calculated due to the absence and or weak reflection of (200).

XRD analyses of the $CeO_2$ films deposited at different oxygen partial pressures and at the substrate temperature of 873 K were carried out (Fig. 4.2). The XRD pattern shows the formation of a polycrystalline film at all oxygen partial pressure conditions containing peaks from (111), (200), (220), (311), (400), (331), (420) and (422) lattice planes. With the increase in the oxygen

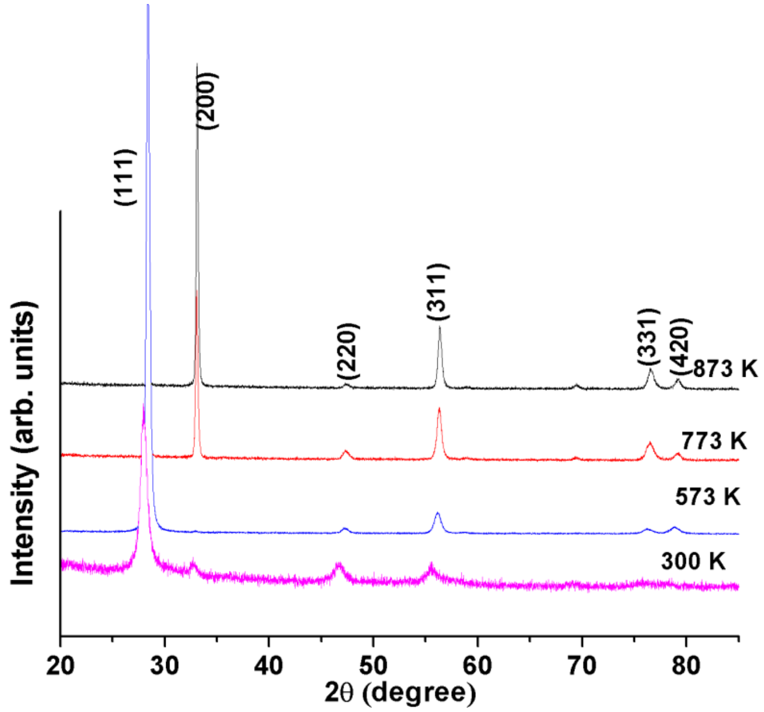

**Fig. 4.1 XRD patterns of $CeO_2$ thin films deposited on Si (100) substrates at various substrate temperatures and oxygen partial pressure of 2 Pa.**

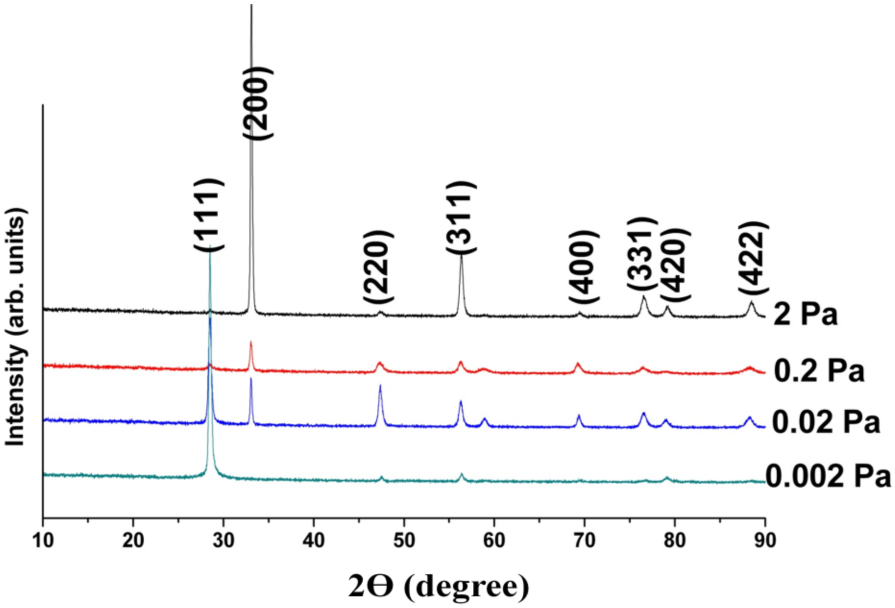

**Fig. 4.2 XRD patterns of $CeO_2$ thin films grown on Si (100) substrates under various oxygen partial pressures and substrate temperature of 873 K.**

**Table 4.3 Microstructural and optical properties of $CeO_2$ films as a function of substrate temperature**

| Substrate temperature (K) | Crystallite Size (± 2 nm), (200) plane | Latice parameter (±0.003 Å) | Roughness (±0.1 nm) | Band Gap (± 0.01eV) |
|---|---|---|---|---|
| **300** | - | 5.018 | 2.1 | 3.50 |
| **573** | - | 5.218 | 3.0 | 3.53 |
| **773** | 38 | 5.414 | 3.2 | 3.54 |
| **873** | 44 | 5.429 | 3.9 | 3.42 |

**Table 4.4 Microstructural and optical properties of $CeO_2$ films as a function of oxygen partial pressure**

| Oxygen partial pressure (Pa) | Crystallite Size ( ± 2 nm), (200) plane | Lattice parameter ( ±0.003Å) | Roughness (±0.1nm) | Band Gap (± 0.01eV) |
|---|---|---|---|---|
| **2** | 44 | 5.429 | 3.9 | 3.42 |
| **0.2** | 39 | 5.422 | 2.5 | 3.52 |
| **0.02** | 38 | 5.419 | 2.0 | 3.49 |
| **0.002** | - | 5.409 | 1.7 | 3.56 |

partial pressure the preferred orientation changes from (111) to (200) reflection. The crystallite size, calculated for the (200) reflection varies from 38 nm to 44 nm. Similar results were also observed by Balakrishnan et al. [28] for $CeO_2$ film deposited by pulsed laser deposition technique.

### 4.3.1.2 Raman analysis

Fig. 4.3 shows a typical Raman spectrum of $CeO_2$ film deposited on Si (100) substrates at 873 K and oxygen partial pressure of 2 Pa. The Raman spectrum shows a peak at 464 $cm^{-1}$ corresponding to $F_{2g}$ Raman active mode. Similar results were also reported by Balakrishnan et al. [28]. The peak at 464 $cm^{-1}$ corresponds to the symmetrical stretching vibrational mode of Ce-O bond [29,30]. The higher intensity and low FWHM indicates the formation of a highly crystalline film in this particular substrate temperature and oxygen partial pressure condition. In addition to the peak at 464 $cm^{-1}$, another peak at 305 $cm^{-1}$ of very weak intensity is also observed, in accordance with the results reported by Shengyue et al. [31] for $CeO_2$ thin films of very small crystallite size.

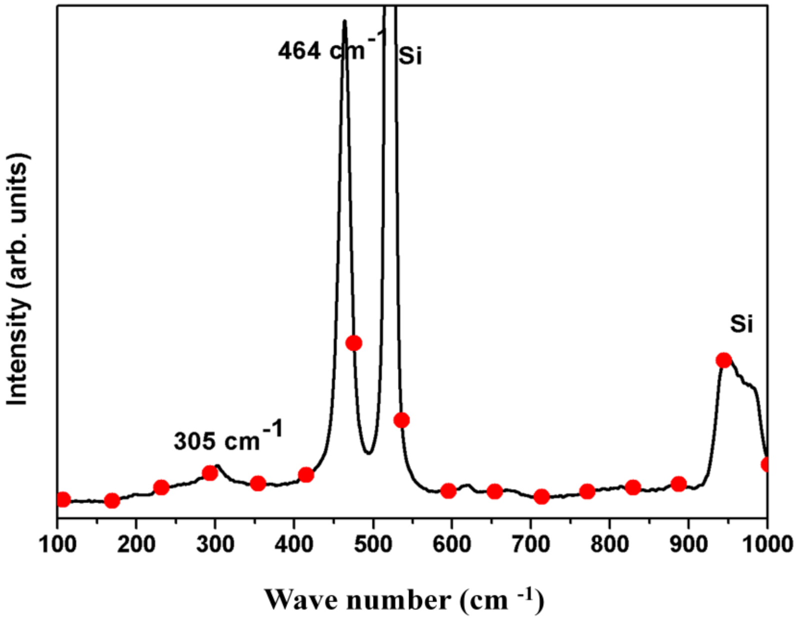

**Fig. 4.3 A typical Raman spectrum of $CeO_2$ film deposited on Si (100) substrate at 873 K and oxygen partial pressure of 2 Pa.**

### 4.3.1.3 Surface morphology study by AFM.

Figure 4.4 shows the AFM images of $CeO_2$ films deposited at different substrate temperature and the oxygen partial pressure of 2 Pa. The AFM image of the film at 300 K shows fine grains indicating a crystalline film even at 300 K. The surface roughness values obtained from the AFM analysis increases from 2.1 to 3.9 nm with increase in the substrate temperature from 300 to 873 K.

The surface morphology of the $CeO_2$ films deposited under various oxygen partial pressure conditions and the substrate temperature of 873 K were studied by AFM analysis (Fig. 4.5). The crystallinity of the films increases with the increase in oxygen partial pressure and the

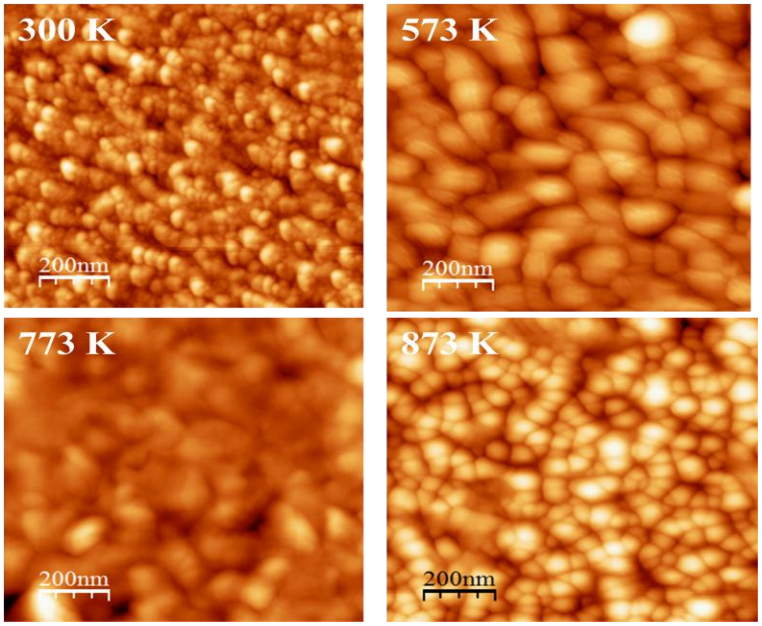

**Fig. 4.4 Surface morphology of $CeO_2$ films grown on Si (100) substrates at various substrate temperatures and oxygen partial pressure of 2 Pa.**

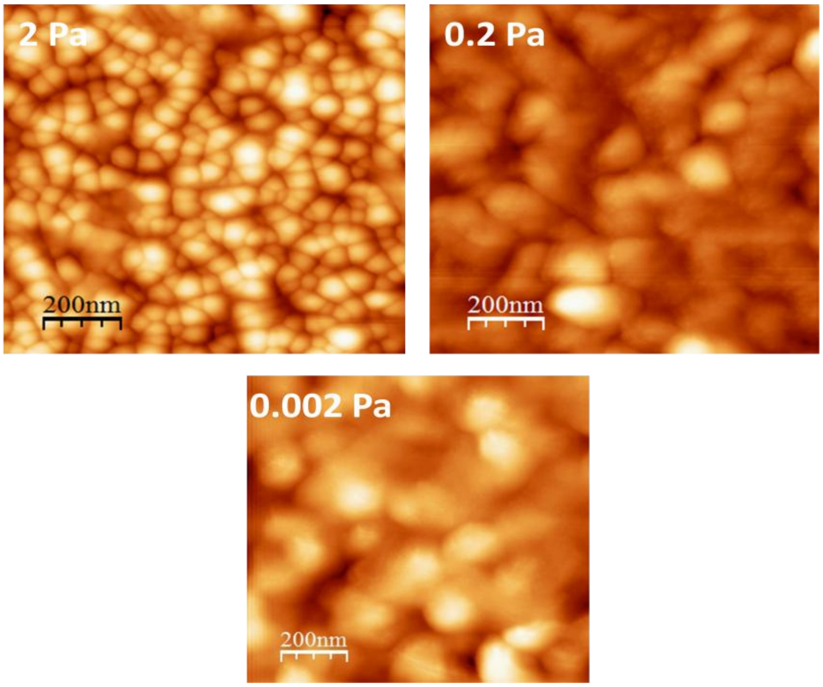

**Fig. 4.5 AFM images of $CeO_2$ films grown under various oxygen partial pressures and substrate temperature of 873 K.**

roughness values determined from the AFM image analysis are found to increase from 1.7 to 3.9 nm with the increase in oxygen partial pressure from 0.002 to 2 Pa due to the increase in the crystallinity. The trend found in the present study on roughness values are in accordance with the results reported by Bueno et al. [32] and Balakrishnan et al. [28].

#### 4.3.1.4 TEM analysis

Figure 4.6 shows the TEM image of $CeO_2$ films grown on Si substrates at 873 K and oxygen partial pressure of 2 Pa. The SAD pattern obtained from the $CeO_2$ film shows the formation of polycrystalline film with reflections from (220, (400), (422), (440) and (620) planes. The presence of ring pattern indicates the polycrystalline nature of the film with relatively smaller crystallites. Figure 4.6 (b) shows the low magnification bright field image of $CeO_2$ crystallites and the crystallite size obtained are in the range of 5-7 nm.

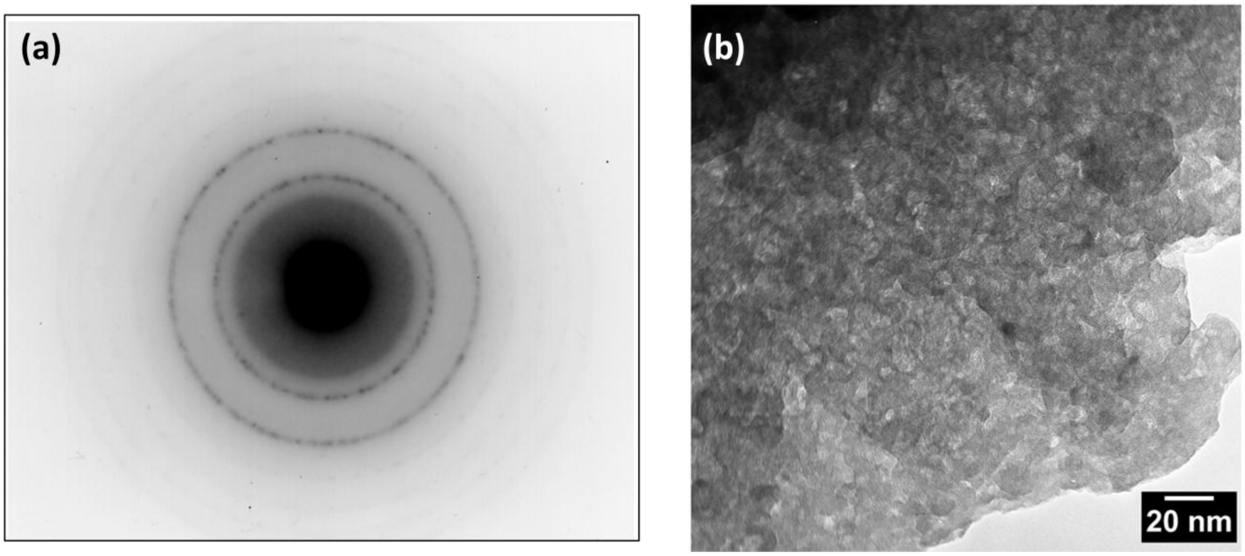

**Fig. 4.6 TEM images of $CeO_2$ films deposited on Si substrate at substrate temperature of 873 K and oxygen partial pressure of 0.2 Pa. (a) SAD pattern (b) low magnification bright field image showing the $CeO_2$ crystallites.**

### 4.3.1.5 Optical property measurements

The optical properties of the $CeO_2$ films were measured using a UV-Visible spectrophotometer in transmission mode. The absorbance and transmittance curves of $CeO_2$ films deposited at different substrate temperature are shown in Fig. 4.7 (a) and (b), respectively. The films show a strong absorbance near wavelength of ~355 nm. The absorption edge of the film deposited at 873 K is found towards higher wavelength, indicating a decrease in the band gap. The transmission curves of $CeO_2$ films grown at various substrate temperature shows a transmittance value of 60- 90 %.

Figure 4.8 (a) and (b) shows the absorbance and transmittance spectra of $CeO_2$ film deposited at various oxygen partial pressure conditions. The films show a strong absorbance at wavelength of 350-355 nm. All the films of $CeO_2$ show a transmittance of 60–90 % for the films grown under various oxygen partial pressure conditions.

The band gap values were determined from Tauc plot. The details of the band gap measurement procedures were already explained in Chapter 2. The band gap values of the $CeO_2$ films deposited at different substrate temperatures varied from 3.42 to 3.54 eV in the temperature range 300 K - 873 K. Also the band gap values of the $CeO_2$ films varied o from 3.42 to 3.56 with decrease in oxygen partial pressure. The refractive index values calculated for the film deposited under various substrate temperatures and oxygen partial pressures were found to vary from 1.92 to 2.01 and 1.90 to 2.0, respectively [27,32].

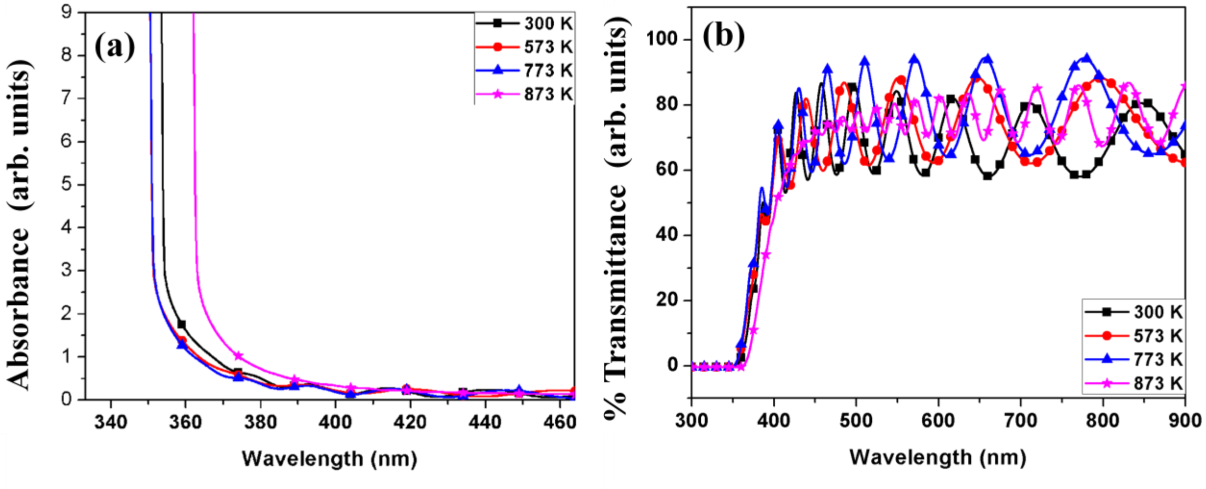

**Fig. 4.7 Variation of (a) absorbance and (b) transmittance versus wavelength plot of $CeO_2$ films deposited on quartz substrates at different substrate temperatures and oxygen partial pressure of 2 Pa.**

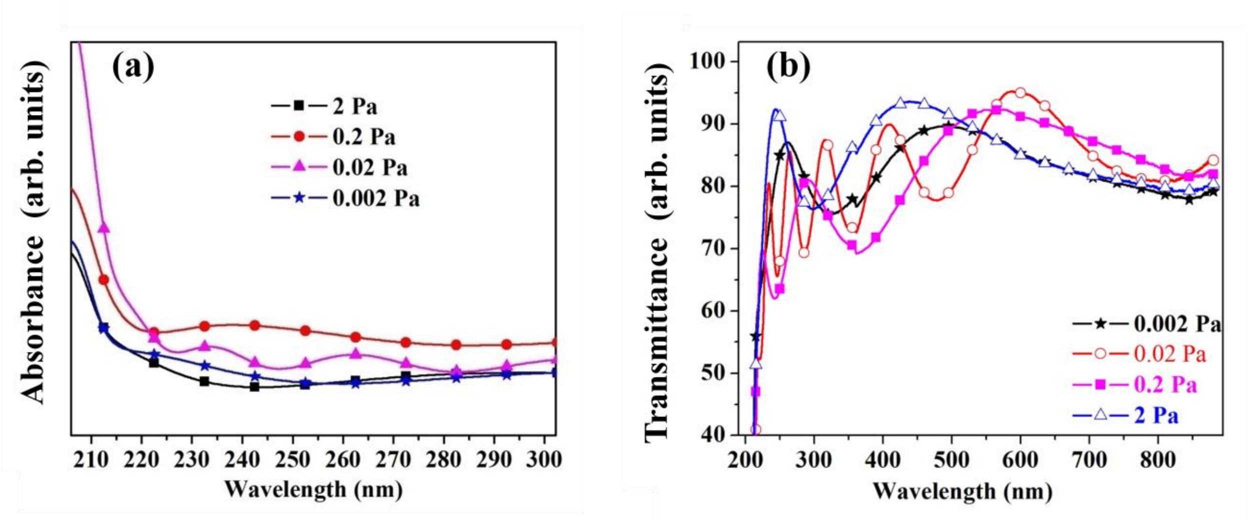

**Fig.4.8 Variation of (a) Absorbance and (b) Transmittance values of $CeO_2$ films deposited on quartz substrates as a function of oxygen partial pressures and substrate temperature of 873 K.**

### 4.3.1.6 Nanomechanical properties

The hardness and the elastic modulus values were measured from the nanoindentation technique. Fig. 4.9 shows the load versus displacement curve for the $CeO_2$ film deposited at the substrate temperature of 873 K and oxygen partial pressure of 2 Pa. The hardness and the elastic modulus values obtained from the nanoindentation test are 5.4 ± 0.6 GPa and 274± 25 GPa, respectively. The hardness value obtained is comparable with the values reported by Mogens et al. (5-6 GPa for the bulk $CeO_2$ ) [33].. Whereas the elastic modulus values are higher than that of the value reported for bulk (181 GPa) in the literature [34]. The hardness values reported in the present study are much higher in comparison to the hardness values reported by Roa et al. [35] i. e. 2.25 GPa for $CeO_2$ thin films. The lower value of hardness reported by Roa et al. [35] has been related to the formation of cracks and stress present in the films.

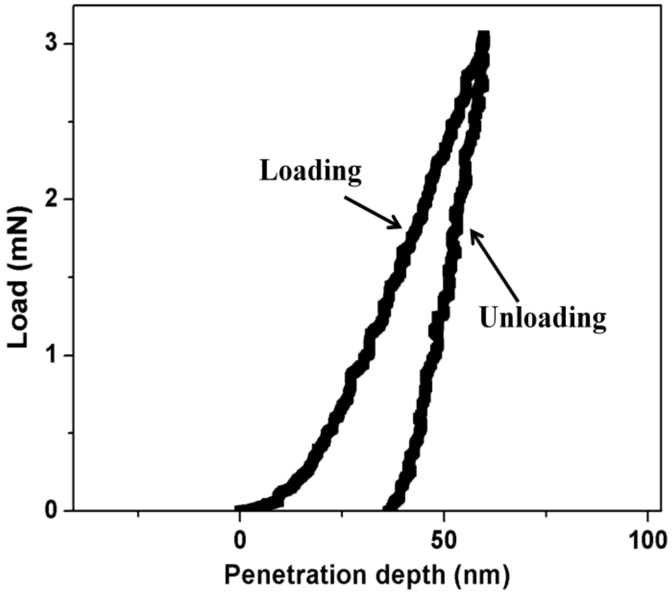

**Fig. 4.9 The load versus displacement curve of $CeO_2$ thin film deposited at substrate temperature of 873 K and oxygen partial pressure of 0.2 Pa.**

### 4.3.2 $Gd_2O_3$ thin films: Microstructural, optical and nanomechanical properties

$Gd_2O_3$ films were prepared on Si (100), quartz and Inconel-783 substrates at different substrates temperatures (300 -873 K) and oxygen partial pressures (0.002-2 Pa) to study the effect of these parameters on the microstructural, optical and nanomechanical properties.

#### 4.3.2.1 XRD analysis

$Gd_2O_3$ films were prepared on Si (100) substrates at different substrate temperatures and oxygen partial pressure of 0.2 Pa. XRD analysis was carried out for the films grown under various substrate temperatures and the XRD patterns are shown in Fig. 4.10. The XRD pattern shows the formation of an amorphous structure at 300 K. The crystallization of $Gd_2O_3$ film starts at 473 K. For the substrate temperatures 473 and 573 K, the films show mainly a polycrystalline monoclinic (m) $Gd_2O_3$ showing peaks for $(\bar{4}01)$, (401), $(\bar{4}02)$, (003), $(\bar{2}03)$, $(\bar{6}01)$, $(\bar{5}11)$, (313), $(\bar{6}02)$, $(\bar{4}04)$, (022), (421), $(\bar{8}04)$, (623) and (714) planes with small volume fraction of cubic phase characterized by the presence of (123), (422) and (444) reflections. The intensity of the (003) peak is highest for the film deposited at 573 K. As the substrate temperature ≥ 673 K only m-$Gd_2O_3$ is observed. The crystallite size was calculated using (003) reflection is found to vary from 19 to 26 nm. The lattice parameter values were also calculated using “unitcell program” for m-$Gd_2O_3$ and listed in Table 4.5. The lattice parameters *a*, *b* and *c*-axis of m-$Gd_2O_3$ is found to vary from 14.073-14.111 Å, 3.576-3.581 Å and 8.770 -8.792 Å, respectively.

Figure 4.11 shows the XRD pattern of $Gd_2O_3$ films deposited on the Si substrates at different oxygen partial pressures and the substrate temperature of 873K. The films

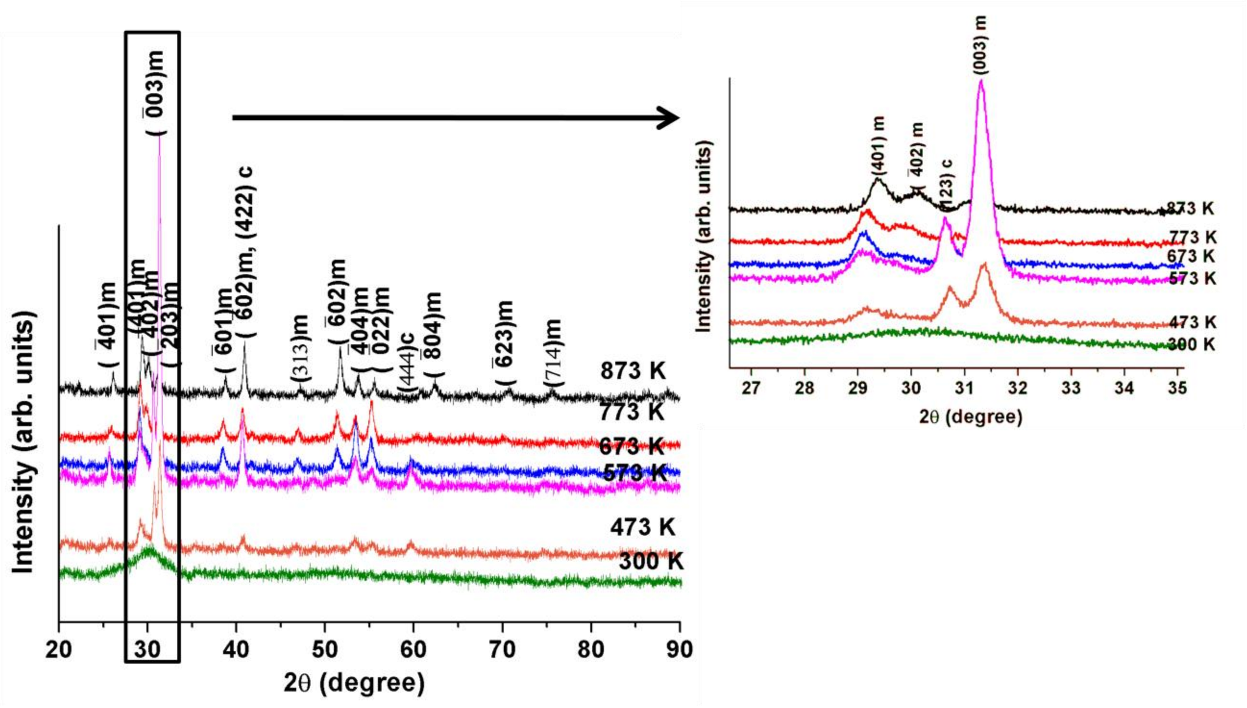

**Fig. 4.10 XRD pattern of $Gd_2O_3$ thin films deposited on Si (100) substrates at different substrate temperatures and oxygen partial pressure of 0.2 Pa.**

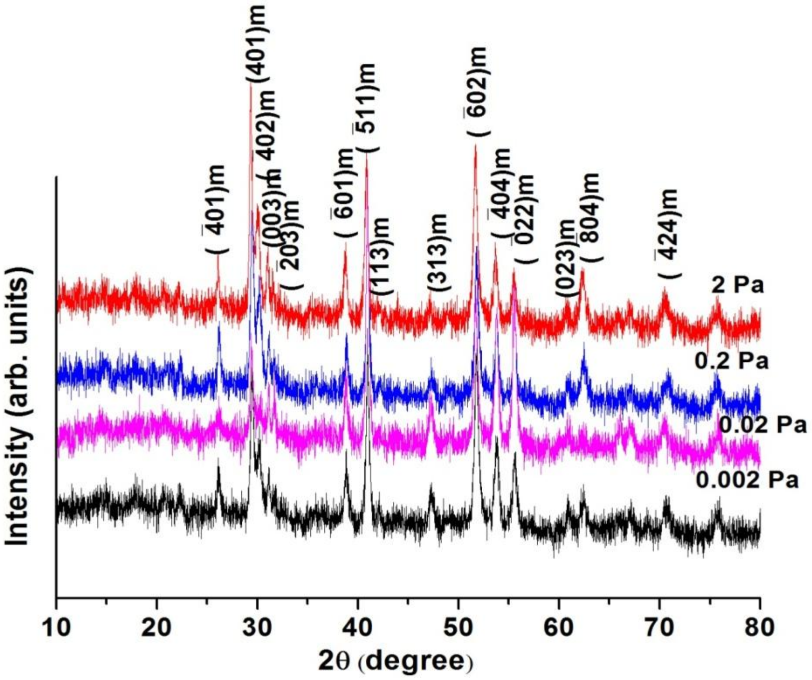

**Fig. 4.11 XRD pattern of $Gd_2O_3$ thin films deposited on Si (100) substrates at different oxygen partial pressures and substrate temperature of 873 K.**

show polycrystalline phase pure m-$Gd_2O_3$ structure showing peaks of $(\bar{4}01)$, (401), $(\bar{4}02)$, (003),$(\bar{2}03)$, $(\bar{6}01)$, $(\bar{5}11)$, (113), (313), $(\bar{6}02)$, $(\bar{4}04)$, (022), (023, $(\bar{8}04)$ and $(\bar{4}24)$. All the films deposited under various oxygen partial pressure conditions show preferred orientation for the (401) reflection. Crystallite size calculated for this particular plane is found to vary from 21to 26 nm at various oxygen partial pressures. The lattice parameters *a*, *b* and *c* of $Gd_2O_3$ films deposited under various oxygen partial pressures are found to vary from 14.111-14.137 Å, 3.586-3.581 Å and 8.764- 8.770 Å, respectively. These values along with the error bars are listed in Table 4.6.

**Table 4.5 Microstructural and optical properties of $Gd_2O_3$ at different substrate temperatures.**

| **Substrate temperature (K)** | **Crystallite Size (± 2 nm )** | **Latice parameter (Å) (±0.003)** | | | **Roughness (nm)** | **Band Gap (eV) (± 0.01)** |
|---|---|---|---|---|---|---|
| | | ***a*** | ***b*** | ***c*** | | |
| 300 | - | - | - | - | 0.4 | 5.76 |
| 573 | 8 | - | - | - | 1.6 | 5.72 |
| 673 | 21 | 14.063 | 3.576 | 8.770 | - | 5.70 |
| 773 | 23 | 14.073 | 3.579 | 8.784 | 2.1 | 5.75 |
| 873 | 29 | 14.111 | 3.581 | 8.792 | 1.0 | 5.80 |

**Table 4.6 Microstructural and optical properties of $Gd_2O_3$ at different oxygen partial pressures.**

| **Oxygen Partial Pressure (Pa)** | **Crystallite Size (± 2 nm )** | **Latice parameter (Å) (±0.003)** | | | **Roughness (nm)** | **Band Gap (eV) (± 0.01)** |
|---|---|---|---|---|---|---|
| | | **a-axis** | **b-axis** | **c-axis** | | |
| 2 | 24 | 14.137 | 3.586 | 8.773 | 1.1 | 5.60 |
| 0.2 | 29 | 14.111 | 3.581 | 8.792 | 1.6 | 5.80 |
| 0.02 | 21 | 14.125 | 3.585 | 8.764 | - | 5.68 |
| 0.002 | 22 | 14.121 | 3.583 | 8.767 | 0.8 | 5.70 |

### 4.3.2.2 Raman analysis

The microstructures of the $Gd_2O_3$ films were also analyzed by Raman spectroscopy and are shown in Fig. 4.12 and 4.13 for the films deposited at different substrate temperature and oxygen partial pressures, respectively.

Figure 4.12 shows Raman peaks at 92 $cm^{-1}$, 103 $cm^{-1}$, 253 $cm^{-1}$, 266 $cm^{-1}$, 413 $cm^{-1}$, 422 $cm^{-1}$ and 433 $cm^{-1}$ of m-$Gd_2O_3$ in comparison to the Raman peaks assigned for m-$Gd_2O_3$ by Zarembowitch et al. [36] and Paul et al. [37]. All the peaks show a shift of ~3-5 $cm^{-1}$ towards lower wave number side, from the value reported by the authors, indicating the presence of stress in the films. Except the peaks for m-$Gd_2O_3$, a small broad peak is observed at 140 $cm^{-1}$ corresponding to cubic phase of $Gd_2O_3$ [38]. The strongest line for the cubic phase was not observed due to the overlapping of the peak with Si peak. The FWHM of the peaks decreases with increase in the substrate temperature in accordance with x-ray analysis.

Raman spectra of the $Gd_2O_3$ films deposited under various oxygen atmosphere conditions are shown in Fig. 4.13. The Raman spectra contains peaks at 92 $cm^{-1}$, 103 $cm^{-1}$, 173 $cm^{-1}$, 253 $cm^{-1}$, 266 $cm^{-1}$, 383 $cm^{-1}$, 417 $cm^{-1}$and 433 $cm^{-1}$ belonging to m-$Gd_2O_3$. The FWHM of the peaks do not show a significant variation although the intensity of the peaks at 417 $cm^{-1}$ and 433 $cm^{-1}$ show highest intensity for the oxygen partial pressure of 0.2 Pa.

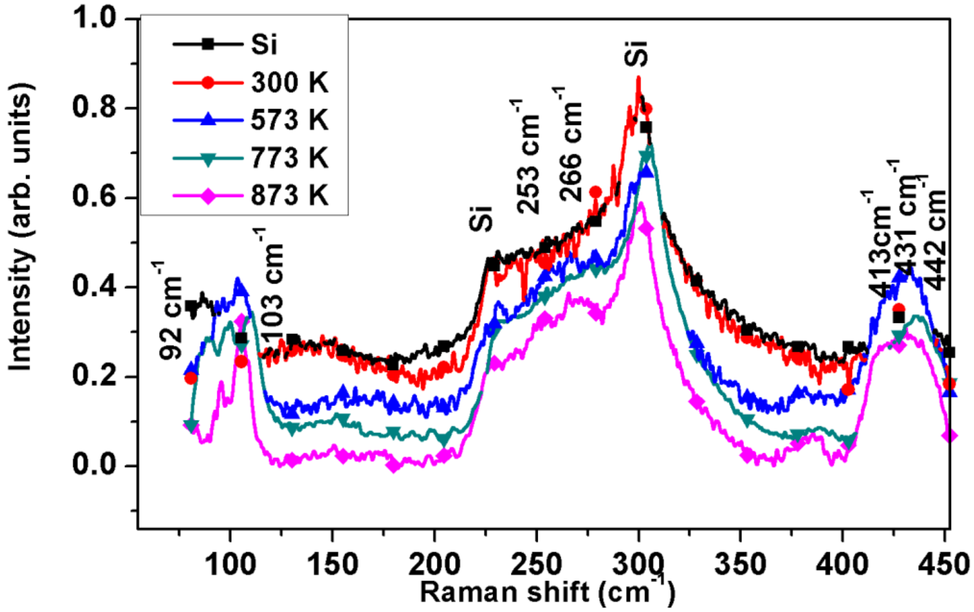

**Fig. 4.12 Raman spectra of $Gd_2O_3$ films deposited on Si (100) substrates at different substrate temperatures and oxygen partial pressure of 0.2 Pa.**

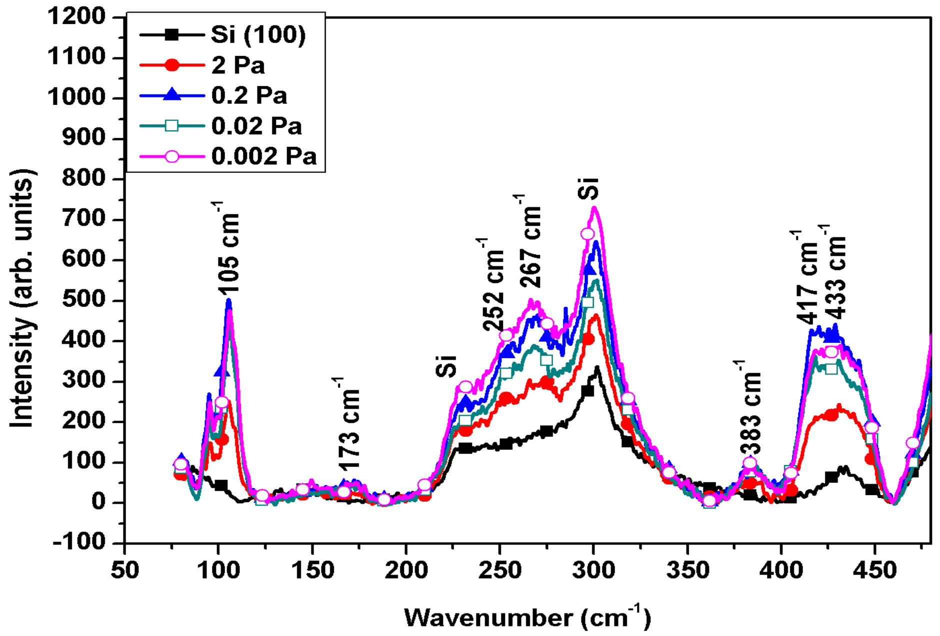

**Fig. 4.13 Raman analysis of $Gd_2O_3$ films deposited at different oxygen partial pressures and substrate temperature of 873 K.**

### 4.3.2.3 AFM analysis

The surface morphology of the $Gd_2O_3$ films, deposited on Si (100) substrates, under various process parameter conditions were studied by AFM image analysis. Figure 4.14 shows the AFM images of $Gd_2O_3$ films grown at various substrate temperatures and the oxygen partial pressure of 0.2 Pa. The microstructure reveals fine globular particles of $Gd_2O_3$ in the film depsoited at 300 K, while the film reveals increase in particle size with increasing substrate temperature. The AFM image of the $Gd_2O_3$ film deposited at 300 K show smooth surface with roughness value 0.4 nm, indicating formation of amorphous $Gd_2O_3$ at 300 K. The roughness values obtained for the films increased from 0.4- 2.0 nm with an increase in the temperature from 300 to 873 K [39,40].

Figure 4.15 show the AFM images of $Gd_2O_3$ films deposited under various oxygen partial pressure conditions and at constant substrate temperature of 873 K. The AFM images show formation of crystalline film at any oxygen partial pressure but no significant changes in the surface morphlogy. Therefore , the roughness values obtained for the films deposited at various oxygen partial pressure condition vary slightly within the range of 0.8 to 1 nm. Both the Fig. 4.14 and 4.15 indicate that substrate temperature has an increased role compared to that of the oxygen partial pressure in influencing crystallite size.

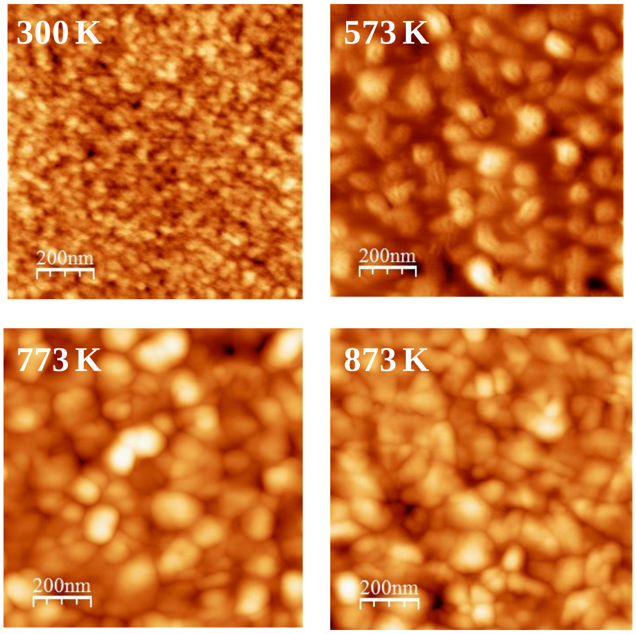

**Fig. 4.14 Study of surface morphology of $Gd_2O_3$ films deposited at oxygen partial pressure of 2 Pa as a function of different substrate temperatures.**

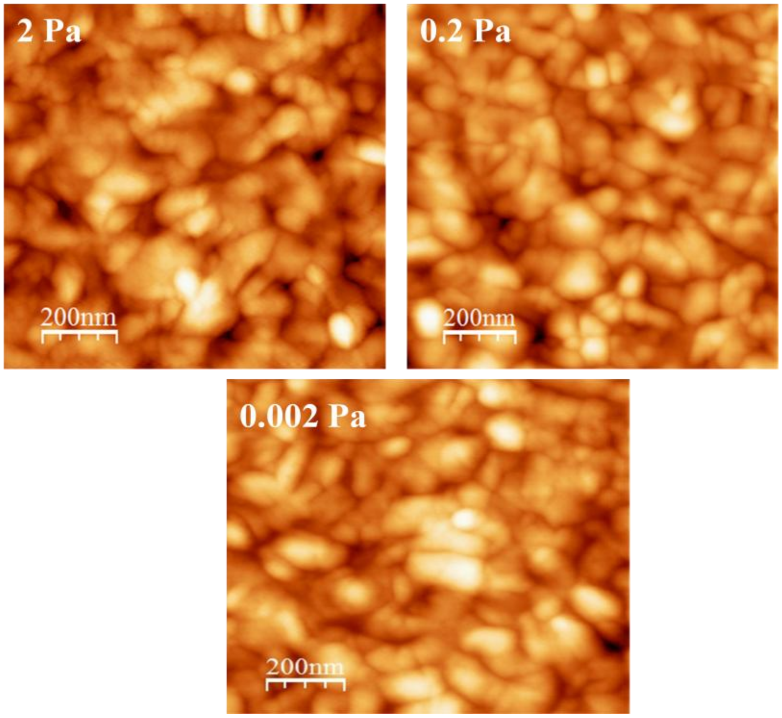

**Fig. 4.15 AFM analysis of $Gd_2O_3$ films deposited at various oxygen partial pressure and substrate temperature of 873 K.**

#### 4.3.2.4 TEM analysis

Microstructural analysis of the $Gd_2O_3$ film deposited at 873 K and oxygen partial pressure of 0.2 Pa was also carried out by TEM (Fig. 4.16) and the corresponding SAD pattern is shown in Fig 4.19 (a). The SAD pattern shows spotty ring patterns, indicating a polycrystalline nature with large crystallite sizes with reflections from $(\bar{2}01)$, (201), (002), (202), $(\bar{4}01)$, $(\bar{4}02)$, $(\bar{1}12)$, $(\bar{1}13)$, $(\bar{6}02)$ and (313) planes. The d-spacings obtained from the SAD pattern are in accordance with the XRD results.

Figure 4.16 (b) shows a bright field image of $Gd_2O_3$ film deposited on Si substrate. The crystallite size measured from the TEM images are found to be within the range of 60-80 nm.

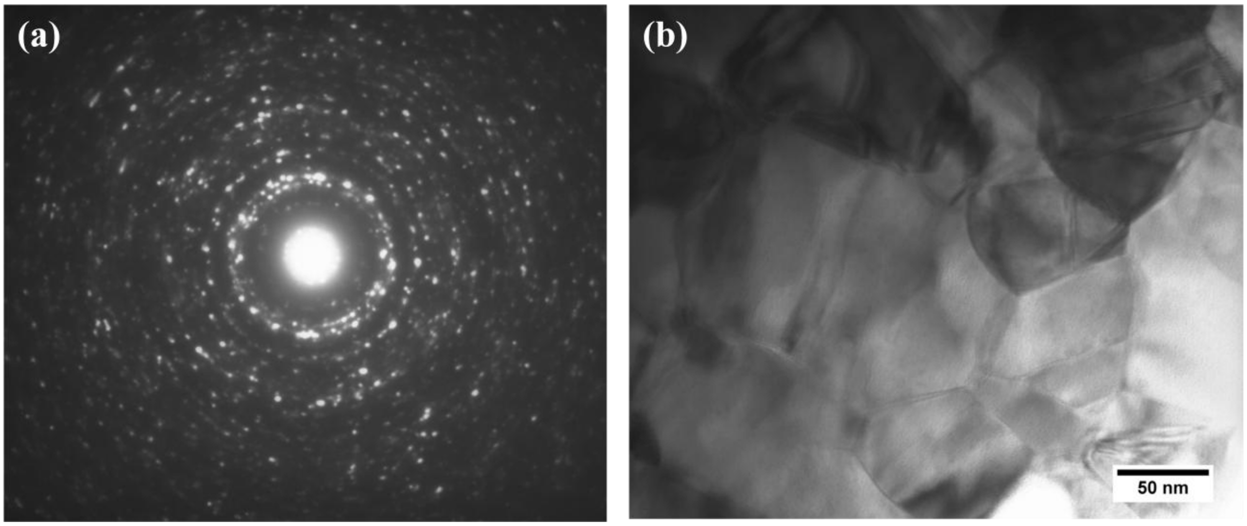

**Fig. 4.16 TEM image of $Gd_2O_3$ film deposited at a substrate temperature of 873 K and oxygen partial pressure of 0.2 Pa (a) SAD pattern and (b) bright field image showing crystallites.**

#### 4.3.2.5 Optical property measurements

The optical properties of the $Gd_2O_3$ films grown under various substrate temperatures were analyzed by UV-Visible spectrophotometer in the wavelength range of 200-900 nm. The absorbance and transmittance values at different wavelengths are plotted and are shown in Fig

4.17 (a) and (b), respectively. The $Gd_2O_3$ films show a strong absorbance near ~220 nm. All the $Gd_2O_3$ films deposited at various substrate temperatures show a transmittance value of 70-90%, except for the film at 673 K. From the absorbance data, the band gap values were calculated using Tauc plot. The band gap values calculated are listed in Table 4.5 and is found to vary from 5.70-5.80 eV in the temperature range 300 to 873 K. The films deposited at 873 K show the highest band gap of 5.80 eV higher than that of the bulk value (~5.2 eV) [41].

Figure 4.18 show the absorbance and transmittance values of $Gd_2O_3$ films deposited under various oxygen partial pressure condition. The films show strong absorbance near wavelength of ~220 nm. The transmittance values vary in the range of 70 - 100 % for different oxygen partial pressure condition. The band gap values were calculated by Tauc plot and are found to vary from 5.66 to 5.80 eV. The films deposited at 873 K and oxygen partial pressure of 2 Pa show the highest band gap value of 5.80 eV.

The refractive index values calculated for the films deposited under various substrate temperature and oxygen partial pressure vary from 1.6-1.8 with the decrease in the substrate temperature from 873 to 300 K and 1.6-1.7 with decrease in oxygen partial pressure from 2 to 0.002 Pa.

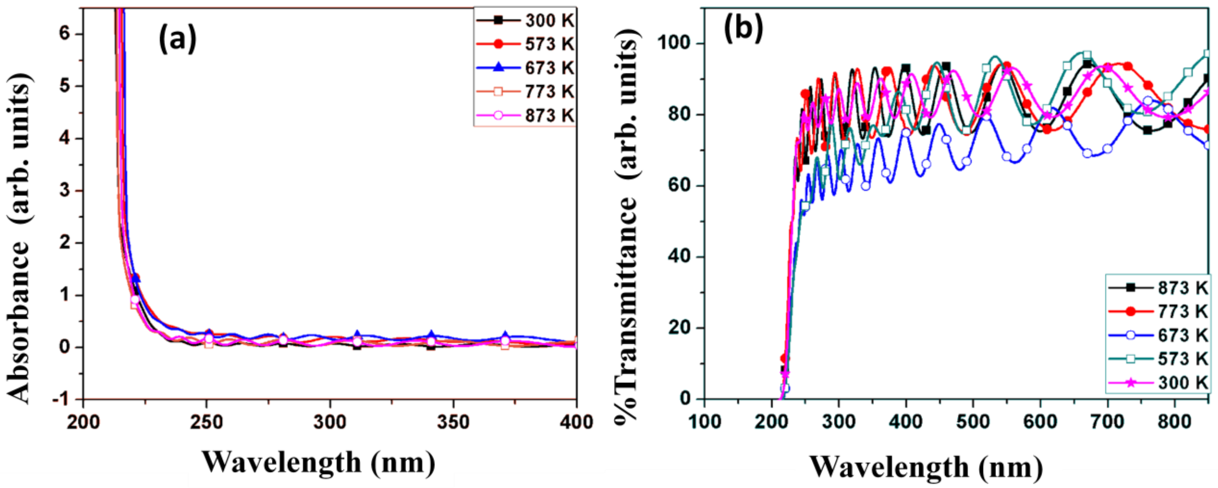

**Fig. 4.17 (a) Absorbance and (b) Transmittance versus wavelength plot of $Gd_2O_3$ films deposited on quartz substrates at different substrate temperatures and oxygen partial pressure of 0.2 Pa.**

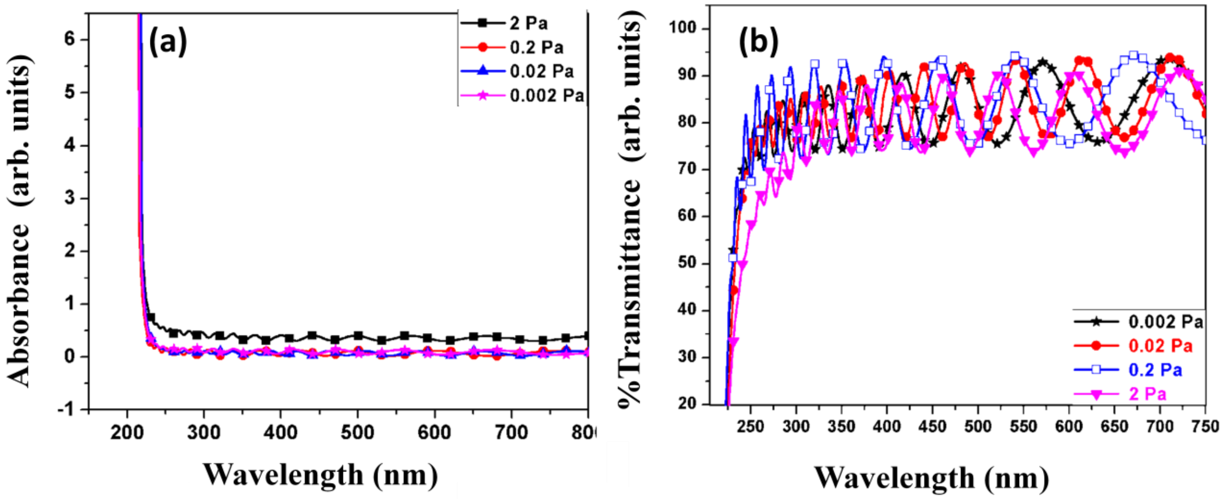

**Fig. 4.18 Variation of (a) Absorbance and (b) Transmittance values of $Gd_2O_3$ films deposited on quartz substrates as a function of oxygen partial pressures and substrate temperature of 873 K.**

### 4.3.2.6 Nanomechanical properties

Figure 4.19 shows the load versus penetration depth plot for $Gd_2O_3$ film deposited at substrate temperature of 873 K and oxygen partial pressure of 2 Pa. The hardness and elastic modulus values were determined by nanoindentation technique and are found to be 5.1 GPa and 151 GPa, which are slightly higher than those of the reported bulk values (~4.7 GPa and 124 GPa) [34]. The increase in hardness and elastic modulus values are the result of smaller crystallite size [42].

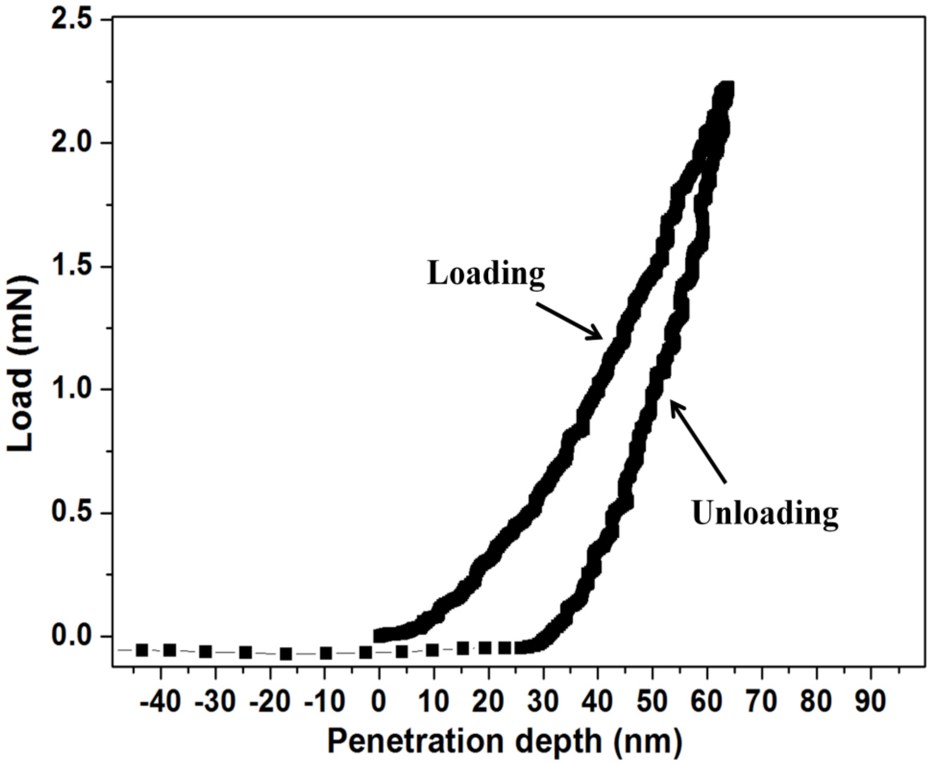

**Fig. 4.19 Load versus displacement plot for the $Gd_2O_3$ film deposited at 873 K and 0.2 Pa.**

### 4.3.3 Properties of $CeO_2/Gd_2O_3$ multilayers

The present section describes the deposition of the $CeO_2/Gd_2O_3$ multilayer films on Si, quartz and Inconel-783 substrates with variation of the $CeO_2$ layer thickness keeping $Gd_2O_3$ layer thickness constant (~10 nm), and studies the effect of the $CeO_2$ layer thickness on microstructural, optical and nanomechanical properties. The total thickness of the multilayer films were kept constant (~120 nm), by varying the number of bilayers. The total numbers of bilayers of the multilayer films are 3, 4, 6 and 8 for $CeO_2$ layer thickness of 30, 20 10 and 5 nm, respectively.

#### 4.3.3.1 Microstructural analysis

Figure 4.20 shows the XRD patterns of $CeO_2/Gd_2O_3$ multilayers deposited at the substrate temperature of 300 K and oxygen partial pressure of 2 Pa. The XRD pattern of the multilayer films deposited at 300 K shows polycrystalline structure with reflections from (111), (200), (220) and (311) planes of cubic-$CeO_2$. The XRD pattern does not contain any peaks from the $Gd_2O_3$, as $Gd_2O_3$ forms amorphous structure at room temperature. The intensity of the (111) reflection increases with increase in the $CeO_2$ layer thickness, which is due to the increase in the $CeO_2$ content with increase in layer thicknesses.

Figure 4.21 shows the $CeO_2/Gd_2O_3$ multilayer films deposited at the substrate temperature of 873 K and oxygen partial pressure of 2 Pa. The XRD pattern shows the formation of polycrystalline films, with increased number of peaks, concluding higher crystallinity at higher substrate temperature. The XRD pattern contains peaks from (111), (200), (220), (311), (222), (400), (331), (420) reflections of c-$CeO_2$ and (211), (222), (123), (400), (440), (622), (444), (800), (662), (840) reflection of c-$Gd_2O_3$. The FWHM values decreases as the $CeO_2$ layer thickness increases.

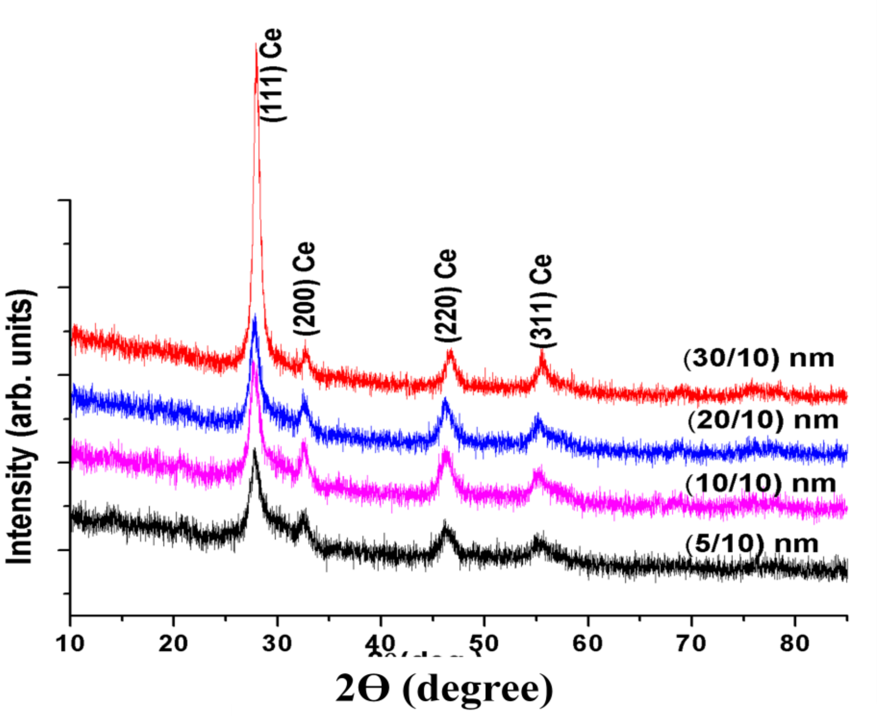

**Fig. 4.20 XRD pattern of $CeO_2/Gd_2O_3$ multilayers with different $CeO_2$ layer thickness deposited on Si (100) substrates at substrate temperature of 300 K and oxygen partial pressure of 2 Pa.**

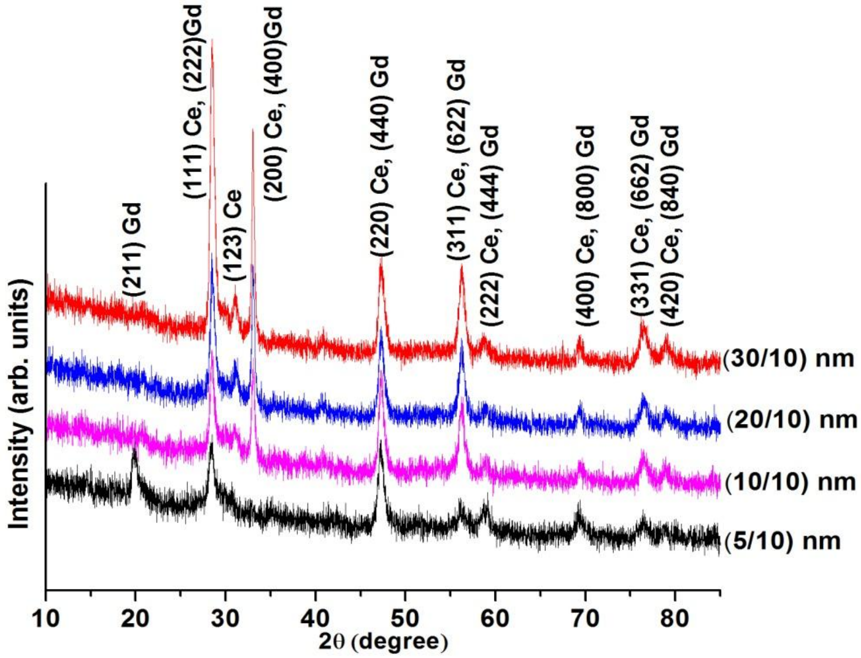

**Fig. 4.21 XRD patterns of $CeO_2/Gd_2O_3$ multilayer films deposited on Si (100) substrates at substrate temperature of 873 K and oxygen partial pressure of 2 Pa with variation in $CeO_2$ layer thickness.**

The crystallite size of $CeO_2$ calculated for the (111) peak of multilayer film grown at 300 K is found to vary from 7 to 11 nm with increase in the $CeO_2$ layer thickness from 5 to 30 nm. The crystallite size calculated for the (111) peak of $CeO_2$ in the multilayers deposited at 873 K is found to vary from 11 to 15 nm with increase in $CeO_2$ layer thickness from 5 to 30 nm. Unlike that of the crystallite size of $CeO_2$, the crystallite size of $Gd_2O_3$ was found to be constant (~15 nm) for the multilayers deposited at 873 K. which is due to the constant layer thickness of $Gd_2O_3$. The decrease in FWHM values of the peaks for the multilayers deposited at 873 K confirms higher crystallinity of phases of the multilayer film at higher substrate temperature.

#### 4.3.3.2 Raman analysis

Microstructural characterization of the multilayer films were also carried out by Raman spectroscopy for the $CeO_2/Gd_2O_3$ mulilayers with the $CeO_2$ layer thickness of 5 and 30 nm, deposited at 873 K and at oxygen partial pressure of 2 Pa(Fig. 4.22). The Raman spectra shows the peaks at 610 and 669 $cm^{-1}$ corresponding to cubic $CeO_2$ and 359 $cm^{-1}$ corresponding to cubic phase of $Gd_2O_3$.

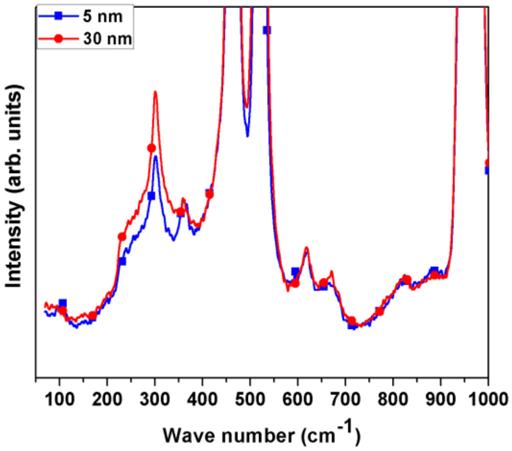

**Fig. 4.22 Raman spectra analysis of $CeO_2/Gd_2O_3$ multilayers deposited at 873K and oxygen partial pressure of 2 Pa with $CeO_2$ layer thickness of 5 and 30 nm.**

Similar results were also reported by Weber et al. [29] and Godinho et al. [43]. The characteristic peak for $CeO_2$ at 476 $cm^{-1}$ was not identified due to the overlapping of the peak of Si substrate at same wave number.

### 4.3.3.3 X-ray reflectivity analysis

To measure the individual layer thickness, surface roughness and interfacial roughness of the $CeO_2/Gd_2O_3$ mutlilayers, the films were analyzed by X-ray reflectivity (XRR) technique. The spectrum was recorded and fitted with Parratt software [44] to get the above parameters. Fig. 4.23 shows a typical XRR profile of $CeO_2/Gd_2O_3$ multilayer of (20/10) nm deposited at 300 K and 873 K, respectively. The results obtained from the XRR profile fitting are listed in Table 4.7. The $CeO_2$ layer thickness obtained from XRR analysis are 6.1, 8.8, 22.1 and 31.9 nm in corresponding to 5, 10, 20 and 30 nm for the films deposited at 300 K. Similarly the layer thickness of $Gd_2O_3$ is measured in the range of 8.5-13.5 nm which corresponds to 10 nm layer thickness. The interfacial roughness values are found to increase with increase in the layer thickness of $CeO_2$ and substrate temperature as a result of the higher crystallinity. Similarly the surface roughness values are also found to be higher for the films deposited at 873 K than that of the films deposited at 300 K. It has been already observed in the XRD analysis that $Gd_2O_3$ forms amorphous structure at 300 K and becomes crystalline at 873 K as a result of which the surface roughness values are increased.

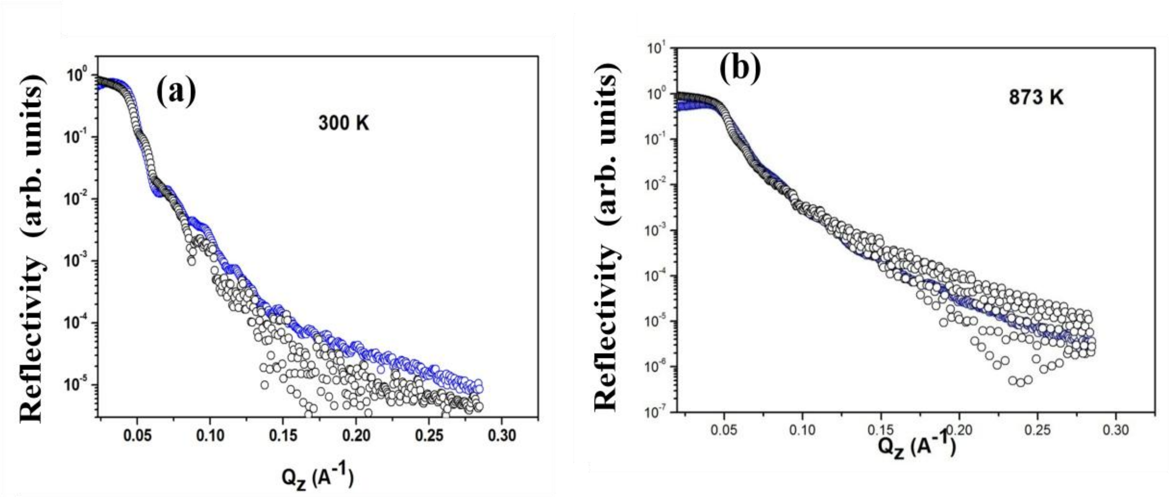

**Fig. 4.23 A typical XRR profile of $CeO_2/Gd_2O_3$ multilayer films of (20/10) nm thickness deposited on Si (100) at oxygen partial pressure of 2 Pa and substrate temperature of (a) 300 K and (b) 873 K.**

**Table 4.7 XRR analysis results obtained for $CeO_2/Gd_2O_3$ multilayers deposited at 300 and 873 K and oxygen partial pressure of 2 Pa on Si (100) substrates.**

| **Bilayer structure $CeO_2/Gd_2O_3$ (nm)** | **Films Deposited at 300 K** | | | **Films Deposited at 873 K** | | |
|---|---|---|---|---|---|---|
| | **Thickness from XRR (nm)** | **Interfacial roughness (nm)** | **Surface roughness (nm)** | **Thickness from XRR (nm)** | **Interfacial roughness (nm)** | **Surface roughness (nm)** |
| (5/10) | 6.1/9.6 | 0.7 | 0.9 | 6.7/9.5 | 0.6 | 0.9 |
| (10/10) | 8.8/8.5 | 0.7 | 0.8 | 9.5/12.5 | 1.1 | 0.9 |
| (20/10) | 22.1/12.1 | 0.9 | 0.7 | 19.5/11 | 1.2 | 0.9 |
| (30/10) | 31.9/13.5 | 1.1 | 0.8 | 30.8/11.1 | 1.5 | 1.2 |

### 4.3.3.4 Surface morphology from AFM analysis

The surface morphology of the $CeO_2/Gd_2O_3$ multilayer films was analyzed by AFM. Fig. 4.24 (a) and (b) shows the typical AFM images of the $CeO_2/Gd_2O_3$ multilayers of (30/10) nm deposited at the substrate temperature of 300 K and 873 K, respectively. The multilayer deposited at 300 K shows amorphous structure, characterized by structureless surface, while the multilayer deposited at 873 K contains a fine distribution of spherical particles. These results are also consistent with the XRD analysis. The surface roughness values obtained from AFM analysis are 0.3 and 1.8 nm for films deposited at 300 and 873 K, respectively.

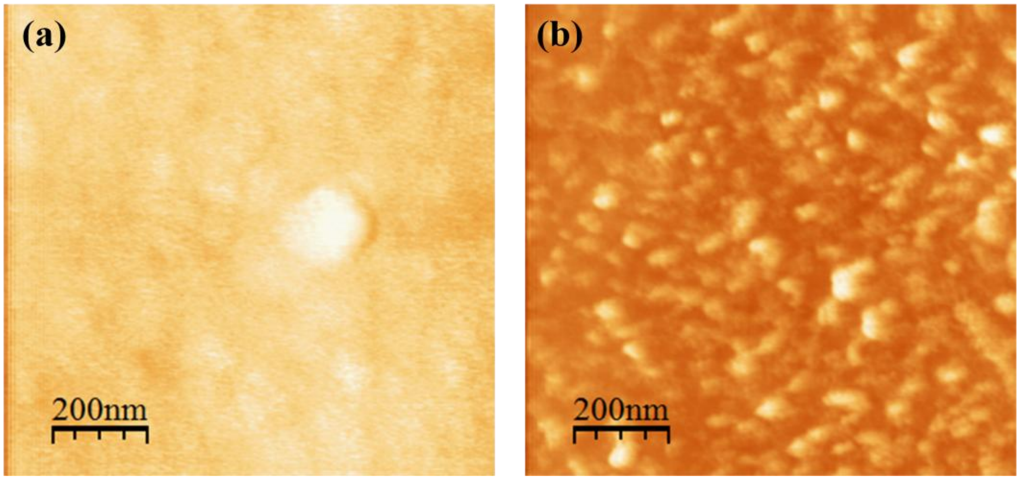

**Fig. 4.24 AFM images of $CeO_2/Gd_2O_3$ multilayer films of (30/10) nm deposited on Si(100) at (a) 300 K (b) 873 K and oxygen partial pressure of 2 Pa.**

### 4.3.3.5 HRTEM analysis

Figure 4.25 (a) shows the SAD pattern of $CeO_2/Gd_2O_3$ multilayer film of (20/10) nm deposited on Si substrates at substrate temperature of 873 K and oxygen partial pressure of 2 Pa. The SAD pattern shows the formation of polycrystalline film with preferred orientation. The film consists of cubic $CeO_2$, cubic $Gd_2O_3$ and a small fraction of m-$Gd_2O_3$. The indexed SAD pattern is shown in Table 4.8. Figure 4.25 (b) shows the low magnification bright field HRTEM image showing the cross sectional view of $CeO_2/Gd_2O_3$ multilayer of (20/10) nm. The dark band belongs to $Gd_2O_3$ and the white bands are due to the $CeO_2$. The thickness of $CeO_2$ and $Gd_2O_3$ layers are found to vary from 21 to 23 nm and 15 to 17 nm, respectively. It must be mentioned that the bands are not very clear unlike the other multilayers, because the images were observed at 160 kV instead of 200 kV.

**Table 4.8 Interplanar distance, d determined from the SAD pattern of $CeO_2/Gd_2O_3$ multilayer of (20/10) nm.**

| **Measured d (nm)** | **c-$CeO_2$ (PDF# 00-004-0593)** | | **c-$Gd_2O_3$ (PDF# 01-086-2477)** | | **m-$Gd_2O_3$ (PDF# 01-077-8312)** | |
|---|---|---|---|---|---|---|
| | **d (nm)** | **hkl** | **d (nm)** | **hkl** | **d (nm)** | **hkl** |
| 0.6825 | | | | | 0.6906 | 2 0 0 |
| 0.4474 | | | 0.4412 | 2 1 1 | | |
| 0.4184 | | | | | 0.4302 | 0 0 2 |
| 0.2751 | 0.2706 | 2 0 0 | | | | |
| 0.2710 | | | 0.2702 | 4 0 0 | | |
| 0.2259 | | | 0.2206 | 4 2 2 | | |
| 0.1766 | 0.1633 | 3 1 1 | | | | |

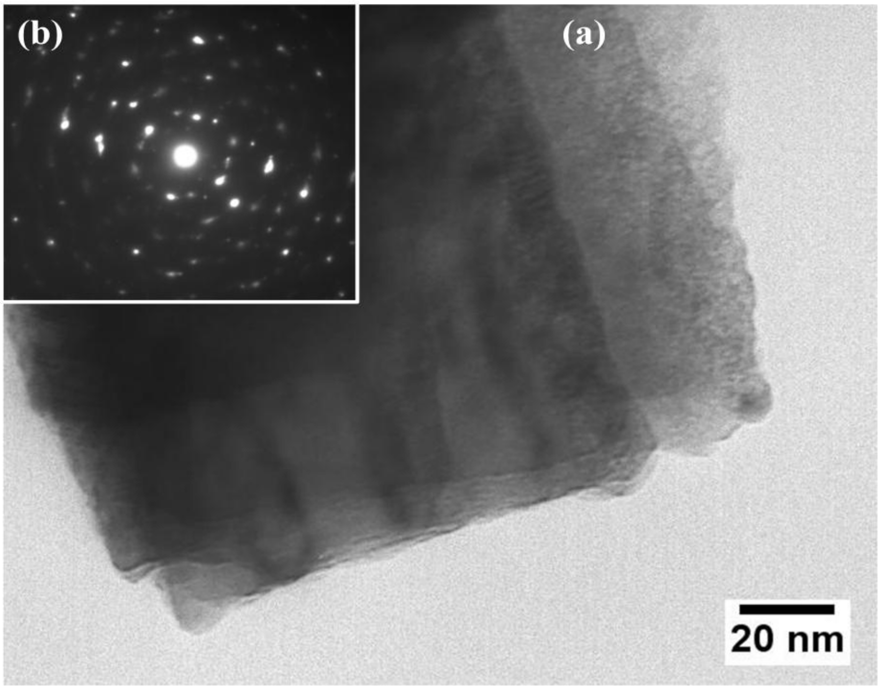

**Fig. 4.25 (a) A typical HRTEM image of $CeO_2/Gd_2O_3$ multilayer of (20/10) nm deposited on Si substrates at 873 K and oxygen partial pressure of 2 Pa and (b) SAD pattern from the multilayer.**

#### 4.3.3.6 Optical properties

To measure the optical properties of the $CeO_2/Gd_2O_3$ multilayers, the films were deposited on quartz substrates. Fig. 4.26 (a) and (b) show the absorbance and transmittance curves of the $CeO_2/Gd_2O_3$ multilayer films deposited at substrate temperature of 300 K and oxygen partial pressure of 2 Pa, for different $CeO_2$ layer thickness. Fig. 4.26 (a) shows absorbance at two wavelengths i.e. 350 and 220 nm belonging to $CeO_2$ and $Gd_2O_3$, respectively. The transmittance values of the multilayers deposited for various $CeO_2$ layer thickness show a maximum of ~80% transmittance for multilayer films with $CeO_2$ layer thickness 5 nm. Although $CeO_2/Gd_2O_3$ multilayer with (5/10) nm layer thickness has highest number of interfaces but still shows the highest transmittance value. Band gap values were calculated using the Tauc plot. The Tauc plot shows two band gaps for each $CeO_2$ and $Gd_2O_3$. The band gap values obtained for different films are listed in Table 4.9. The band gap values for $CeO_2$ increase with increase in the $CeO_2$ layer thickness, whereas the band gap of $Gd_2O_3$ decreases from 5.69 to 5.32 eV.

Figure 4.27 (a) and (b) shows the absorbance and transmittance curves of the $CeO_2/Gd_2O_3$ multilayers deposited at substrate temperature of 873 K and oxygen partial pressure of 2 Pa. The multilayer films show two absorption edges at 220 nm and 350 nm for the $Gd_2O_3$ and $CeO_2$, respectively. All the films show almost similar transmittance for each $CeO_2$ layer thickness. The band gap values calculated for the $CeO_2$ varies from 3.91 to 4.0 eV with increase in the $CeO_2$ layer thickness from 5 to 30 nm. Similarly the band gap values of $Gd_2O_3$ increases from 5.71 to 5.85 eV with the increase in the $CeO_2$ layer thickness from 5 to 30 nm.

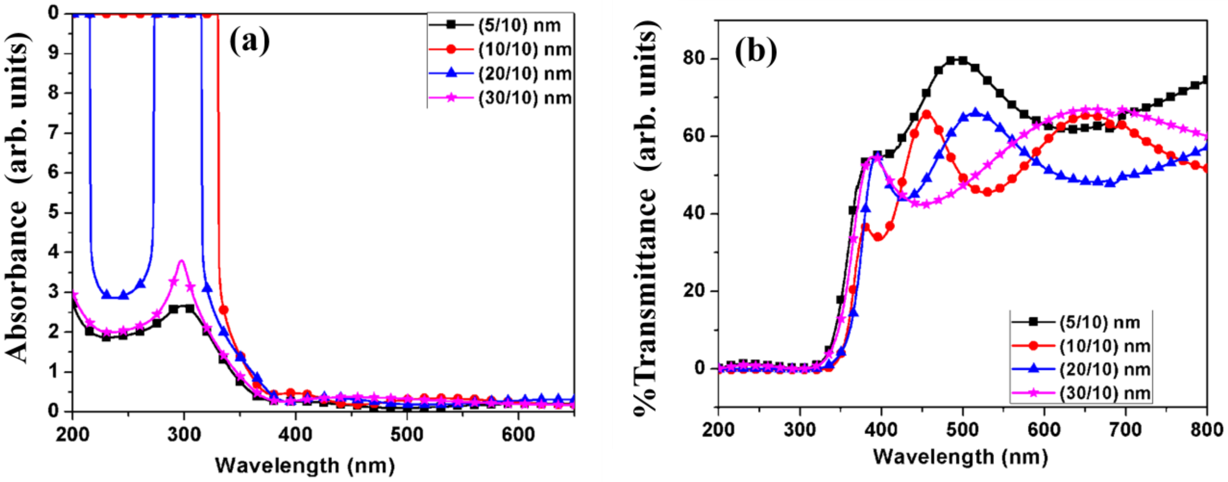

**Fig. 4.26 Effect of $CeO_2$ layer thickness on the (a) absorbance and (b) transmittance values of $CeO_2/Gd_2O_3$ multilayers deposited on quartz substrates at substrate temperature of 300 K and oxygen partial pressure of 2 Pa.**

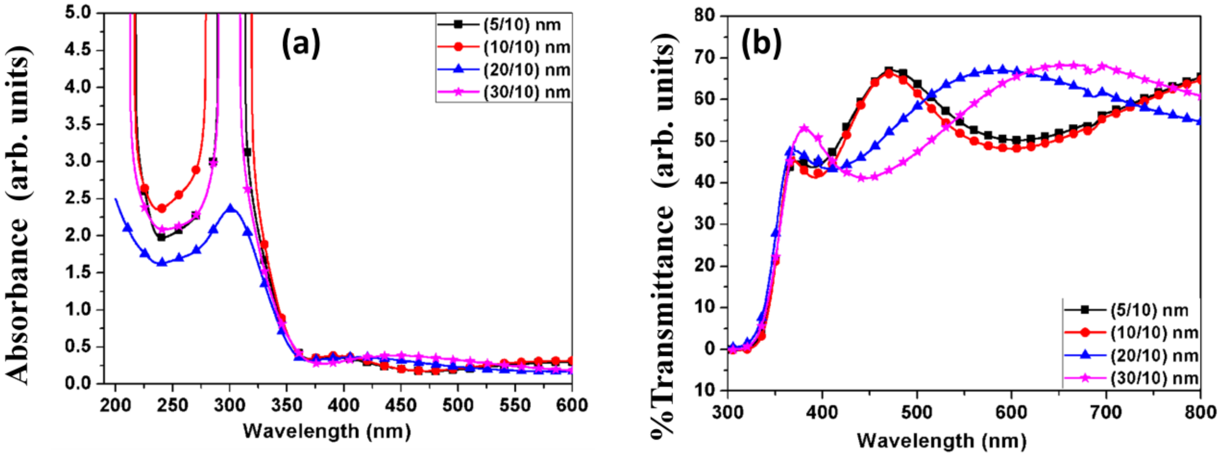

**Fig. 4.27 Variation in the (a) absorbance and (b) transmittance values of $CeO_2/Gd_2O_3$ multilayers deposited on quartz substrates at 873 K and oxygen partial pressure of 2 Pa as a function of $CeO_2$ layer thickness.**

**Table 4.9 Optical properties for the $CeO_2/Gd_2O_3$ multilayers for different layer thickness and substrate temperatures.**

| Bilayer thickness ($CeO_2/Gd_2O_3$) nm | Substrate temperature of 300 K | | Substrate temperature of 873 K | |
|---|---|---|---|---|
| | Band gap of $CeO_2$ (eV) | Band gap of $Gd_2O_3$ (eV) | Band gap of $CeO_2$ (eV) | Band gap of $Gd_2O_3$ (eV) |
| (5/10) | 3.62 | 5.69 | 3.91 | 5.71 |
| (10/10) | 3.65 | - | 3.90 | 5.74 |
| (20/10) | 3.75 | 5.58 | 3.92 | 5.75 |
| (30/10) | 3.84 | 5.32 | 4.0 | 5.85 |

### 4.3.3.7 Nanomechanical property analysis

Nanomechanical properties of the $CeO_2/Gd_2O_3$ multilayer films deposited at 873 K and the oxygen partial pressure of 2 Pa were measured by nanoindentation technique as a function of $CeO_2$ layer thickness (Fig 4.27). The hardness and the elastic modulus values are plotted as a function of $CeO_2$ layer thickness. The values of both hardness and elastic modulus of the multilayers are lower for $CeO_2$ layer of thickness of 5 nm. The hardness values are quite high for the multilayers with $CeO_2$ layer thickness in the range of 10 - 30 nm, than that of the values measured for $CeO_2$ (~5.4 GPa)

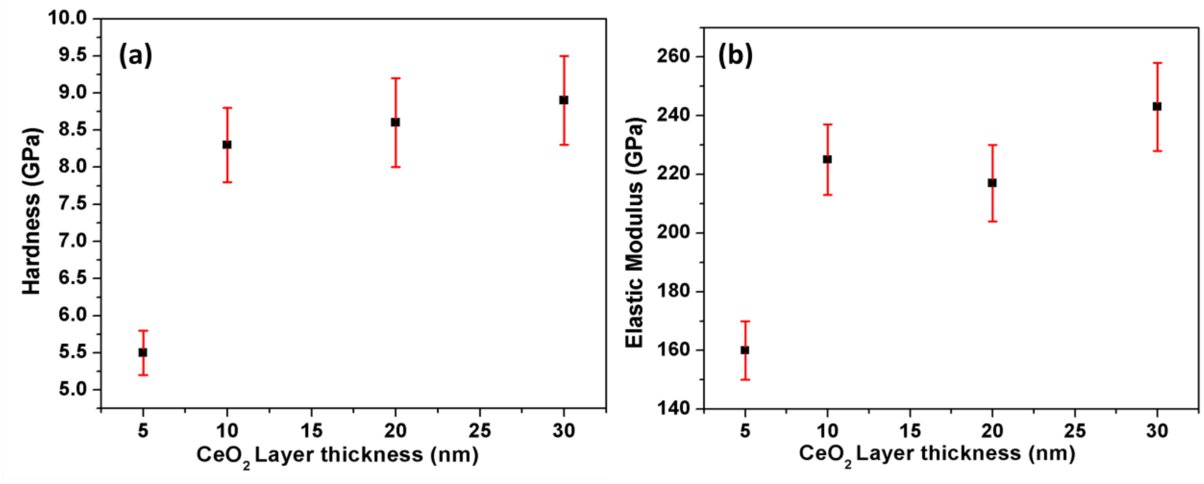

**Fig. 4.28 (a) Hardness and (b) elastic modulus values of $CeO_2/Gd_2O_3$ multilayers as a function of $CeO_2$ layer thickness deposited on Inconel-783 substrates at 873 K and oxygen partial pressure of 2 Pa .**

and $Gd_2O_3$ (~5.1 GPa) films. The elastic modulus values of the multilayers are in between than that of the $CeO_2$ and $Gd_2O_3$. The hardness as well as elastic modulus values of the multilayer with 5 nm of $CeO_2$ layer thickness is lower than that of the other multilayers and comparable with $Gd_2O_3$.

## 4.4 Discussion

The following section includes the discussion of the results obtained for $CeO_2$, $Gd_2O_3$ and their multilayers.

### 4.4.1 Growth and properties of $CeO_2$ and $Gd_2O_3$ thin films

$CeO_2$ thin films were deposited on Si and quartz substrates at various substrate temperatures and oxygen partial pressures. The XRD analysis shows the formation of a crystalline film even at room temperature. The films deposited at 300 K and 573 K shows a preferred orientation for (111) reflection. As the substrate temperature increases, the preferred orientation changes from (111) to (200) plane due to low surface energy for (200) plane [46] and Similar results were also observed by Balakrishnan et al. [45] and Elidrissi et al. [47] for $CeO_2$ thin film.

When the films of $CeO_2$ were deposited at different oxygen partial pressures, the preferred orientation changes from (111) to (200) with increase in the oxygen partial pressure from 0.002 to 2 Pa. Although an increase in crystallite size is expected with decrease in oxygen partial pressure, the present study shows a decreased crystallite size as a function of decrease in the oxygen partial pressure [48,49].

In contrast to $CeO_2$, $Gd_2O_3$ thin films are found to be X-ray amorphous when deposited at the substrate temperature of 300 K. Crystallization of $Gd_2O_3$ is noticed at the substrate temperature ≥ 473 K. The films are polycrystalline in nature with monoclinic phase as the major phase along with a small volume fraction of cubic phase at the temperature of 473 and 543 K. With increase in the substrate temperature, the film becomes purely monoclinic. Shoujing et al. [50] have reported similar results for $Gd_2O_3$ thin films deposited by magnetron sputtering on Si (100) substrates, in which an increase in the substrate temperature results in an increase in monoclinic phase content as a result of stress relaxation. Molle et al. [51] have reported a thickness dependant phase transformation for $Gd_2O_3$ films and reported 16.5 nm as the critical layer thickness beyond which cubic to monoclinic phase transformation takes place. A thin film growth by PLD is a nonequillibrium growth process, leading to formation of high temperature phases at room temperature. Increase in film thickness and growth temperature leads to decrease in stress in the films. This results in a transformation from cubic to monoclinic phase due to the relaxation in crystal structure [51]. Similar observations were also made by Chakraborty et. al. [52] in Ti thin films where the room temperature FCC structure has been transformed to hexagonal structure with increase in film thickness as a result of the decrease in compressive stress. The intrinsic stress in the thin films is compressive in nature during the initial stages of thin film growth, which latter transforms to tensile stress when film thickness increases beyond a particular value [52].

The crystallite size calculated for the highest intensity peak of (401) varies from 8 to 29 nm with increase in the substrate temperature from 300 to 873 K. The increase in crystallite size is due to the increase in adatom mobility at the substrate surface and therefore the atoms are able to form the lowest energy structure [45].

The XRD pattern of the $Gd_2O_3$ films deposited under different oxygen partial pressures and substrate temperature of 873 K shows the formation of phase pure polycrystalline m-$Gd_2O_3$

phase at higher substrate temperature. The crystallite size calculated for the films does not show a significant change with change in the oxygen partial pressure, which may be due to the higher substrate temperature for the thin film deposition.

The surface morphology of the $CeO_2$ and $Gd_2O_3$ films were studied by AFM analysis. The crystallite size obtained from the AFM analysis is slightly higher than that of the values obtained from XRD analysis. The crystallite size obtained from the AFM is indicative of the coalesced grains [53,54], whereas the XRD gives the average crystallite sizes of a particular plane or planes. The roughness values obtained from the AFM image for both $CeO_2$ and $Gd_2O_3$ are found to increase with increase in the crystallite size [55].

Transmittance of a film is highly dependent on the microstructure, mixed phases, porosity, grain boundary scattering, thickness and surface roughness values [56]. The transmittance of the $CeO_2$ and $Gd_2O_3$ films show a maximum of 90 % transmittance for the films deposited under various process parameters. The transmittance value of $CeO_2$ is low at higher substrate temperature due to increase in the surface roughness and crystallite sizes. However the optical transmittance of $Gd_2O_3$ film does not show a significant variation with the microstructure of the films, due to the presence of mixed phases. Transmittance of a film depends on the density of the materials. As the density of cubic $Gd_2O_3$ is lower than that of the monoclinic structure the transmittance of cubic phase is higher than that of the monoclinic phase. As a result of the contribution from cubic phases, the transmittance of the $Gd_2O_3$ films grown at lower substrate temperature has higher transmittance value [57].

The absorbance spectra of $CeO_2$ and $Gd_2O_3$ films show a strong absorbance near the wavelength of 350 nm and 220 nm, respectively. The band gaps of the films were determined from the Tauc plot and indicate that both $CeO_2$ and $Gd_2O_3$ are direct band gap materials. The band gap values calculated for $CeO_2$ were found to vary from 3.6 to 3.4 eV with increase in the substrate temperature. According to quantum confinement theory, the band gap should decrease with the increase in the crystallite size. But the band gap values show significant changes only when the crystallite size is less than twice of the exciton Bohr radii of a particular material. As $CeO_2$ crystallite sizes are quite larger, the change in the band gap cannot be truly related to the crystallite sizes and may be associated with the stress and defects in the films.

The band gap values calculated for the $Gd_2O_3$ films is found to be highest for the films deposited at 873 K and oxygen partial pressure of 0.2 Pa. Band gap of a material is highly dependent on the stress, microstructure, vacancies and mixed phases [56]. It has been reported by Singh et al. [58] that the band gap of $Gd_2O_3$ films would increase with the presence of cubic phases. Since, a small volume fraction of cubic phase was also present at low substrate temperature, the band gap values of the $Gd_2O_3$ films is higher than that of the film deposited at 673 K. A phase pure m- $Gd_2O_3$ showed the highest value of band gap at 873 K and oxygen partial pressure of 0.2 Pa.

The hardness value for $CeO_2$ film grown on Inconel-783 substrate at 873 K and oxygen partial pressure of 2 Pa was measured by the nanoindentaion technique. The hardness and elastic modulus values are comparable with the bulk values reported by Mogen et al. [33]. The increase in elastic modulus values are due to the smaller crystallite size of $CeO_2$ than that of the bulk, which results in the formation of high density film [59]. The hardness values obtained for $Gd_2O_3$ film are higher than that of the reported bulk values due to the decrease in crystallite sizes [60].

### 4.4.2 Discussion on $CeO_2/Gd_2O_3$ multilayer films

$CeO_2/Gd_2O_3$ multilayer films were deposited on Si (100), quartz and Inconel-783 substrates to investigate the microstructural, optical and nanomechanical properties. The multilayers were grown at two different substrate temperatures and oxygen partial pressure of 2 Pa. XRD patterns of the films deposited at 300 K shows that the $CeO_2$ is present in polycrystalline nature, while $Gd_2O_3$ forms amorphous structure. The increase in the intensity of the peaks with increase in $CeO_2$ layer thickness is due to the increase in overall quantity of $CeO_2$. At 873 K there is an increase in number of peaks and peak intensities of multilayer films, due to the increase in the crystallinity. Presence of additional lines of $Gd_2O_3$ confirms that at 873 K, it forms crystalline structure. Unlike that of the single layer of $Gd_2O_3$, where mostly monocilinic phase was noticed at different substrate temperatures and oxygen partial pressures, whereas in all the multilayers $Gd_2O_3$ exists only cubic structure. This is due to the smaller layer thickness of $Gd_2O_3$ film grown on cubic phase of $CeO_2$. It has been reported by Alessandro et al. [45] that $Gd_2O_3$ phase transformation also is dependent on layer thickness. The authors have reported a critical layer thickness of 16.5 nm for the cubic to monoclinic phase transformation. Since in the present study, the layer thickness of $Gd_2O_3$ is limited to ~10 nm, the formation of cubic phase of $Gd_2O_3$ is more promoted by the cubic structure of cubic $CeO_2$.

Microstructuras of the films were also analyzed by Raman analysis and confirms the presence of both c-$CeO_2$ and c-$Gd_2O_3$. TEM analysis was carried out to measure the individual layer thickness of each layer of the multilayer. The layer thickness obtained from the XRR and TEM are in accordance with each other. Surface and interfacial roughness are found to increase with increase in the substrate temperature due to the increase in the crystallinity of the films.

The optical properties of the films deposited at 300 K and 873 K are measured using UV-visible spectrophotometer. The films show two absorption edges at 350 and at 220 nm for $CeO_2$ and $Gd_2O_3$, respectively. The films deposited at 300 K show transmittance of ~60 % while the multilayers deposited at 873 K indicated ~70 % transmittance because of better crystallinity of $CeO_2$ and $Gd_2O_3$.

The band gap values estimated for $CeO_2$ and $Gd_2O_3$ of the multilayers deposited at 300 K show opposite trend, while the band gap values of $CeO_2$ and $Gd_2O_3$ increases with increasing layer thickness of $CeO_2$ for the multilayer deposited at 873 K. The band gap values are known to increase with increased crystallinity [58] and therefore the band gap values of both the materials show increasing trend with temperature. In the case of multilayers deposited at 300 K, the $Gd_2O_3$ forms amorphous structure, while the $CeO_2$ layer shows crystalline structure. Also the crystallinity of the $CeO_2$ increases with increase in layer thickness. Therefore $CeO_2$ shows increase in band gap while $Gd_2O_3$ shows a decreasing trend with increase in layer thickness of $CeO_2$.

Hard coatings are useful in many industrial applications such as tribological components, cutting tools etc. The hard coatings include mainly nitrides, carbides and borides. But the applications of these coatings are limited due to lower stability. Transition metal oxides are the best alternatives to overcome such problems, if the hardness values can be enhanced. Such attempts have been made by many authors (Christina et. al, [61] Barshilia et. al [62]). Recent research includes enhancement of hardness by forming multilayer structure [63,64]. The nanomechanical properties of the $CeO_2/Gd_2O_3$ multilayer films were measured by the naoindentation technique. The hardness values of the multilayers with the $CeO_2$ layer thickness of 10-30 nm are higher than that of the $CeO_2$ and $Gd_2O_3$. The enhancement in hardness and elastic modulus is due to the effect of difference in elastic modulus of the two materials [65]. The hardness and elastic modulus values are lower for the multilayer with $CeO_2$ layer thickness of 5 nm, and is comparable to the $Gd_2O_3$ values. This may be due to the more contribution from

$Gd_2O_3$. The resistance to plastic deformation of the multilayer were qualitatively measured by $H^3/E^2$ and plotted as a function of the $CeO_2$ layer thickness in Fig 4.28.The results suggests that the resistance to plastic deformation measured by $H^3/E^2$, is significantly influenced by layer thickness of $CeO_2$. Appropriate selection of the layer thickness of $CeO_2$ has been found to be necessary in order to design multilayer of enhanced nanomechanical properties.

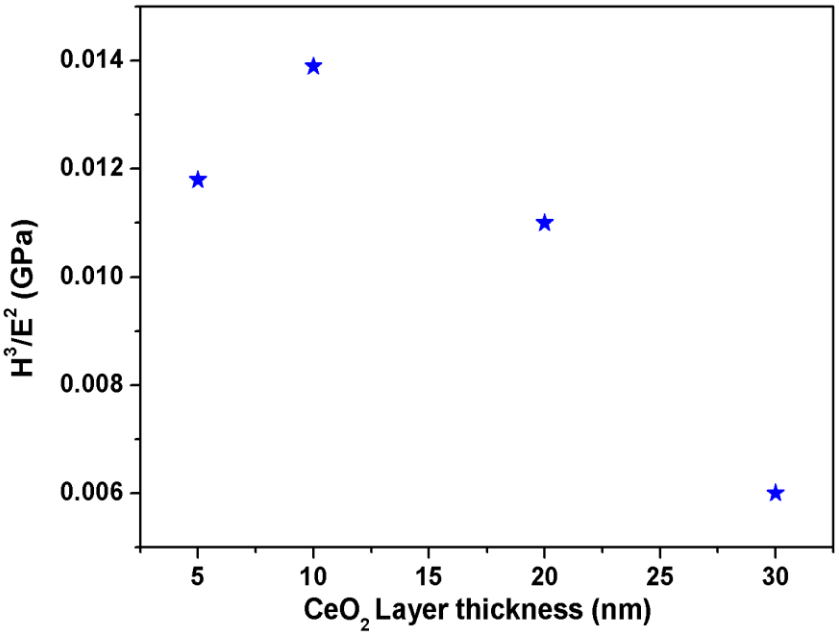

**Fig. 4.29 $H^3/E^2$ of $CeO_2/Gd_2O_3$ multilayers with variation in $CeO_2$ layer thickness deposited on Inconel-783 substrates at 873 K and oxygen partial pressure of 2 Pa.**

## 4.5 Summary and Conclusions

The present chapter describes the effect of process parameters on the microstructural and optical properties of $CeO_2$ and $Gd_2O_3$ thin films. Multilayers of $CeO_2/Gd_2O_3$ are grown on Si (100), quartz and Inconel-783 substrates at two different substrate temperature and variation in $CeO_2$ layer thickness from 5-30 nm to study the change in microstructural, optical and nanomechanical properties.

### 4.5.1 $CeO_2$ thin films

(i) $CeO_2$ films grown under different substrate temperature (300-873 K) and oxygen partial pressures (2-0.002 Pa) are polycrystalline with cubic fluorite structure.

(ii) The preferred orientation changes from (111) to (200) with increase in the substrate temperature and oxygen partial pressure. Crystallite size calculated from Scherrer formula showed an increasing trend with increase in substrate temperature but oxygen partial pressure does not show a significant influence on the crystallite sizes.

(iii) The surface roughness values obtained from AFM analysis increases with increase in the temperature and oxygen partial pressure as a result of the increase in crystallite size

(iv) The $CeO_2$ films show transmittance of ~60-90%. The band gap values obtained from the Tauc plot show a decrease with increase in the temperature and oxygen partial pressure.

### 4.5.2 $Gd_2O_3$ thin films

(i) Microstructure of the $Gd_2O_3$ films deposited on Si substrate were analyzed by XRD, Raman spectroscopy, AFM and TEM. At 300 K, $Gd_2O_3$ forms amorphous structure, and the film becomes crystalline at 473 K. The film consists of monoclinic phase of $Gd_2O_3$ except for small amount of c- $Gd_2O_3$ at 300 K, which is not stable at higher substrate temperature. The crystallite size increases from 8 to 29 nm with increase in the substrate temperature from 300- 873 K. Oxygen partial pressure does not show a significant effect on the crystallinity. The Raman analysis of the films shows the presence of m- $Gd_2O_3$ for whole range of temperature and oxygen partial pressure. AFM analysis shows increases in roughness value due to the increase in crystallite size.

(ii) The films show good transmittance in the wavelength range of 200-900 nm. The film deposited at 873 K and oxygen partial pressure of 0.2 Pa shows the highest band gap i.e. 5.80 eV, indicating the best quality film formation under these temperature and pressure conditions.

The hardness and elastic modulus values show higher values than that of the bulk, as a result of smaller crystallite size.

### 4.5.3 $CeO_2$/$Gd_2O_3$ multilayers

(i) Multilayers films of $CeO_2$/$Gd_2O_3$ were prepared on Si, quartz and inconel-783 substrates to analyze the microstructural, optical and nanomechanical properties, respectively.

(ii) The XRD patterns show formation of polycrystalline film at 300 K for all ranges of $CeO_2$ layer thickness. The crystallinity is higher for the multilayer with 30 nm $CeO_2$ layer thickness and for the films deposited at 873 K. Multilayer films deposited at 873 K show peaks from c-$CeO_2$ and c-$Gd_2O_3$.

(iii) The layer thickness obtained from XRR and HRTEM analysis is comparable with each other. The surface and interfacial roughness values obtained from XRR shows an enhancement with increase in the substrate temperature and $CeO_2$ layer thickness.

(iv) The multilayers show good transmittance of ~70%, and the band gap value increases with increase in the substrate temperature and layer thickness of $CeO_2$. Nanomechanical properties for the multilayers were measured by nanoindentation technique for the films deposited on Inconel-783 substrates and found to be higher than that of both $CeO_2$ and $Gd_2O_3$, except for the film with 5 nm $CeO_2$ layer thickness.

## 4.6 References

1. P.F. Wahid, K.B. Sundaram, P.J. Sisk, Optics Laser Technol. 24 (5) (1992) 263.
2. J. Gerblinger, W. Lohwasser, U. Lampe, H. Meixner, Sensor. Actuator. B 26-27 (1995) 93.
3. E. Stewart, M.S. Bhuiyan, S. Sathyamurthy, M. Paranthaman, Mater. Res. Bull. 41 (2006) 1063.
4. I. Porqueras, C. Person, E. Bertran, Thin Solid Films 447 –448 (2004) 119.
5. A. Trovarelli, Catalysis by Ceria and related Materials, Catalytic Science Series, 2 Imperial College Press, London, 2002.
6. A. Tschtipe, J. Y. Ying, H. L. Tuller, Sensor. Actuator. B 31 (1996) 111.
7. C. C. Chin , R. J. Lin, Y. C. Yu, C. W. Wang, E. K. Lin, W. C. Tsai, T. Y. Tseng, Physica C 260 (1996) 86.
8. C. Breinlich, J. Markus Essen, E. Barletta, K. Wandelt, Thin Solid Films 519 (2011) 3752.
9. P.J. King, M. Werner, P.R. Chalker, A.C. Jones, H.C. Aspinall, J. Basca, J.S. Wrench, K. Black, H.O. Davies, P.N. Heys, Thin Solid Films 519 (2011) 4192.
10. M. Pan, G.Y. Meng, H.W. Xin, C.S. Chen, D.K. Peng, Y.S. Lin, Thin Solid Films 324 (1998) 89.
11. A. Ramirez-Duverger, A. Rabdel Ruiz-Salvador, M.P. Hernandez-Sanchez, M.F. Garcia-Snchez, G. Rodriguez-Gattorno, Solid State Ionics 96 (1997) 89.
12. T. Chaudhuri, S. Phok, R. Bhattacharya, Thin Solid Films 515 (2007) 6971.
13. G. Bonnet, M. Lachkar , J. P. Larpin, J. C. Colson, Solid State Ionics 72 (1992) 344.

14. N. K. Sahoo, S. Thakur, M. Senthilkumar, D. Bhattacharyya, N.C. Das, Thin Solid Films 440 (2003) 155.
15. R. Lupatak, K. Frohlich, A. Rosova, K. Husekova, M. Apajna, D. Machajdik, M. Jergel , J. P. Espinos, C. Mansilla, Microelectron. Eng. 80 (2005) 154.
16. G. Niu, B. Vilquin, N. Baboux, C. Plossu, L. Becerra, G. Saint-Grions, G. Hollinger, Microelectron. Eng. 86 (2009) 1700**.**
17. T. Echtermeyer, H.D.B. Gottlob, T. Wahlbrink, T. Mollenhauer, M. Schmidt, J.K. Efavi, M.C. Lemme, H. Kurz, Solid State Electronics 51 (2007) 617.
18. I. Zhitomirsky, A. Petric, Mater. Lett. 42 (2000) 273.
19. S. Yue, F. Wei, Yi Wang, Z. Yang, J. Du, J. Phys.: Conference Series 152 (2009) 012004.
20. N.K. Sahoo, S. Thakur, M. Senthilkumar, N. C. Das, Appl. Surf. Sci. 206 (2003) 271.
21. H. Guo, X. Yang, T. Xiao,W. Zhang,L. Lou, J. Mugnier, Appl. Surf. Sci. 230 (2004) 215.
22. Ke Xu, R. Ranjith, A. Laha, H. Parala, A. P. Milanov, R. A. Fischer, E. Bugiel, J. Feydt, S. Irsen, T. Toader, C. Bock, D. Rogalla, H. Osten, U. Kunze, A. Devi, Chem. Mater. 24 (2012) 651.
23. K. Chang, L. Hsieh, S. Huang, C. Lee, Y. Chiu, J. Cryst. Growth 310 (2008) 1961.
24. H. C. Barshilia, B. Deepthi, K. S. Rajam, J. Appl. Phys. 104, (2008) 113532.
25. H. Shinguu, M. M. H. Bhuiyan, T. Ikegami, K. Ebihara, Thin Solid Films 506–507 (2006) 111.
26. S. Burinskas, V. Adomonis, J. Dudonis, G. Laukaitis, V. Minialga, D. Milcius, Solid State Ionics 184 (2011) 14.
27. N. Rao, K. L. Shivlingappa, S. Mohan, Mater. Sci. Eng. B, 98 (2003) 38.

28. G. Balakrishnan, P. Kuppusami, T. N. Sairam, R. Thirumurugesan, E. Mohandas, D. Sastikumar. J. Nanosci. Nanotech. 9 (2009) 5421.
29. W. H. Weber, K. C. Haas, J. R. Mcbride, Phys. Rev B 48 (1) (1993) 178.
30. M.T. Ta, D. Briand, Y. Guhel, J. Bernard, J.C. Pesant, B. Boudart, Thin Solid Films 517 (2008) 450.
31. S. Wang, W. Wang, J. Zuo, Y. Qian, Mater. Chem. Phys. 68 (2001) 246.
32. R. M. Bueno, J. M. Martinez-Duart, M. Hernandez-Velez, L. Vazquez, J. Mater. Sci. 32 (1997) 1861.
33. M. Mogensen, N. M. Sammes, G. A. Tompsett, Solid State Ionics 129 (2000) 63.
34. W. Martienssen, H. Warlimont "Handbook of Condensed Matter and Materials Data" (2005) ISBN-3-540-44376-2.
35. J. J. Roa, E. Gilioli, F. Bissoli, F. Pattini, S. Rampino, X. G. Capdevila, M. Segarra, Thin Solis Films 518 (2009) 227.
36. J. Zarembowitch, J. Gouteron, A. M. Lejus, J. Raman Spetroscopy, 9 (4) (1980) 263.
37. N. Paul, M. Devi, D. Mohanta, Materials Research Bulletin 46 (2011) 1296.
38. N. Dilwar, S. Mehrota, D. Varandani, B. V. Kumaraswamy, S. K. haldar, A. K. Bandyopadhyay, Mater. Characterization 59 (2008) 462.
39. J. Niinisto, N. Petrova, M. Putkonen, L. Niinisto, K. Arstila, T. Sajavaara, J. Cry. Growth 285 (2005) 191.
40. X. Weng, D. A. Grave, Z. R. Hughes, D. E. Wolfe, J. A. Robinson, J. Vac. Sci.Technol.A 30(2012)041512.
41. S. Pal, S.K. Ray., B .R. Chakraborty, S.K.Lahiri, D.N. Bose, J. Appl. Phys. 90 (2001) 4103.

42. V. Richter, M.V. Ruthendorf, International Journal of Refractory Metals & Hard Materials 17 (1999) 141.
43. M. J. Godinho, R. F. Goncalves, L. P. S. santos, J. A. Varela, E. Longo, E. R. Leite, Materials Lett. 61 (2007) 1904.
44. L. G. Parratt, Phy. Rev. 95 (2) (1954) 359.
45. Z. Zhang , Max G. Lagally, Science 276 (1997) 377.
46. G. Balakrishnan, S. Tripura Sundari, P. Kuppusami, P. Chandramohan, M. P. Srinivasan, E. Mohandas, V. Ganesan, D. Sastikumar, Thin Solid Films 519 (2011) 2520.
47. B. Elidrissi, M. Addou, M. Regragui, C. Monty, A. Bougrine, A. Kachouane, Thin Solid Films 379 (2000) 23.
48. M. Mishra, P. Kuppusami, T. N. Sairam, A. Singh, E. Mohandas, Appl. Surf. Sci. 257 (2011)7665.
49. M. Mishra, P. Kuppusami, A. Singh, S. Ramaya, V. Sivasubramanian, E. Mohandas, Appl. Surf. Sci. 258(2012)5157.
50. Y. Shoujing, W. feng, wang Zhimin, Tu Hailing, Du Jun , J. Rare Earths, 26 (3) (2008) 371.
51. A. Molle, C. Weimer, Md. Nurul bhuiyan, G. Tallarida, M. fanciulli, Appl. Phys. Let. 90 (2007) 193511.
52. J. Chakraborty, Kishor Kumar, Rajeev Ranjan, S. Ghosh Chowdhury, S.R. Singh, Acta Materialia 59 (2011) 2615.
53. Z. B. Fang, Z. J. Yan, Y. S. tan, x. Q. Liu, Y. Y. Wang, Appl. Surf. Sci. 241 (2005) 303.
54. Y. Lee, S. Hu, W. Water, K. Tiong, Z. Feng, Y. Chen, J. Huang, J. Lee, C. Huang, J. Shen, M. Cheng, J. Luminescence 129 (2009) 148.

55. B. Rajesh Kumar, T. Subba Rao, Digest J. of Nanomaterials and Biostructures 6 (3) (2011)1281.
56. D. Beena, K.J. Lethy, R. Vinodkumar, V.P. Mahadevan Pillai, V. Ganesan, D.M. Phase, S.K. Sudheer, Appl. Surf. Sci. 255 (2009) 8334.
57. Diana Mardare, M. Tasca, M. Delibas, G.I. Rusu, Appl. Surf. Sci. 156 (2000) 200.
58. M. P. Singh, S. A. Shivashankar, J. Cry. Growth. 276 (2005) 148.
59. V.C. Nardone , K. M. Prewo, Scripta Metallurgica 20 (1986) 43.
60. A. Cavaleiro, C. Louro, Vacuum 64 (2002)211.
61. C. A. Freyman, Y. Chung, Surf. Coat. Technol. 202(2008)4702.
62. H. C. Barshilia, K. S. Rajan, J. Appl. Phys. 98 (2005) 014311.
63. J. Xu, M. Kamiko, Y. Zhou, G. Lu, R. Yamamoto, Appl. Phys. Lett. 81 (2002)1189.
64. S. P. Wen, R. L. Zong, F. Zeng, Y. Gao, F. Pan, Acta. Materialia 55 (2007)345.
65. X. Chu, S. A. Barnett, J. Appl. Phys. 77 (1995)4403.

# Chapter 5

# Thermal Expansion Behavior of Single and Multilayer Films

## 5.1 Introduction

Evaluation of coefficient of thermal expansion (CTE) of films is an important parameter to choose a material for different applications such as solid oxide fuel cells (SOFC), thermal barrier coatings (TBC), Microelectronis and micromechanical systems. The common techniques that are being used to measure the CTE values for bulk materials are mechanical dilatometry [1], optical interferometry [2] and diffraction techniques [3]. In case of thin film structures, these methods cannot be used because of lack of accuracy in the measurements due to smaller thickness. Measurement of the CTE values of a thin film can be carried out by HTXRD [4], ellipsometer [5] and micromachined cantilever techniques [6]. Out of all the techniques high temperature X-Ray diffraction (HTXRD) finds its importance in determination of CTE values due to the advantages like: smaller size of sample can be studied and also the expansion along different directions can also be determined. However, HTXRD is suitable for crystalline films. HTXRD is an important technique to study the thermal stability, phase evolution as well as inter diffusion phenomenon occurring during the heat treatment.

Swamy et al. [7] have studied the structural transitions and thermal expansion behavior of $Y_2O_3$ from room temperature to its melting point. The axial thermal expansion of $ZrO_2$ has been studied by Patil et al. [8] and they have reported the CTE values to be 11.6 and 16.08 x $10^{-6}$ $K^{-1}$ along *a* and *c* axes, respectively for t-$ZrO_2$. The thermal expansion property analysis of $CeO_2$ has been carried out by Schwab et al. [9] and the reported CTE value is 11.6x$10^{-6}$ $K^{-1}$. Sawbridge et al. [10] have studied the crystallography and thermal expansion behavior of cubic and monoclinic $Gd_2O_3$ for the temperature range 293 -1173 K.

Although phase stability and calculation of the CTE values for single oxide layer have been reported by many authors, a very few research papers have been published on multilayer systems. Balakrishnan et al. [11,12] have analyzed the thermal stability and thermal expansion behavior of $ZrO_2/Al_2O_3$ and $CeO_2/ZrO_2$ multilayer films deposited by PLD technique. Barshilia et al.[13] have prepared $ZrO_2/Al_2O_3$ and $ZrO_2/Y_2O_3$ by sputtering technique and analyzed the microstructural and nanomechanical properties of the films. $CeO_2/Gd_2O_3$ multilayers have been prepared by Burinskas et al. [14] by magnetron sputtering technique to prepare gadolinia doped ceria electrolyte by solid state reactions at interfaces. However, analysis of the thermal stability and CTE of the multilayers $ZrO_2/Y_2O_3$ and $CeO_2/Gd_2O_3$ as a function $ZrO_2$ and $CeO_2$ layer thickness, respectively have not been reported so far.

The present study includes the deposition of $Y_2O_3$, $ZrO_2$, $CeO_2$ and $Gd_2O_3$ thin films and $ZrO_2/Y_2O_3$ and $CeO_2/Gd_2O_3$ by PLD technique using the predetermined deposition rates. The phase stability and thermal expansion property of the films were analyzed by HTXRD.

## 5.2 Experimental Procedure

$Y_2O_3$, $ZrO_2$, $CeO_2$ and $Gd_2O_3$ targets were used to deposit respective films of ~1 μm thickness on Si (100) substrates at the substrate temperature of 300 K and oxygen partial pressure of 2 Pa. The details of the target sintering methods and their characterization were already discussed in Chapter 2. The multilayers of $ZrO_2/Y_2O_3$ and $CeO_2/Gd_2O_3$ were prepared on Si substrates at 300 K and 873 K, respectively. The details of the deposition parameters were listed in Table 1. In case of multilayers, the layer thickness of $ZrO_2$ and $CeO_2$ were varied from 5 to 30 nm, whereas the $Y_2O_3$ and $Gd_2O_3$ layer thickness was kept at 10 nm. The total thickness of the multilayer films was kept constant by varying the bilayer thickness (modulation wavelength) (Table 1). The total number of bilayers that were deposited for the $ZrO_2$ and $CeO_2$ layer thickness of 5, 10, 20 and 30 nm was 65, 50, 35 and 25, respectively.

The HTXRD experiments for the single and multilayer films were carried out using an INEL XRG-3000 X-ray diffractometer, attached with a high temperature attachment. The thin film sample was kept on a tantalum strip surrounded with a tantalum heater assembly and heated from 300 to 1373 K in vacuum (0.002 Pa) with a heating rate of 10 K/min. Data was collected for every 100 K interval using a curved position sensitive detector for 15 min, in the 2Ө range of 10-95°, with a step size of 0.0125˚ and incident angle (ω) of 5˚. Temperature of the surrounding as well as sample was measured by a W-Re thermocouple with ± 2° K tolerance. The sample was cooled with a rate of 50 K/min, after obtaining the data at 1373 K. Measurement of CTE values by HTXRD is only applicable for crystalline films [15], and also it is a well known phenomena that all the thin film structures are always associated with internal stress due to presence of defects, incorporation of residual atoms and voids [16,17]. To overcome these difficulties, Lebrun et al. [18] have suggested annealing the film at suitable temperatures followed by heat treatments. Heat treatment of the films was done for two times: the first heat treatment was carried out to relieve stress and form a crystalline film and the second heat treatment was carried out to collect the data on lattice parameter in order to determine the thermal expansion values. From the HTXRD patterns, the phase evolution, lattice parameter (equation 2.2-2.3) and average coefficient of thermal expansion (CTE) and instantaneous coefficient of thermal expansion (CTE) (equation 2.6, 2.7) for each film was calculated. The details of the calculation method were already discussed in Chapter 2. In all the cases, the average CTE values are only tabulated and referred in the present work.

The heat treated samples were analyzed by HRTEM to study the stability of the multilayers across the interfaces.

**Table 5.1 Experimental details for the multilayer formation.**

| **Parameters** | **$ZrO_2/Y_2O_3$** | **$CeO_2$/ $Gd_2O_3$** |
|---|---|---|
| Laser energy | 300 mJ/pulse | 300 mJ/pulse |
| Repetition rate | 10 Hz | 10 Hz |
| Substrate temperature | 300 K | 873 K |
| Oxygen partial pressure | 2 Pa | 2 Pa |
| Deposition rate | $Y_2O_3$ (8 nm/min)<br>ZrO2 (5 nm/min) | $CeO_2$ (6 nm/ min)<br>$Gd_2O_3$ (14 nm/min) |
| $ZrO_2$ and $CeO_2$ layer thickness (nm) measured By deposition rate. | 5,10,20,30 | 5,10,20,30 |

## 5.3 Results

In this section, the HTXRD results of the single as well as multilayers in situ heat treated in the temperature range of 300- 1373 K to study the phase evolution, stability and thermal expansion properties.

### 5.3.1 HTXRD of $Y_2O_3$, $ZrO_2$, $CeO_2$ and $Gd_2O_3$ thin films

This section includes the thermal stability and coefficient of thermal expansion analysis of the thin films of $Y_2O_3$, $ZrO_2$, $CeO_2$ and $Gd_2O_3$ deposited on Si (100) substrates at the substrate temperature of 300 K and oxygen partial pressure of 2 Pa.

### 5.3.1.1 HTXRD of $Y_2O_3$ film

Figure 5.1 (a) shows the HTXRD pattern of the $Y_2O_3$ film in the temperature range 300-1373 K, deposited on Si (100) at 300 K and oxygen partial pressure of 2 Pa. XRD pattern shows that at room temperature, the $Y_2O_3$ film is X-ray amorphous. Crystallization was found to occur at 773 K. For temperature ≥ 773 K, the film becomes polycrystalline in nature, showing peaks from (211), (222), (400), (411), (332), (431), (521), (440), (433), (611), (541), (622), (631), (444), (721), (800), (811), (653), (660), (662) and (840) reflections. All the reflections were from cubic phase of $Y_2O_3$ (JCPDS file no: 41-1105), which indicates the formation of phase pure cubic $Y_2O_3$. The stability of the cubic phase in the above temperature range is in accordance with the phase diagram reported by Swamy et al. [19] and HTXRD analysis of bulk $Y_2O_3$ carried out by Swamy et al.[7].

The crystallite size of the highest intensity peak (222) of $Y_2O_3$ was calculated as a function of temperature and is found to vary between 37 - 50 nm. The lattice parameter values were calculated using "Unit cell program" for the films from the HTXRD pattern (Fig. 5.1 (b)) recorded for the second time, after the first heat treatment in the temperature range of 300-1373 K. The lattice parameter values were found to increase linearly from 10.592 ± 0.003 Å to 10.668 ±0.003 Å with the increase in temperature from 300 to 1373 K (Fig. 5.2(a)). The lattice parameter values as a function of temperature was fitted for second order polynomial fitting and follows the equation (5.1).

$$\boldsymbol{a_Y}(\text{Å}) = \mathbf{10.577 \times 10^{-10} + 4.804 \times 10^{-15} \times \boldsymbol{T} + 1.490 \times 10^{-18} \times \boldsymbol{T}^2} \quad \textbf{..... (5.1)}$$

From the equation 5.1 the coefficient of thermal expansion (CTE) values were calculated using equation 2.6. The CTE values are found to vary from 5.37 to 8.39 $\times 10^{-6}$ $K^{-1}$ with increase in the temperature from 300 to 1373 K (Fig. 5.2 (b)), which are in close agreement with the bulk values (~9.3 x $10^{-6}$ $K^{-1}$) [20].

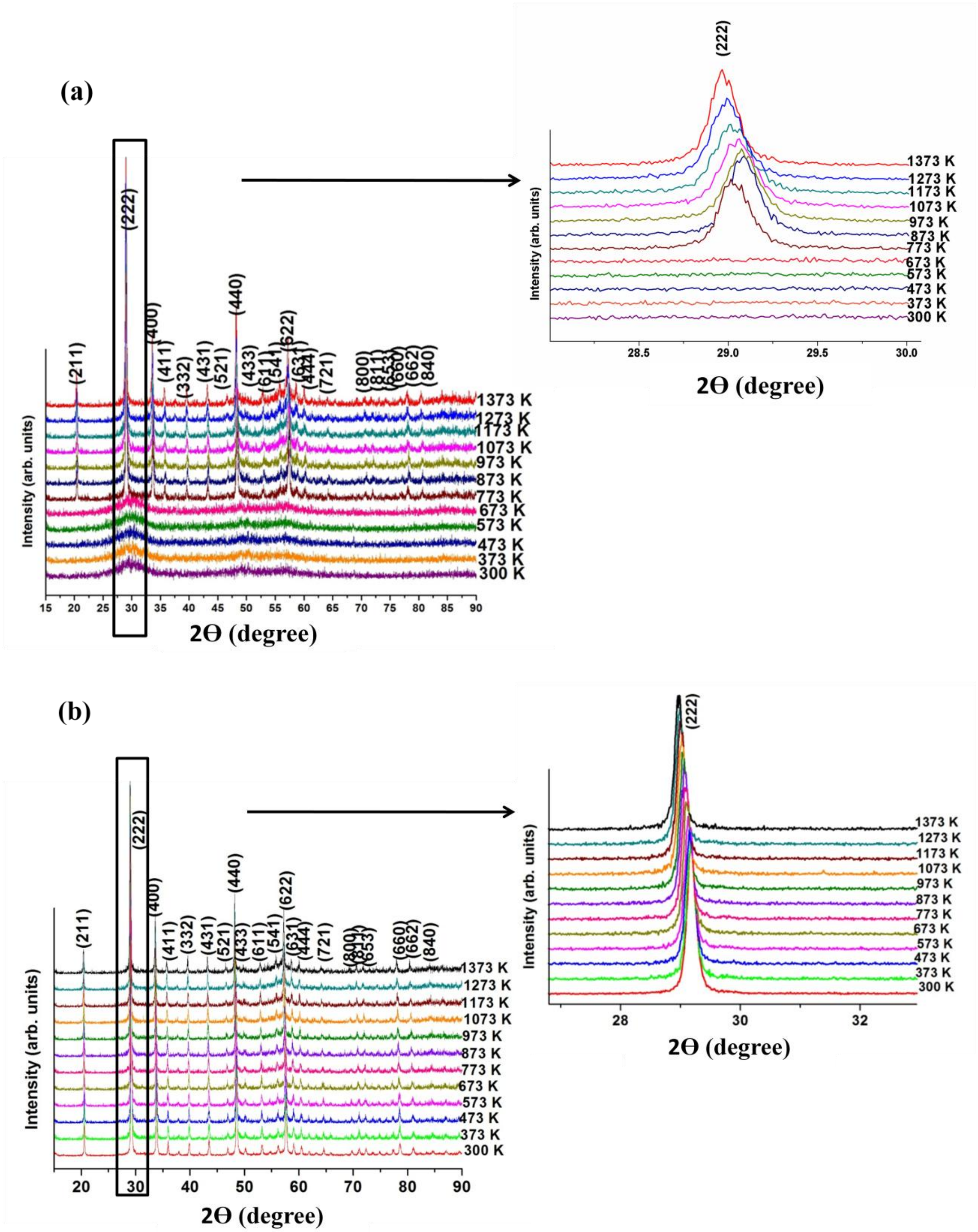

**Fig. 5.1 HTXRD pattern of $Y_2O_3$ film deposited on Si (100) at 300 K and 2 Pa oxygen partial pressure of 2 Pa during the (a) first heat treatment (b) second heat treatment in the temperature range 300-1373 K. The inset shows the shift in the 2Θ position of (222) reflection versus temperature.**

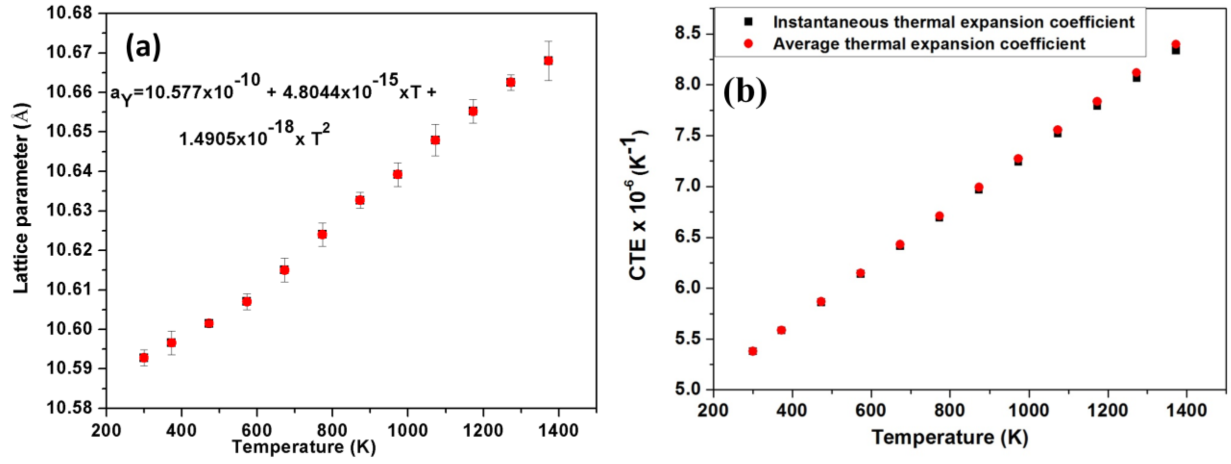

**Fig. 5.2 Variation in the (a) lattice parameter and (b) average and instantaneous CTE values of $Y_2O_3$ with change in temperature.**

**Table 5.2 Lattice parameter and average CTE values of $Y_2O_3$ at different temperature.**

| **Temperature (K)** | **Lattice parameter (Å)** | **CTE x $10^{-6}$ ($K^{-1}$)** |
|---|---|---|
| 300 | 10.592 | 5.37 |
| 373 | 10.596 | 5.58 |
| 473 | 10.602 | 5.86 |
| 573 | 10.607 | 6.14 |
| 673 | 10.615 | 6.42 |
| 773 | 10.624 | 6.71 |
| 873 | 10.633 | 6.99 |
| 973 | 10.639 | 7.27 |
| 1073 | 10.647 | 7.55 |
| 1173 | 10.655 | 7.83 |
| 1273 | 10.662 | 8.11 |
| 1373 | 10.668 | 8.39 |

#### 5.3.1.2 Analysis of $ZrO_2$ film by HTXRD

$ZrO_2$ film was in situ heat treated from 300 to 1373 K (Fig. 5.3 (a)). The HTXRD patterns show the existence of $ZrO_2$ as amorphous structure from 300 to 573 K. XRD pattern of the films shows the formation of polycrystalline $ZrO_2$ at the temperature 673 K. Unlike the phase pure c-$Y_2O_3$, HTXRD pattern of $ZrO_2$ shows a mixture of monoclinic and tetragonal phases. The HTXRD patterns show peaks from ($\bar{1}$11), (002), (131) and (140) of monoclinic phase and (011), (002), (112), (020), (121), (202) and (123) reflections of tetragonal $ZrO_2$. The crystallite sizes calculated for the (011) reflection of t-$ZrO_2$ and ($\bar{1}$11) reflection of m-$ZrO_2$ are found to vary from 29 to 51 nm and 16 to 54 nm, respectively as a function of temperature.

After the first heat treatment was completed, the sample was cooled down to room temperature and again heat treated for second time from 300 to 1373 K (Fig. 5.3 (b)) to determine the change in lattice parameters and CTE values of t-$ZrO_2$ with the increase in temperature.

The lattice parameters were calculated and listed in Table 5.3. Fig. 5.4 (a) and 5.5 (a) show the plot of the lattice parameters of t-$ZrO_2$ along *a* and *c*- axes, respectively as a function of temperature. The lattice parameter values vary from 3.578 to 3.598 Å along *a*-axis and 5.130 to 5.193 Å along *c*-axis. The data on the change in the lattice parameter values along *a* and *c* axes versus temperature were fitted for 2nd order polynomial fitting and have been found to obey the equation 5.2 and 5.3, respectively.

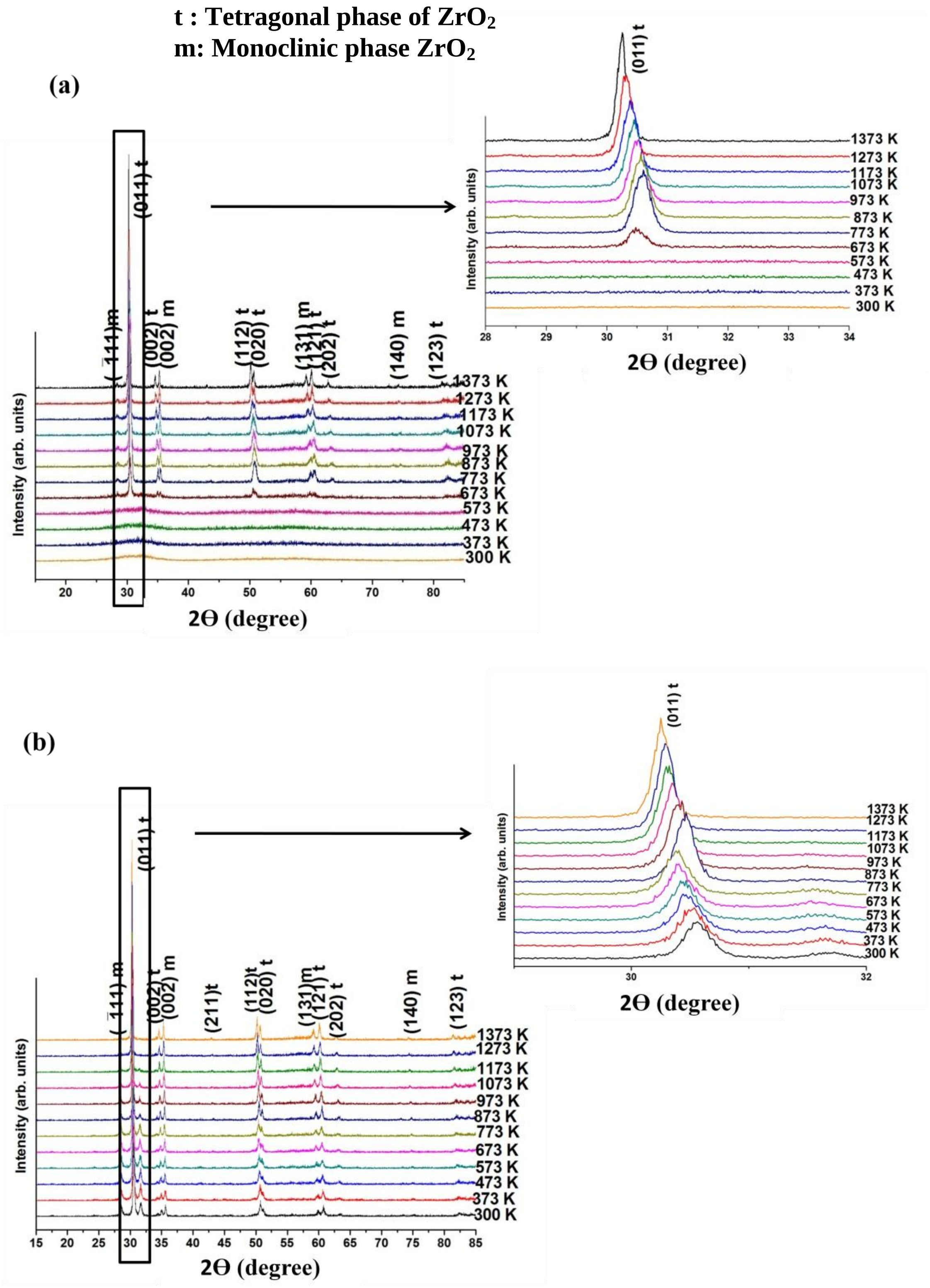

Fig. 5.3 The HTXRD pattern of $ZrO_2$ film deposited on Si (100) at 300 K and oxygen partial pressure of 2 Pa, recorded during the (a) first heat treatment and (b) second heat treatment in the temperature range 300-1373 K. The inset shows the shift in the 2Θ position of (011) of t-$ZrO_2$ with temperature.

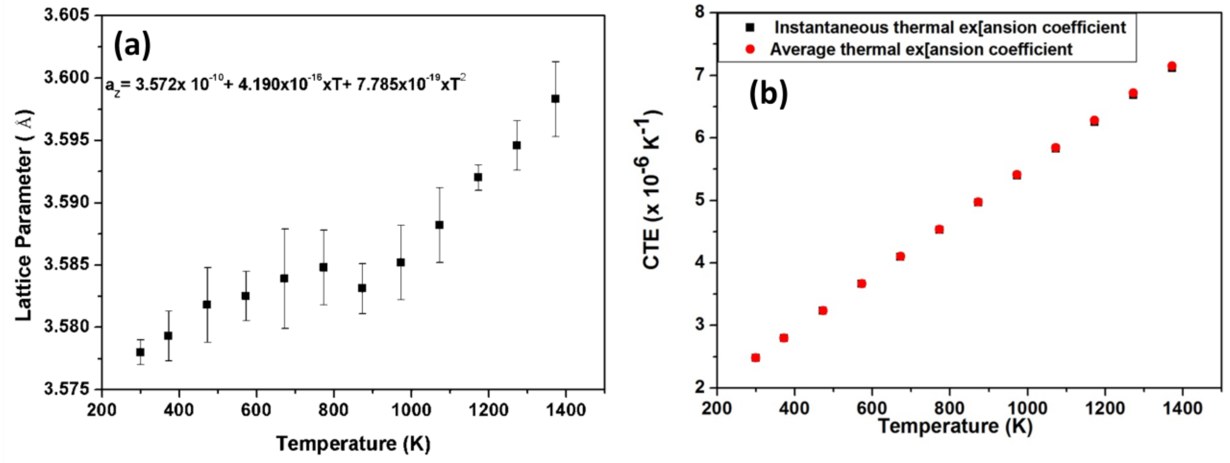

**Fig. 5.4 (a) Lattice parameter and (b) average and instantaneous CTE of t-$ZrO_2$ film as a function of temperature along a-axis.**

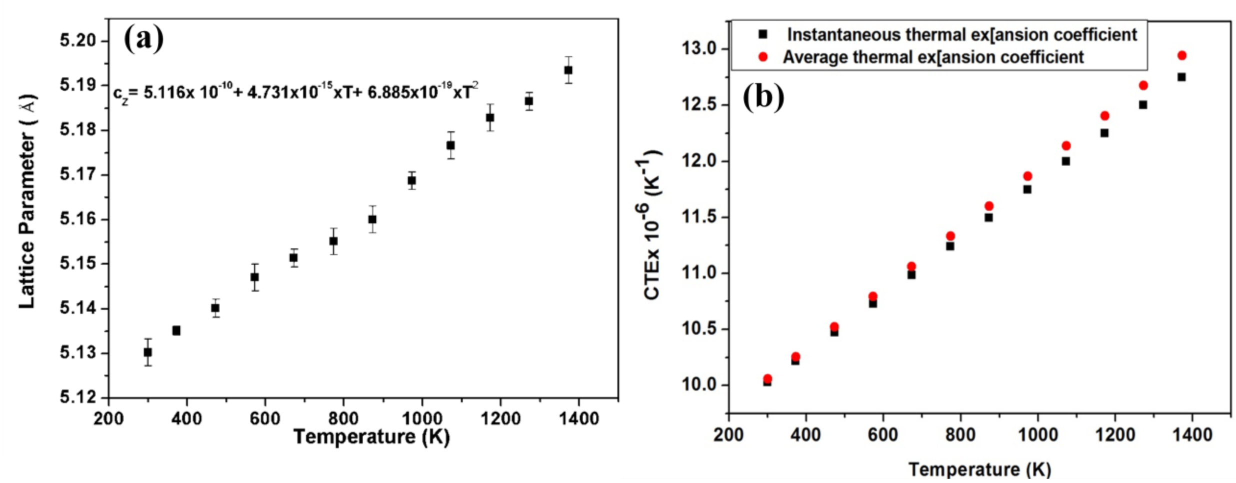

**Fig. 5.5 Variation in the (a) lattice parameter and (b) ) average and instantaneous CTE of t-$ZrO_2$ thin films along c-axis with the increase in temperature.**

**Table 5.3 Lattice parameter and average CTE values of t-$ZrO_2$ film at different temperature.**

| **Temperature (±1 K)** | **Lattice parameter *a* (Å)** | **CTE x $10^{-6}$ ($K^{-1}$) along *a*-axis** | **Lattice parameter *c* (Å)** | **CTE x $10^{-6}$ ($K^{-1}$) along *c*-axis** |
|---|---|---|---|---|
| 300 | 3.578 | 2.47 | 5.130 | 10.05 |
| 373 | 3.579 | 2.79 | 5.135 | 10.25 |
| 473 | 3.582 | 3.23 | 5.140 | 10.52 |
| 573 | 3.582 | 3.66 | 5.147 | 10.79 |
| 673 | 3.584 | 4.10 | 5.151 | 11.06 |
| 773 | 3.585 | 4.53 | 5.155 | 11.33 |
| 873 | 3.583 | 4.97 | 5.160 | 11.59 |
| 973 | 3.585 | 5.40 | 5.168 | 11.86 |
| 1073 | 3.588 | 5.84 | 5.176 | 12.13 |
| 1173 | 3.592 | 6.27 | 5.182 | 12.40 |
| 1273 | 3.595 | 6.71 | 5.186 | 12.67 |
| 1373 | 3.598 | 7.15 | 5.193 | 12.94 |

$$\boldsymbol{a_Z}(\text{Å}) = \mathbf{3.576} \times \mathbf{10^{-10}} + \mathbf{4.190} \times \mathbf{10^{-16}} \times \boldsymbol{T} + \mathbf{7.785} \times \mathbf{10^{-19}} \times \boldsymbol{T^2} \ldots\ldots \text{ (5.2)}$$

$$\boldsymbol{c_Z}(\text{Å}) = \mathbf{5.116} \times \mathbf{10^{-10}} + \mathbf{4.731} \times \mathbf{10^{-15}} \times \boldsymbol{T} + \mathbf{6.885} \times \mathbf{10^{-19}} \times \boldsymbol{T^2} \ldots\ldots \text{ (5.3)}$$

The average CTE values of t-$ZrO_2$ both along a and c axes were calculated and listed in Table 5.3. The CTE values obtained for t-$ZrO_2$ along a and c axes are in the range of 2.47 - 7.15 x $10^{-6}$ $K^{-1}$ and 10.05- 12.95 x $10^{-6}$ $K^{-1}$, respectively (Fig 5.4 (b) and 5.5 (b)). The CTE values obtained in the present analysis are lower compared to the results reported by Patil et al. (CTE for *a* and *c* axes are 11.6x$10^{-6}$ and 16.08x$10^{-6}$ per K) [8] for bulk t-$ZrO_2$ samples. Whereas the results are in accordance with the values reported by Bhagwat et al. [21] for nanocrystalline t-$ZrO_2$ thin films. The decreases in the CTE values of $ZrO_2$ than that of the bulk value are due to the presence of mixed phasesk leading to presence of stress in the films. The difference in the CTE values along *a* and *c*- axis shows the anisotropic expansion of $ZrO_2$ and higher expansion along z direction.

### 5.3.1.3 HTXRD of $CeO_2$

Figure 5.6 (a) shows the HTXRD pattern of $CeO_2$ thin film deposited on Si (100) substrates at 300 K and oxygen partial pressure of 2 Pa, recorded in the temperature range 300 – 1373 K during the first heat treatment. $CeO_2$ forms a polycrystalline structure even at room temperature. All the peaks in HTXRD pattern belongs to cubic $CeO_2$ (c-$CeO_2$), which concludes, the existence of $CeO_2$ in a phase pure cubic state in the above temperature range. The film shows peaks from (111), (200), (220), (311), (400), (331), (420) and (422) planes. Crystallite size was calculated for the strongest (200) reflection and is found to vary from 46 to 58 nm with increase in temperature. The stress value was estimated for the $CeO_2$ films from the XRD pattern of the film before and after the first heat treatment from $\Delta d/d_0$ (where $\Delta d = d- d_0$ and d is the d-spacing measured for the sample and $d_0$ is the d-spacing of the annealed sample from the JCPDS file) and were found to be 0.013 and 0.001 respectively. This clearly indicated a stress relief by heat treatment.

After the first heat treatment, the film was cooled down to room temperature and was again heat treated from 300 to 1373 K in vacuum (Fig. 5.6 (b)) and the lattice parameter values were calculated at each temperature, using the “unit cell” program and listed in Table 5.4. The lattice parameter of $CeO_2$ increases from 5.420 to 5.488 Å with the increase in temperature from 300 to 1373 K. The equation obtained after fitting the lattice parameter versus temperature plot for a second order polynomial is given below (equation 5.4).

$$\boldsymbol{a_{Ce}}(\text{Å}) = \mathbf{5.412 \times 10^{-10} + 1.436 \times 10^{-15} \times \boldsymbol{T} + 2.9429 \times 10^{-18} \times \boldsymbol{T}^2}\ldots\ldots \textbf{(5.4)}$$

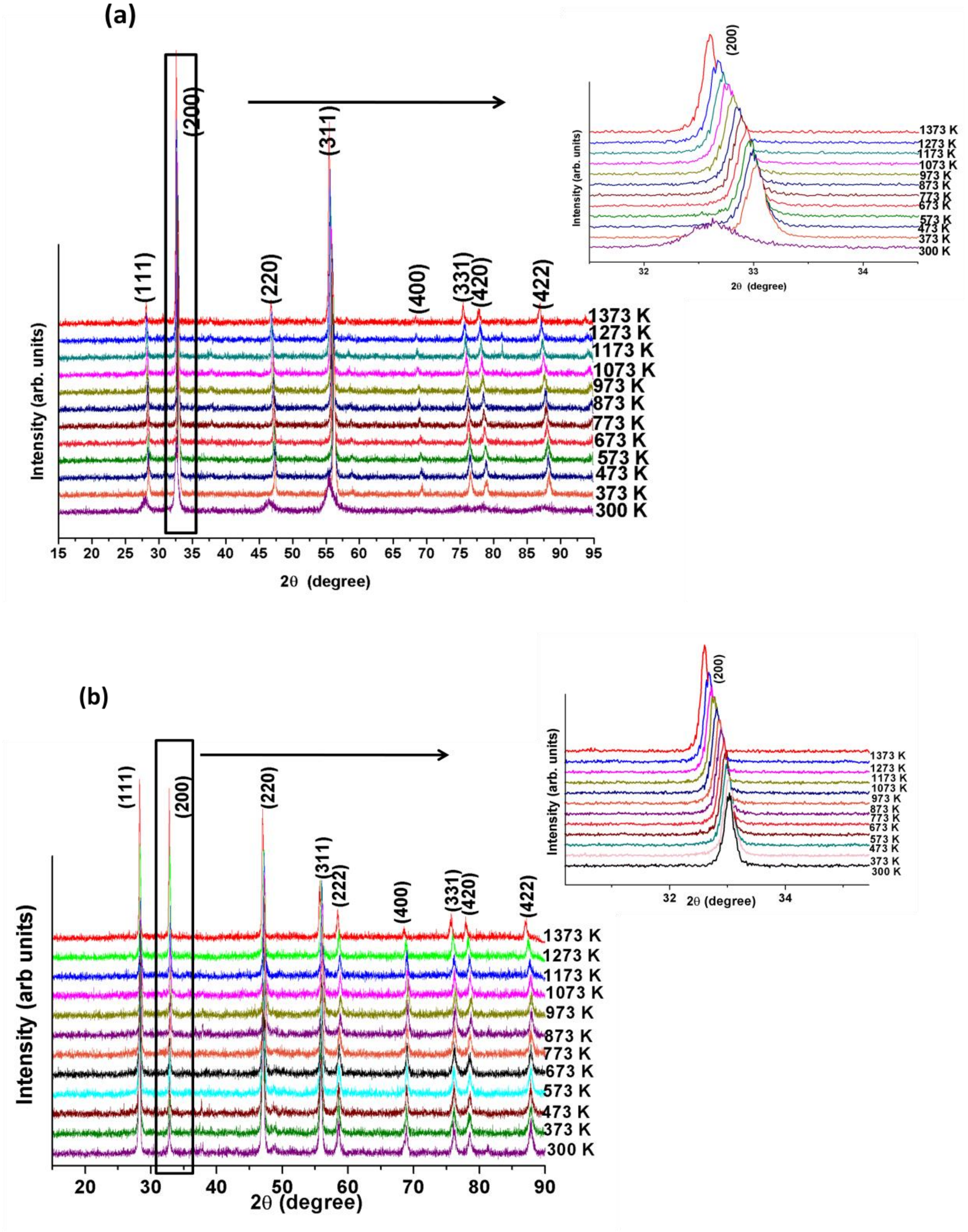

**Fig. 5.6 shows the diffractogram of $CeO_2$ film deposited on Si(100) at the substrate temperature of 300 K and oxygen partial pressure of 2 Pa, obtained during the (a) first heat treatment and (b) second heat treatment in the temperature range 300 -1373 K. The inset shows the shift in (200) reflection with increase in temperature.**

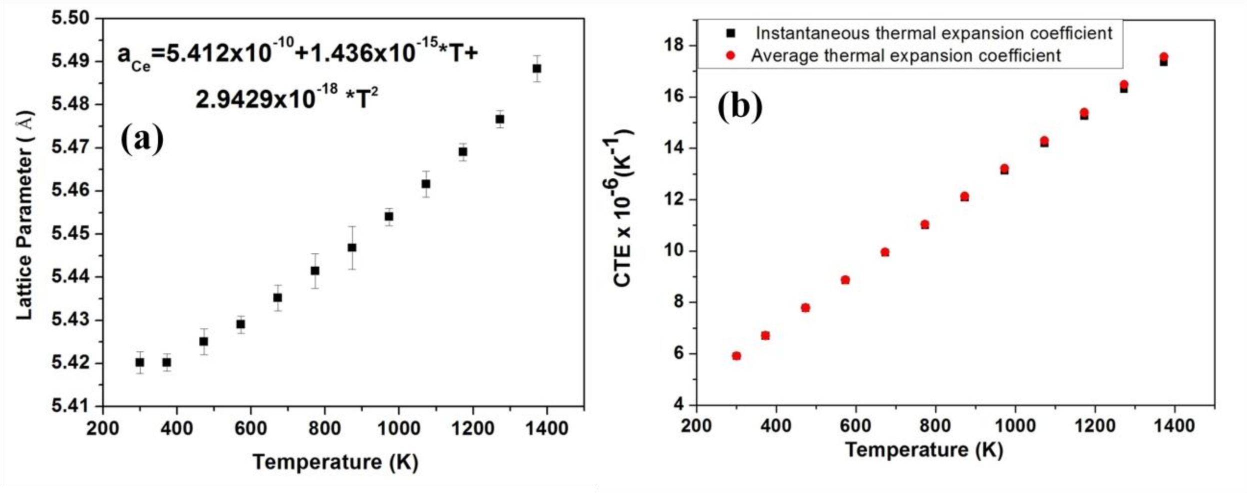

**Fig. 5.7 Variation in the (a) lattice parameter and (b) average and instantaneous CTE values of $CeO_2$ with change in temperature.**

**Table 5.4 The lattice parameters and average CTE values of $CeO_2$ at different temperature.**

| **Temperature (K)** | **Lattice parameter ( Å)** | **Average CTE x $10^{-6}$ ($K^{-1}$)** |
|---|---|---|
| 300 | 5.420 | 5.90 |
| 373 | 5.420 | 6.70 |
| 473 | 5.425 | 7.78 |
| 573 | 5.429 | 8.87 |
| 673 | 5.435 | 9.95 |
| 773 | 5.441 | 11.04 |
| 873 | 5.446 | 12.13 |
| 973 | 5.454 | 13.21 |
| 1073 | 5.462 | 14.30 |
| 1173 | 5.469 | 15.39 |
| 1273 | 5.476 | 16.47 |
| 1373 | 5.488 | 17.56 |

The average CTE values were calculated using equation 5.3 are listed in Table 5.4. The CTE values obtained varies from 5.90 x $10^{-6}$- 17.56 x $10^{-6}$ $K^{-1}$ with increases in temperature. The CTE values obtained are slightly differing from the bulk values reported in literature (~11.5 x$10^{-6}$ $K^{-1}$) [9], where as the result are in accordance with the average CTE values reported in the literature for $CeO_2$ thin films [22,23].

#### 5.3.1.4 HTXRD of $Gd_2O_3$

Figure 5.8 (a) shows the HTXRD pattern of $Gd_2O_3$ film deposited on Si (100) at 300 K and oxygen partial pressure of 2 Pa in the temperature range 300- 1373 K. The film was found to be X-ray amorphous, up to the temperature 673 K. For temperature ≥ 773 K the film became polycrystalline nature. The $Gd_2O_3$ was stabilized in cubic phase in the temperature range of 773-1373 K. No other phases were observed which may be due to the phase transformation range of $Gd_2O_3$ [24]. The XRD pattern shows peaks for (211), (222), (123), (411), (332), (134), (440), (611), (145), (622), (444), (662) and (048) reflections. At all temperatures, the (222) reflection shows the highest peak intensity similar to that of the JCPDS file (#01-076-8040). The crystallite size calculated for the (222) reflection of $Gd_2O_3$ varied from 52 to 68 nm at different temperatures.

After the first heat treatment, the $Gd_2O_3$ film was heat treated for the second time and the data were recorded from 300 to 1373 K, to calculate the lattice parameter and CTE values and are shown in Fig. 5.8 (b). Lattice parameter values were calculated using “unit cell program” from the HTXRD pattern of the $Gd_2O_3$ film, recorded for the second time and were listed in Table 5.5. The lattice parameter showed an increasing trend with increase in temperature up to 1373 K (Fig. 5.9(a)). The equation obtained after fitting the lattice parameter versus temperature is given in equation 5.5.

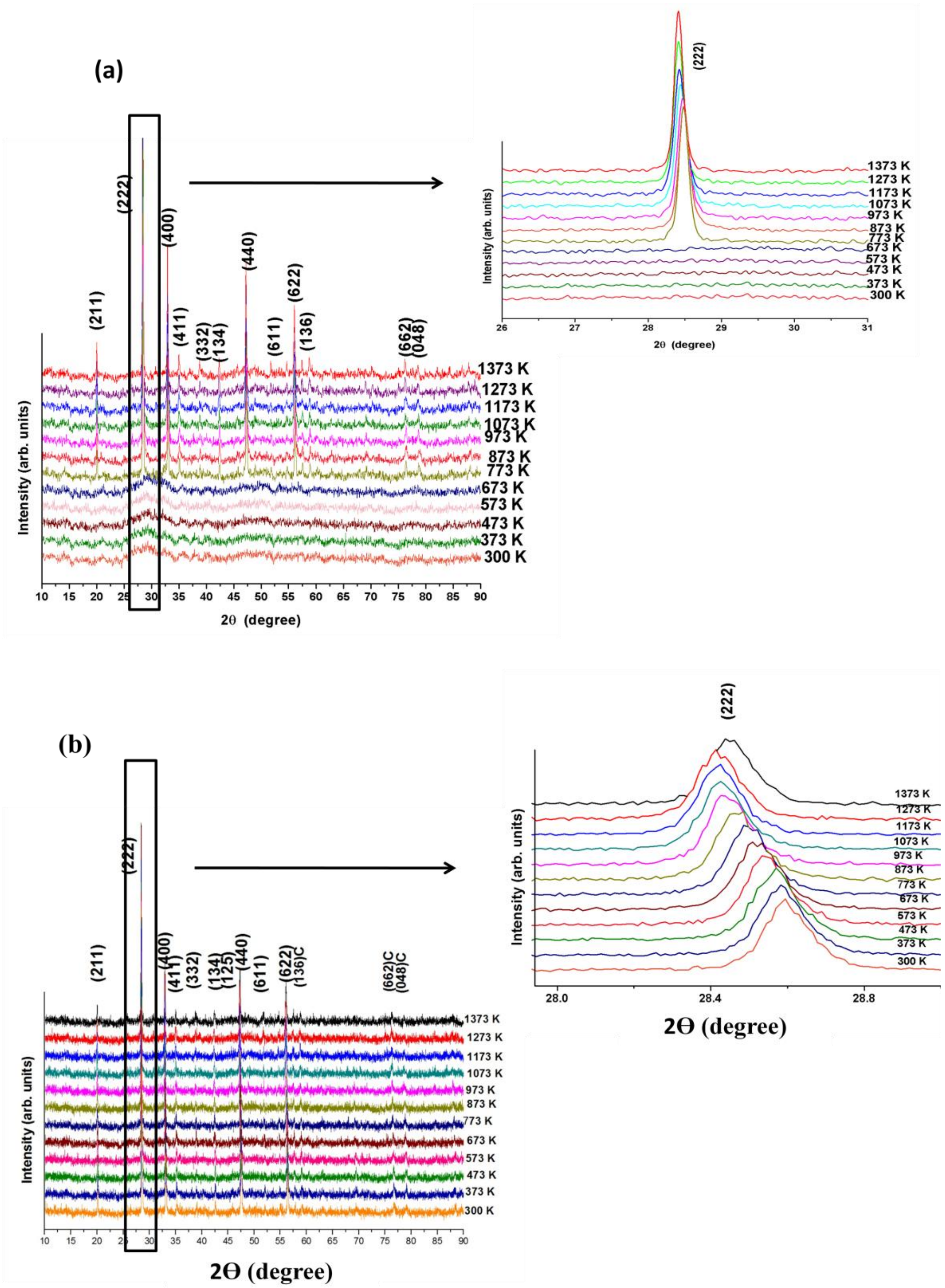

Fig. 5.8 The HTXRD pattern of $Gd_2O_3$ film deposited on Si (100) at 300 K and oxygen partial pressure of 2 Pa for the temperature range 300 -1373 K, recorded during the (a) first heat treatment and (b) second heat treatment. The inset shows the shift in 2ϴ positions of (222) reflection as a function of temperature.

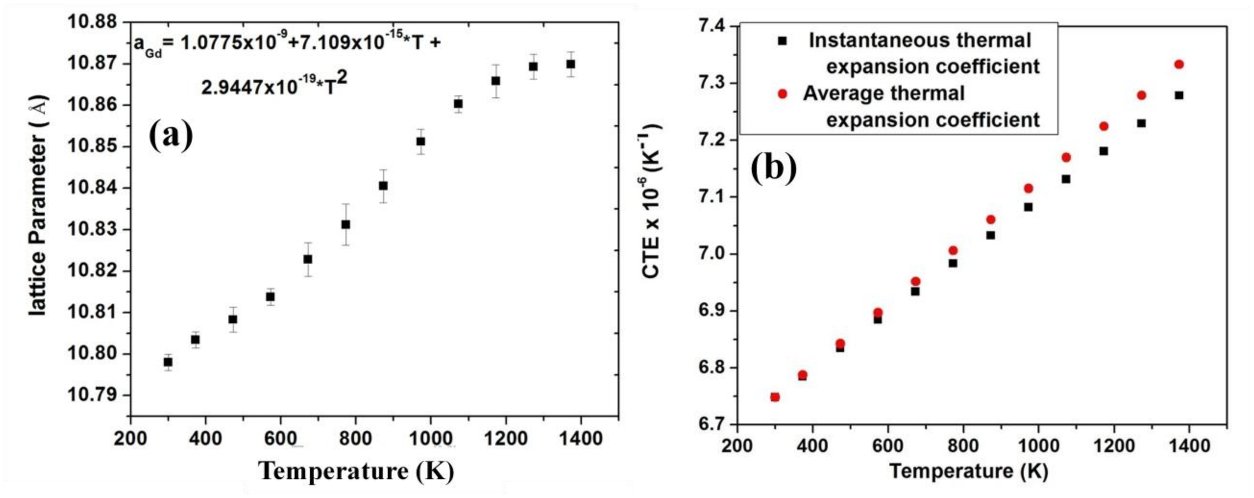

**Fig. 5.9 Variation of the (a) lattice parameter and (b) average and instantaneous CTE values of $Gd_2O_3$ with the change in temperature.**

**Table 5.5 The lattice parameter and average CTE values of $Gd_2O_3$ obtained at different temperature.**

| **Temperature (K)** | **Lattice parameter ( Å)** | **CTE x $10^{-6}$ ($K^{-1}$)** |
|---|---|---|
| 300 | 10.798 | 6.89 |
| 373 | 10.803 | 6.95 |
| 473 | 10.808 | 7.00 |
| 573 | 10.814 | 7.06 |
| 673 | 10.823 | 7.11 |
| 773 | 10.831 | 7.16 |
| 873 | 10.841 | 7.22 |
| 973 | 10.851 | 7.27 |
| 1073 | 10.860 | 7.33 |
| 1173 | 10.866 | 6.89 |
| 1273 | 10.869 | 6.95 |
| 1373 | 10.869 | 7.00 |

$$\boldsymbol{a_{Gd}}(\text{Å}) = \mathbf{1.0775 \times 10^{-9} + \ 7.109 \times 10^{-15} \times \boldsymbol{T} + 2.9447 \times 10^{-19} \times \boldsymbol{T}^2 \ldots\ldots\ (5.5)}$$

Using the above equation the CTE values were calculated and listed in Table 5.5. The CTE values varied from 6.8 to 7.3 x $10^{-6}$ $K^{-1}$. The calculated CTE values are in accordance with the values reported in literature (~7.5 x $10^{-6}$ $K^{-1}$ ) [25]. The $Gd_2O_3$ films show very small change in CTE values with change in the temperature.

### 5.3.2 HTXRD of multilayers of $ZrO_2/Y_2O_3$ and $CeO_2$ /$Gd_2O_3$

The present section describes the thermal stability and CTE analysis carried out by the HTXRD technique of the multilayer films, and studies the effect of bilayer thickness on phase stability and thermal expansion behavior. The total thickness of the multilayers was kept constant by varying the total number of bilayers. Thermal expansion behavior of the multilayers of bilayer thickness (30/10), (20/10), (10/10) and (5/10) nm of $ZrO_2/Y_2O_3$ and $CeO_2$ /$Gd_2O_3$ are investigated.

#### 5.3.2.1 HTXRD of $ZrO_2/Y_2O_3$ multilayer (30/10) nm

Multilayer of $ZrO_2/Y_2O_3$ of (30/10) nm was deposited on Si(100) at 300 K and oxygen partial pressure of 2 Pa. The sample was heat treated in the temperature range 300 -1373 K in vacuum and the HTXRD pattern is shown in Fig. 5.10 (a). The film was found to be X-ray amorphous at 300 K and started to crystallize at the temperature 773 K. The film was polycrystalline in nature showing peaks from (211), (222), (400), (431), (440), (622), (631), (640) and (011), (002), (112), (020), (121), (220), (123), (222) planes of c-$Y_2O_3$ and t-$ZrO_2$, respectively. $Y_2O_3$ and $ZrO_2$ exist in cubic and tetragonal phase in the temperature the temperature range 773 -1373 K. A small volume fraction of metastable m-$Y_2O_3$ was also observed in the temperature range of 773-873 K, along with c-$Y_2O_3$ and disappeared as the temperature ≥ 973 K. Gourlaouen et al. [26] have reported the formation of small volume fraction of m-$Y_2O_3$ along with the c-$Y_2O_3$ as the major phase, when deposited in the form of thin films as a result of large amount of stress formation during the deposition of film. As reported in the literature, m-$Y_2O_3$ is a high pressure phase of $Y_2O_3$. During the initial crystallization process significant amount of stress is generated as the film is a multilayer structure, which leads to formation of small fraction of m-$Y_2O_3$. As the temperature increased, the stress was relieved and the monoclinic phase disappeared. Unlike that of the $Y_2O_3$, $ZrO_2$ was stabilized in phase pure tetragonal structure for entire temperature range. The crystallite size was calculated for the (222) reflection of $Y_2O_3$ and (011) reflection of t-$ZrO_2$ and were of the order of individual layer thickness of $Y_2O_3$ and t-$ZrO_2$. The lattice parameter values were also calculated from the HTXRD data obtained during the first heat treatment, for t-$ZrO_2$ in the multilayer of (30/10) nm thickness at different temperatures and were found to vary from 3.597 to 3.601 Å and 5.153 to 5.183 along *a* and *c* axes, respectively. The lattice parameter of c-$Y_2O_3$ was found to vary from 10.535 to 10.603 Å. The lattice parameter of c-$Y_2O_3$ was found to decrease with increases in the temperature up to 1073 K and then remains almost constant.

After the first heat treatment, the multilayer structure was heat treated for the second time in the temperature range 300 – 1373 K to calculate the lattice parameter as well as the CTE of both $Y_2O_3$ and t-$ZrO_2$. The lattice parameter values were calculated using the “unit cell” program and listed in Table 5.6. The lattice parameters of t-$ZrO_2$ and $Y_2O_3$ showed an increasing trend with the increase in the temperature (Fig. 5.11 (a), Fig. 5.12 (a) and Fig. 5.13 (a)). Lattice parameter versus temperature plots were fitted for the second order polynomial fitting and the fitted polynomials are represented by equation 5.6, 5.7 and 5.8 for t-$ZrO_2$ along *a* and *c*- axis and c-$Y_2O_3$, respectively.

$$\boldsymbol{a_Z}(\text{Å}) = \mathbf{3.5846 \times 10^{-10} + 1.0352 \times 10^{-15} \times \boldsymbol{T} + 1.3386 \times 10^{-20} \times \boldsymbol{T}^2} \text{.........}\mathbf{(5.6)}$$

$$\boldsymbol{c_Z}(\text{Å}) = \mathbf{5.1852 \times 10^{-10} + 3.6693 \times 10^{-16} \times \boldsymbol{T} + 8.4531 \times 10^{-18} \times \boldsymbol{T}^2} \text{.........}\mathbf{(5.7)}$$

$$\boldsymbol{a_Y}(\text{Å}) = \mathbf{1.0435 \times 10^{-9} + 1.0541 \times 10^{-14} \times \boldsymbol{T} + 3.8290 \times 10^{-19} \times \boldsymbol{T}^2} \text{.........}\mathbf{(5.8)}$$

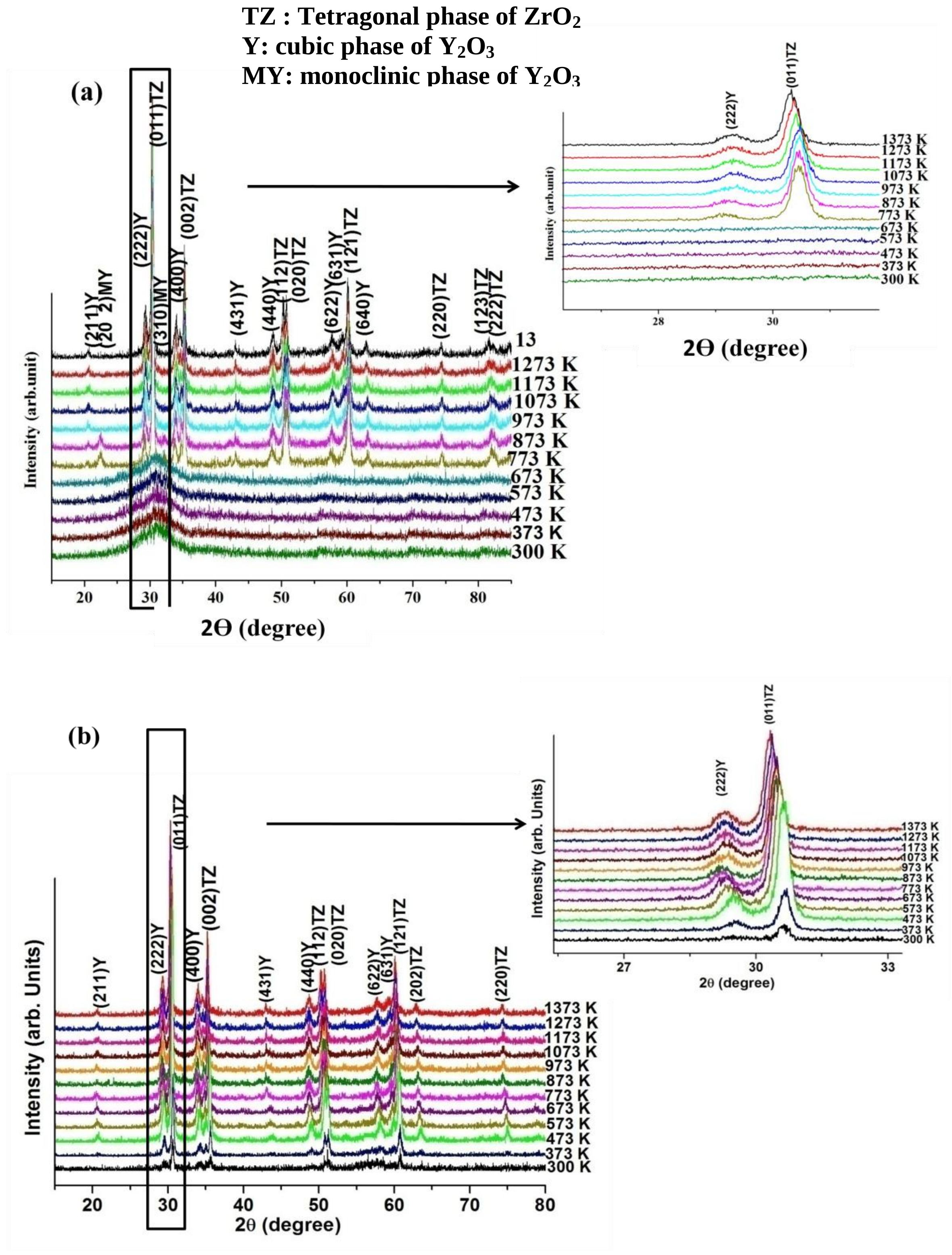

Fig. 5.10 The HTXRD pattern of $ZrO_2/Y_2O_3$ multilayer of (30/10) nm deposited on Si (100) at 300 K and 2 Pa oxygen partial pressure, recorded in the temperature range of 300 -1373 K during the (a) first heat treatment and (b) second heat treatment. The inset shows the shift in 2ϴ positions of the (222) and (011) reflections of $Y_2O_3$ and $ZrO_2$ as a function of temperature.

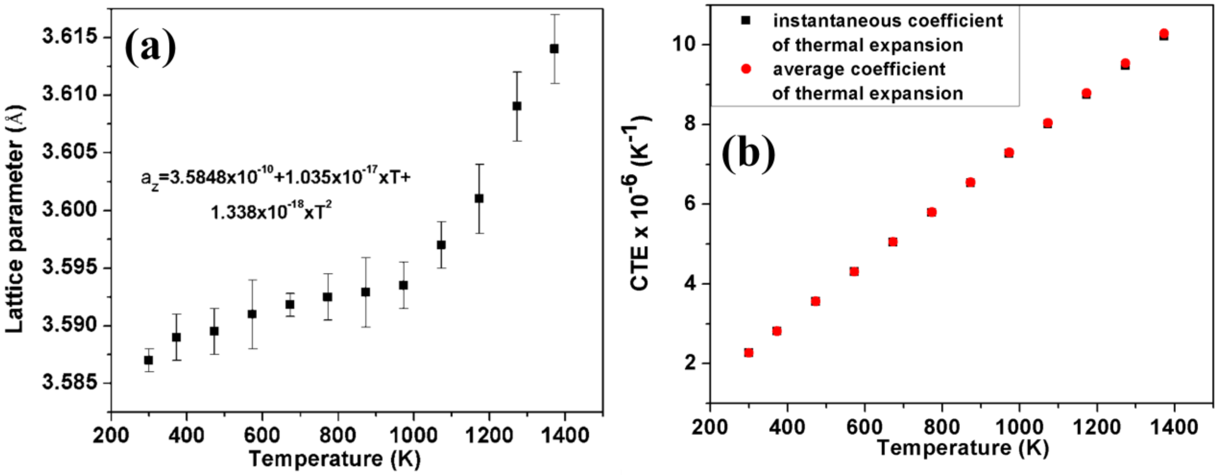

**Fig. 5.11** Variation of the (a) lattice parameter and (b) average and instantaneous CTE values of t-$ZrO_2$ along a-axis with change in temperature in the $ZrO_2/Y_2O_3$ multilayer of (30/10) nm.

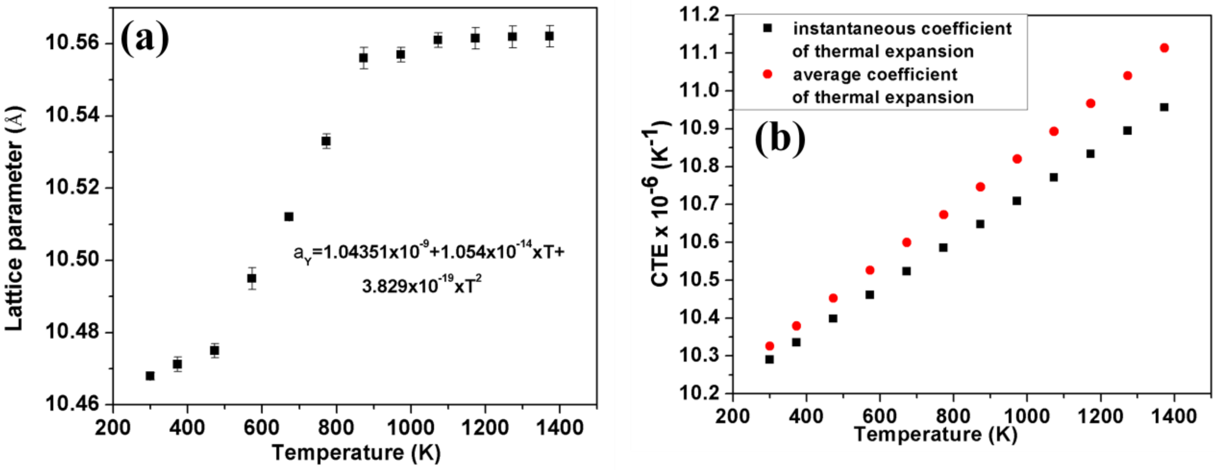

**Fig. 5.12** Variation of the (a) lattice parameter and (b) average and instantaneous CTE values of t-$ZrO_2$ along c-axis as a function of temperature of the $ZrO_2/Y_2O_3$ multilayer of (30/10) nm.

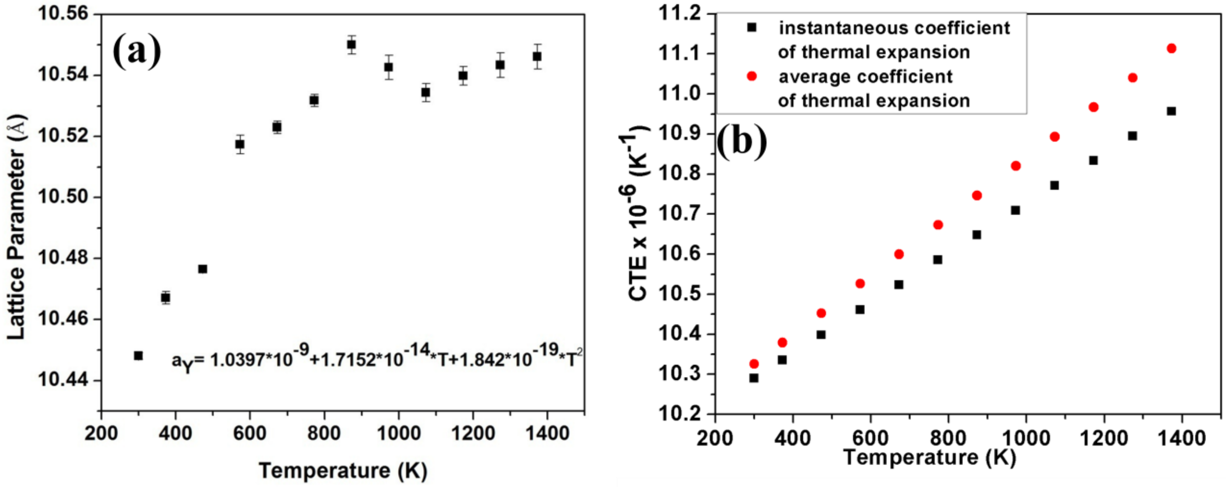

**Fig. 5.13** The variation in (a) lattice parameter and (b) average and instantaneous CTE values of $Y_2O_3$ with increase in the temperature in $ZrO_2/Y_2O_3$ multilayer of (30/10) nm.

**Table 5.6 The lattice parameter and average CTE values of $Y_2O_3$ and $ZrO_2$ at different temperatures for multilayer of $ZrO_2/Y_2O_3$ of (30/10) nm.**

| **Temperature (K)** | **$Y_2O_3$** | | **$ZrO_2$** | | | |
|---|---|---|---|---|---|---|
| | **Lattice parameter ( Å)** | **CTE x $10^{-6}$ ($K^{-1}$)** | **Lattice parameter *a* (Å)** | **CTE x $10^{-6}$ ($K^{-1}$) along a-axis** | **Lattice parameter *c* ( Å)** | **CTE x $10^{-6}$ ($K^{-1}$) along c-axis** |
| 300 | 10.467 | 10.32 | 3.587 | 2.26 | 5.192 | 8.05 |
| 373 | 10.471 | 10.37 | 3.589 | 2.81 | 5.201 | 8.29 |
| 473 | 10.475 | 10.45 | 3.589 | 3.56 | 5.209 | 8.61 |
| 573 | 10.495 | 10.52 | 3.591 | 4.30 | 5.212 | 8.94 |
| 673 | 10.512 | 10.59 | 3.591 | 5.05 | 5.216 | 9.27 |
| 773 | 10.533 | 10.67 | 3.592 | 5.80 | 5.218 | 9.59 |
| 873 | 10.556 | 10.74 | 3.592 | 6.54 | 5.221 | 9.92 |
| 973 | 10.557 | 10.81 | 3.593 | 7.29 | 5.226 | 10.24 |
| 1073 | 10.561 | 10.89 | 3.597 | 8.04 | 5.231 | 10.57 |
| 1173 | 10.561 | 10.96 | 3.601 | 8.78 | 5.239 | 10.90 |
| 1273 | 10.562 | 11.04 | 3.609 | 9.53 | 5.245 | 11.22 |
| 1373 | 10.562 | 11.11 | 3.614 | 10.28 | 5.255 | 11.55 |

The average CTE values of t-$ZrO_2$ obtained from the above equations are ~2-10 x$10^{-6}$ $K^{-1}$ and 8-11 x$10^{-6}$ $K^{-1}$ along *a* and *c*-axes, respectively. The CTE values obtained for c-$Y_2O_3$ was almost constant (10-11 $K^{-1}$).

#### 5.3.2.2 HTXRD of $ZrO_2/Y_2O_3$ multilayers of (20/10) nm

The HTXRD pattern of the $ZrO_2/Y_2O_3$ multilayer of (20/10) nm deposited at 300 K and oxygen partial pressure of 2 Pa was heat treated in the temperature range of 300 -1373 K. the XRD patterns recorded are shown in Fig. 5.14 (a). The film was found to be X-ray amorphous at 300 K and crystallization was found to be initiated at the temperature of 773 K. The film showed polycrystalline nature with peaks from (211), (222), (400), (332), (434), (631) and (831) reflections of c-$Y_2O_3$ and (011), (002), (112), (020), (121), (220), (123) and (222) planes of t-$ZrO_2$. Except c-$Y_2O_3$ and t-$ZrO_2$, small volume fraction of m- $Y_2O_3$ was also observed at temperatures of 773 and 873 K, and disappeared when the temperature was increased beyond 873 K. Similar observation were also made in case of $ZrO_2/Y_2O_3$ multilayer of (30/10) nm. Crystallite size was calculated for (011) and (222) reflections of $ZrO_2$ and $Y_2O_3$, and were found to be of the order of layer thickness. The lattice parameter of c-$Y_2O_3$ was calculated for the film from the HTXRD data recorded during the first heat treatment and was found to decrease from 10.612 to 10.570 Å with the increase in temperature from 773 to 1273 K. The lattice parameter changes for $ZrO_2$ are significant when the temperature was increased beyond 1073 K.

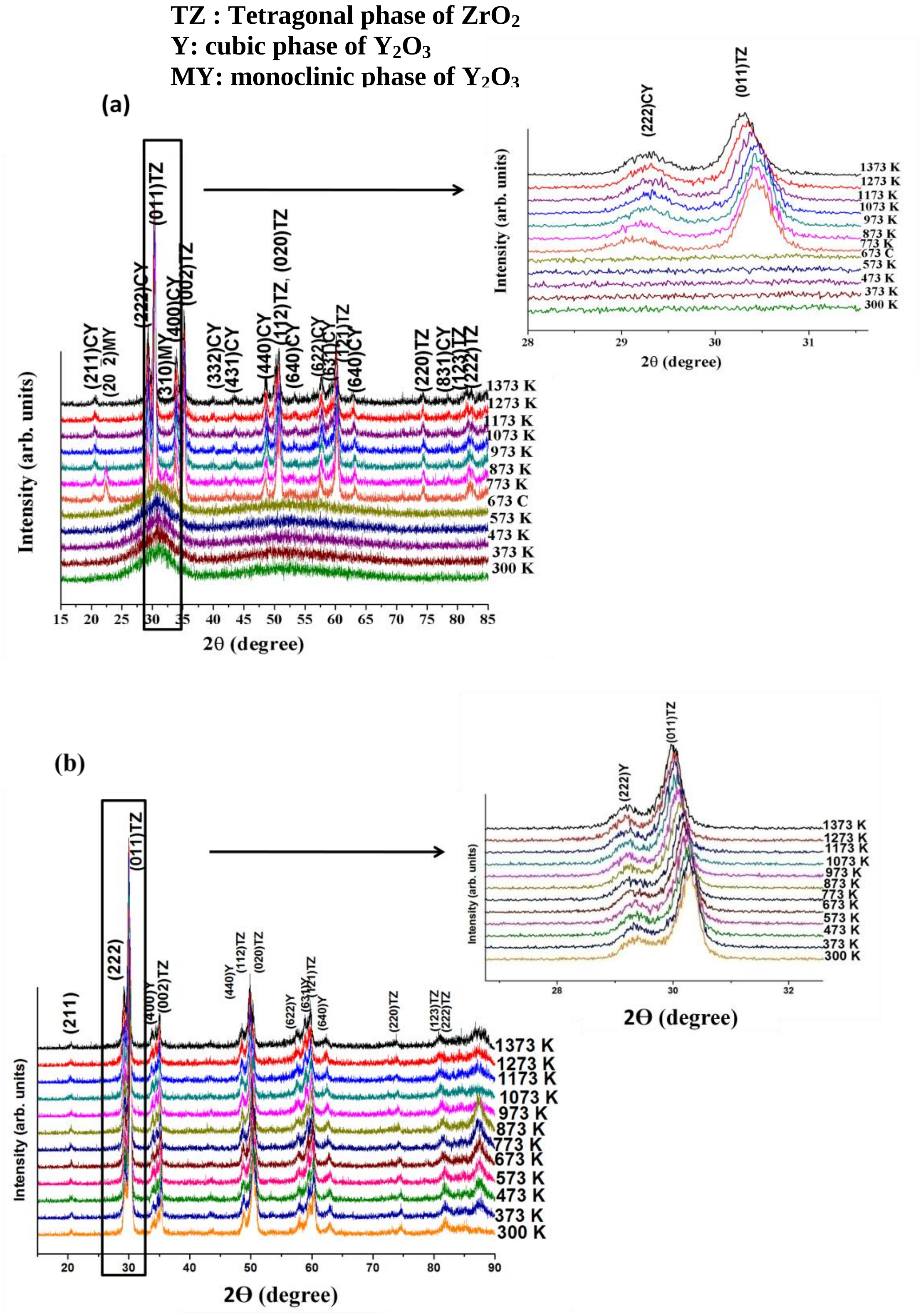

Fig. 5.14 HTXRD pattern of $ZrO_2/Y_2O_3$ film of (20/10) nm deposited on Si (100) at 300 K and oxygen partial pressure of 2 Pa. (a) During first heat treatment and (b) during second heat treatament. The inset shows the shift in position of (222) and (011) reflection of $Y_2O_3$and t-$ZrO_2$, respectively.

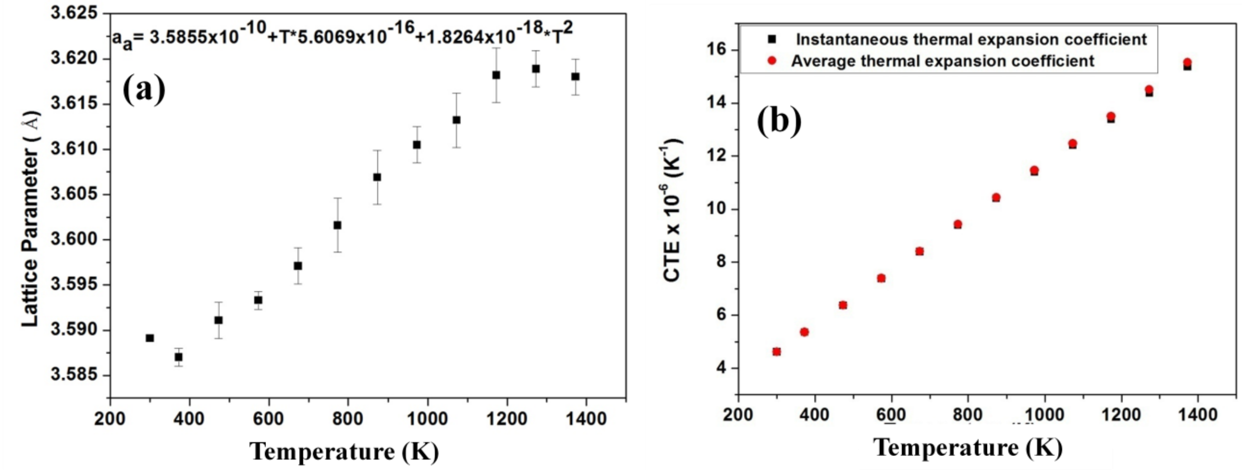

**Fig. 5.15 The variation of (a) lattice parameter and (b) average and instantaneous CTE values of $ZrO_2$ as a function of temperature along a-axis, for the $ZrO_2/Y_2O_3$ multilayer of (20/10) nm.**

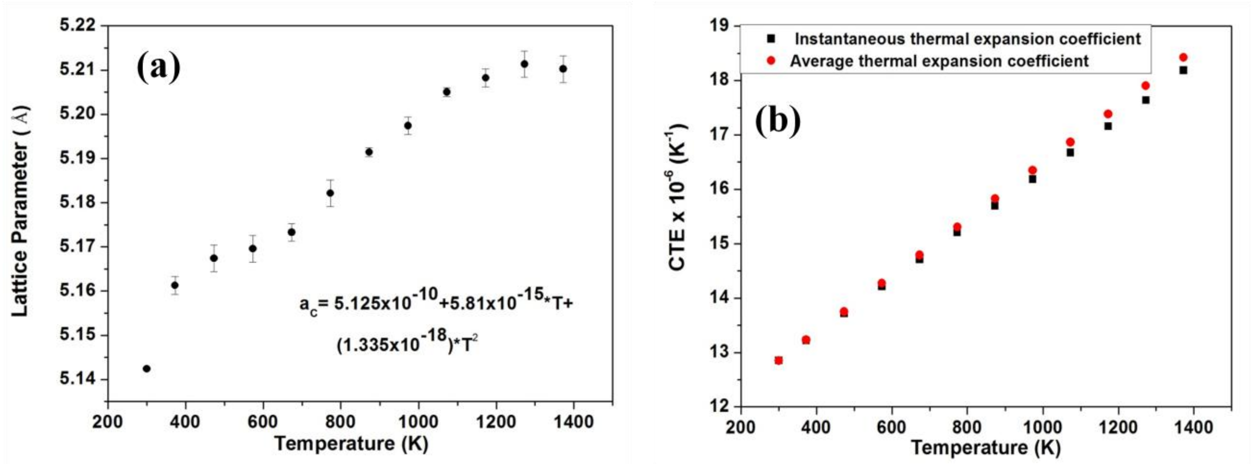

**Fig. 5.16 The (a) lattice parameter and (b) average and instantaneous CTE values of $ZrO_2$ as a function of temperature along c-axis for the $ZrO_2/Y_2O_3$ multilayer of (20/10) nm.**

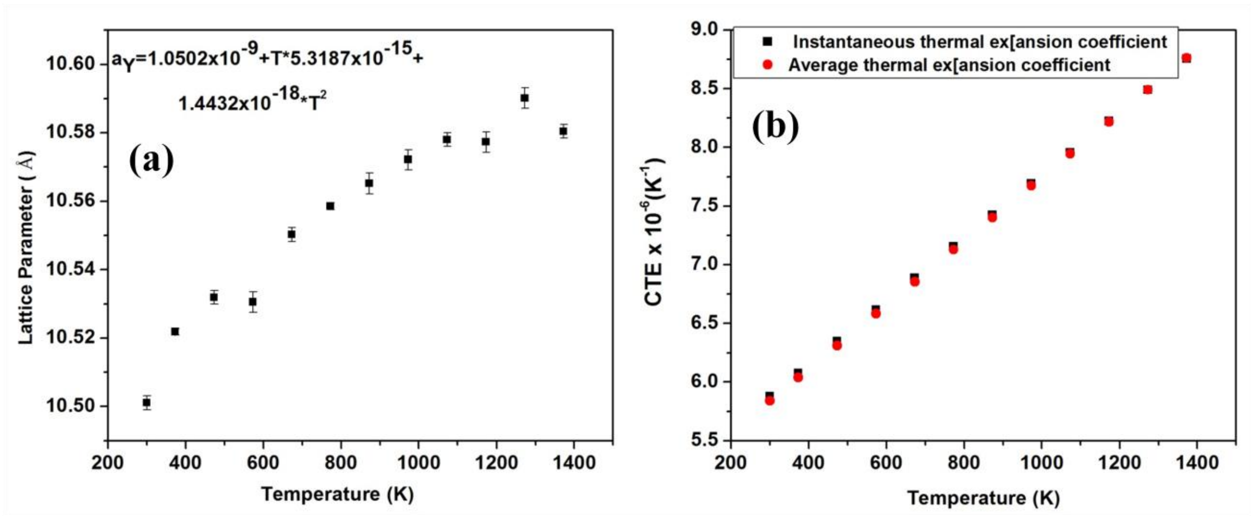

**Fig. 5.17 Variation of the (a) lattice parameter and (b) average and instantaneous CTE values of $Y_2O_3$ as a function of temperature for the $ZrO_2/Y_2O_3$ multilayer of (20/10) nm.**

**Table 5.7 The lattice parameter and the average CTE values of $Y_2O_3$ and $ZrO_2$ at different temperatures for the $ZrO_2/Y_2O_3$ multilayer of (20/10) nm.**

| **Temperature (K)** | $Y_2O_3$ | | $ZrO_2$ | | | |
|---|---|---|---|---|---|---|
| | **Lattice parameter ( Å)** | **CTE x 10$^{-6}$ (K$^{-1}$)** | **Lattice parameter *a* ( Å)** | **CTE x 10$^{-6}$ (K$^{-1}$) along *a*-axis** | **Lattice parameter *c* (Å)** | **CTE x 10$^{-6}$ (K$^{-1}$) along *c*-axis** |
| 300 | 10.501 | 5.83 | 3.589 | 4.61 | 5.1424 | 12.85 |
| 373 | 10.521 | 6.03 | 3.587 | 5.35 | 5.1613 | 13.23 |
| 473 | 10.531 | 6.31 | 3.591 | 6.37 | 5.1674 | 13.75 |
| 573 | 10.530 | 6.58 | 3.593 | 7.39 | 5.1696 | 14.27 |
| 673 | 10.550 | 6.85 | 3.597 | 8.41 | 5.1733 | 14.78 |
| 773 | 10.558 | 7.12 | 3.601 | 9.43 | 5.1821 | 15.30 |
| 873 | 10.565 | 7.40 | 3.606 | 10.44 | 5.1914 | 15.82 |
| 973 | 10.572 | 7.67 | 3.610 | 11.46 | 5.1974 | 16.34 |
| 1073 | 10.577 | 7.94 | 3.613 | 12.48 | 5.2050 | 16.86 |
| 1173 | 10.577 | 8.21 | 3.618 | 13.50 | 5.2082 | 1784 |
| 1273 | 10.590 | 8.49 | 3.619 | 14.51 | 5.2113 | 17.03 |
| 1373 | 10.580 | 8.76 | 3.619 | 15.53 | 5.2102 | 18.42 |

Figure 5.14 (b) shows the HTXRD pattern of the (20/10) nm multilayer of $ZrO_2$ /$Y_2O_3$ multilayer during the second heat treatment. The figure shows (211), (222), (400), (440), (622), (631) and (640) reflections of $Y_2O_3$ and (011), (002), (112), (020), (121), (220), (123) and (222) reflections of t-$ZrO_2$. The lattice parameter values were calculated for t-$ZrO_2$ and c-$Y_2O_3$ and

listed in Table 5.7. The variation in the lattice parameter values of $ZrO_2$ and $Y_2O_3$ with the increase in the temperature is shown in Fig. 5.15 (a), 5.16 (a) and Fig. 5.17 (a), respectively. The lattice parameter values were plotted against temperature for t-$ZrO_2$ and $Y_2O_3$ and were fitted for the second order polynomial fitting satisfying equation 5.9, 5.10 and 5.11 for $ZrO_2$ along *a* and *c* axis and $Y_2O_3$, respectively.

$$\boldsymbol{a_Z}(\text{Å}) = \mathbf{5.125} \times \mathbf{10^{-10}} + \mathbf{5.81} \times \mathbf{10^{-15}} \times \boldsymbol{T} + \mathbf{1.335} \times \mathbf{10^{-18}} \times \boldsymbol{T^2} \text{.......... } \mathbf{(5.9)}$$

$$\boldsymbol{c_Z}(\text{Å}) = \mathbf{3.585} \times \mathbf{10^{-10}} + \mathbf{5.606x10^{-16}} \times \boldsymbol{T} + \mathbf{1.826} \times \mathbf{10^{-18}} \times \boldsymbol{T^2} \text{ ......... } \mathbf{(5.10)}$$

$$\boldsymbol{a_Y}(\text{Å}) = \mathbf{10.502} \times \mathbf{10^{-10}} + \mathbf{5.318x10^{-15}} \times \boldsymbol{T} + \mathbf{1.443} \times \mathbf{10^{-18}} \times \boldsymbol{T^2} \text{...... } \mathbf{(5.11)}$$

Using the above equations the average CTE values were calculated in the temperature range of 300 - 1373 K and are listed in Table 5.7. The average CTE values of t-$ZrO_2$ and c-$Y_2O_3$ was found to vary from 4.61- 15.53 x $10^{-6}$, 12.85- 18.42 x $10^{-6}$ and 5.83- 8.76 x $10^{-6}$ $K^{-1}$, respectively.

### 5.3.2.3 HTXRD of $ZrO_2/Y_2O_3$ multilayers of (10/10) nm

The HTXRD pattern of $ZrO_2/Y_2O_3$ multilayer of (10/10) nm, recorded during the first heat treatment in the temperature range 300-1373 K is shown in Fig. 5.18 (a). Absence of any peaks suggested that the film was X- ray amorphous in the temperature range of 300–673 K and became polycrystalline at temperature ≥ 773 K. XRD pattern contains peaks from (211), (222), (400), (420), (431), (440), (611), (622), (640) planes of c-$Y_2O_3$. Except c-$Y_2O_3$, the XRD pattern also contains peaks from (011), (002), (112), (020), (121), (220) and (222) planes of t-$ZrO_2$. $Y_2O_3$ exists in cubic phase in the above temperature range, except low intensity peaks of monoclinic phase at 773 and 873 K. The crystallite size was calculated for the (222) and (011) reflection of c-$Y_2O_3$ and t-$ZrO_2$ and were found to be comparable with that of the layer thickness. Lattice parameter values were calculated for both c-$Y_2O_3$ and t-$ZrO_2$ and were found to vary from 10.565 to 10.536 Å. The decrease in the lattice parameter values could be due to the combine effect of the interdiffusion as well as crystallization. The lattice parameter of $ZrO_2$ did not change significantly up to the temperature 1073 K and then increases significantly.

The multilayer was again heat treated for the second time, in the temperature range 300 - 1373 K and the HTXRD pattern is shown in Fig. 5.18 (b). The XRD pattern showed the presence of c-$Y_2O_3$ and t-$ZrO_2$ for the whole temperature range of the study. The lattice parameters was calculated for $Y_2O_3$ and were found to vary from 10.533 to 10.599 Å (Fig. 5.21(a) ) and for t-$ZrO_2$ the lattice parameter was found to be in the range of 3.588-3.623 (Fig. 5.19 (a)) and 5.090-5.182 Å (Fig. 5.20 (a)) with the increase in temperature. The variation in the lattice parameter values with temperature was fitted for second order polynomial fitting shown in equation 5.12, 5.13 and 5.14 for $Y_2O_3$ and $ZrO_2$ along a and c axis, respectively.

$$\boldsymbol{a_Y}(\text{Å}) = \mathbf{1.051 \times 10^{-9} + 7.129 \times 10^{-15} \times \boldsymbol{T} + 9.536 \times 10^{-20} \times \boldsymbol{T^2}} \ldots\ldots\ldots\ldots\ldots \textbf{(5.12)}$$

$$\boldsymbol{a_Z}(\text{Å}) = \mathbf{3.585 \times 10^{-10} + 5.299 \times 10^{-16} \times \boldsymbol{T} + 1.575 \times 10^{-18} \times \boldsymbol{T^2}} \ldots\ldots\ldots\ldots\ldots \textbf{(5.13)}$$

$$\boldsymbol{c_Z}(\text{Å}) = \mathbf{5.065 \times 10^{-10} + 7.762 \times 10^{-15} \times \boldsymbol{T} + 5.319 \times 10^{-19} \times \boldsymbol{T^2}} \ldots\ldots\ldots\ldots\ldots \textbf{(5.14)}$$

From the above three equations, the thermal expansion coefficient values were calculated and are listed in Table 5.8. The CTE values of $Y_2O_3$ were lower than that of the values in multilayers with 30 and 20 nm $ZrO_2$ layer thicknesses. Similarly for $ZrO_2$, the CTE values are higher in comparison to the CTE values of multilayers of (30/10) and (20/10) nm. This may be due to the higher interdiffusion of $Y_2O_3$ in to $ZrO_2$ layers as a result of the increase in number of interfaces.

TZ : Tetragonal phase of $ZrO_2$
Y: cubic phase of $Y_2O_3$
MY: monoclinic phase of $Y_2O_3$

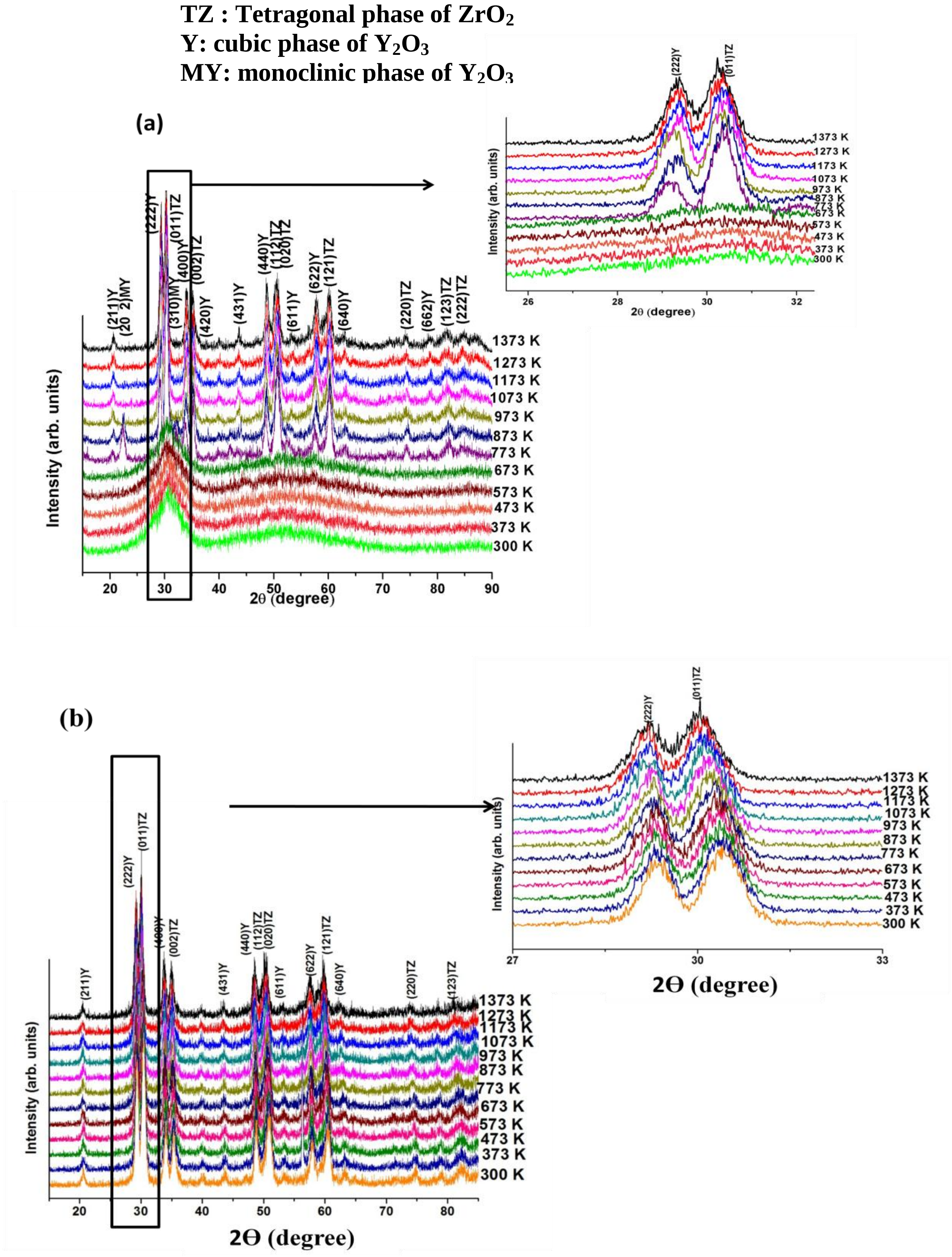

Fig. 5.18 The HTXRD patterns recorded in the temperature range of 300-1373 K for $ZrO_2/Y_2O_3$ multilayer film of (10/10) nm, deposited on Si (100) at 300 K and oxygen partial pressure of 2 Pa (a) first heat treatment and (b) second heat treatment. The inset shows the shift in the (222) and (011) reflections as an increase in temperature.

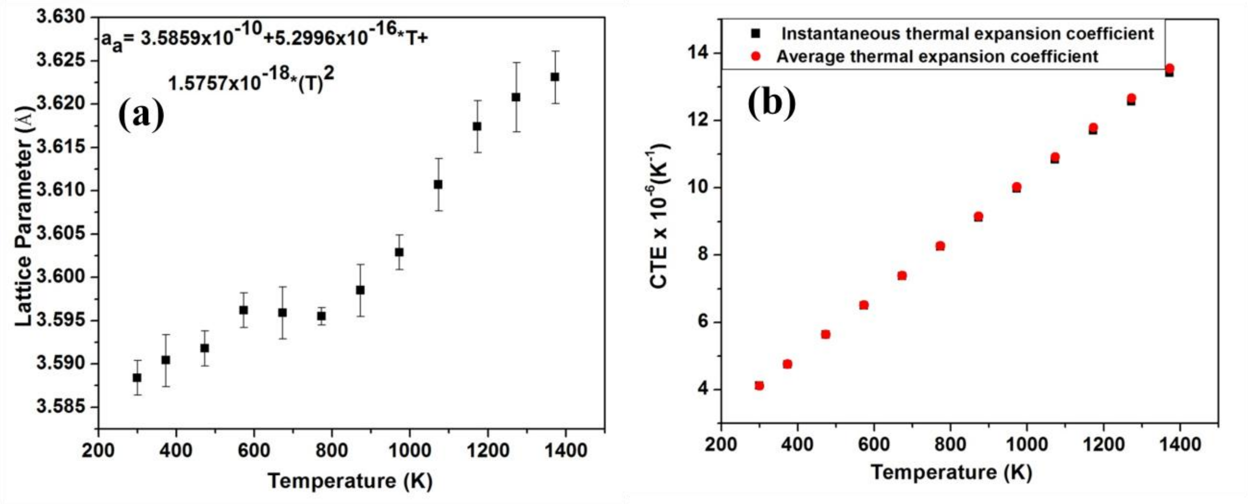

Fig. 5.19 (a) Lattice parameter and (b) average and instantaneous CTE variation of $ZrO_2$ with change in the temperature along a-axis for the $ZrO_2/Y_2O_3$ multilayer of (10/10) nm.

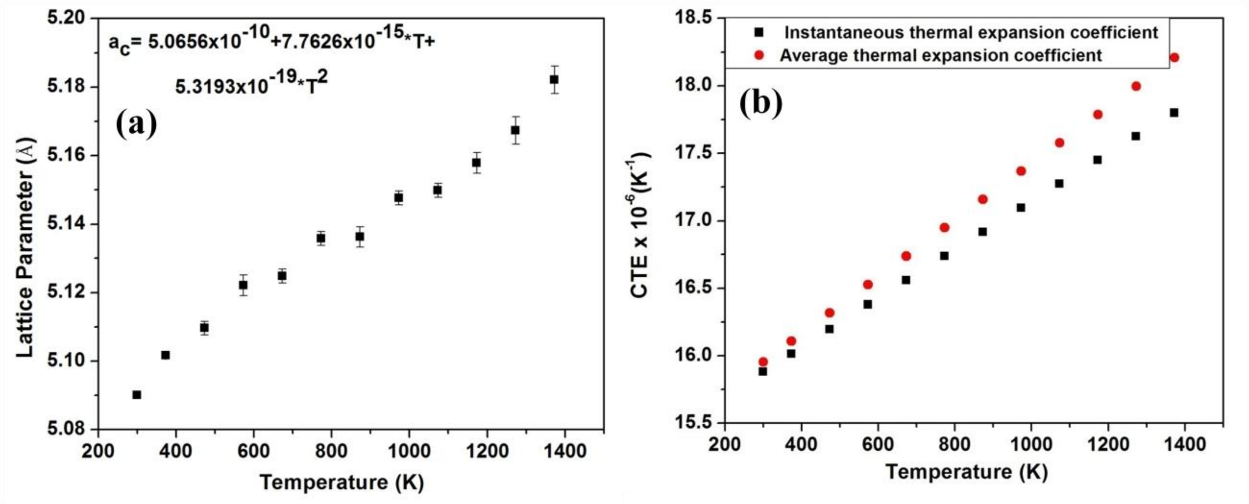

Fig. 5.20 Variation in the (a) lattice parameter (b ) average and instantaneous CTE values for $ZrO_2$ along c-axis, as a function of temperature for the $ZrO_2/Y_2O_3$ multilayer of (10/10) nm.

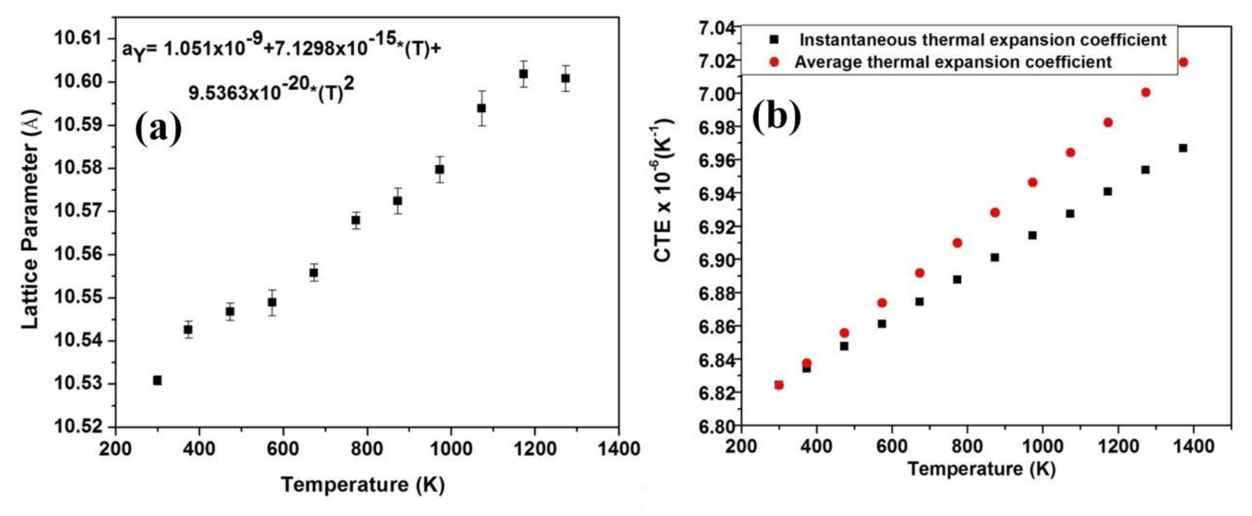

**Fig. 5.21 Variation of the (a) lattice parameter and (b) average and instantaneous CTE values of $Y_2O_3$ as a function of temperature for the $ZrO_2/Y_2O_3$ multilayer of 10 nm $ZrO_2$ layer thickness.**

**Table 5.8 Lattice parameter values and average CTE values of $Y_2O_3$ and $ZrO_2$ at different temperatures for the $ZrO_2/Y_2O_3$ multilayer with $ZrO_2$ layer thickness of 10 nm.**

| **Temperature (K)** | **$Y_2O_3$** | | **$ZrO_2$** | | | |
|---|---|---|---|---|---|---|
| | **Lattice parameter (Å)** | **CTE x $10^{-6}$ ($K^{-1}$)** | **Lattice parameter , *a* (Å)** | **CTE x $10^{-6}$ ($K^{-1}$) along *a*-axis** | **Lattice parameter , c (Å)** | **CTE x $10^{-6}$ ($K^{-1}$) along c-axis** |
| 300 | 10.533 | 6.82 | 3.588 | 4.11 | 5.090 | 15.95 |
| 373 | 10.543 | 6.83 | 3.590 | 4.75 | 5.101 | 16.11 |
| 473 | 10.547 | 6.85 | 3.592 | 5.63 | 5.109 | 16.32 |
| 573 | 10.548 | 6.87 | 3.596 | 6.51 | 5.122 | 16.52 |
| 673 | 10.556 | 6.89 | 3.596 | 7.39 | 5.125 | 16.73 |
| 773 | 10.568 | 6.90 | 3.595 | 8.27 | 5.135 | 16.94 |
| 873 | 10.572 | 6.92 | 3.598 | 9.15 | 5.136 | 17.15 |
| 973 | 10.579 | 6.94 | 3.603 | 10.02 | 5.147 | 17.36 |
| 1073 | 10.594 | 6.96 | 3.610 | 10.90 | 5.149 | 17.57 |
| 1173 | 10.602 | 6.98 | 3.617 | 11.78 | 5.157 | 17.78 |
| 1273 | 10.601 | 7.00 | 3.621 | 12.66 | 5.167 | 17.99 |
| 1373 | 10.599 | 7.01 | 3.623 | 13.54 | 5.182 | 18.21 |

#### 5.3.2.4 HTXRD of $ZrO_2/Y_2O_3$ multilayers of (5/10) nm

The HTXRD for the $ZrO_2/Y_2O_3$ multilayer of (5/10) nm, deposited at 300 K and oxygen partial pressure of 2 Pa was carried out and presented in Fig.5.22 (a). The pattern shows unique peaks from (211), (222), (400), (420), (431), (440) and (622) reflections of c-$Y_2O_3$, along with (011), (002), (112), (020) and (121) reflections of t-$ZrO_2$. At the temperature 773 and 873 K small amount of monoclinic phase of $Y_2O_3$ was also observed along with c-$Y_2O_3$.

The multilayer film was subjected to second heat treatment in the temperature range 300 K to 1373 K. XRD pattern of the multilayer at each temperature was recorded and is shown in Fig. 5.22 (b). Fig. 5.22 (b) showed peaks for (211), (222), (400), (332), (431), (440), (622), (631) and (640) planes of c-$Y_2O_3$ and (011), (002), (112), (020) and (121) planes of t-$ZrO_2$. The lattice parameter values of $Y_2O_3$ were calculated and plotted as a function of temperature (Fig. 5.23) and second order polynomial fitting was carried out and given in . The polynomial that fits to the plot of lattice parameter of $Y_2O_3$ versus temperature is given in equation 5.15.

$$\boldsymbol{a_Y}(\text{Å}) = \mathbf{1.053 \times 10^{-9} + 4.012 \times 10^{-15} \times \boldsymbol{T} + 1.862 \times 10^{-18} \times \boldsymbol{T}^2} \ldots\ldots\ldots \text{(5.15)}$$

Using the above equation the CTE values for $Y_2O_3$ were calculated and listed in Table 5.9. Both the average and instantaneous CTE were almost same. The CTE values of $Y_2O_3$ in the multilayer of (5/10) nm thickness were comparable with the CTE values obtained for the $Y_2O_3$ thin film in the previous section. Lattice parameter values of $ZrO_2$ were calculated but did not show any significant trend with change in temperature. This may be due to the severe inter-diffusion of $ZrO_2$ into the $Y_2O_3$ layers.

**TZ : Tetragonal phase of $ZrO_2$**
**Y: cubic phase of $Y_2O_3$**
**MY: monoclinic phase of $Y_2O_3$**

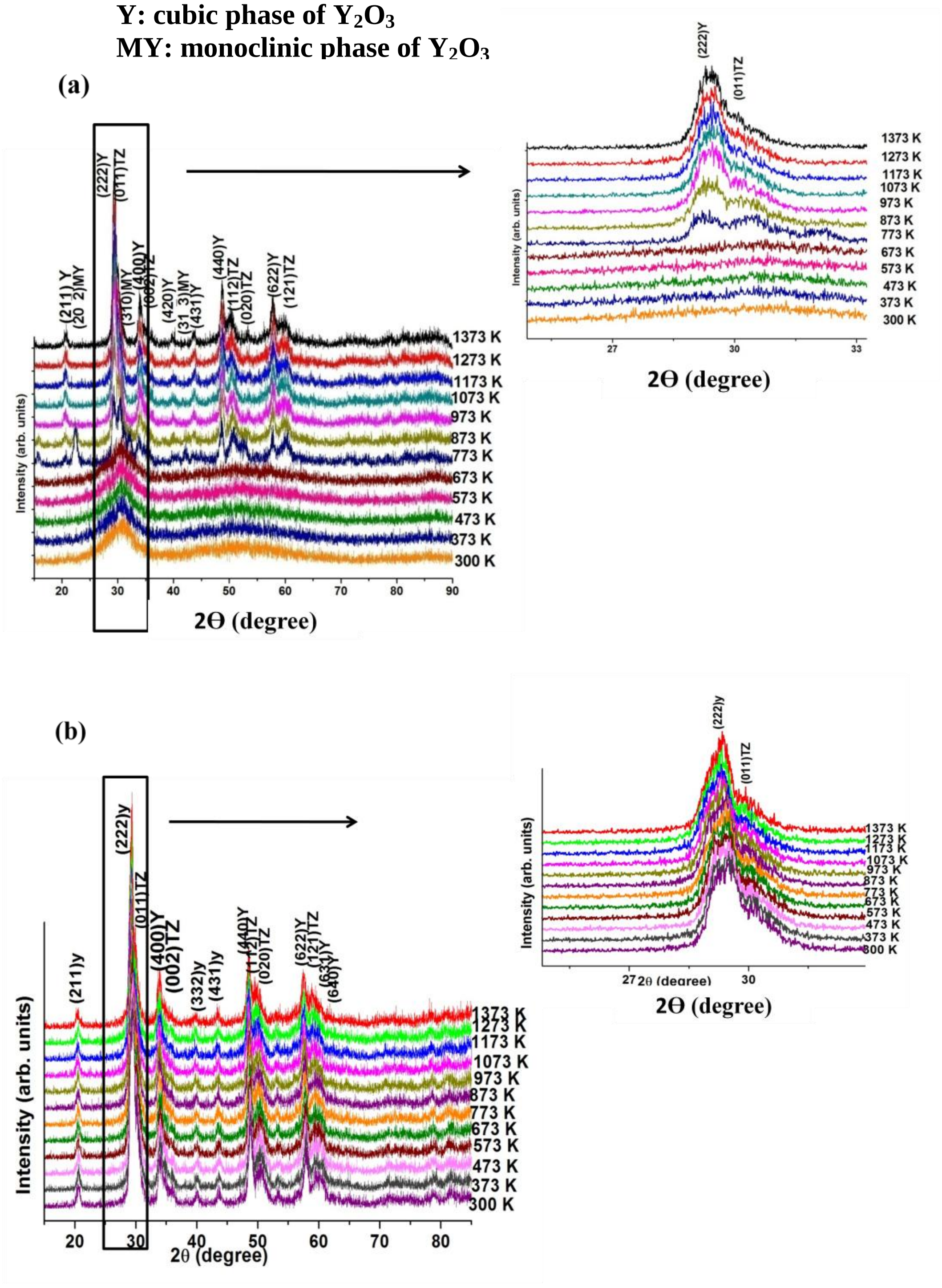

**Fig. 5.22 HTXRD pattern recorded during the (a) first heat treatment and (b) second heat treatment for the $ZrO_2/Y_2O_3$ multilayer film of (5/10) nm deposited on Si (100) at 300K and oxygen partial pressure of 2 Pa in the temperature range of 300-1373 K. The shift in the 2Θ position of the (222) reflection and (011) reflection are shown in the inset.**

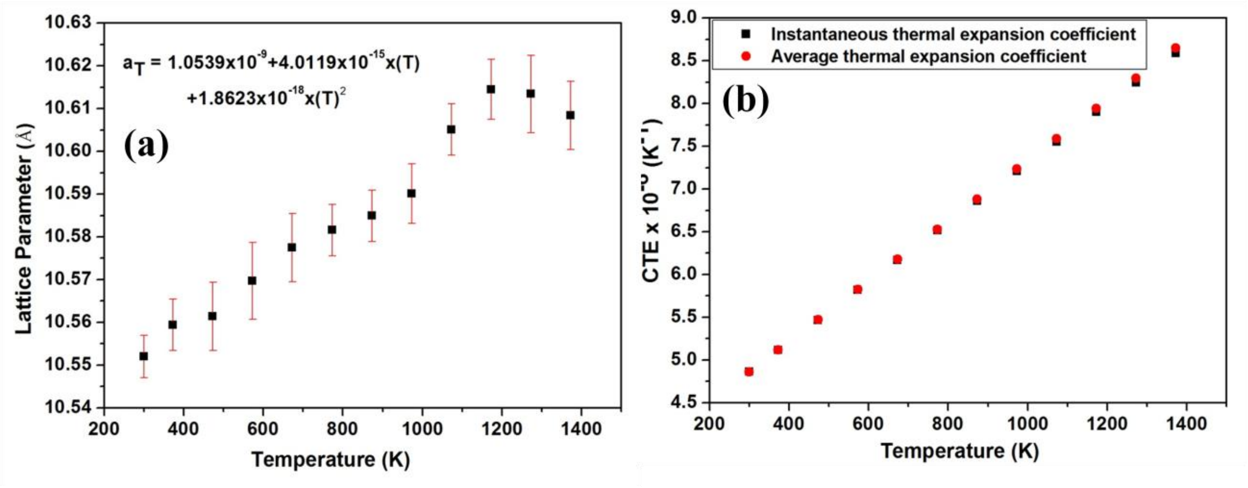

**Fig. 5.23 Variation of the (a) lattice parameter and (b) average and instantaneous CTE values of $Y_2O_3$ with an increase in temperature for the $ZrO_2/Y_2O_3$ multilayer of (5/10)nm.**

**Table 5.9 Lattice parameters and average CTE values of $Y_2O_3$ at different temperature for multilayer of $ZrO_2/Y_2O_3$ of (5/10) nm.**

| **Temperature (K)** | $Y_2O_3$ | |
|---|---|---|
| | **Lattice parameter (Å)** | **CTE x 10$^{-6}$ (K$^{-1}$)** |
| 300 | 10.552 | 4.86 |
| 373 | 10.559 | 5.11 |
| 473 | 10.561 | 5.47 |
| 573 | 10.569 | 5.82 |
| 673 | 10.577 | 6.17 |
| 773 | 10.581 | 6.53 |
| 873 | 10.584 | 6.88 |
| 973 | 10.590 | 7.23 |
| 1073 | 10.605 | 7.58 |
| 1173 | 10.614 | 7.94 |
| 1273 | 10.613 | 8.29 |
| 1373 | 10.608 | 8.64 |

### 5.3.2.5 HRTEM analysis of the $ZrO_2/Y_2O_3$ multilayer of (30/10) nm

Figure 5.24 shows the HRTEM images of $ZrO_2/Y_2O_3$ multilayer of (30/10) nm. The phases were confirmed by the SAD pattern obtained from the bands. The heat treated film showed the formation of t-$ZrO_2$ and c- $Y_2O_3$. The dark band corresponds to the $ZrO_2$ layers and the light band corresponds to the $Y_2O_3$ layers. The layer thickness obtained from the low magnification bright field image (Fig.5.24 (a)) was 32-36 nm and 12-15 nm for $ZrO_2$ and $Y_2O_3$, respectively. The high magnification images showed the inter-diffusion across the interfaces of the multilayer.

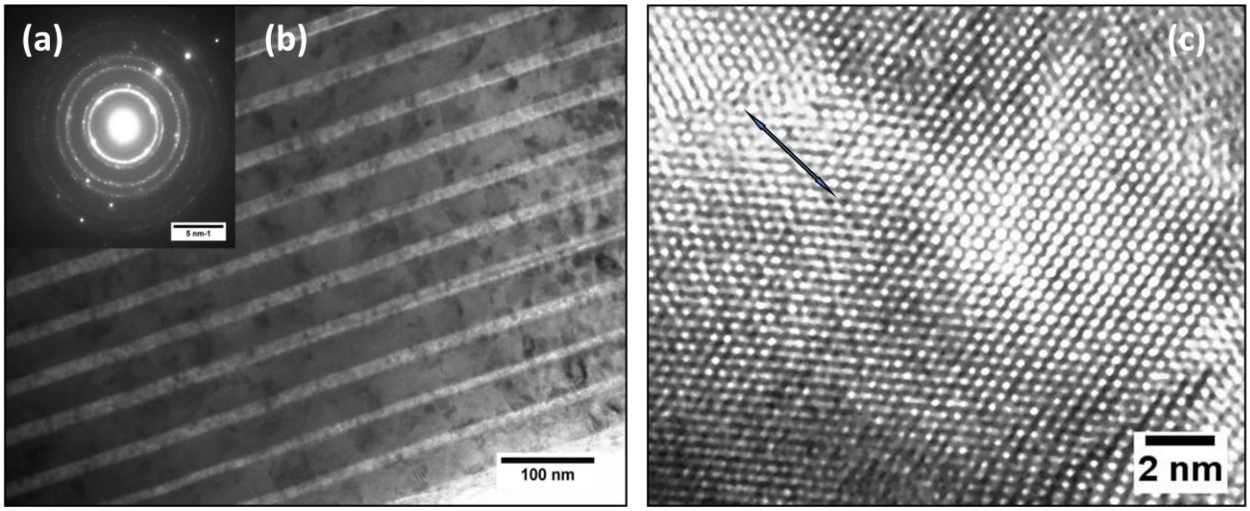

**Figure 5.24 A typical HRTEM image $ZrO_2/Y_2O_3$ multilayer of (30/10) nm after the first heat treatment (a) SAD pattern, (b) low magnification bright field image and (c) lattice imaging. The arrow mark indicates the interfaces of $ZrO_2$ and $Y_2O_3$.**

### 5.3.3 HTXRD of $CeO_2/Gd_2O_3$ multilayers

Multilayers of $CeO_2/Gd_2O_3$ were prepared on Si (100) substrates at 873 K and oxygen partial pressure of 2 Pa. HTXRD studies of all the multilayers were subjected to two heat treatment cycles in the temperature range 300 -1373 K.

#### 5.3.3.1 HTXRD studies of $CeO_2/Gd_2O_3$ of (30/10) nm

Figure 5.25 (a) shows the HTXRD pattern of $CeO_2/Gd_2O_3$ thin films of (30/10) nm deposited on Si (100) substrates in the temperature range 300 - 1373 K, recorded during the first heat treatment. The multilayer shows polycrystalline nature with peaks from cubic phase of $CeO_2$ and $Gd_2O_3$. HTXRD pattern showed peaks from (111), (200), (220), (311), (222), (400), (331), (420) and (422) planes of c-$CeO_2$ as well as (222), (400), (440), (622), (444), (800), (662), (840) and (844) plane of c-$Gd_2O_3$. Except these common reflections a unique reflection, corresponding to (123) reflection of c-$Gd_2O_3$ was also observed. As the lattice parameter of c-$Gd_2O_3$ (~10.8 Å) is twice than that of the lattice parameter of c-$CeO_2$, enough care was taken to monitor the phase changes as a function of temperature.

Although the target contains phase pure monoclinic $Gd_2O_3$, the multilayer films contains only cubic phase which may be due to the smaller layer thickness of $Gd_2O_3$. It has been reported by Molle et al. [27], that $Gd_2O_3$ thin films have a thickness dependence phase transition and when the thickness is $\geq$ 16.5 nm the phase transformation occurs from cubic to monoclinic structure. In the present investigation the layer thickness was kept ~10 nm for $Gd_2O_3$ as a result of which only cubic phase of $Gd_2O_3$ is observed. The lattice parameter values were calculated for both c-$CeO_2$ and c-$Gd_2O_3$ at different temperatures and are found to vary from 5.417 to 5.493 Å and 10.758 to 10.833 Å respectively. The stress value of the multilayer was estimated from the

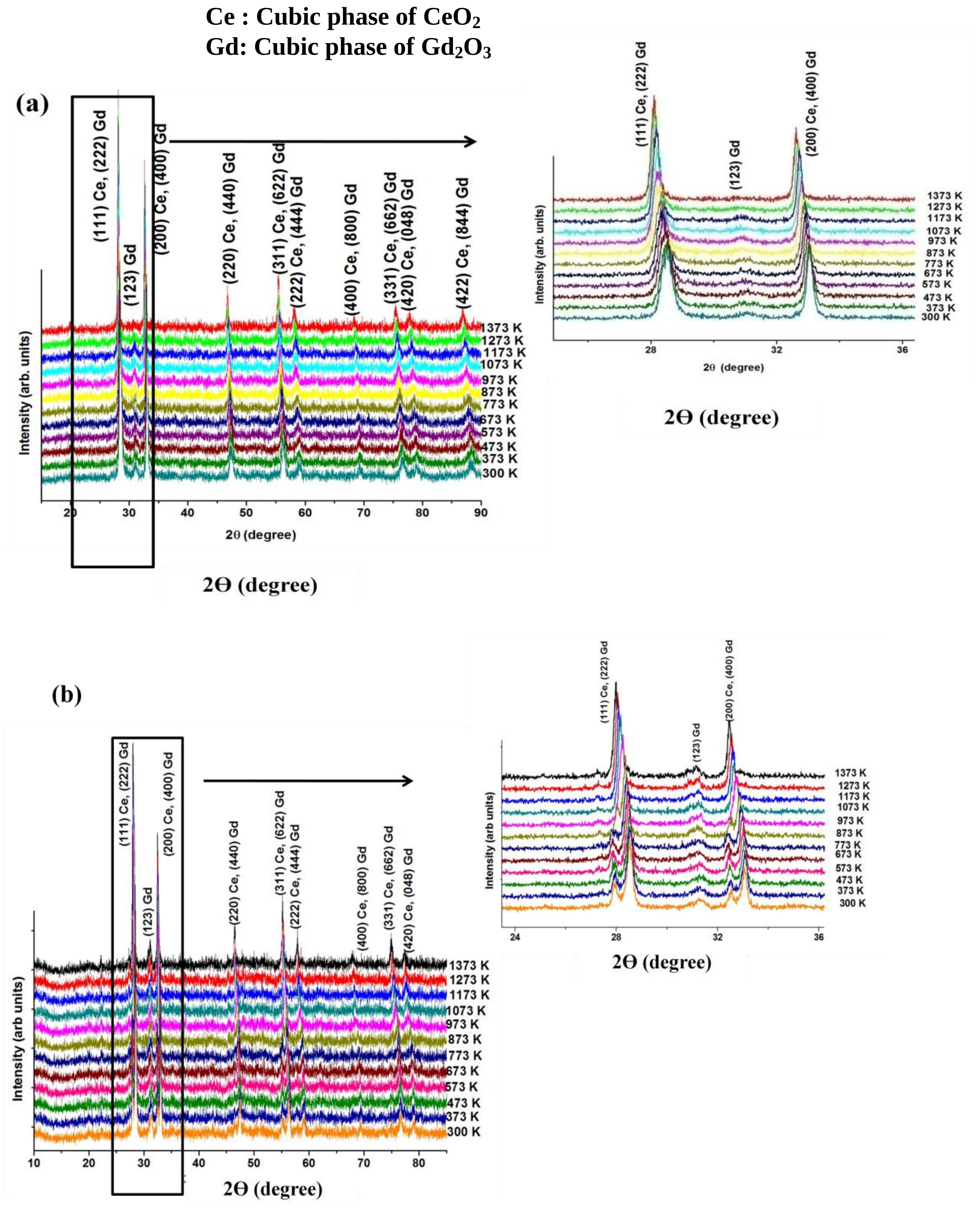

**Fig. 5.25 HTXRD patterns of $CeO_2/Gd_2O_3$ multilayer of (30/10) nm deposited on Si (100) at 873 K and the oxygen partial pressure of 2 Pa, recorded during the (a) first heat treatment (b) second heat treatment, in the temperature range 300 -1373 K. the inset shows the shift in 2Ө positions of (111), (222) and (123) peaks.**

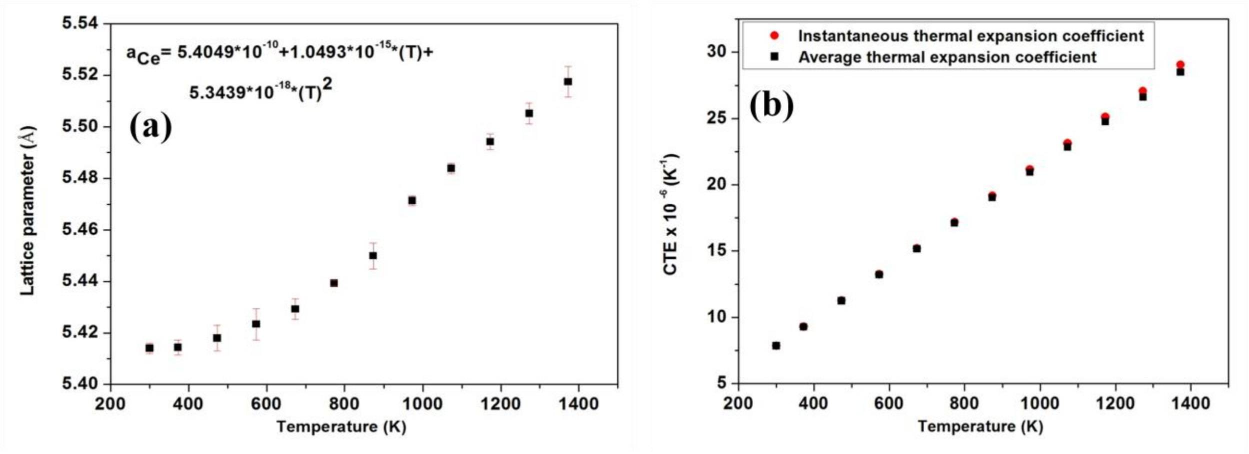

**Fig. 5.26 Variation in the (a) lattice parameter and (b) average and instantaneous CTE values of $CeO_2$ as a function of temperature for the $CeO_2$/$Gd_2O_3$ multilayer of (30/10) nm thickness.**

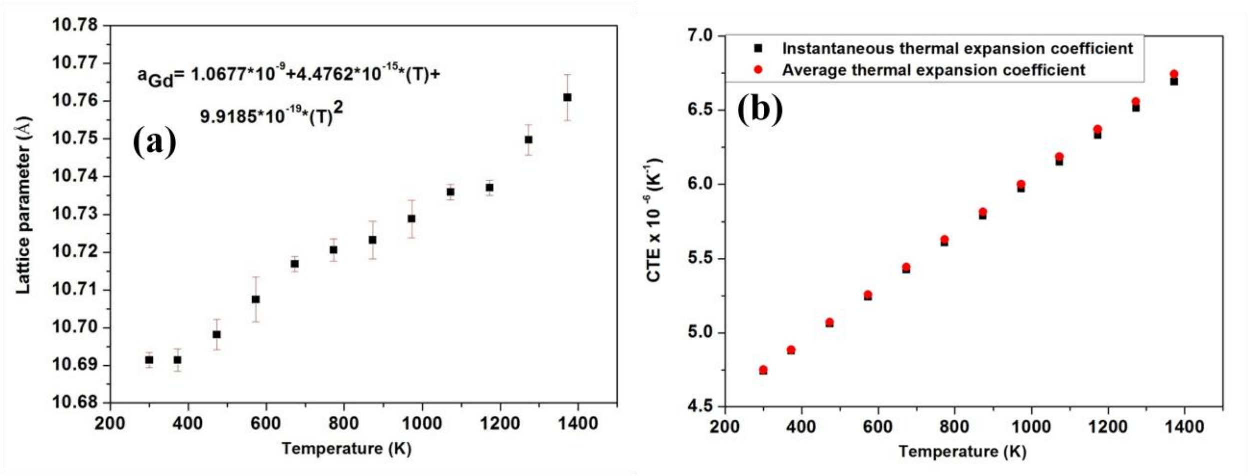

**Fig. 5.27 (a) lattice parameter and (ii) ) average and instantaneous CTE values of $Gd_2O_3$ as a function of temperature in the $CeO_2$/$Gd_2O_3$multilayer of (30/10) nm.**

**Table 5.10 Lattice parameter values and the average CTE values of $CeO_2$ and $Gd_2O_3$ at different temperature for multilayer of $CeO_2/Gd_2O_3$ of (30/10) nm.**

| **Temperature (K)** | **$CeO_2$** | | **$Gd_2O_3$** | |
|---|---|---|---|---|
| | **Lattice parameter (Å)** | **CTE x $10^{-6}$ ($K^{-1}$)** | **Lattice parameter (Å)** | **CTE x $10^{-6}$ ($K^{-1}$)** |
| 300 | 5.414 | 7.86 | 10.691 | 4.749 |
| 373 | 5.414 | 9.30 | 10.692 | 4.885 |
| 473 | 5.418 | 11.27 | 10.698 | 5.071 |
| 573 | 5.423 | 13.25 | 10.707 | 5.256 |
| 673 | 5.429 | 15.22 | 10.716 | 5.442 |
| 773 | 5.439 | 17.20 | 10.720 | 5.628 |
| 873 | 5.449 | 19.17 | 10.723 | 5.814 |
| 973 | 5.471 | 21.15 | 10.728 | 6.000 |
| 1073 | 5.483 | 23.12 | 10.735 | 6.185 |
| 1173 | 5.494 | 25.09 | 10.737 | 6.371 |
| 1273 | 5.505 | 27.07 | 10.749 | 6.557 |
| 1373 | 5.517 | 29.04 | 10.761 | 6.743 |

After the first heat treatment, the multilayer film was cooled to room temperature and again heat treated from 300 to 1373 K and the XRD patterns were recorded at each temperature (Fig. 5.25(b)). Lattice parameter values were calculated for both c-$CeO_2$ and c-$Gd_2O_3$ (Table 5.10) and plotted as a function temperature (Fig. 5.26 (a) and 5.27 (a)). The lattice parameters versus temperature plots of $CeO_2$ and $Gd_2O_3$ after second order polynomial fit are given in equation 5.16 and 5.17, respectively.

$$\boldsymbol{a_{Ce}}(\text{Å}) = \mathbf{5.4049 \times 10^{-10} + 1.0493 \times 10^{-15} \times (\boldsymbol{T}) + 5.3439 \times 10^{-18} \times \boldsymbol{T}^2} \;\ldots\ldots\; \mathbf{(5.16)}$$

$$\boldsymbol{a_{Gd}}(\text{Å}) = \mathbf{1.0677 \times 10^{-9} + 4.4762 \times 10^{-15} \times (\boldsymbol{T}) + 9.9185 \times 10^{-19} \times \boldsymbol{T}^2} \;\ldots\ldots\; \mathbf{(5.17)}$$

The lattice parameters of c-$CeO_2$ and c-$Gd_2O_3$ were found to vary from 5.414 to 5.517 Å and 10.691 to 10.761 Å, respectively with increase in the temperature (Table 5.10). Using the above two equations the average as well as instantaneous CTE values were calculated and were found to vary from 7.86 to 29.04 x$10^{-6}$ $K^{-1}$ and 4.74 to 6.74x $10^{-6}$ $K^{-1}$ for $CeO_2$ and $Gd_2O_3$, respectively. The larger variation of CTE values for $CeO_2$ than that of the CTE values of single layer $CeO_2$ can be attributed to the interdiffusion of $Gd^{3+}$ ions into $Ce^{4+}$ sites.

#### 5.3.3.2 HTXRD studies of $CeO_2$/$Gd_2O_3$ of (20/10) nm

The HTXRD pattern of the $CeO_2$/$Gd_2O_3$ mutilayer, with $CeO_2$ and $Gd_2O_3$ layer thickness of 20 and 10 nm, deposited on Si(100) at the substrate temperature of 873 K and oxygen partial pressure of 2 Pa were recorded during the first heat treatment in the temperature range 300-1373 K (Fig. 5.28 (a)). The film shows the polycrystalline nature with reflections from cubic phase of $CeO_2$ and $Gd_2O_3$. The film shows the formation of phase pure cubic $CeO_2$ and cubic $Gd_2O_3$ for the whole range of temperature. HTXRD pattern contains peaks from (111), (200), (220), (311), (331), (420) and (422) planes of cubic $CeO_2$ as well as (222), (400), (440), (622), (662), (840) and (844) planes of c-$Gd_2O_3$. Formation of cubic $Gd_2O_3$ from a monoclinic $Gd_2O_3$ target can be explained on the basis of layer thickness effect on cubic phase formation of $Gd_2O_{3.}$ The lattice parameter values, calculated from the XRD results of first heat treatment was found to vary from 5.4209 to 5.5020 Å and 10.753 to 10.903 Å for $CeO_2$ and $Gd_2O_3$, respectively.

After the first heat treatment, the multilayer was again heat treated from 300 to 1373 K to calculate the CTE values of $CeO_2$ and $Gd_2O_3$. The XRD patterns recorded at each temperature are shown in Fig. 5.28 (b).

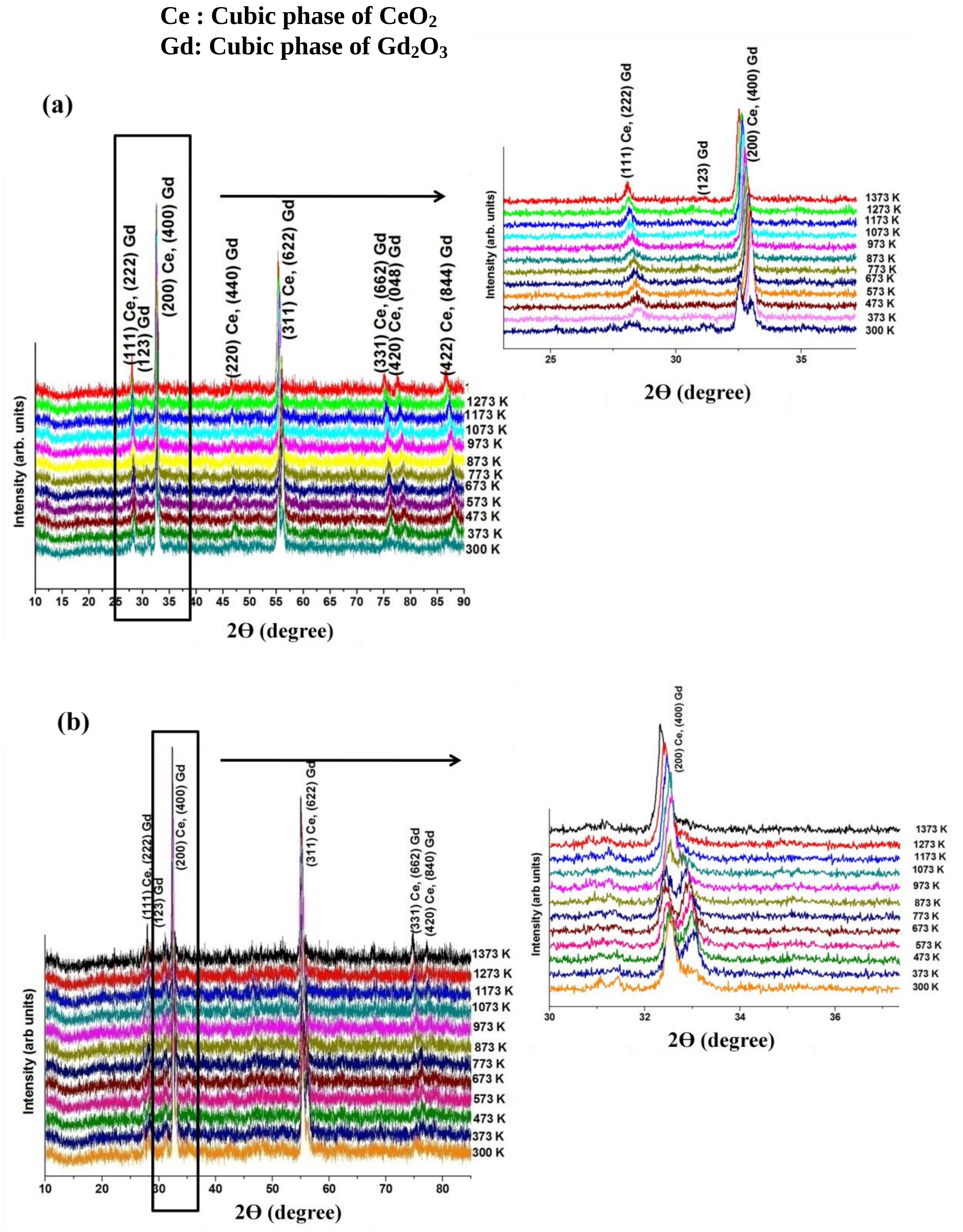

**Fig. 5.28 HTXRD pattern of CeO$_2$/Gd$_2$O$_3$ multilayer of (20/10) nm deposited on Si (100) at 873 K and oxygen partial pressure of 2 Pa, obtained during the (a) first heat treatment and (b) second heat treatment. The inset shows the peaks shift of the (111) and (200) reflections of CeO$_2$ and (222), (123) and (400) peak of Gd$_2$O$_3$ as a function of temperature.**

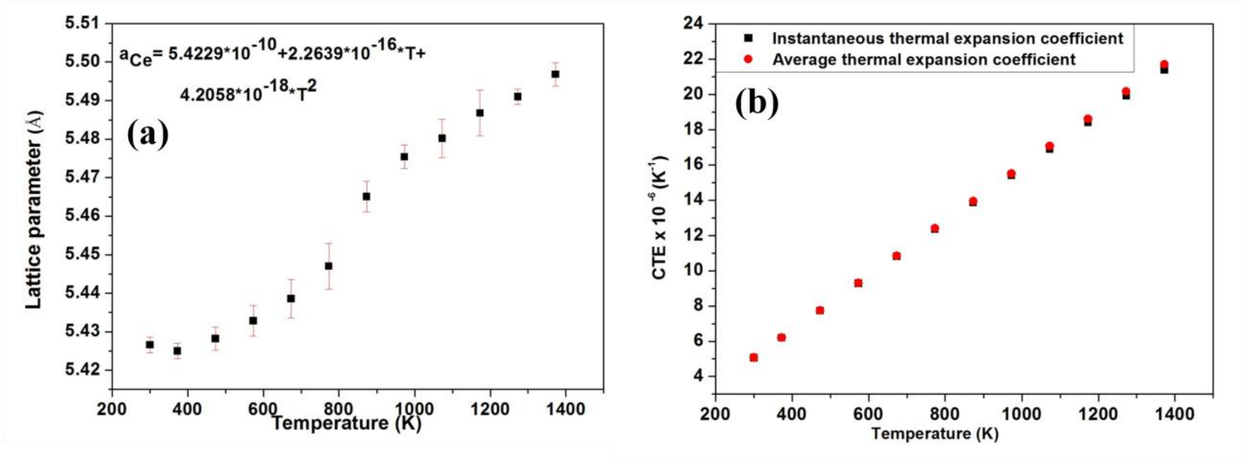

**Fig. 5.29** Variation in the (a) lattice parameter and (b) average and instantaneous CTE values of $CeO_2$ of $CeO_2/Gd_2O_3$multilayer of (20/10) nm as a function of temperature.

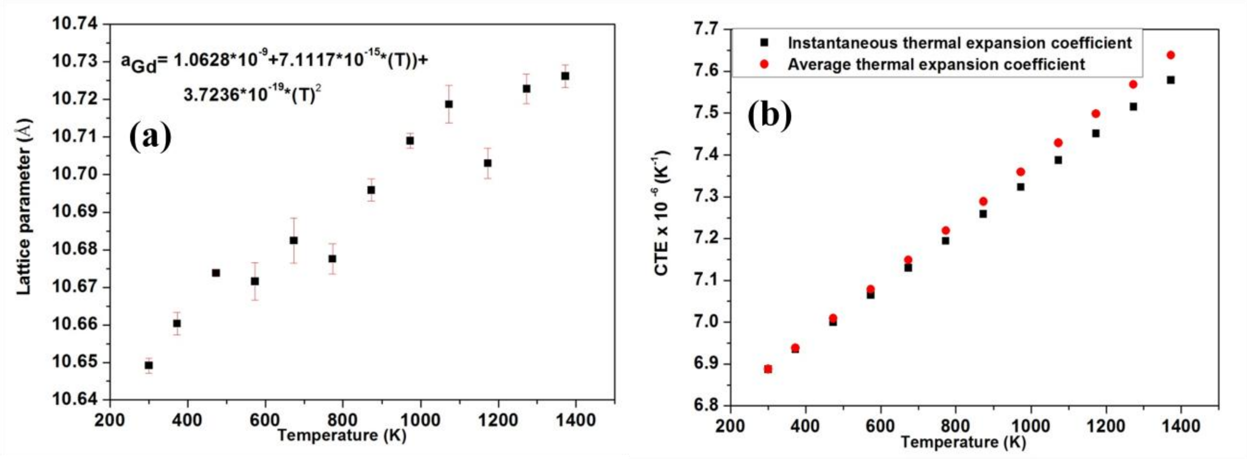

**Fig. 5.30** (a) lattice parameter and (b) average and instantaneous CTE values of $Gd_2O_3$ as a function of temperature for the multilayer with $CeO_2$ layer thickness of 20 nm.

Table 5.11 Lattice parameter values and average CTE values of $CeO_2$ and $Gd_2O_3$ at different temperature for multilayer of $CeO_2/Gd_2O_3$ of (20/10) nm.

| **Temperature (K)** | $CeO_2$ | | $Gd_2O_3$ | |
|---|---|---|---|---|
| | **Lattice parameter (Å)** | **CTE x $10^{-6}$ ($K^{-1}$)** | **Lattice parameter (Å)** | **CTE x $10^{-6}$ ($K^{-1}$)** |
| 300 | 5.426 | 5.07 | 10.649 | 6.88 |
| 373 | 5.425 | 6.20 | 10.660 | 6.93 |
| 473 | 5.428 | 7.75 | 10.673 | 7.01 |
| 573 | 5.432 | 9.30 | 10.671 | 7.07 |
| 673 | 5.438 | 10.85 | 10.682 | 7.14 |
| 773 | 5.447 | 12.40 | 10.677 | 7.21 |
| 873 | 5.465 | 13.95 | 10.695 | 7.28 |
| 973 | 5.475 | 15.50 | 10.708 | 7.35 |
| 1073 | 5.480 | 17.06 | 10.718 | 7.42 |
| 1173 | 5.486 | 18.61 | 10.703 | 7.49 |
| 1273 | 5.491 | 20.16 | 10.722 | 7.56 |
| 1373 | 5.496 | 21.71 | 10.726 | 7.63 |

The lattice parameters of both $CeO_2$ and $Gd_2O_3$ were calculated using unit cell program and are listed in Table 5.11. Fig. 5.29 and 5.30 shows the variations in the lattice parameters of $CeO_2$ and $Gd_2O_3$ with an in increase in temperature. The lattice parameter versus temperature plots were fitted for second order polynomial fitting as represented by equation 5.18 and 5.19, respectively.

$$\boldsymbol{a_{Ce}}(\text{Å}) = \mathbf{5.4229 \times 10^{-10} + 2.2639 \times 10^{-16} \times (\boldsymbol{T}) + 4.2058 \times 10^{-18} \times \boldsymbol{T}^2} \dots\dots\dots \mathbf{(5.18)}$$

$$\boldsymbol{a_{Gd}}(\text{Å}) = \mathbf{1.0628 \times 10^{-9} + 7.1117 \times 10^{-15} \times (\boldsymbol{T}) + 3.7236 \times 10^{-19} \times \boldsymbol{T}^2} \dots\dots\dots \mathbf{(5.19)}$$

Using the above two equations, the average and instantaneous CTE values for both $CeO_2$ and $Gd_2O_3$ were calculated and only average values are listed in Table 5.11. The calculated CTE values were plotted as function of temperature (Fig. 5.29 (b) and 5.30 (b)). The variation in CTE values of $CeO_2/Gd_2O_3$ multilayer with $CeO_2$ layer thickness of 20 nm is lower in comparison to the CTE values of multilayers with $CeO_2$ layer thickness as 30 nm.

### 5.3.3.3 HTXRD studies of $CeO_2/Gd_2O_3$ of (10/10) nm

Figure 5.31(a) shows the HTXRD pattern of $CeO_2/Gd_2O_3$ multilayer of (10/10) nm multilayer in the temperature range 300 to 1373 K, recorded during the first heat treatment. The film shows a polycrystalline structure for the above temperature range, showing peaks for (111), (200), (220), (311), (331), (420) and (422) reflections of cubic $CeO_2$ and (222), (400), (440), (622), (662), (840) and (844) planes of c-$Gd_2O_3$. Although the planes of c-$CeO_2$ and $Gd_2O_3$ have significant overlapping, the presence of $Gd_2O_3$ is confirmed from the reflection of (123) plane. In comparison to multilayer structure with 30 nm $CeO_2$ layer thickness, intensity of (200) of $CeO_2$ or (400) of $Gd_2O_3$ is higher, showing a preferred orientation along c-axis at lower $CeO_2$ layer thickness. The lattice parameter of $CeO_2$ and $Gd_2O_3$ were calculated for the first heat treatment, using “unit cell” program and is found to vary from 5.424 to 5.511 Å and 10.759 to 10.821 Å for $CeO_2$ and $Gd_2O_3$, respectively with increase in temperature. The stress value was estimated using $\Delta d/d_0$ for the film before and after the first heat treatment and found to decrease from 0.002-0.0005.

After the first heat treatment, the sample was cooled to room temperature and was again heat treated from 300 to 1373 K to calculate the CTE values. The XRD patterns were recorded at each temperature with 100 K interval and are shown in Fig. 5.31 (b). The lattice parameters for c-$CeO_2$ and c-$Gd_2O_3$ were calculated and listed in Table 5.12. The variation of lattice parameter for $CeO_2$ and $Gd_2O_3$ were plotted as a function of temperature and fitted for second order polynomial fitting using equation 5.20 and 5.21, respectively.

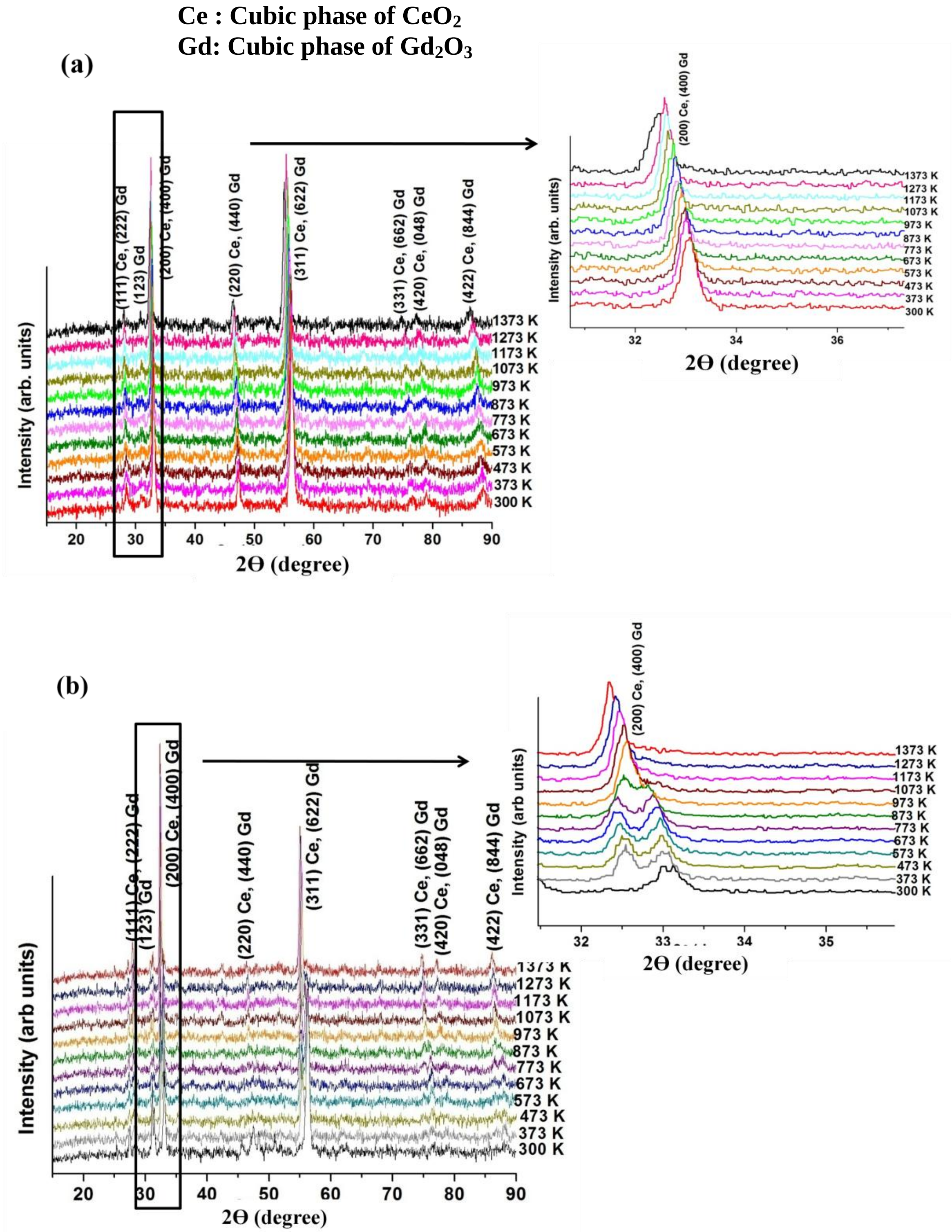

**Fig. 5.31 HTXRD patternobtained during (a) the first heat treatment and (b) the second heat treatment of $CeO_2/Gd_2O_3$ mutlilayer film of (10/10) nm deposited on Si (100) at 873 K and oxygen partial pressure of 2 Pa. The inset shows the shift in peak positions of the (200) and (400) peak of $CeO_2$and $Gd_2O_3$, respectively.**

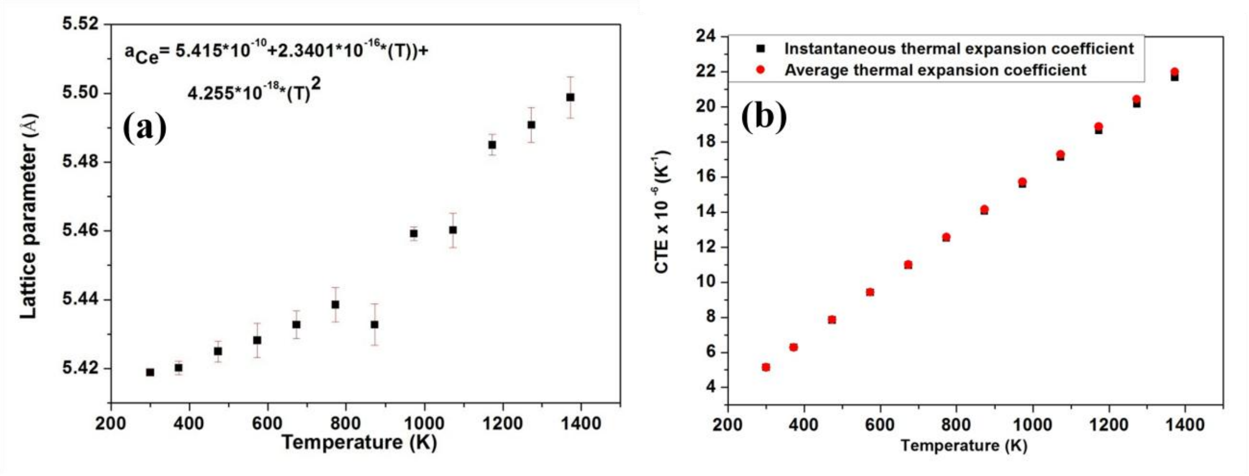

**Fig. 5.32 Variation in the (a) lattice parameter and the (b) average and instantaneous CTE values of $CeO_2$ with increase in the temperature for the $CeO_2/Gd_2O_3$ multilayer of (10/10) nm.**

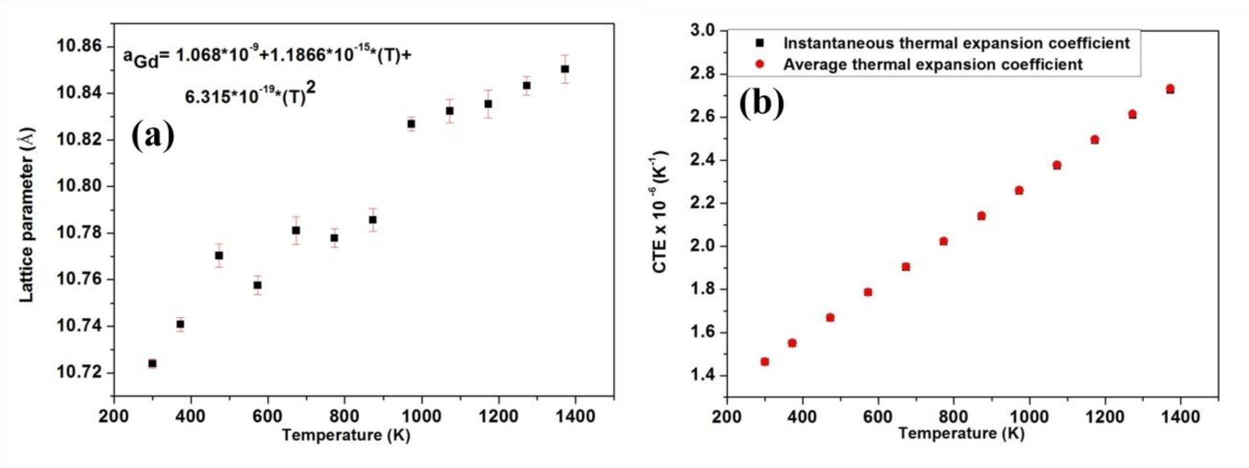

**Fig. 5.33 The variation in the (a) lattice parameter and the (b) average and instantaneous CTE values of $Gd_2O_3$ as a function of temperature for the $CeO_2$/ $Gd_2O_3$ multilayer with $CeO_2$ layer thickness of 10 nm.**

**Table 5.12 Lattice parameter values and the average CTE values of $CeO_2$ and $Gd_2O_3$ at different temperature for multilayer of $CeO_2/Gd_2O_3$ of (10/10) nm.**

| Temperature (K) | $CeO_2$ | | $Gd_2O_3$ | |
|---|---|---|---|---|
| | Lattice parameter (Å) | CTE x $10^{-6}$ ($K^{-1}$) | Lattice parameter (Å) | CTE x $10^{-6}$ ($K^{-1}$) |
| 300 | 5.418 | 5.14 | 10.723 | 1.46 |
| 373 | 5.420 | 6.29 | 10.740 | 1.55 |
| 473 | 5.425 | 7.86 | 10.770 | 1.66 |
| 573 | 5.428 | 9.43 | 10.757 | 1.78 |
| 673 | 5.432 | 11.01 | 10.781 | 1.90 |
| 773 | 5.438 | 12.58 | 10.777 | 2.02 |
| 873 | 5.432 | 14.15 | 10.785 | 2.14 |
| 973 | 5.459 | 15.72 | 10.826 | 2.25 |
| 1073 | 5.460 | 17.29 | 10.832 | 2.37 |
| 1173 | 5.485 | 18.86 | 10.835 | 2.49 |
| 1273 | 5.490 | 20.43 | 10.843 | 2.61 |
| 1373 | 5.498 | 22.01 | 10.850 | 2.73 |

$$\boldsymbol{a_{Ce}}(\text{Å}) = \mathbf{5.415 \times 10^{-10} + 2.3401 \times 10^{-16} \times (\boldsymbol{T}) + 4.255 \times 10^{-18} \times \boldsymbol{T^2}} \ldots\ldots\ldots \mathbf{(5.20)}$$

$$\boldsymbol{a_{Gd}}(\text{Å}) = \mathbf{1.068 \times 10^{-9} + 1.1866 \times 10^{-15} \times (\boldsymbol{T}) + 6.315 \times 10^{-19} \times \boldsymbol{T^2}} \ldots\ldots\ldots \mathbf{(5.21)}$$

Using the above two equations the average and instantaneous CTE values for $CeO_2$ and $Gd_2O_3$ were calculated for the multilayer structure with both $CeO_2$ and $Gd_2O_3$ layer thickness of 10 nm, and listed in Table 5.12. The CTE values of $Gd_2O_3$ were less in comparison to the CTE values of multilayers with $CeO_2$ layer thickness 30 and 10 nm. The least thermal expansion was observed for multilayer structure with least $CeO_2$ layer thickness due to increase in the number of interfaces and in the thickness along the z-direction of the multilayer. The peaks are quite broadened, which may be due to the dissolution of major part of layers of $CeO_2$ into $Gd_2O_3$.

### 5.3.3.4 HTXRD studies of $CeO_2/Gd_2O_3$ of (5/10) nm

HTXRD was carried out for the multilayer structure with $CeO_2$ layer thickness of 5 nm and $Gd_2O_3$ layer thickness of 10 nm. The multilayer was heat treated in the temperature range

**Ce : Cubic phase of $CeO_2$**
**Gd: Cubic phase of $Gd_2O_3$**
**m Gd: Monoclinic phase of $Gd_2O_3$**

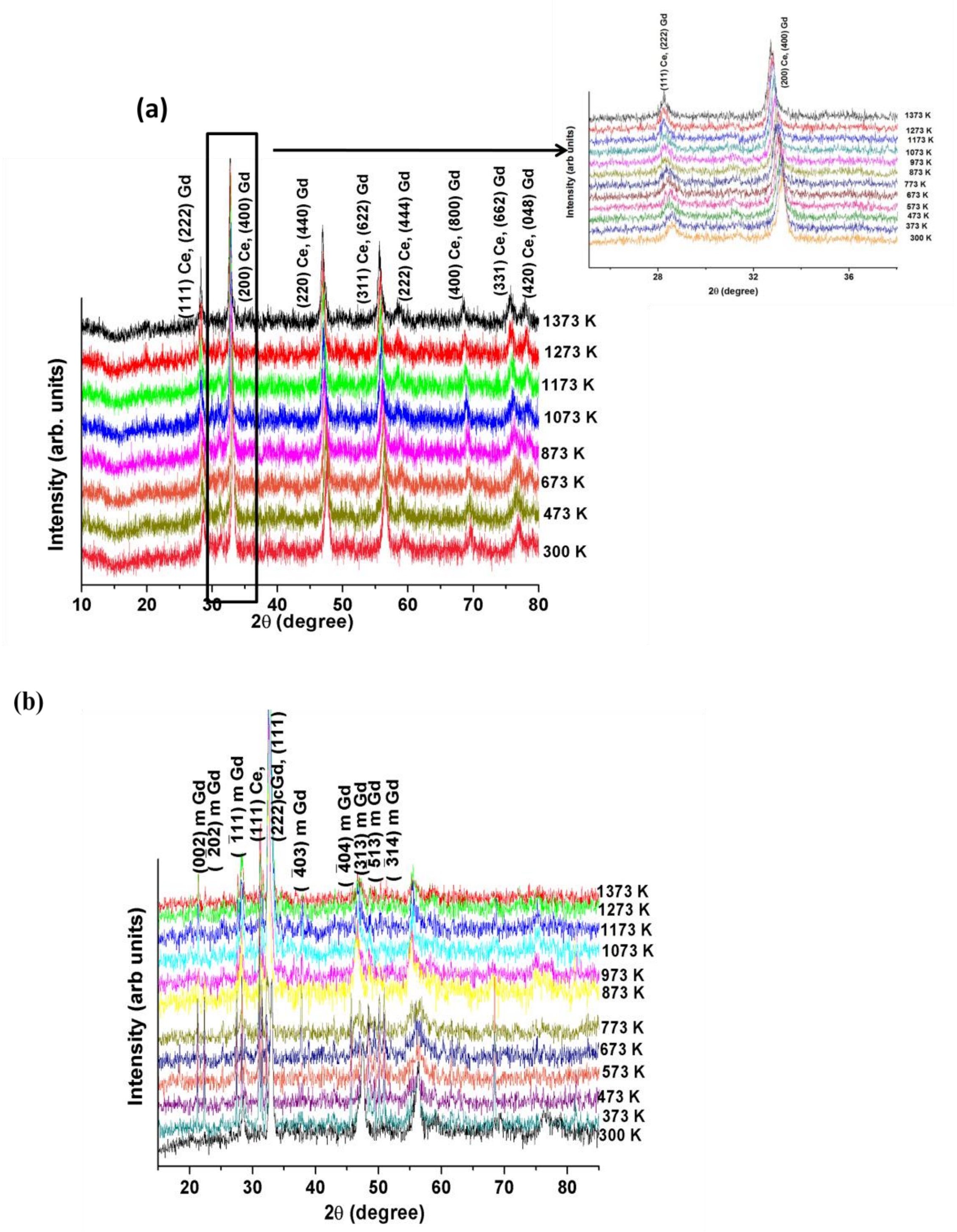

**Fig. 5.34 HTXRD pattern of $CeO_2/Gd_2O_3$ multilayer of (5/10) nm deposited on Si (100) at 873 K and oxygen partial pressure of 2 Pa in the temperature range 300-1373 K (a) first heat treatment (b) second heat treatment. The inset shows the peak shift of the (200) and (400) plane of $CeO_2$ and $Gd_2O_3$ respectively.**

300 – 1373 K and XRD patterns were recorded at an interval 100 K. The HTXRD pattern (Fig. 5.34 (a)) shows the formation of a polycrystalline film with peaks from (111), (200), (220), (311), (222), (400), (331) and (420) reflections respectively of c-$CeO_2$ and c-$Gd_2O_3$.

After the first heat treatment, the multilayer was cooled to room temperature and again heat treated from 300 to 1373 K (Fig. 5.34 (b)). Unlike that of the first heat treatment, the HTXRD pattern showed peaks from both cubic and monoclinic $Gd_2O_3$. The formation of m-$Gd_2O_3$ can be due to the inetrdiffusion effects. Since the $Gd_2O_3$ and $CeO_2$ have similar structures and lattice parameters, they tend to form solid solution at higher temperature. Therefore in the present case, during the heat treatment cycles, the $CeO_2$ could diffuse into $Gd_2O_3$ layers. Due to the interdiffusion, the thickness constrain for $Gd_2O_3$ was lost and the whole multilayer behaves as a single $Gd_2O_3$ layer. The lattice parameter as well as the CTE values was not calculated for this multilayer due to broadening of peaks and secondary phase formation.

#### 5.3.3.5 HRTEM analysis of $CeO_2$/$Gd_2O_3$ multilayer

A typical HRTEM study carried out on (20/10) nm thick bilayer of $CeO_2$/$Gd_2O_3$ is shown in Fig. 5.35. Figure 5.35 (a) shows the SAD pattern of the $CeO_2$/$Gd_2O_3$ multilayer after first heat treatment in HTXRD. The SAD pattern shows the formation of polycrystalline film with reflections from (111), (200), (220), (311), (400) and (331) of $CeO_2$ and (222), (400), (440), (622), (800) and (662) reflections of $Gd_2O_3$. The strong spots seen in the SAD pattern indicates the reflections from (100) Si.

Figure 5.35 (b) shows a low magnification bright field image of the $CeO_2$/$Gd_2O_3$ multilayer. The layer thickness obtained for $CeO_2$ and $Gd_2O_3$ are in the range of 15- 17.5 nm and 10-11 nm, respectively.

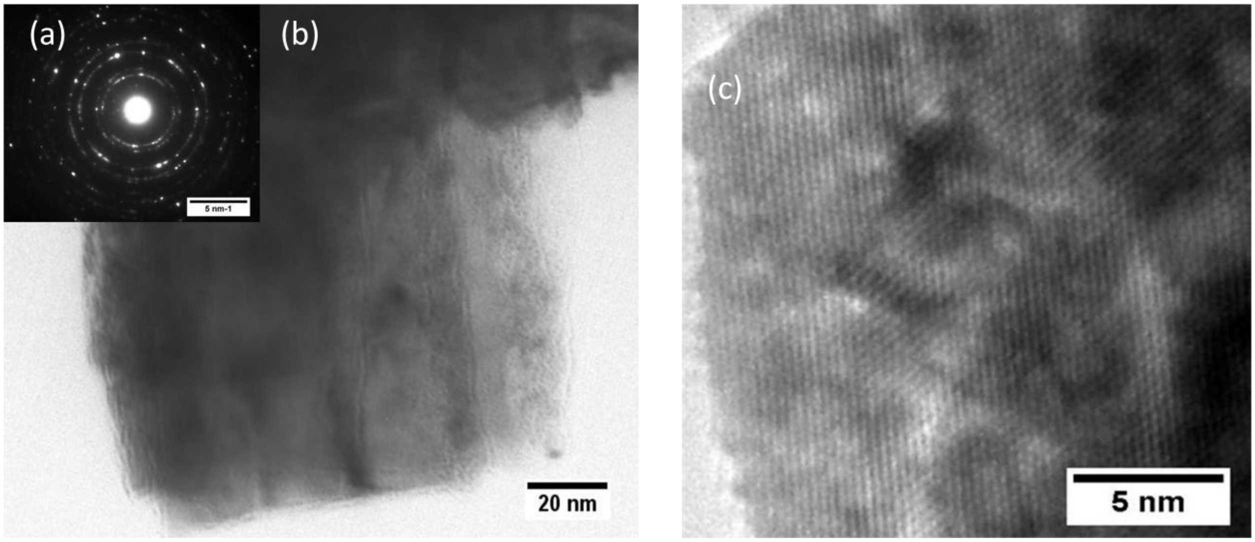

**Fig 5.35 TEM analysis of $CeO_2$/$Y_2O_3$ multilayer of (20/10) nm after the first heat treatment (a) SAD pattern (b) low magnification bright field image (c) lattice image of $CeO_2$ grain near the interface region.**

Figure 5.35 (c) shows the HRTEM image of a $CeO_2$ crystallite near the interface region, with d-spacings of 0.36 and 0.30 nm. The image indicates that the interface is no more planar and there is a clear atomic mixing due to inter-diffusion effects.

## 5.4 Discussion

### 5.4.1 Analysis of $Y_2O_3$, $ZrO_2$, $CeO_2$, $Gd_2O_3$ films

Thermal stability and phase evolution studies for $Y_2O_3$, $ZrO_2$, $CeO_2$, $Gd_2O_3$ thin films were carried out by HTXRD experiments. $Y_2O_3$, $ZrO_2$ and $Gd_2O_3$ films were found to be X-ray amorphous in the as deposited films, whereas $CeO_2$ formed a polycrystalline cubic structure at 300 K, which were already reported in the previous Chapters. The crystallization temperature for $Y_2O_3$, $ZrO_2$ and $Gd_2O_3$ films were found to be 773 K, 673 K and 773 K respectively. $Y_2O_3$, $CeO_2$ and $Gd_2O_3$ formed in cubic structure for the temperature range 300 - 1373 K and are in accordance with the phase diagram and in agreement with the results reported by other authors [7-9,19-24]. However, $ZrO_2$ film existed as a mixture of monoclinic and tetragonal phases in the above temperature range. However it has been shown in the present stydy that cubic phase of $ZrO_2$ was established by abalating a YSZ target containing 8 mol% of $Y_2O_3$.

Most of the materials have a tendency to expand when heated. The expansion is due to the anharmonic pair potentials between the atoms in a solid. When temperature increases the atoms starts to vibrate along the mean distance between the atoms and the thermal expansion is reflected by the increase in average distance between atoms. The thermal expansion behavior can be explained from the potential energy versus inter-atomic distance curve. Thermal expansion is due to the asymmetric part of the curve. When temperature increases the mean distance between the atoms also increases, leading to increase in mean distance between atoms. The extent of thermal expansion is dependent on the bond strength of the material. For materials with high bond energy the curve becomes deeper and narrower. As a result with increase in temperature the change in interatomic distance is not high. So the thermal expansion is also lower [28].

The thermal expansion behavior is not straight forward in case of thin film structures. Because thin film structures are associated with large amount of stress, defects as well as smaller crystallite sizes (leading to an increase in grain boundary area). Since grain boundary area is higher in this films, the grain boundary dominates the thermal expansion behavior [29,30]. As the atoms are weakly bonded near the grain boundaries, the expansion increases with increase in the temperature. The CTE of a material is also dependent on the porosity. In case of thin film structure, stress also contributes to thermal expansion. If a film is associated with compressive stress then CTE decreases, whereas tensile stress increases the CTE values.

The present study showed an increase in the lattice parameter for all the films with increase in temperature, with lower values of CTE for $Y_2O_3$ and $Gd_2O_3$ than that of $ZrO_2$ and $CeO_2$. Zhao et al. [31] have reported thickness dependence crystallization for $ZrO_2$ and found that the crystallization temperature increases with decrease in layer thickness. Bhagwat at al. [21] have also reported a linear increase in thermal expansion values with increase in temperature both along *a* and *c* axes. The CTE values of $CeO_2$ thin films also have been reported by many workers and the values vary from 4.6-13.17 x $10^{-6}$ $K^{-1}$ [9,32]. The difference in the CTE values reported by many workers was mainly due to the difference in measurement technique as well as microstructure due to deposition in the form of thin films.

Theoretical studies of the thermal expansion behavior have suggested an increase in CTE values for nanocrystalline materials than that of the bulk due to increase in the contribution thermal expansion from grain boundaries [33]. However literature information gives inconsistent observations on this issue. It has been reported that the CTE is independent of crystallite size [34,35], and showed an increasing trend with decrease in crystallite size [36], and decreasing trend with decreasing crystallite size [37]. Kuru et al. [38] have analyzed the crystallite size dependence of the thermal expansion behavior and suggested to anneal the thin film structure before measuring the CTE of thin films to induce grain growth and decrease crystal imperfection. Therefore, in the present study, we have reported the CTE values of these oxides after the first annealing treatment.

### 5.4.2 HTXRD of the mutlilayers

Phase stability and thermal expansion behavior of the $ZrO_2/Y_2O_3$ and $CeO_2/Gd_2O_3$ multilayers were analyzed by HTXRD experiments as a function of different layer thickness of $ZrO_2$ and $CeO_2$, respectively. The films were heat treated two times to make the film stress free and to estimate the CTE accurately. The multilayer films showed good stability with respect to the substrate. But the stability of interfaces was found to be decreased with decrease in layer thickness due to interdiffusion effects. The inter diffusion effects were also observed from the

HRTEM analysis of the multilayers across the interfaces. Therefore, the reported CTE in the present work is influenced by the thermal and interdiffusion effects.

Unlike the single layer films of $ZrO_2$ having a two phase structure, $ZrO_2$ was stabilized in tetragonal structure for all the multilayers. The multilayer structures were found to be X-ray amorphous at 300 K as both $ZrO_2$ and $Y_2O_3$ form amorphous structure when deposited at 300 K (already reported in the previous chapters). The films became crystalline at 773 K. $Y_2O_3$ was stabilized in cubic phase in the whole range of temperature and $ZrO_2$ layer thickness, except small volume fraction of monoclinic phase at 773 and 873 K [26]. Monoclinic $Y_2O_3$ was reported to be the high pressure phase of $Y_2O_3$ [39].

The multilayers of $CeO_2/Gd_2O_3$ were found to be polycrystalline. Single layer films of $Gd_2O_3$ deposited at 873 K (already reported in Chapter 4) was monoclinic, but when deposited in the form of multilayer it was found to be stabilized in cubic structure. This was attributed to the thickness dependant phase transformation of $Gd_2O_3$ film already reported by many authors [27].

The lattice parameter values of $Y_2O_3$, was found to decrease with increase in temperature, during the first heat treatment. This was due to the interdiffusion effect. $Y_2O_3$ and $ZrO_2$ are known to form a good solid solution. Because of the solubility of $ZrO_2$ in $Y_2O_3$ is ~20 % where as solubility of $Y_2O_3$ in $ZrO_2$ ~50-55% (from the phase diagram of $Y_2O_3$ and $ZrO_2$) [40]. The ionic radii of $Y^{3+}$ (~101 pm) [41] is greater than that of $Zr^{4+}$ ions (~80 Pm) [42]. When temperature was increased, the $Y^{3+}$ sites were replaced by $Zr^{4+}$ resulting in a lattice contraction [43]. The decrease in the lattice parameter values with the increase in temperature, has also been reported in literature as a result of replacement of atomic lattice by relatively smaller sized ions [44].

In the present study, the lattice parameter values of both $CeO_2$ and $Gd_2O_3$ were found to increase with increase in temperature in all the multilayers during the first heat treatments. This may be due to the smaller difference in ionic radii of Ce $^{4+}$ (~90Å) [45] and $Gd^{3+}$ (~97 Å) ) [45]. The CTE values of both $CeO_2$ and t-$ZrO_2$ in the multilayers were found to be higher than that of the values reported for the single layer films in the previous sections. The reason could be the replacement of the $Zr^{4+}$ (~84 pm) and $Ce^{4+}$ (~90Å) [45] sites by $Y^{3+}$(101 pm) and $Gd^{3+}$ (~97 Å) [45], respectively. The CTE values of t-$ZrO_2$ in multilayers increases with decrease in $ZrO_2$ layer thickness which result in higher thermal expansion with increase in temperature [46] than that of the pure materials.

The thermal expansion behavior of the multilayers were studied as a function of bilayer thickness and it was found for $ZrO_2/Y_2O_3$ multilayer structure the CTE values of t-$ZrO_2$ increases with decrease in $ZrO_2$ layer thickness. The increase in average CTE of t-$ZrO_2$ values is due to the replacement of smaller $Zr^{4+}$ ions with larger $Y^{3+}$ ions leading to higher expansion. Interdiffusion will also lead to formation of oxygen vacancies. The increase in oxygen vacancy concentration will lead to an increase in the thermal expansion. With the decrease in layer thickness of $ZrO_2$, the interdiffsion increases due to the increase in number of interfaces and increase in total interdiffusion area. Similar results were also reported by Hayashai et al. [47] for gadolinia doped ceria (GDC). It has been reported by the authors that with increase in gadolinia content, the CTE values increases as a result of the increase in oxygen vacancies and decrease in bond energy [47]. At the same time, the CTE value of $CeO_2$ in the multilayers show opposite trend. This may be due to the smaller variation in ionic radii of $Ce^{4+}$ and $Gd^{3+}$.

The measurement of CTE values is quite complex in $ZrO_2/Y_2O_3$ and $CeO_2$/ $Y_2O_3$, because the measured property involves interdiffusion, ionic repulsion, oxygen vacancies as well as thermal expansion simultaneously. However, detailed careful experiments along with HRTEM are very important towards understanding of the thermal behavior of the multialyers. The present work presented a very detailed data on thermal expansion behavior of four oxides and their multilayers. These data would be of great relevance in selection of theses multilayers for many technological applications.

## 5.5 Summary

### 5.5.1 $Y_2O_3$, $ZrO_2$, $CeO_2$ and $Gd_2O_3$ single layer films

**(i)** $Y_2O_3$, $ZrO_2$ and $Gd_2O_3$ formed amorphous structure at room temperature, whereas $CeO_2$ was polycrystalline even at room temperature. The crystallization temperature for $Y_2O_3$ and $Gd_2O_3$ were found to be 773 K, whereas $ZrO_2$ was crystallized at 673 K.

**(ii)** The lattice parameter values were found to increase with increase in temperature due to lattice vibration. The CTE values calculated for the films were comparable with the reported literature values.

**(iii)** The films show good thermal stability in the temperature range of 300 -1373 K.

### 5.5.2 $Y_2O_3/ZrO_2$ and $CeO_2/Gd_2O_3$ multilayer structures

**(i)** Multilayers of $ZrO_2/Y_2O_3$, $CeO_2/Gd_2O_3$ were also prepared on Si (100) substrates at oxygen partial pressure of 2 Pa and substrate temperature of 300 K and 873 K, respectively.

(ii) HTXRD analysis of $ZrO_2/Y_2O_3$ showed that in all the multilayers, $ZrO_2$ was stabilized in tetragonal phase. $Y_2O_3$ mainly existed in cubic structure except for a small volume fraction of metastable monoclinic phase at 773 and 873 K.

(iii) Multilayer structures of $CeO_2/Gd_2O_3$ were doubly heat treated in the temperature range of 300 – 1373 K to study the effect of $CeO_2$ layer thickness on the thermal expansion and phase stability. $CeO_2$ existed in cubic phase in the whole temperature range. $Gd_2O_3$ was also stabilized in cubic phase for the multilayers with $CeO_2$ layer thickness 30-10 nm, as a result of smaller layer thickness

(iv) The CTE values calculated for both $ZrO_2$ and $CeO_2$ showed higher values than those of the CTE of single layers. The increase in CTE values was mainly due to the interdiffusion effects occurring in the multilayers.

## 5.6 References

1. J. M. Shapiro, D. R. Taylor, G. M. Graham, Can. J. Phys. 42 (1964) 835.
2. R. E. Kinzly, Appl. Optics, 6(1967)137., S. F. Jacobs, J. N. Bradford, J. W, berthold, Appl. Opt. 9(1970) 2477.
3. J. D. James, J. A. Spittle, S. G. R. Brown, R. W. Evans, Meas. Sci. Technol. 12 (2001)R1.
4. D. N. Batchelder, R. O. simmons, J. Chem. Phys. 41 (1964) 2324.
5. H. Rafla-Yuan, B. P. Hichwa, T. H. Allen, J. Vac. Sci. Technol. A 16 (1998) 3119.
6. W. Fang, Hsin-Chung Tsai, Chun-yen Lo, Sensors and actuators, 77(1999)21.
7. V. Swamy , N. A. Dubrovinskaya, L. S. dubrovinsky, J. Mat. Res. 14 (2) (1999) 456.
8. R. N. Patil. E. C. Subbarao, J. Appl. Cryst. 2 (1696) 281.
9. R. G. Schwab, R. A. Steiner, G. Mages, H. J. Beie, Thin Solid Films, 207 (1992) 288
10. P. T. Sawbridge, N. A. Waterman, J. Materials Sciences 3(1968) 15.
11. G. Balakrishnan, P. Kuppusami, S. Murugesan, C. Ghosh, R. Divakar, E. Mohandas, D. Sastikumar, Materials Chemistry and Physics,133 (2012) 299.
12. G. Balakrishnan, P. Kuppusami, S. Murugesan, C. Ghosh, R. Divakar, E. Mohandas, D. Sastikumar, Trans. IIM, 64 (3) (2011) 297.
13. H. C. Barshilia, B. Deepthi, K. S. Rajam, J. Appl. Phys. 104 (2008) 113532.

14. S. Burinskas, V. Adomonis, V. Zalanierukynas, J. Dudonis, D. milcius, Mater. Sci., 16 (1) (2010) 67.
15. L. H. Van Vlack, Elements of Material Sci. Eng. Addison Wesley,1989.
16. W. Backel, J. Vac. Soc. Techn. 6 (1969) 606, L. Eckertova, Physics of thin solid films, (Plenum press) (1967) 202.
17. E. A. Hill, G. R. Hoffman, Br. J. Appl. Phys. 18 (1967) 13.
18. G. Lebrun, J. Denault, Composited Part A: 41 (2010) 101.
19. V. Swamy , H. J. Seifert, F. Aldinger, J. Alloy. Compd. 269 (1998) 201.
20. C. E. Curtis, J. Am. Ceram. Soc. 40 (8) (1957) 274.
21. M. Bhagwat, V. Ramaswamy, Mater. Res. Bull. 39 (2004) 1627.
22. G. I. Zhuravlev, Sov. Powder Metall. Met. Ceram. (1966)793.
23. Y. A. Piragov, Refractories 27 (1962) 356.
24. M. Zinkevich, Prog. Mater. Sci. 52 (2007) 597.
25. A. C. Momin, M. D. Mathews, Ind, J. Chem. 15A (1977) 1096.
26. V. Gourlaouen, G. Schnedecker, A. M. Lejus, M. Boncoeur, R. Collongues, Mat. Res. Bull. 28 (1993) 415.
27. A. Molle, C. Weimer, Md. Nurul bhuiyan, G. Tallarida, M. Fanciulli, Appl. Phys. Let. 90 (2007) 193511.
28. G. D. Barrera, J. A. O. Bruno, T. H. K. Barron, N. L. Allan, J. Phys: Condensed Matter, 17 (2005) R217.
29. R. Daniel, D. Holec, M. Bartosik, J. Keckes, C. Mitterer, Acta Materialia 59(2011) 6631.
30. M. Kiguchi, T. Yokoyama, D. Matsumura, H. Kondoh, O. Endo, T. Ohta, Phys. Rev. B61 (2000)14020.

31. C. Zhao, G. Roebben, H. Bender, E. Young, S. Haukka, Microelectron Eng. 41(2001)995.
32. G.I. Zhuravlev, Soy. Powder Metall. Met. Ceram. (1966) 793.
33. M. Wagner, Phys. Rev. B 45 (1992) 635.
34. J. Harada, K. Ohshima, Surf. Sci. 106 (1981) 51.
35. J. A.Eastman, M. R. Fitzsimmons, L. J. Thompson, A. C. Lawson, R. A. Robinson, Nanostruct. Mater. 1 (1992) 465.
36. K. Lu, M. L. Sui, Acta. Metal. Mater. 43(1995) 3325.
37. W. Wang, C. Y. Lo, Sens. Actuator, 84 (2000) 310.
38. Y. Kuru, M. Wohlschlogel, U. welzel, E. J. Mittemeijer, Appl. Phys. Lett. 90 (2007) 243113.
39. E. Husson, C. Proust, P. Gillet, J.P. Itie, Mater . Res. Bull. 34 (12-13) (1999) 2085.
40. P. Duwez, F. H. Brown, J. F. Odell, J. Electrochem.Soc. 98 (9) (1951) 356.
41. D. Kim, S. Hyun,S. Kim, M. Yashima, J. Am. Ceram. Soc. 77 (2) (1994) 597.
42. N. K. Karan, R. S. Katiyar, T. Maiti, R. Guo, A. S. Bhalla, J. Raman Spectr. 40 (4) (2009) 370.
43. J. Friedel (1955), LX. Deviations from Vegard's law, Philosophical Magazine Series 7, 46:376, 514.
44. R. Roy, D. K. Agrawal, H. A. McKinstry, Annu. Rev. Mater. Sci. 19 (1989) 59.
45. R. D. Shannon, Acta. Crystallogr. A 32 (1976) 751.
46. V. Grover, A. K. Tyagi, Mater. Res. Bull. 39 (2004) 859.
47. H. Hayashi, M. Kanoh, C. JiQuan, H. Inaba, S. Wang, M. Dokiya, H. Tagawa, Solid State Ionics 132 (2000) 227.

# Chapter 6

## *Summary and Conclusions*

# 6. Summary and Conclusions

The present work describes of the deposition and characterization of $Y_2O_3$, $ZrO_2$, $CeO_2$ and $Gd_2O_3$ thin films prepared by pulsed laser deposition. The effect of the substrate temperature and oxygen partial pressure on the microstructural, optical and nanomechanical properties of these films were studied. The preparation of multilayer structures of $ZrO_2/Y_2O_3$ and $CeO_2/Gd_2O_3$ at 300 K and 873 K with constant $Y_2O_3$ and $Gd_2O_3$ layer thickness were carried out to investigate the effect of the substrate temperature and layer thickness on the microstructural, optical, nanomechanical and thermal expansion properties. Both the single layer films and the multilayer films of these oxides were deposited on Si (100), quartz and Inconel-783 substrates to study the microstructural, optical and nanomechanical properties, respectively. The important conclusions drawn from the present work reported in Chapters 3, 4 and 5 are listed below:

## 6.1 $Y_2O_3$ Thin Films

(i) At room temperature $Y_2O_3$ film was found to be x-ray amorphous. The crystallinity of the film was found to increase with increase in the substrate temperature. The roughness values were dependent on the crystallite size of the film and are found to increase with increase in temperature due to increase in the crystallite size.

(ii) The optical properties of $Y_2O_3$ films deposited at different substrate temperatures are found to be influenced by variation in substrate temperature. Whereas the optical properties of $Y_2O_3$ films do not show significant changes with respect to change in oxygen partial pressure. The film deposited at 873 K and oxygen partial pressure of 2 Pa was found to have highest transmittance and band gap values, indicating the formation of best quality film at this particular substrate temperature and oxygen partial pressure.

## 6.2 $ZrO_2$ Thin Films

(i) $ZrO_2$ films showed both temperature and oxygen partial pressure dependant phase transformation. The tetragonal phase content was found to increase with the increase in the substrate temperature and oxygen partial pressure. But a phase pure film of pure t-$ZrO_2$ or m-$ZrO_2$ could not be achieved from a target containing mixture of t-$ZrO_2$ or m- $ZrO_2$ phases.

(ii) The roughness values of the films were highly influenced by the crystallite size which in turn affects the optical properties of the films. The films deposited at higher substrate temperature showed lower value of transmittance than that of the films deposited at lower substrate temperature.

(iii) The refractive index was found to increase with increase in substrate temperature and decrease in oxygen partial pressure as a consequence of the variation in microstructure of the films.

## 6.3 $ZrO_2/Y_2O_3$ Multilayers

(i) The multilayers of $ZrO_2/Y_2O_3$ were found to be x-ray amorphous at room temperature and became polycrystalline at 873 K with c-$Y_2O_3$, t-$ZrO_2$ and m-$ZrO_2$ phases. The surface and interfacial roughness values were found to increase with increase in the substrate temperature and the layer thickness due to the increase in crystallinity of the films.

(ii) The transmittance of the $ZrO_2/Y_2O_3$ multilayers deposited at the substrate temperature of 873 K are found to be lower than that of the multilayer films deposited at 300 K, as a result of the loss of light by scattering due to higher surface roughness values of the multilayers. The transmittance of the multilayers with lower bilayer thickness was found to be lower than that of the films with higher bilayer thickness. This was due to the increase of number of interfaces with decrease in the bilayer thickness which causes the loss of light by scattering at the interface.

(iii) Nanomechanical properties of the $ZrO_2/Y_2O_3$ multilayer structures were found to be unaffected by the change in bilayer thickness. This is explained on the basis of the similar elastic modulus values of $ZrO_2$ and $Y_2O_3$.

### 6.4 $CeO_2$ Thin Films

(i) $CeO_2$ was found to form a polytcrystalline cubic structure even at room temperature. The crystallinity was found to increase with the change in preferred orientation from (111) to (200) with increase in the substrate temperature and the oxygen partial pressure due to the lowering of surface energy along this direction.

(ii) The optical transmittance was found to be ~70-85 %. The transmittance value was found to decrease with increase in the substrate temperature as a consequence of an increase in the roughness values which results in the loss of light by interface scattering.

(iv) No significant changes in the refractive index values were found as a function of substrate temperature and oxygen partial pressure.

### 6.5 $Gd_2O_3$ Thin Films

(i) $Gd_2O_3$ films formed an amorphous structure at 300 K and a crystalline film at 473 K. The film mainly contained monoclinic phase of $Gd_2O_3$ with small volume fraction of cubic phase at lower substrate temperatures. With increase in the substrate temperature, pure monoclinic phase was formed as a result of the decrease in stress values.

(ii) The surface roughness values were found to be dependent on crystallite sizes and increases with increase in the crystallite sizes.

(iii) The transmittance values of $Gd_2O_3$ films were found to be in the range of 60-90 %. The variation of transmittance as a function of microstructure could not be brought out clearly due to the formation of mixed phases at intermediate temperature range.

(iv) A phase pure $Gd_2O_3$ film with highest band gap of 5.80 eV was obtained at 873 K and oxygen partial pressure of 0.2 Pa.

(v) The refractive index of the $Gd_2O_3$ film was found to vary from 1.6-1.8 with decrease in the substrate temperature as a result of the formation of good quality film at higher substrate temperature.

## 6.6 $CeO_2/Gd_2O_3$ Multilayers

(i) The $CeO_2/Gd_2O_3$ multilayer films was found to be polycrystalline at room temperature. This is because the $CeO_2$ is stabilized in cubic form even at room temperature. The crystallinity was higher for the multilayer with higher bilayer thickness. At 873 K the film was found to have cubic phases of both $CeO_2$ and $Gd_2O_3$, in contrast to the monoclinc phase formation in single layers of $Gd_2O_3$. The formation of cubic phase of $Gd_2O_3$ was attributed to the smaller layer thickness of $Gd_2O_3$ grown on cubic phase of $CeO_2$, and high amount of stress present in the multilayer structure.

(ii) The absorption spectra showed two absorption edges at ~350 nm and ~220 nm corresponding to $CeO_2$ and $Gd_2O_3$, respectively. The band gap values of the films of $CeO_2$, were found to increase with the increase in the substrate temperature and layer thickness of $CeO_2$. The band gap of $Gd_2O_3$ was found to increase with increase in temperature. The layer thickness of $CeO_2$ shows opposite effects for the films grown at 300 K and 873 K. The band gap of $Gd_2O_3$ increases with increase in layer thickness of $CeO_2$ for the multilayer deposited at 873 K, whereas it decreases for the multilayers deposited at 300 K.

(iv) The hardness and elastic modulus values of the $CeO_2/Gd_2O_3$ multilayer films were found to be higher for the multilayers with $CeO_2$ layer thickness in the range of 10-30 nm. The multilayer structure with 10 nm $CeO_2$ layer thickness was found to have higher resistance to plastic deformation values due to the difference in elastic modulus values of $CeO_2$ and $Gd_2O_3$.

## 6.7 Thermal Stability and Thermal Expansion

(i) All the films show a good thermal stability on Si substrates in the temperature range of 300-1373 K. $Y_2O_3$, $CeO_2$ and $Gd_2O_3$ were found to form cubic structure, where as $ZrO_2$ was formed as a mixture of phases.

(ii) The CTE values obtained for $Y_2O_3$, $ZrO_2$, $CeO_2$ and $Gd_2O_3$ thin films are comparable with the CTE values reported for bulk materials.

(iii) The CTE values of t-$ZrO_2$ and $CeO_2$ are higher in multilayers than that of the single layers due to inter-diffusion effects.

(iv) In case of $ZrO_2/Y_2O_3$ multilayers, the $ZrO_2$ was found to be stabilized in tetragonal phase for all layer thickness. During heat treatment the lattice parameter values of $Y_2O_3$ were found to decrease with increase in temperature as a result of the inter-diffusion effects.

(v) In addition to the expansion of the lattices due to thermal effect, the thermal expansion behavior of the multilayers studied in the present work was appeared to be complex owing to the inter-diffusion of the layers at higher annealing temperatures.

## Future Directions

1. Some of the phase transformations occurring in multilayers are influenced by the crystallite size in single layer films and thickness of the individual layers in multilayer films. A series of efforts need to be taken to measure the residual stress in these films and multilayers to conclude the role of stress in the stabilization of metastable phase and on the phase transformation.
2. A detailed work on HRTEM as a function of layer thickness is necessary to conclude on the mechanism of interdiffusion, phase transformation at the interfaces and compositional changes produced as a consequence of interdiffusion.
3. In the present work, the optical properties of the films and multilayers were investigated using UV-Visible spectroscopy. However, other methods such as ellipsometry, photoluminescence spectroscopy must be tried on the basis of several models which take several interfaces into consideration.
4. In the present work, a lot of data on thermal expansion behavior of the multilayers as a function of layer thicknesses has been generated. However, this data is a result of simultaneous influence of thermal expansion due to thermal annealing and inter-diffusion. Theoretical and experimental approaches must be undertaken to deconvolute these informations more accurately.

## List of Publications

1. **"Effect of Substrate Temperature and Oxygen Partial Pressure on Microstructure and Optical Properties of Pulsed Laser Deposited Yttrium Oxide Thin Film". M. Mishra**, P. Kuppusami, T. N. Sairam, Akash Singh, E.Mohandas, Appl. Surf. Sci. 257 (2011) 7665.
2. **"Phase Evolution in Zirconia Thin Films Prepared by Pulsed Laser Deposition". M. Mishra**, P. Kuppusami, A. Singh, S. Ramya, V. Sivasubramanian, E. Mohandas, Appl. Surf. Sci. 258 (2012) 5157.
3. **"Microstructural and Optical Characterization of $ZrO_2/Y_2O_3$ Multilayers Prepared by Pulsed Laser Deposition". M. Mishra**, P. Kuppusami, V. R. Reddy, A. Singh, G. Chinnamma, C. Ghosh, R. Divakar, E. Mohandas, J. NanoSci. Lett. (2013) 3:4.
4. **"Influence of $CeO_2$ Layer Thickness on the Properties of $CeO_2/Gd_2O_3$ Multilayers Prepared by Pulsed Laser Deposition". M. Mishra**, Maneesha Mishra, P. Kuppusami, V. R. Reddy, C. Ghosh, R. Divakar, R. Ramaseshan, Akash Singh and E. Mohandas. (Manuscript under Review: Surface and Coating Technology).

5. **"Study of structural and optical properties of $Gd_2O_3$ thin films as a function of oxygen partial pressure". M. Mishra**, P. Kuppusami, A. Singh, R. Thirumurugesan, E. Mohandas (To be communicated to Thin Solid Films).
6. **"Stability of $ZrO_2/Y_2O_3$ multilayer structures By HTXRD". M. Mishra**, P. Kuppusami, A. Singh, S. Murugesan, R. Thirumurugesan, E. Mohandas. (To be submitted to Materials Chemistry and Physics).
7. **"Study of Thermal Stability of $CeO_2/Gd_2O_3$ multilayers prepared using pulsed laser deposition". M. Mishra**, P. Kuppusami, A. Singh, R. Thirumurugesan, E. Mohandas. (To be communicated to J. Alloys and Compounds).